Experimental and numerical analysis of behavior of electromagnetic annular linear induction pump

Linards Goldsteins

THÈSE

Pour obtenir le grade de

DOCTEUR DE L'UNIVERSITÉ GRENOBLE ALPES

préparée dans le cadre d'une cotutelle entre l'*Université Grenoble Alpes* et *Université de Lettonie*

Spécialité : **IMEP2 / MECHANIQUE DES FUIDES, PROCEDES, ENERGETIQUE**

Arrêté ministériel : le 6 janvier 2005 - 7 août 2006

Présentée par

Linards GOLDŠTEINS

Thèse dirigée par **Yves FAUTRELLE** et **Leonīds BULIGINS**
codirigée par **Christine BISCARRAT**

préparée au sein des **SIMAP/EPM**

dans **IMEP2 / MECHANIQUE DES FUIDES, PROCEDES, ENERGETIQUE**

Analyse expérimentale et numérique du comportement électromagnétique de pompe à induction linéaire annulaire

Thèse soutenue publiquement le **« 30/10/2015 »**,
devant le jury composé de :

Mr. Thierry ALBOUSSIERE
Docteur, Université de Lyon, Président
Mr. André THESS
Professeur, Université de Stuttgart, Rapporteur
Mme. Inta VOLODKO
Professeur, Université Technique de Riga, Rapporteur
Mr. Yves FAUTRELLE
Professeur, Université Grenoble Alpes, Membre
Mr. Leonīds BULIGINS
Professeur, Université de Lettonie, Membre
Mme. Christine BISCARRAT
Docteur, *Commissariat à l'énergie atomique et aux énergies alternatives*, Membre

University of Latvia

Grenoble Institute of Technology

Commissariat à l'énergie atomique et aux énergies alternatives (CEA) Cadarache

PhD Thesis:

Experimental and numerical analysis of behaviour of electromagnetic annular linear induction pump

Author: Linards Goldšteins

Thesis supervisor: Leonīds Buligins (University of Latvia)

Thesis supervisor: Yves Fautrelle (Grenoble Institute of Technology)

Riga/Grenoble/Cadarache

2015

Table of Contents

List of symbols and abbreviations

Symbols (if not specified otherwise in text):

$A\ \left[\frac{Wb}{m}\right]$, magnetic vector potential

$B\ [T]$, magnetic field flux (B_e – external, B_i – induced, B_0 – amplitude, B_x, B_z – components)

$E\ \left[\frac{V}{m}\right]$, electrical field intensity

$j\ \left[\frac{A}{m^2}\right]$, current density ($j_e$ – external)

$\rho_q\ \left[\frac{C}{m^3}\right]$, charge density

$\mu_0\ \left[\frac{H}{m}\right]$ & μ, magnetic permeability of vacuum and relative magnetic permeability

$\varepsilon_0\ \left[\frac{F}{m}\right]$, dielectric permittivity of vacuum

$\sigma\ \left[\frac{S}{m}\right]$, conductivity

$\omega_B\ \left[\frac{rad}{s}\right]$, angular frequency of magnetic field

$\varphi,\ \theta\ [rad]$, angular dimension

$v\ \left[\frac{m}{s}\right]$, velocity ($v_z, v_\varphi$ ... - components, v_B – magnetic field)

$\rho\ \left[\frac{kg}{m^3}\right]$, mass density

$f\ \left[\frac{N}{m^3}\right]$, force density ($f_{EM}$ – electromagnetic, f_λ - friction)

$p\ \left[\frac{N}{m^2}\right]$ & $\Delta p\ \left[\frac{N}{m^2}\right]$, pressure and pressure difference

$\eta\ \left[\frac{N}{m^2 \cdot s}\right]$, dynamic viscosity

λ_h, friction factor

$\zeta_h\ \left[\frac{1}{m}\right]$, linear density of friction

$d_h\ [m]$, height of the channel (d_m - non-magnetic gap)

$\omega\ \left[\frac{rad}{s}\right]$, vorticity

$\tau\ [m]$, half wave length

$\alpha = \frac{\pi}{\tau}\ \left[\frac{rad}{m}\right]$, wave number

$L\ [m]$, length of the channel

$R\ [m]$, mean radius of channel

$j_{lin}\ \left[\frac{A}{m}\right]$, linear current density (J – effective value)

$Q\ \left[\frac{m^3}{s}\right]$, volumetric flowrate

m, - azimuthal wavenumber

κ_m – geometrical parameter (κ_m' - modified)

Tilde over the symbol ($\tilde{p}$) signifies dimensionless parameter.

$\tilde{v}, \tilde{b}$ – dimensionless velocity and magnetic field

$\delta\tilde{v}, \delta\tilde{b}$ – dimensionless amplitudes of velocity and magnetic field perturbations

$\widetilde{v_z}, \widetilde{b_c}$ – dimensionless steady state solutions of axial velocity and amplitude of magnetic field

n, γ - complex spatial and temporal development rates

$\tilde{p}$ – dimensionless pressure ($\tilde{p}_m$ – convective instability threshold, $\tilde{p}_a$ – absolute instability threshold)

$\sum_{\pm} e^{\pm i}$ – sum of complex number and its conjugate

$Re[\dots]$, real part of complex number

Dimensionless numbers:

Re, Reynolds number

Rm, magnetic Reynolds number

Rm_s, slip magnetic Reynolds number

Re_λ, modified Reynolds number

N_λ, modified interaction parameter

N, interaction parameter

Abbreviations used:

EMIP – electromagnetic induction pump

ALIP – annular linear induction pump

FLIP – flat linear induction pump

EM – electromagnetic

MHD – magnetohydrodynamics

SFR – sodium fast reactor

ASTRID - Advanced Sodium Technological Reactor for Industrial Demonstration

AC – alternating current

DC – direct current

CFD - Computational Fluid Dynamics

RANS - Reynolds Averaged Navier-Stokes

CCS - Cartesian coordinate system

DSF – double supply frequency

LF – low frequency

RHS – right hand side

PC – personal computer

INTRODUCTION

The transportation of liquid metals usually poses significant challenge due to the chemically active nature (corrosion, oxidation) and high temperature. However, because of another unique property - electrical conductivity – a motion of liquid metals may be achieved using magnetic field therefore to understand these phenomena involved the laws of electromagnetism and hydrodynamics are combined under the field of studies named *magnetohydrodynamics* (MHD).

The study of MHD as a distinct subject gained its broader recognition in the late 1930s. These studies focus on the interaction of electroconductive but nonmagnetic (relative magnetic permeability $\mu = 1$) fluids (liquid metals, electrolytes and ionized gases) with magnetic fields. First of all, the relevance of the subject is connected to astro-, geophysical phenomena and magnetic field self-excitation [1]. In the 1960s development of MHD in engineering became more and more important mostly due to the issues of power generation in thermonuclear reactor (the problem of plasma containment) and sodium cooled fast breeder reactors (SFR) for transport of liquid metal using electromagnetic (EM) pumps [2]. The latter is still an actual topic of engineering and physical studies up to date and also present work.

In the context of French GEN IV SFR research and development program for ASTRID (Advanced Sodium Technological Reactor for Industrial Demonstration) a study of use of high discharge Annular Linear Induction Pumps (ALIP) in the secondary cooling loops has been launched [3] [4] [5] Fig. 1.

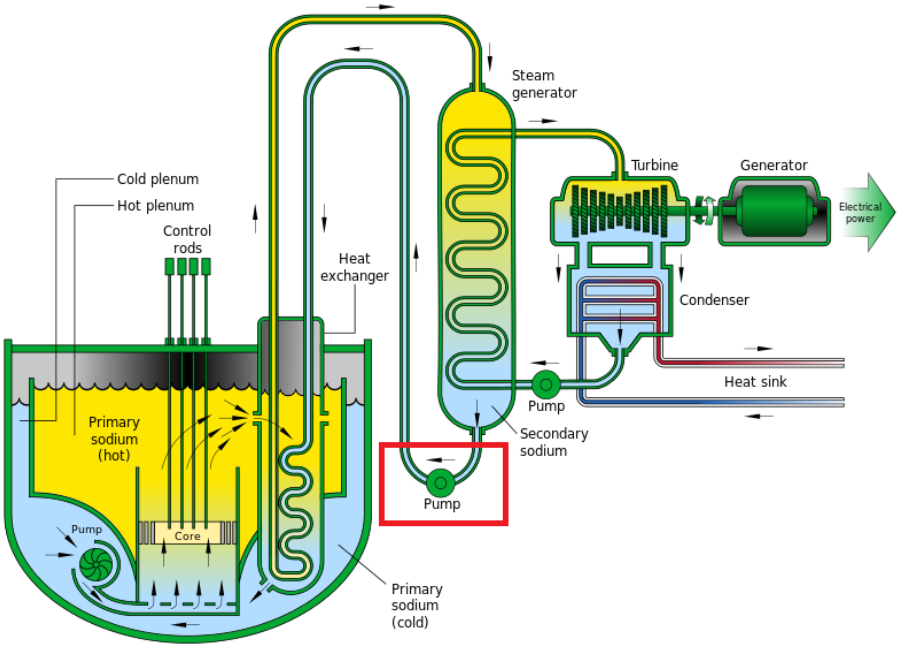

Fig. 1. Schematic of SFR [6]. Secondary pump is marked with red rectangle.

In the framework of these activities a large size ALIP called PEMDYN has been designed in CEA Cadarache with foreseen maximum flowrate about 1500 m^3/h (416 L/s) and developed pressure 2.5 bar shown in Fig. 2.

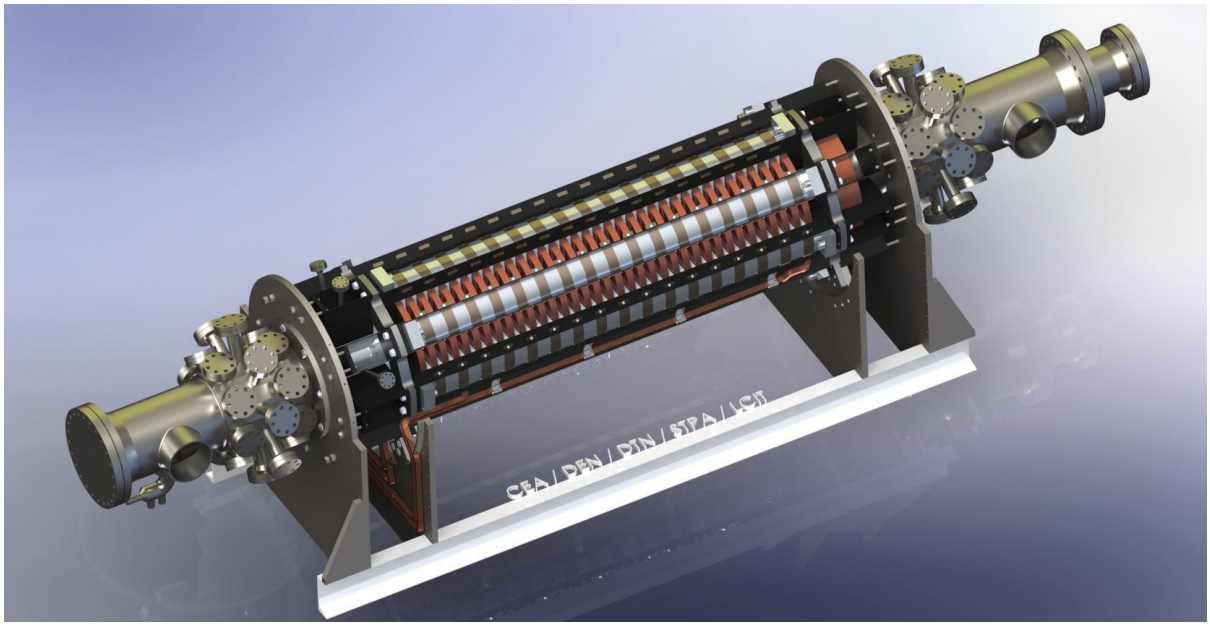

Fig. 2. PEMDYN ALIP.

PEMDYN is equipped with 24 instrumentation slots in the inlet and outlet. The construction is designed so that inner core can be removed and modified (equipped with sensors) independently, without losing hermetization of the sodium circuit. The pump is installed in the relatively compact loop (Fig. 3.) having all principal components, such as 3x heat exchangers, flow meter and flowrate control valve. The experimental program of PEMDYN is foreseen in Q4 2015 and the following years.

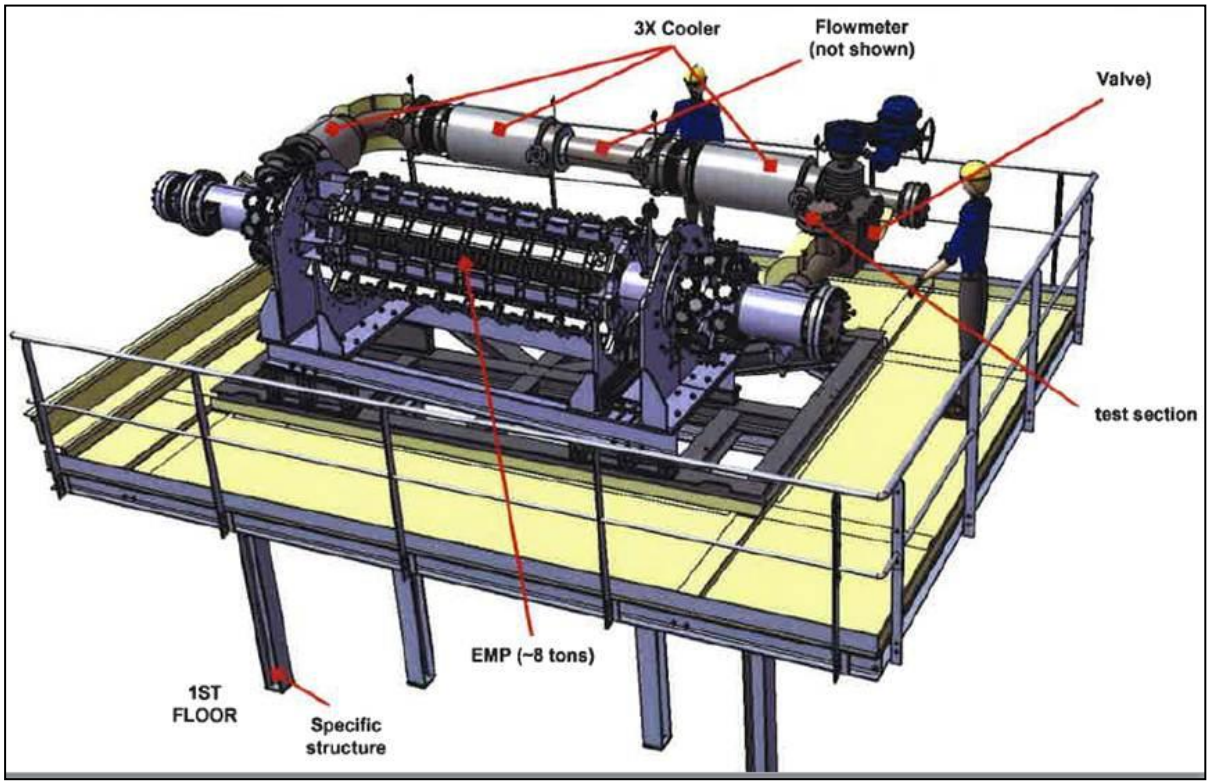

Fig. 3. PEMDYN experimental loop.

The use of ALIP in SFR has been a continuous concern since 1980s [7] [8] [9]. Currently, there are both existing examples of ALIP used in SFRs, and experimental

installations that model pumps of similar scale confirming that practically such technology is feasible [10] [11] [12].

ALIP is a subdivision of electromagnetic induction pumps (EMIP) which are widely used for the transportation of liquid metal in variety of technological processes. Main advantage of these devices is contactless pumping of liquid metal using EM force and having immobile parts, therefore hermetic construction can be designed with significant safety improvements in comparison to mechanical pumps while compromising the efficiency. It is commonly assumed that ALIP is more preferential than a flat linear induction pump (FLIP) from both – construction and efficiency point of view since it has considerably simpler geometry of windings and transversal end effects do not occur [13] [14] [15].

The design and the principle of EM force generated in ALIP are shown in Fig. 4. It consists of (1) at least one inductor where coils are embedded in laminated ferromagnetic core, (2) an annular channel where liquid metal flows in the direction of traveling magnetic field and (3) an inner ferromagnetic core or secondary inductor. The goal of this construction is to generate a perpendicular (radial) component of travelling magnetic field applying a three phase current to coils. The obtained form of magnetic field will induce currents in a liquid metal and the cross-product created generates EM force in the direction of traveling field.

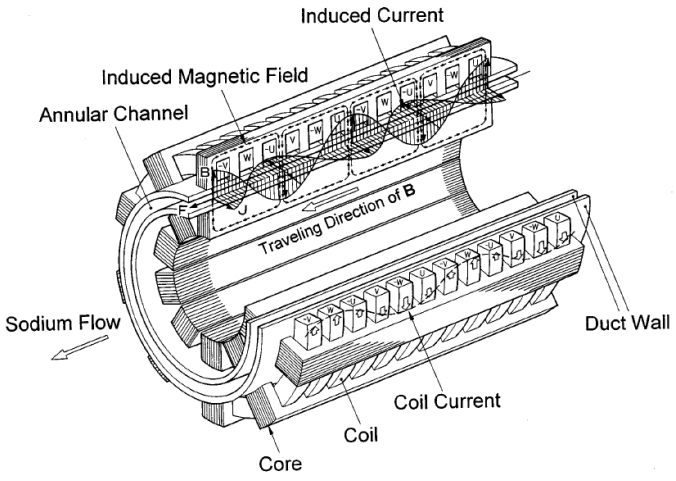

Fig. 4. Schematic drawing of annular linear induction pump [16]

In general EMIP is a linear asynchronous motor driven by alternating current (AC) with a liquid secondary circuit. Frequently they both share similar characteristics and a great part of classical theory of EMIP published in 1960s was built up from the theory of linear AC motors considering flow of bulk liquid metal and applying a solid body approximation [13] [14]. This assumption simplifies the mathematical setup of the problem from MHD to electrodynamics. However, the further experimental and theoretical results revealed that solid body approximation provides reliable results up to the slip magnetic Reynolds number (Rm_s) around the value of 1 and *liquidity* of melted metal cannot always be neglected [17] [18] [19] [20]. This is due to the inhomogeneity of the flow, low frequency fluctuations of electrical parameters and pressure, vibrations and additional pressure losses that have been observed in a large ALIP using Na when Rm_s is relatively high [21].

The abovementioned problem is known at least since the 1970s as MHD instability in ALIP first discussed by Gailītis et al. [18] shedding light on the main physical mechanisms behind this phenomenon in a model of an ideal ALIP. The most important result of this work is the derivation of the criteria for the possible existence of steady azimuthal modes - the threshold of a convective instability being experimentally confirmed in many works [7] [21] [22]. Some stabilization methods have been proposed over the course of the last decades [23]

[24] and showing that stabilization of the flow can be achieved up to some extent [25], however do not resolving the problem entirely.

Therefore, the problematic discussed is both of academic and applied importance. From the application point of view a stable operation of ALIP and stabilization methods are necessary, whereas from the academic – more detailed theoretical analysis of instability phenomena and experimental verification of these results should be scrutinized. It is undeniable that the scale and amount of work in such study is too large to approach all the problems and resolve all the questions at once as it has not been done for the past 30 years. However, the problem is still worth to tackle presuming that with a more profound understanding gained through more extended and intensified work it might be eventually solved.

Taking into account that **goals of this PhD thesis** are following:

1) To elaborate conditions and parameters that characterize MHD instability in ideal ALIP and verify them
2) To analyse numerical model of realistic EMIP and verify results with experiment

Therefore **questions of the research** are:

1) What are the conditions of an ideal ALIP becoming unstable?
2) Is it possible to avoid these conditions?
3) How to verify theoretical results of an ideal ALIP?
4) How to create a realistic numerical model of EMIP?
5) What are the parameters to be analysed in numerical model and to compare with experiment?
6) How all necessary parameters should be measured experimentally?
7) How the experimental data should be processed?

Accordingly, **tasks of the work** are:

1) to analyse a system of MHD equations for ideal ALIP theoretically and to identify conditions when perturbations start to amplify
2) to discuss the theoretical results of the thesis in the context of the existing research
3) to examine theoretically the stable operation and stabilization of ideal ALIP
4) to calculate and compare the theoretical and numerical perturbation growth rates for an ideal ALIP
5) to develop the numerical model of realistic EMIP and elaborate potentially unstable regimes
6) to conduct an experiment equivalent to the numerically developed model and compare the results.

Methods and approaches

The approach of the research is twofold applying both quantitative methods for the theoretical, numerical and experimentation analysis and qualitative interpretation of the results developed. Accordingly, the study focuses on the coherence between all three research aspects with particular interest in two important points of their intersection. That is:

- Comparison of theoretical and numerical investigations in ideal ALIP
- Analysis of numerical and experimental investigations in realistic EMIP

On the one hand, such an approach is necessary due to the fact that it is difficult in the theoretical work to take into account all the realistic effects, e.g. finite geometry, discrete distribution of currents. That can be also considered as a verification of numerical model (or theory). On the other hand, it is practically impossible to create an ideal EMIP experimentally if exact comparison of all aspects is not included.

Theoretical study in great part is based on the analysis of linear stability of vorticity (or Navier-Stokes), induction and continuity equations of 2D case (in plane φ-z).

For the numerical study commercial software ANSYS FLUENT with MHD module is used to solve an unsteady system of MHD equations numerically using finite volume method and SIMPLE algorithm for pressure correction. An implicit time stepping scheme was used with second order upwind for momentum equation and first order for magnetic field.

For few calculations of magnetic field in frequency domain COMSOL Multiphysics commercial software is used being based on finite element method.

The data of the experimental investigations are save in digital format using National Instruments hardware and LabView software.

Most of the post-processing work is done using MatLab commercial software where functions, such as Fast Furrier Transform, fitting, visualizing etc. are implemented. A great part of images in this work is obtained via MatLab.

1. BIBLIOGRAPHICAL REVIEW

In this chapter literature on theoretical, experimental and numerical investigations about MHD instability in ALIP is reviewed in details to have state-of-art of the problem.

First of all, in theoretical part governing equations of MHD problem are discussed. Then classical problems of ideal EMIP and EMIP with finite length inductor are summarized and most important results shown. Reported theoretical results on MHD instability analysis presented. Secondly, experimental studies on MHD instability in ALIP are summarized along with most significant results which help to characterize the phenomenon. Thirdly, reported 2D asymmetric numerical models capable of modelling MHD instability in EMIP are discussed. In the end, short summary of bibliographical review is done and problems state-of-art given as a reference point of current work.

1.1. Governing system of equations

1.1.1. Electromagnetic part

In continuum physics any electromagnetic process can be described by the system of Maxwell equations:

$$\nabla \cdot \boldsymbol{E} = \frac{\rho_q}{\varepsilon_0} \tag{1}$$

$$\nabla \times \boldsymbol{E} = -\frac{\partial \boldsymbol{B}}{\partial t} \tag{2}$$

$$\nabla \cdot \boldsymbol{B} = 0 \tag{3}$$

$$\nabla \times \boldsymbol{B} = \mu_0(\boldsymbol{j} + \boldsymbol{j_e}) + \mu_0 \varepsilon_0 \frac{\partial \boldsymbol{E}}{\partial t} \tag{4}$$

And Ohms law in differential form:

$$\boldsymbol{j} = \sigma(\boldsymbol{E} + \boldsymbol{v} \times \boldsymbol{B}) \tag{5}$$

In broad range of 2D cases it is very useful to introduce magnetic vector potential defined as [13]:

$$\nabla \times \boldsymbol{A} = \boldsymbol{B} \tag{6}$$

$$\nabla \cdot \boldsymbol{A} = 0 \tag{7}$$

Since there are no charge density sources ρ_q with introduction of (5) divergence of electrical field reads:

$$\nabla \cdot \boldsymbol{E} = -\nabla \cdot (\boldsymbol{v} \times \boldsymbol{B}) \tag{8}$$

Also displacement currents in (4) are negligible [2]. Current density in RHS of (9) is a sum of induced currents and external currents $\boldsymbol{j_e}$ which are assumed to be known and are source of magnetic field in the first place:

$$\nabla \times \boldsymbol{B} = \mu_0(\boldsymbol{j} + \boldsymbol{j_e}) \tag{9}$$

By inserting (5) into (9) and applying curl (rotor) operator, it follows:

$$\nabla \times \nabla \times \boldsymbol{B} = \mu_0\sigma[\nabla \times \boldsymbol{E} + \nabla \times (\boldsymbol{v} \times \boldsymbol{B})] + \mu_0 \nabla \times \boldsymbol{j_e} \tag{10}$$

Using (2), (3) induction equation for magnetic flux density $\boldsymbol{B}$ is obtained:

$$\Delta \boldsymbol{B} = \mu_0\sigma\left[\frac{\partial \boldsymbol{B}}{\partial t} - \nabla \times (\boldsymbol{v} \times \boldsymbol{B})\right] - \mu_0 \nabla \times \boldsymbol{j_e} \tag{11}$$

Induction equation can be also rewritten in terms of vector potential $\boldsymbol{A}$:

$$\Delta \boldsymbol{A} = \mu_0\sigma\left[\frac{\partial \boldsymbol{A}}{\partial t} - (\boldsymbol{v} \times \nabla \times \boldsymbol{A})\right] - \mu_0 \boldsymbol{j_e} \tag{12}$$

Further focus on (11), which can be simplified since $\boldsymbol{B}$ and $\boldsymbol{v}$ are solenoidal fields:

$$\Delta \boldsymbol{B} - \mu_0\sigma\left[\frac{\partial \boldsymbol{B}}{\partial t} - (\boldsymbol{B}\nabla)\boldsymbol{v} + (\boldsymbol{v}\nabla)\boldsymbol{B}\right] = -\mu_0 \nabla \times \boldsymbol{j_e} \tag{13}$$

When magnetic field is found using (13), electromagnetic force can be calculated as:

$$\boldsymbol{f_{EM}} = \boldsymbol{j} \times \boldsymbol{B} = \left(\frac{\nabla \times \boldsymbol{B}}{\mu_0} - \boldsymbol{j_e}\right) \times \boldsymbol{B} = \frac{(\boldsymbol{B}\nabla)\boldsymbol{B}}{\mu_0} - \nabla\left(\frac{\boldsymbol{B^2}}{2\mu_0}\right) - \boldsymbol{j_e} \times \boldsymbol{B} \tag{14}$$

Force calculated from (14) must be used as source term in Navier – Stokes equation.

1.1.2. Alternative formulation of the induction equation

Another approach of solving the induction equation is superposition magnetic field by dividing it into external and induced part:

$$\boldsymbol{B} = \boldsymbol{B_e} + \boldsymbol{B_i} \tag{15}$$

The external magnetic field $\boldsymbol{B_e}$ is assumed to be already known in the domain without presence (but the result) of external currents. It is magnetic field which would exist if studied domain is not conductive [2] [14] [26]. Then from (9) it follows that $\boldsymbol{B_e}$is irrational:

$$\nabla \times \boldsymbol{B_e} = 0 \quad \rightarrow \quad \Delta \boldsymbol{B_e} = 0 \tag{16}$$

After which induction equation is solved with regard to induced magnetic field $\boldsymbol{B_i}$ using $\boldsymbol{B_e}$ as a source term:

$$\Delta \boldsymbol{B_i} - \mu_0 \sigma \left[\frac{\partial \boldsymbol{B_i}}{\partial t} - (\boldsymbol{B_i} \nabla)\boldsymbol{v} + (\boldsymbol{v} \nabla)\boldsymbol{B_i} \right] = \mu_0 \sigma \left[\frac{\partial \boldsymbol{B_e}}{\partial t} - (\boldsymbol{B_e} \nabla)\boldsymbol{v} + (\boldsymbol{v} \nabla)\boldsymbol{B_e} \right] \quad (17)$$

And induced currents can be calculated from $\boldsymbol{B_i}$ using Amperes' law:

$$\nabla \times \boldsymbol{B_i} = \mu_0 \boldsymbol{j} \quad (18)$$

Then EM force can be expressed as follows:

$$\boldsymbol{f_{EM}} = \boldsymbol{j} \times \boldsymbol{B} = \left(\frac{\nabla \times \boldsymbol{B_i}}{\mu_0} \right) \times \boldsymbol{B} \quad (19)$$

Strictly speaking $\boldsymbol{B_e}$should be calculated from external currents, then (17) is identical to (13). The advantage of this approach is possibility to study cases with simplified forms of $\boldsymbol{B_e}$, therefore characterizing global phenomenon. In such case the limits and precision of the approximation must be considered.

1.1.3. Hydrodynamic part

A small remark should be done before proceeding. The topics of hydrodynamics and CFD are very large and conspective outline has been given below. This has been done intentionally, to mainly discuss equations and argument assumptions used later in the work.

In fluid dynamics incompressible fluid and comparatively slow (Mach number < 0.2) gas flow is modelled by Navier – Stokes (20) and Continuity equation (21) [27]:

$$\rho \left[\frac{\partial \boldsymbol{v}}{\partial t} + (\boldsymbol{v} \nabla)\boldsymbol{v} \right] = -\nabla p + \eta \Delta \boldsymbol{v} + \boldsymbol{f} \quad (20)$$

$$\nabla \cdot \boldsymbol{v} = 0 \quad (21)$$

Solving this system is not trivial. Even more, there is no mathematical proof of existence and smoothness of the solution in 3D space and it is still one of the Millennium problems by Clay institute [28].

Some exact analytical solutions are found only for couple special cases involving significant simplifications (e.g. Stokes flow around the sphere, which is highly important result in physics). Since system is nonlinear, in praxis widely accepted approach is to solve it iteratively by numerical means and practically separate branch of science – Computational Fluid Dynamics (CFD) has been intensively developing since 1950-ies [29].

Globally nature of the flow is characterized by Reynolds similarity principle – a dimensionless (Reynolds) number a ratio between inertial and viscose forces [27]:

$$Re = \frac{\rho v L}{\eta} \quad (22)$$

Depending on value of *Re* several types of flow can be qualitatively distinguished:

1. $Re \ll 1$ – Creeping or Stokes flow (Viscose forces dominate)
2. $Re = 1 \ldots 2000$ – Laminar flow (Stable inertial flow, e.g. Poiseille flow)
3. $Re = 2000 \ldots 3000$ – Transition flow
4. $Re > 3000$ – Turbulent (hydrodynamically unstable) flow

In Fig. 5 illustrative sketch of different type flows over cylinder are presented:

By estimating characteristic Reynolds number, it turns out that in many practically significant cases flow is turbulent (unstable). This is a problem, since behaviour of the global flow is mainly determined by larger size eddies comparable to the size of the system, but somewhat laminar behaviour exists only in small scales. Therefore from numerical point of view, to directly solve (20) for highly turbulent flows high spatial and temporal discretization is required [2] [29].

However, frequently engineering interest is in global, temporally average behaviour of the flow to estimate global pressure losses, drag coefficient or similar. Therefore high popularity have gained Reynolds Averaged Navier-Stokes (RANS) models, which are capable of modelling isotropic, time averaged turbulence.

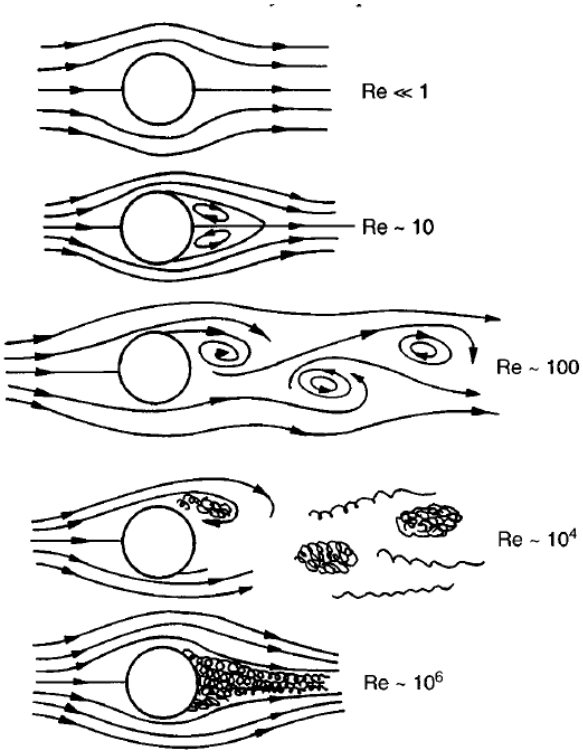

Fig. 5. A scheme of flow around the cylinder with different Reynolds number. [2]

In short, such approach is based on Boussinesq's hypothesis of eddy viscosity which can be up to several orders higher then dynamic viscosity of fluid and qualitatively explains higher energy dissipation (pressure losses) in turbulent flows. By introducing additional equations, closure problem appears and requires semi-empirical inputs, which are usually optimized for large class of flows, but are not universal. Nevertheless, in most cases RANS models show acceptable precision, therefore are widely used [29].

Finally, one of the oldest approaches and still widely used in simplified calculations is semi-empirical description of the turbulence effect using formula of *inertial-losses* since flow in the channel is close to unidirectional [30] (23). Such approach of modelling dissipative forces requires definition of friction factor λ_h where Blasius (24) or Nikuradse (25) correlations are frequently used [15]:

$$\boldsymbol{f}_{\boldsymbol{\lambda}} = -\frac{\lambda_h}{d_h} \cdot \rho \frac{\boldsymbol{v}|\boldsymbol{v}|}{2} \tag{23}$$

$$\lambda_h = 0.316Re^{-0.25} \;\; if \; Re \leq 10^5 \tag{24}$$

$$\lambda_h = 0.032 + 0.221Re^{-0.25} \;\; if \; Re > 10^5 \tag{25}$$

Attempts of correcting friction factor in case of applied traveling magnetic field have been also made showing that in case of low interaction parameter N (sometimes called Stewarts number – ration of EM and inertial forces) it follows correlation [31]:

$$\lambda_m = \lambda_h + const \cdot N \tag{26}$$

It is important to note simplicity of (23) and emphasize that by use of such semi-empirical formula only resulting effects of turbulent flow not the turbulence (as hydrodynamic instability) is modelled. Similar can be said about any RANS model, keeping in mind that they are, of course, much more detailed and advanced.

Using (14) and (23) Navier-Stokes equation if transformed to:

$$\rho\left[\frac{\partial \boldsymbol{v}}{\partial t} + (\boldsymbol{v}\nabla)\boldsymbol{v}\right] = -\nabla p - \frac{\lambda_h}{d_h}\cdot\rho\frac{\boldsymbol{v}|\boldsymbol{v}|}{2} + \frac{(\boldsymbol{B}\nabla)\boldsymbol{B}}{\mu_0} - \nabla\left(\frac{\boldsymbol{B^2}}{2\mu_0}\right) - \boldsymbol{j_e}\times\boldsymbol{B} \tag{27}$$

Similarly as magnetic vector potential in electromagnetics, in cases of 2D flow it is useful to work with vorticity [2]:

$$\boldsymbol{\omega} = \nabla \times \boldsymbol{v} \tag{28}$$

$$\nabla \cdot \boldsymbol{\omega} = 0 \tag{29}$$

Then (27) can be transformed into vorticity equation:

$$\rho\left(\frac{\partial \boldsymbol{\omega}}{\partial t} + (\boldsymbol{v}\nabla)\boldsymbol{\omega} - (\boldsymbol{\omega}\nabla)\boldsymbol{v}\right) = \nabla \times \left(\frac{(\boldsymbol{B}\nabla)\boldsymbol{B}}{\mu_0} - \frac{\lambda_h}{d_h}\cdot\rho\frac{\boldsymbol{v}|\boldsymbol{v}|}{2} - \boldsymbol{j_e}\times\boldsymbol{B}\right) \tag{30}$$

Finally, system of governing equations used in this work consists of (13), (21), (30).

It might be important to emphasize that, no magnetic field effect on friction factor (and turbulence for that matter) is considered in this work. The flow is assumed to be isotropically turbulent – having macroscopically stable averaged profile and higher dissipation rate than laminar flow. Perhaps it is sufficient to note that, magnetic field in ALIP strongly differs (inhomogeneous, AC field) from classically studied examples of MHD turbulence (homogeneous, DC field) [2] and it is not clear whether in such conditions stable 2D turbulence can settle at all, therefore it is out of scope of current study.

In short, study MHD instability of ALIP, presented in details later, discusses inhomogeneity of averaged profile in turbulent flow - a macroscopic effect only, which impacts global operation of a pump.

1.2.Analytical investigations

1.2.1. Ideal EMIP in Cartesian Coordinate System (CCS)

In this subchapter main results of ideal EMIP from [13] [14] [15] are discussed along with setup of the model and deviation of developed pressure.

An ideal EMIP is infinitely long machine with channel located between two perfect ferromagnetic yokes with height d_m and has no walls. Magnetic field in such machine is created by infinitely thin layer of linear current density j_{lin} with effective value J and liquid layer with height d_h and conductivity σ is moving with a constant velocity v_z as a solid body in z direction Fig. 6

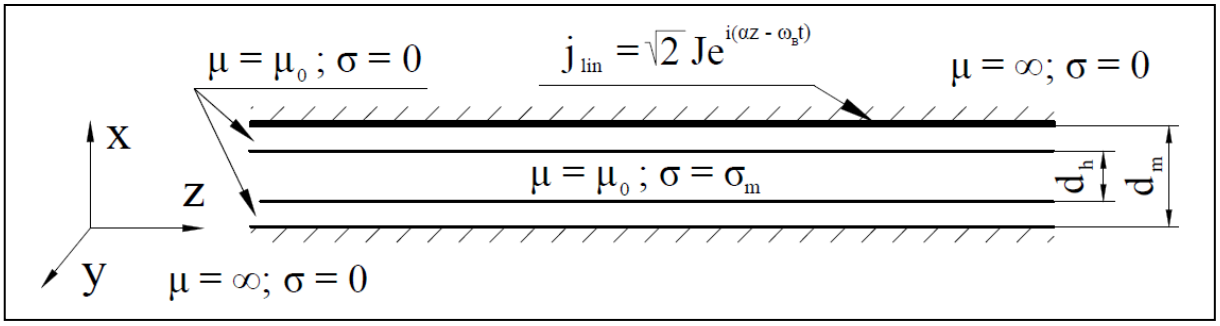

Fig. 6. A model of an ideal EMIP in CCS.

For ideal machine following relation of dimensions holds:

$$d_h < d_m \ll \tau < L \tag{31}$$

In particular case of ideal EMIP only principle harmonic is considered:

$$j_{lin} = \sqrt{2}J \cdot e^{i(\alpha z - \omega_B t)} \tag{32}$$

In this 2D case induction equation for vector potential reads:

$$\frac{\partial^2 A}{\partial x^2} + \frac{\partial^2 A}{\partial z^2} - \mu_0 \sigma \frac{d_h}{d_m}\left[\frac{\partial A}{\partial t} + \left(v_z \frac{\partial A}{\partial z}\right)\right] = 0 \tag{33}$$

And boundary conditions are:

$$\left.\frac{\partial A}{\partial x}\right|_{x=0} = 0 \tag{34}$$

$$\left.\frac{\partial A}{\partial x}\right|_{x=d_m} = \mu_0 j_{lin} \tag{35}$$

Look for solution in complex harmonic form:

$$A = A_0(x) \cdot e^{i(\alpha z - \omega_B t)} \tag{36}$$

Then 2nd order differential equation for complex amplitude of vector potential is:

$$\frac{\partial^2 A_0(x)}{\partial x^2} - \lambda^2 A_0(x) = 0 \tag{37}$$

Where complex coefficient λ^2 and silp magnetic Reynolds number reads:

$$\lambda^2 = \alpha^2(1 - iRm_s) \tag{38}$$

$$Rm_s = \frac{\mu_0 \sigma (v_B - v_z)}{\alpha} \cdot \frac{d_h}{d_m} \tag{39}$$

Complex amplitude of vector potential is:

$$A_0(x) = Csh(\lambda x) + Dch(\lambda x) \tag{40}$$

Applying boundary conditions one finds that distribution of vector potential:

$$A(x,z) = \frac{\mu_0 \sqrt{2} J}{\lambda} \cdot \frac{ch(\lambda x)}{sh(\lambda d_m)} \cdot e^{i(\alpha z - \omega_B t)} \tag{41}$$

Then from (6) B_x is:

$$B_x(x,z) = -i\frac{\mu_0 \sqrt{2} J \alpha}{\lambda} \cdot \frac{ch(\lambda x)}{sh(\lambda d_m)} \cdot e^{i(\alpha z - \omega_B t)} \tag{42}$$

(31) suggests, that effects can be rather correctly averaged over the height. Then height average B_x can be found:

$$B_x(z) = -i\frac{\mu_0 \sqrt{2} J \alpha}{d_m \lambda^2} \cdot e^{i(\alpha z - \omega_B t)} = \frac{\mu_0 \sqrt{2} J}{d_m \alpha} \cdot \frac{1}{i + Rm_s} \cdot e^{i(\alpha z - \omega_B t)} \tag{43}$$

Developed quasi – stationary EM force can be estimated as reactive force fluid is pushed away from the inductor, by using multiplication of complex amplitudes [18]:

$$f_{EM}\boldsymbol{e_z} = -\frac{1}{2}\frac{\sqrt{2}J}{d_h}\boldsymbol{e_y} \times Re\left[\frac{\mu_0 \sqrt{2} J}{d_m \alpha} \cdot \frac{1}{i + Rm_s}\right]\boldsymbol{e_x} \tag{44}$$

This leads to simple expression of EM force density:

$$f_{EM} = \frac{\sigma {B_{x0}}^2}{2}(v_B - v_z) \tag{45}$$

Height averaged amplitude of total magnetic field is:

$$B_{x0} = \frac{\mu_0 \sqrt{2} J}{\alpha d_m \sqrt{1 + Rm_s^2}} \tag{46}$$

And in the case of $Rm = 0$ amplitude of external magnetic field is:

$$B_{xe} = \frac{\mu_0 \sqrt{2} J}{\alpha d_m} \tag{47}$$

Then developed pressure of ideal EMIP by subtracting fiction losses over length of channel is:

$$\Delta p = \frac{\sigma}{2}\left(\frac{\mu_0 \sqrt{2} J}{\alpha d_m}\right)^2 \cdot \frac{v_B - v_z}{1 + Rm_s^2} L - \lambda_h \frac{L}{d_h} \rho \frac{v_z |v_z|}{2} \tag{48}$$

First RHS term can be also transformed in following form:

$$\Delta p_{EM} = \frac{{B_{xe}}^2}{2\mu_0} \cdot \frac{\alpha L d_m}{d_h} \cdot \frac{Rm_s}{1 + Rm_s^2} \tag{49}$$

Then, first term in (49) is a function of applied external magnetic field - current, second term is factor of dimensions and last term describes that developed EM pressure is non-linear function of slip magnetic Reynolds number. Behaviour of the last term can be easily analysed considering two cases:

1. $Rm_s \ll 1$, in such case quadratic term can be neglected and it follows that for small values of Rm_s pressure grows linearly:

$$\Delta p_{EM} \sim Rm_s \tag{50}$$

2. $Rm_s \gg 1$, in such case quadratic term is much more significant than 1 and it follows, that for large values of Rm_s pressure decays proportionally to Rm_s:

$$\Delta p_{EM} \sim \frac{1}{Rm_s} \tag{51}$$

By plotting these functions of Rm_s, statements discussed above are illustrated Fig. 7. Note that function (49) has maximum $Rm_s = 1$. Obtained *falling* curve when $Rm_s > 1$ is common to induction machines and is also one of the basic concepts qualitatively analysing instabilities.

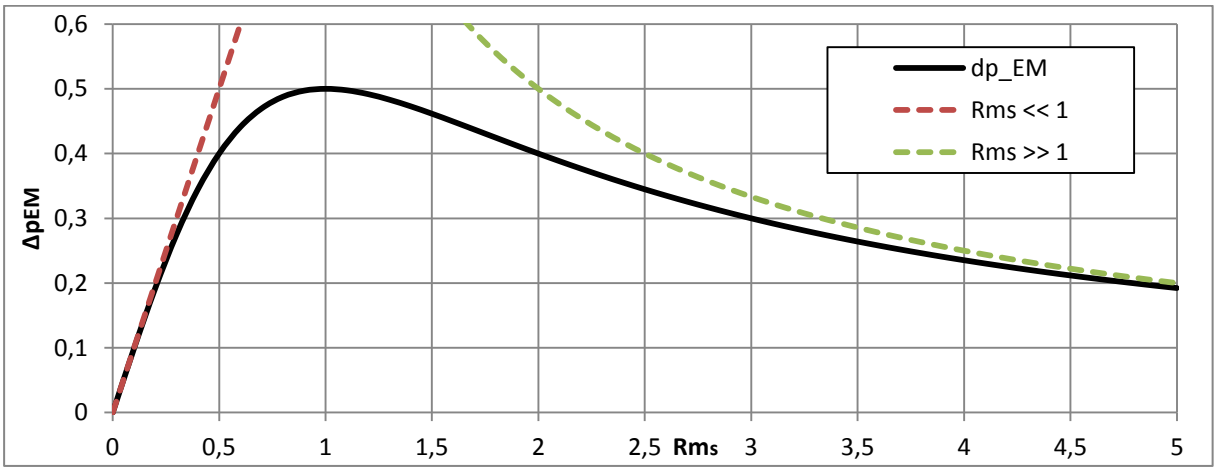

Fig. 7. Developed EM pressure as function of Rms.

Generally, in the cases of ALIP problem should be solved in cylindrical coordinate system. By working similarly as in presented case, it follows that solution of amplitude of magnetic vector potential can be found in form of modified Bessel functions of first and second kind [14]. Nevertheless, it is shown, that influence of curvature on developed pressure is negligible (order of 1 – 2 %) if relations below are satisfied [14]:

$$\frac{R}{d_m} \geq 2\ldots3 \tag{52}$$

$$\frac{\tau}{d_m} \geq 2\ldots3 \tag{53}$$

Both of these conditions meet in the model of ideal ALIP. Moreover they are frequently satisfied in problems of practical significance e.g. large flowrate pumps. This makes valid also in cases studied further.

1.2.2. A finite length effect and DSF pulsations

In order to take into account longitude end effects of finite inductor with length *L*, some analytical results were obtained in [32] and following case in Fig. 8 is considered.

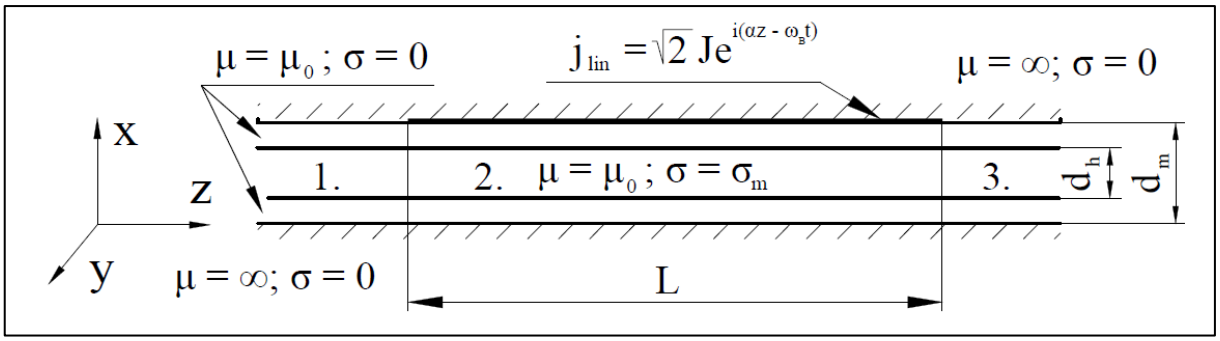

Fig. 8. A model of EMIP with finite length layer of external current density .

Studied case resembles quite significantly to the model of ideal EMIP. Only difference is that external current is applied in finite length *L* – a length of active part of EMIP:

$$L = 2\tau p \tag{54}$$

Where *p* – number of pole pairs.

Authors consider only single height averaged x component of magnetic field to simplify the solution. One should expect that magnetic field in zones 1, 3 is somewhat exponentially decreasing; while in zone 2 it has form of traveling wave.

Solution of external magnetic field amplitude in zones 1, 2, 3 according to [32] is:

$$B_{xe}{}^{(1,3)} = \frac{\mu_0\sqrt{2}J}{\alpha d_m} sin(\pi p)\, cos(\omega_B t) \tag{55}$$

$$B_{xe}{}^{(2)} = \frac{\mu_0\sqrt{2}J}{\alpha d_m}[sin(\omega_B t - \alpha z) - cos(\pi p)sin(\omega_B t)] \quad (56)$$

There are 2 cases with practical significance which can be studied depending on *p*:

1. If $p = 1/2, 3/2, 5/2 \ldots$ it follows that there is pulsating magnetic field in inlet and outlet zones of EMIP, but only travelling in zone of inductor.

2. If $p = 1, 2, 3 \ldots$ which corresponds to even number of poles, magnetic field in inlet and outlet zones of EMIP is zero, but in zone of inductor pulsating component appears.

Even though more sophisticated models of finite length EMIP can be analysed [33], the important result here is that additional pulsating component of magnetic field appears in a real EMIP due to finite geometry and is purely electromagnetic effect. This component leads to double supply frequency (DSF) pressure pulsations and classically was one of the most important effects to study and suppress [13] [14]. Some detailed and recent works on suppression of DSF pulsations can be found [16] [34] which will be discussed slightly more later on.

However, the fact itself is rather significant, that pressure pulsations in EMIP appear not only due to some unstable hydrodynamic behaviour. They may as well be caused by pulsations of magnetic field.

1.2.3. Analytical investigations of MHD instability

As mentioned before, not in all cases/regimes of EMIP fluid nature of melted metal can be neglected. This is rather serious issue, since introduction of Navier-Stokes equation inevitably leads to system of non-linear differential equations, solution of which can be found only in some partial cases like Hartmann flow [13], where low magnetic Reynolds number and laminar flow is considered. Neither is true for EMIPs using liquid Na.

Historically, first of all, experiments showed bizarre behaviour of large Na pumps characterized by intense vibrations, fluctuations of pressure and flowrate, inhomogeneous flow in the channel and decrease of efficiency. It became obvious that such behaviour cannot be explained simply by electromagnetic effects; therefore liquidity Na must come into play.

One of the most significant articles on MHD instability in ALIP is work by A. Gailītis and O. Lielausis [18], where possible mechanisms of this phenomenon are discussed. First of all, steady state solution of ideal ALIP in Fig. 9 is analysed in solid body approximation, similar to one presented before. Following ratio of dimensions is considered which allows height average the effects:

$$d_h < d_m \ll \tau < \pi R < L \quad (57)$$

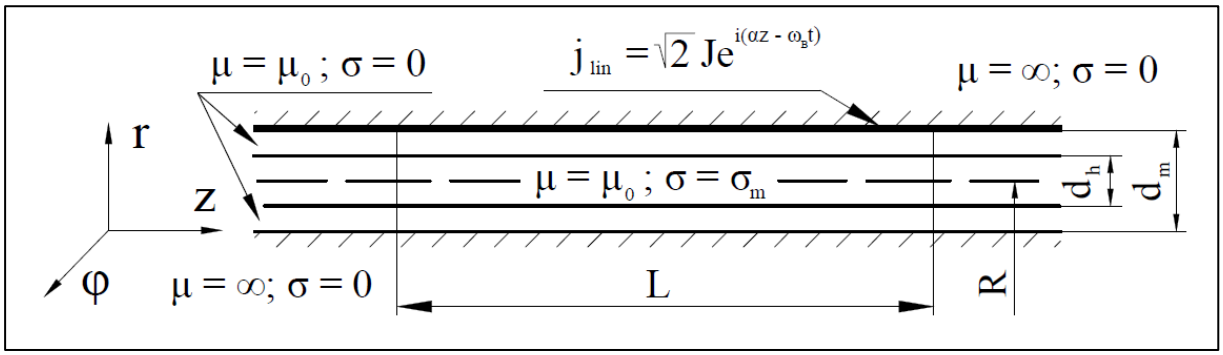

Fig. 9. A model of an ideal ALIP in cylindrical coordinate system.

System of induction equation for radial magnetic field amplitude and force balance equation is satisfied with solid body approximation.

$$\left(\frac{\partial^2}{(\alpha R)^2\partial\varphi^2} - 1 + iRm_s\right)B_0 = i\frac{\mu_0\sqrt{2}J}{d_m\alpha} \tag{58}$$

$$\frac{\Delta p}{L} = \frac{\sqrt{2}J}{d_h}\cdot\frac{Re[B_0]}{2} - \frac{\lambda_h}{d_h}\rho\frac{v|v|}{2} \tag{59}$$

And dimensionless system reads:

$$\left[\frac{\partial^2}{\tilde{R}^2\partial\varphi^2} - 1 + iRm(1-\tilde{v})\right]\widetilde{b_0} = i \tag{60}$$

$$\tilde{p} = \frac{N_\lambda}{Rm}Re\left[\widetilde{b_0}\right] - \tilde{v}|\tilde{v}| \tag{61}$$

Where modified interaction parameter – a ratio of EM and friction forces is (in work [18] symbol j^2 instead N_λ ; ε instead Rm and A instead J is used):

$$N_\lambda = \frac{2\sigma d_h}{\lambda_h\rho v_B}\left(\frac{\mu_0 J}{d_m\alpha}\right)^2 \tag{62}$$

The steady state solution in dimensionless form reads:

$$\tilde{v} = \tilde{v_z} \tag{63}$$

$$\widetilde{b_0} = \widetilde{b_c} = \frac{1}{i + Rm_s} \tag{64}$$

From which dimensionless developed pressure is:

$$\tilde{p} = \frac{N_\lambda(1-\tilde{v_z})}{1+Rm_s^2} - \tilde{v_z}|\tilde{v_z}| \tag{65}$$

Then, authors analyse model of composite pump consisting of several elementary pumps (in particular only 2) which are connected hydraulically in parallel but electrically in series Fig. 10. a). Then total developed pressure and flowrate is:

$$p = p_1 = p_2 \tag{66}$$

$$Q = Q_1 + Q_2 \tag{67}$$

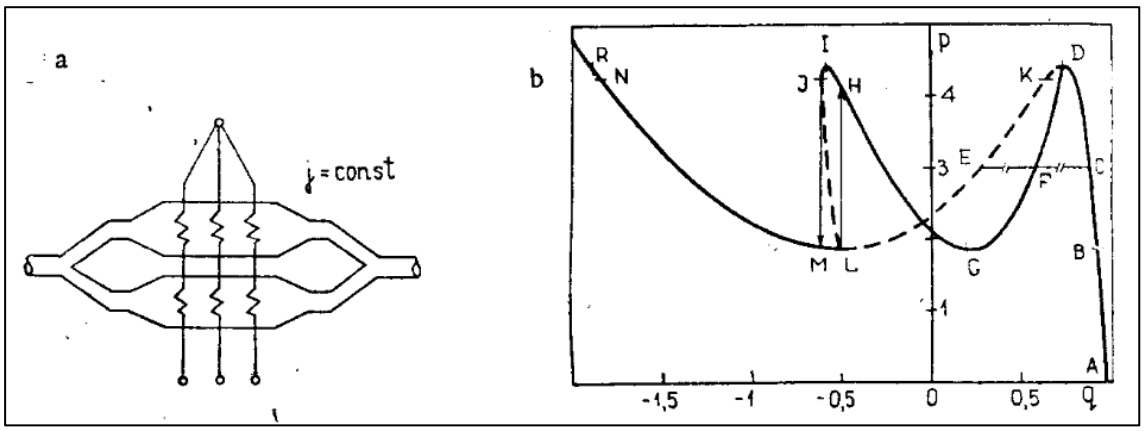

Fig. 10. a) Simplest model of two parallel connected channels with same pressure but different flowrates to approximate the real channel. b) p – q characteristics of single channel EMIP (ABCDKELMRN) and sum of two parallel connected channels (ABCDFGHIJL) [18]

Connecting possible operating points of same pressure and bisectrising those, new branches of p-Q characteristics can be plotted for such parallel connection (ABCDFGHIJL) Fig. 10 b). Following criteria in order to define stable zones of such machine is suggested:

$$\frac{d}{dQ_1}[p_1(Q_1) - p_2(Q - Q_1)] < 0 \tag{68}$$

Such condition means that EMIP is stable in regimes, when by increasing flowrate developed pressure decreases (A-D), but unstable if pressure increases as well (D-E) in Fig. 10.

Another significant result of this paper is that deviation of discharge in composite pump model does not change impedance of composite pump and regime of power supply (constant current or voltage) can have no effect on generation of instability.

Finally, linear stability analysis is performed and existence condition for stable (neither increasing, nor decreasing) azimuthal modes of magnetic field and velocity perturbations is found. Perturbed axial velocity and magnetic field amplitude is in form:

$$\tilde{v} = \widetilde{v_z} + \delta\tilde{v}_m cos(m\varphi) \tag{69}$$

$$\widetilde{b_0} = \widetilde{b_c} + \delta\tilde{b}_m cos(m\varphi) \tag{70}$$

m is a wavenumber of azimuthal mode representation of which is shown below.

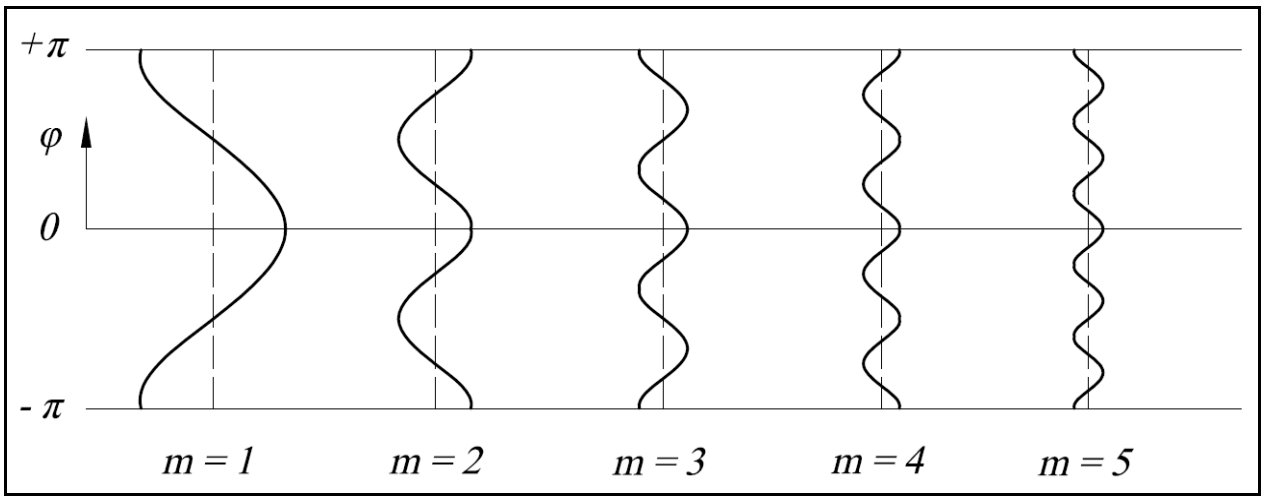

Fig. 11. A sketch of azimuthal m modes.

Inserting (69) and (70) into (60) and (61) the linearized system is:

$$\delta\tilde{b}_m = \frac{i\widetilde{b_c}}{iRm_s - 1 + \kappa_m}\delta\tilde{v}_m \tag{71}$$

$$2|\tilde{v}|\delta\tilde{v}_m = \frac{N_\lambda}{Rm} Re\left[\delta\tilde{b}_m\right] \tag{72}$$

From which using (65) the stability threshold of any azimuthal mode is derived in terms of dimensionless pressure:

$$\tilde{p}_m = \frac{2|\widetilde{v_z}|((1+\kappa_m)^2 + Rm_s^2)(1-\widetilde{v_z})}{Rm_s^2 - 1 - \kappa_m} - \widetilde{v_z}|\widetilde{v_z}| \tag{73}$$

Plot of (73) or excitation thresholds of several azimuthal modes on particular example are shown Fig. 12. Obviously, by decreasing mean velocity/flowrate mode m = 1 will be excited, then m = 2 etc.

In the case of practical significance stability criteria can be simplified and expressed in terms of slip magnetic Reynolds number (74). This result with m = 1 is used as reference criteria for MHD instability in many other works [35] [22] [36].

$$Rm_s \geq \sqrt{1+\kappa_m} = \sqrt{1 + \left(\frac{\tau m}{R\pi}\right)^2} \tag{74}$$

In this work for brevity, additional parameter is introduced:

$$\kappa'_m = 1 + \kappa_m \tag{75}$$

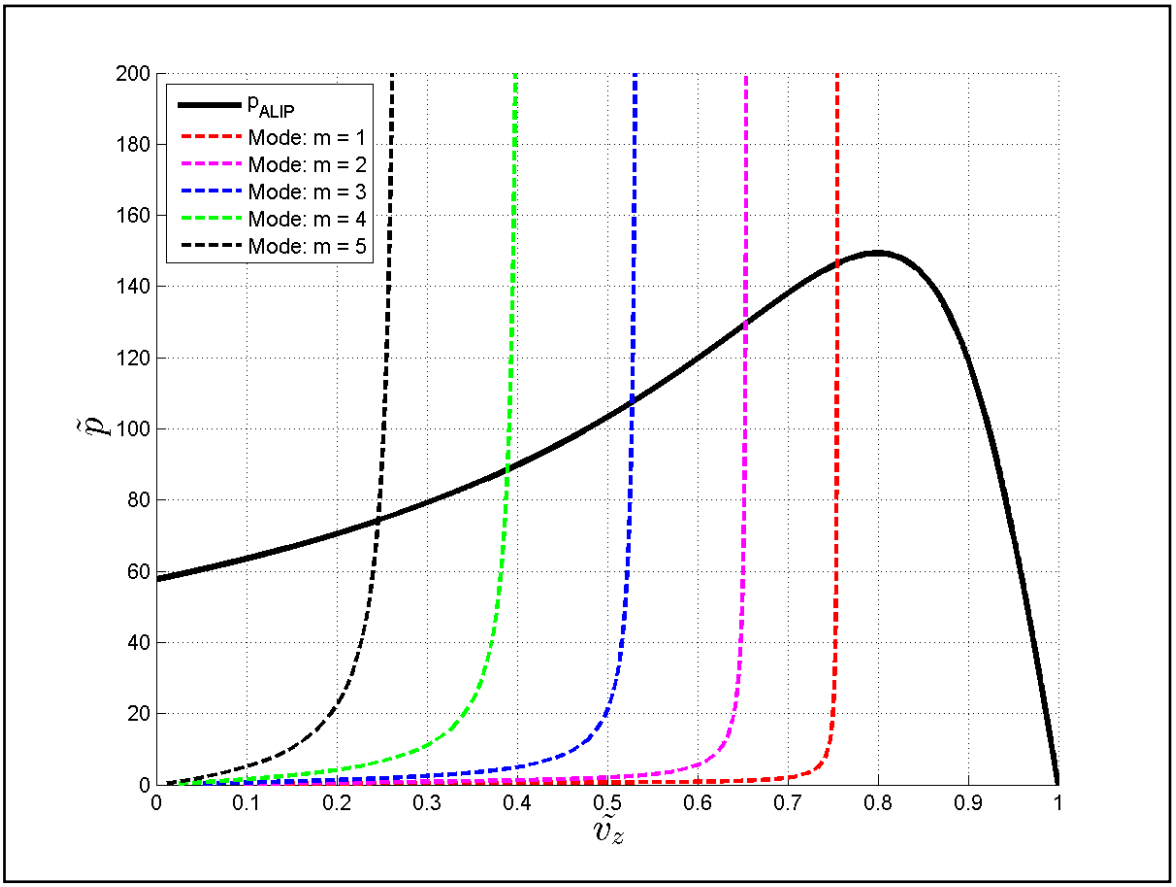

Fig. 12. An example of azimuthal modes excitation thresholds in a large ALIP with: $N_\lambda = 1500$, $Rm = 5$ *and* $\tilde{R} = 1.43$

1.2.4. Final remarks on analytical analysis

There are number of theoretical works and questions not discussed in context of work in details, but which deserve mentioning in context of general EMIP problematic.

First of all, significant amount of literature can be found describing design and calculation of EMIP, most of the using equivalent circuits [13] [14] [15] [37] [38] [39] [40].

Another branch of works is devoted to estimations of effect which appear in real EMIP e.g. already mentioned finite length effect [33] [41] and shunting effect of conductive channel walls [42] [14] [13].

Theoretical works on phenomenon in FLIPs can be separated as well, since inhomogeneous distribution of EM force is present by default leading to different velocity distribution than ALIP [17] [43] [20].

There are also some works devoted to optimization of channel form and coil dimensions/distribution to achieve higher efficiency [44] [45], though none of these methods are used in praxis.

Finally, there are some additional theoretical works on stability questions in ALIPs. In [46] velocity profile stability over channel height is discussed, which classically has never been in question. Impact of longitude and transverse end effects on stability threshold is

estimated in [47], but left without recognition. Stabilization technique using additional windings over azimuth to modify magnetic field is discussed in [24]. Using linear stability analysis feasibility of such technique is shown; however, it has never been tested and remains theoretical.

In the end it might be useful briefly discuss why in ideal ALIP (first of all) azimuthal modes characterize MHD instability rather than phenomena over the height of the channel e.g. formation of Hartmann type flow.

Start by common consensus that solid body approximation provides close to reality results in the stable branch of characteristic. Therefore there is no reason why it should be considered that radial profile strongly deviates from mean velocity (even though it, of course, exists and might even fluctuate [48]), same can be said about magnetic field. Thus it is valid to analyse stability of such base state in the first place.

Then it is possible analyse (by very similar means as just reviewed) stability over the height of the channel, considering homogeneity in transversal direction. This can be easily done in CCS. Only difference will be that Laplacian term in the induction equation and forms of perturbations will contain height dependence. Eventually, one should arrive to threshold similar to:

$$Rm_s \geq \sqrt{1 + \left(\frac{2\tau m}{d_h}\right)^2} \tag{76}$$

Obviously, only difference form (74) is ratio of dimensions under square root and considering (57), it is now clear that stability of azimuthal modes will be lower, thus the study of them is of primary importance. Indeed, strong perturbations over azimuth have been experimentally observed and discussed in the next chapter.

Effects over the height cannot be forgotten completely, since MHD problem is strongly coupled and definitely some influence on a more complex 3D flow exists. However, such case is too general and currently out of reach for the author. Some simplifications have to be made and (as shown) the most reasonable one is to study 2D φ-z (height averaged) case.

1.3. Experimental investigations of MHD instability

In this chapter some of outstanding experimental works are reviewed. The common feature of these experiments is that they succeed (up to some extent) quantify instability phenomena with measurements of velocity and magnetic field perturbations over azimuth, which is predicted by theory [18].

First of all, it is work of Kirillov and Ostapenko [22] where local characteristics of ALIP are analysed. The sketch of experimental pump is shown in Fig. 13. In this experiment axial velocity distribution over azimuth was measured using 8 Pitot tubes in 3 cross sections as well as magnetic field measurements using 8 wire contours over azimuth in 7 cross sections. It was also possible to reconnect windings to have either 4 magnetic poles with length $\tau = 225$ mm or 6 poles - $\tau = 150$ mm having magnetic Reynolds number: $Rm = 7.7$ and $Rm = 3.2$ accordingly. By varying applied voltage (current) and modified interaction parameter was changed in range: $10 \leq N_\lambda \leq 60$.

Moreover, authors claim that it was possible to asymmetrically vary nonmagnetic gap and add 8 conductive side walls over the length of the channel to compare behaviour of ALIP in those configurations.

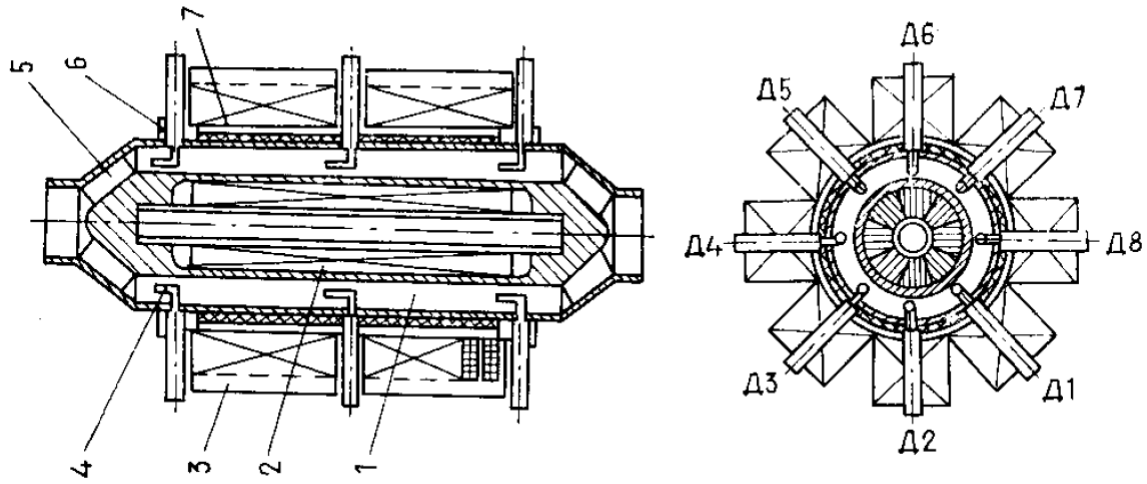

Fig. 13. A drawing of experimental ALIP equipped with Pitot tubes in the channel. [22]

Results of velocity distribution over azimuth in cross sections of middle and outlet of pump are shown in Fig. 14. All configurations show that not only velocity (and magnetic field) perturbations exist; they have been amplified over the length rather significantly. In more details this effect is shown in Fig. 15. Interestingly, it can be observed that amplification over the length increases with increment of the slip. However, at higher value of slip (in this particular case s = 0.67) some sort of saturation is achieved and measured amplification of perturbations is effectively lower than for the case of s = 0.62.

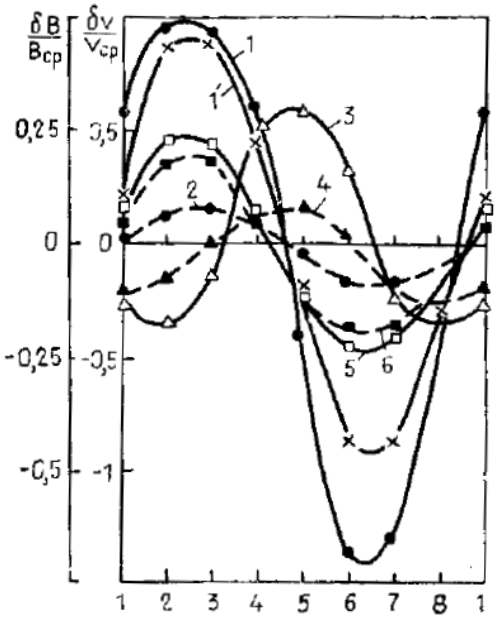

Fig. 14. Velocity (1-6) and magnetic field (1') perturbation in middle of the pump (dotted lines) and outlet (continuous lines). U = 150V, s = 0.62 and 6 poles. 1, 1', 2, 5, 6 symmetrical air gap (5, 6 – with lateral sidebars), 3 and 4 asymmetric gap. [22]

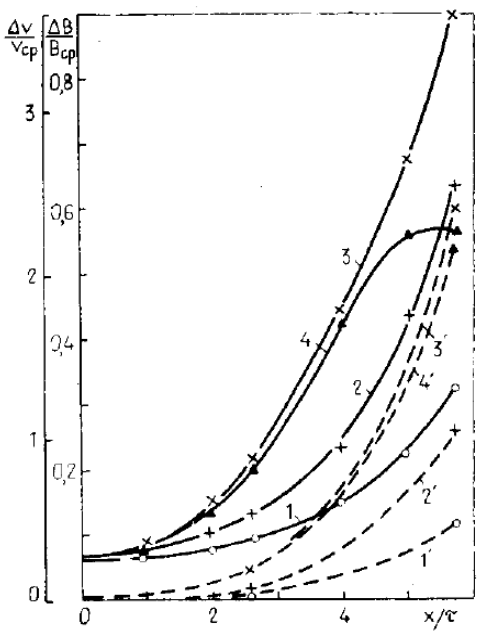

Fig. 15. Velocity (dotted lines) and magnetic field (continuous lines) perturbations over length of the pump. U = 150V and 6 poles. 1,1' – s = 0.32; 2,2' – s = 0.48; 3,3' – s = 0.62; 4,4' – s = 0.67. [22]

Mentioned effect is shown in details in Fig. 16 where perturbation of velocity is amplified with increase of slip (s = 0.32; 0.48; 0.62) but at some point (s = 0.72) it behaves completely different – not only amplitude is relatively lower, but it also have changed phase. Presented velocity profile seems to be more complicated than single azimuthal mode.

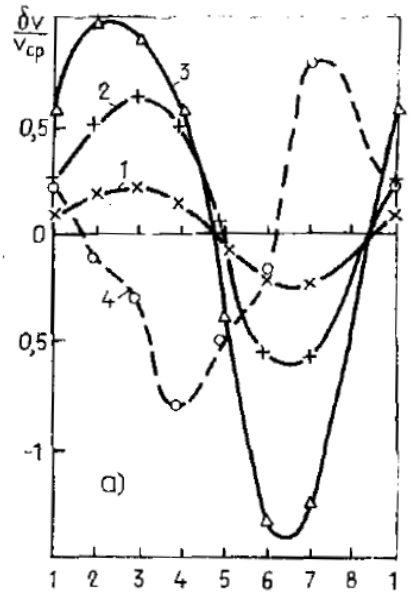

Fig. 16. Velocity perturbation over azimuth. U = 150V, 6 poles, $13 \leq N_\lambda \leq 21$ *1– s = 0.32; 2 – s = 0.48; 3 – s = 0.62; 4, – s = 0.72. [22]*

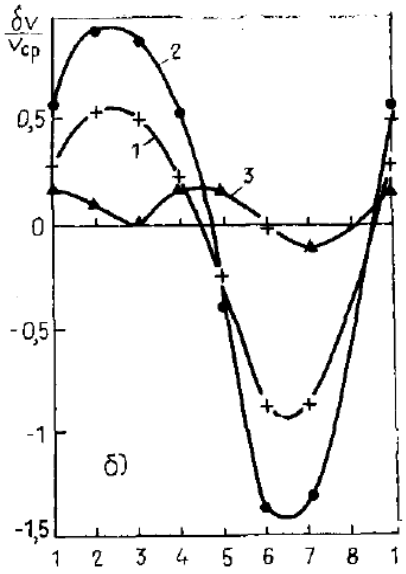

Fig. 17. Velocity perturbation over azimuth. s = 0.62 and 6 poles, 1 – U = 110V, $N_\lambda \leq 11.5$*; 2 – U = 150V,* $N_\lambda \leq 21$ *; 3 – U = 200V,* $N_\lambda \leq 60$*. [22]*

In Fig. 17 velocity profiles are shown with different modified interaction parameter N_λ. One can observe that, first of all, amplitude of perturbation increases with N_λ, then again – it decreases, is out of phase with previous profiles and has no simple harmonic shape.

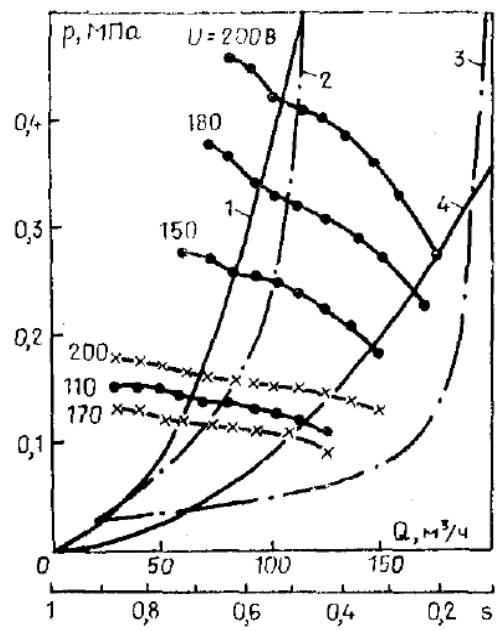

Fig. 18. p-Q characteristics with 6 poles (dots) and 4 poles (crosses). 1,4 – hydraulic curves of external circuit; 2 – instability threshold according to [18], 3 – estimated stability threshold. [22]

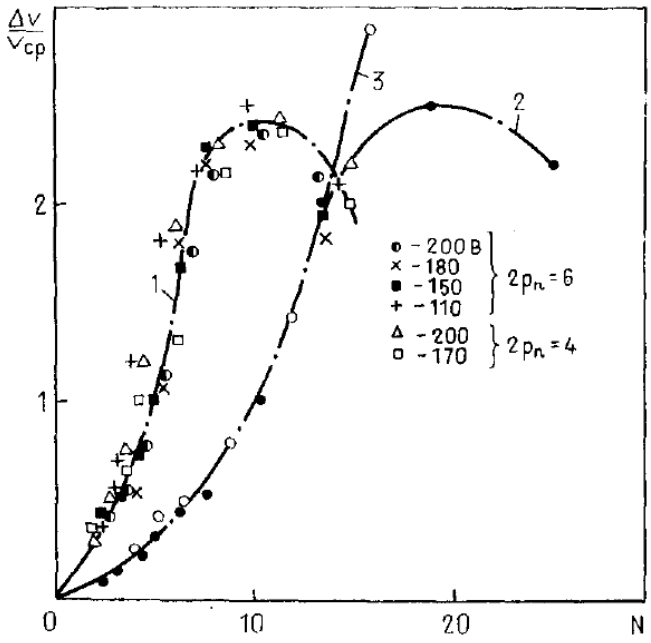

Fig. 19. Velocity perturbation as function of interaction parameter $N = \frac{p_{EM}}{\rho v^2}$ with 1- symmetric air gap; 2- asymmetric air gap; 3 – with lateral side bars. [22]

In Fig. 18 obtained p-Q characteristics are shown and authors note local decrease of developed parameters in practically every case. It is shown, that this bump, lies on same hydraulic curve of the circuit (Fig. 18 curve 1) and is above instability threshold (Fig. 18 curve 2). By analysing velocity perturbation as function of interaction parameter defined as: $N = \frac{p_{EM}}{\rho v^2}$, authors are able to show mentioned saturation and decreasment effect of perturbations in Fig. 19.

However, it is important to note that even measured amplitudes of perturbations apparently decrease on the right side of curve 1 Fig. 19, unstable behaviour of ALIP is registered from point of view of pressure and flowrate oscillations. An example of this is shown in Fig. 20 – even though maximal velocity perturbation amplitudes are registered in point 1. p-Q oscillations do not exceed 0.5%, but low frequency (LF) pressure pulsations reach up to 7% in point 4.

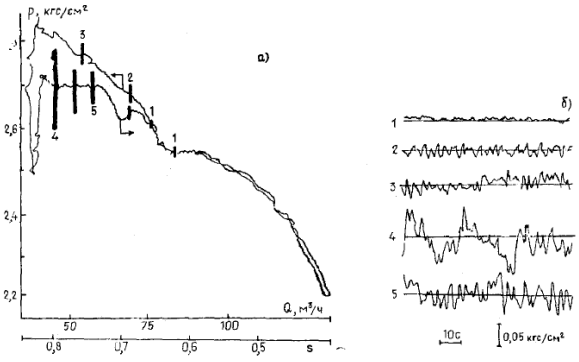

Fig. 20. Pulsations of pressure and flowrate. U = 150V and 6 poles. [22]

The question of pressure pulsations and MHD instability in ALIP has been analysed in details in [16] [34] [35] [25]. These works were carried out in the same experimental facility setup of which is shown in Fig. 21. Phenomena in vertical ALIP-2 developing of nominal flowrate are investigated mainly using measurement of magnetic field, pressure and vibrations.

In order to quantify DSF and LF (up to 10 Hz) pulsations pressure measurements in inlet (Fig. 21 cuts B-B and C-C) and outlet (Fig. 21 cuts A-A and D-D) pressure measurements are performed using 3 different methods:

1. Manometers – P_0
2. Strain gauges – P_S
3. Piezo-electric sensors P_P

Accelometers were used (Ac1-6) to measure vibrations in different parts of the ALIP.

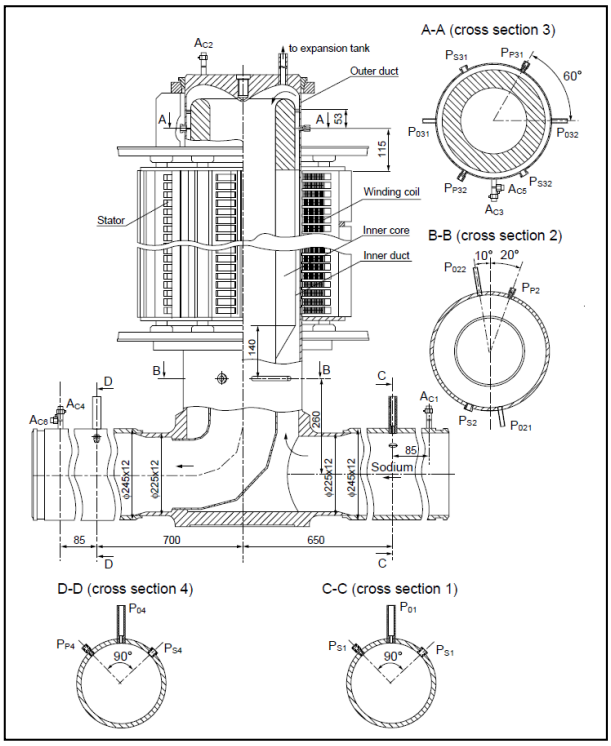

Fig. 21. Schematic drawing of vertical ALIP-2. [35]

A local maximum of p-Q characteristic Fig. 22 and afterwards strong increase of LF pulsations was observed also in this experiment. Moreover, authors were able to show that in regime $Rm_s < 1$ DSF pulsations dominate Fig. 23, but tend to decrease with increase of Rm_s. When $Rm_s > 1$ DSF are relatively small, LF pulsations start to rapidly increase Fig. 23.

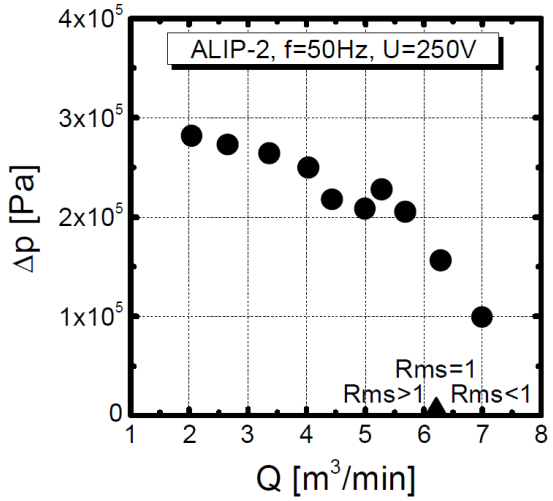

Fig. 22. p-Q characteristic f = 50 Hz. [35]

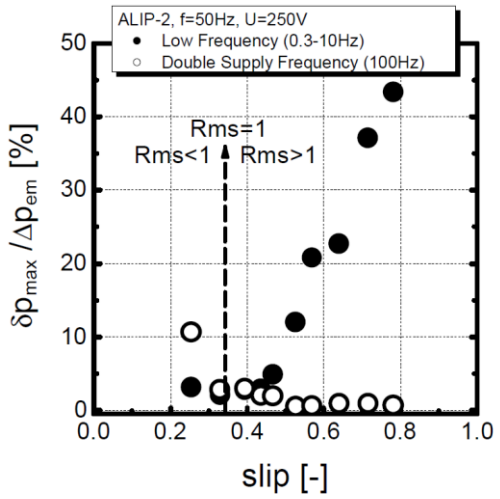

Fig. 23. Amplitude of pressure pulsations f = 50Hz. [35]

An example of pressure pulsations and corresponding spectrum is shown in. While in regime of $Rm_s < 1$ strong DSF peak is observed in Fig. 24 , but in regime $Rm_s > 1$ a broad band of LF have appeared Fig. 25.

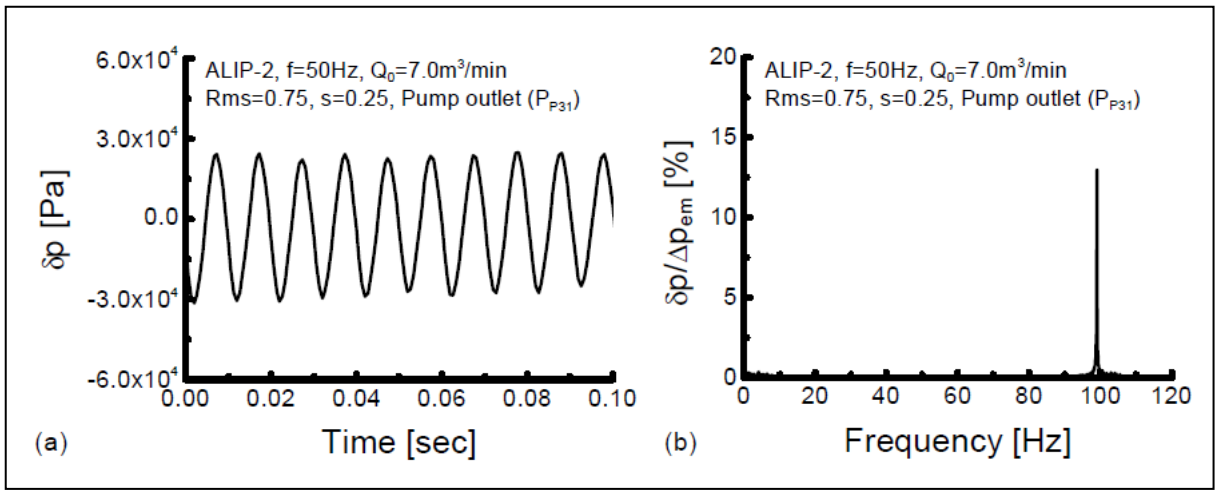

Fig. 24. Pressure pulsations and its spectrum. Rm_s = 0.75. [35]

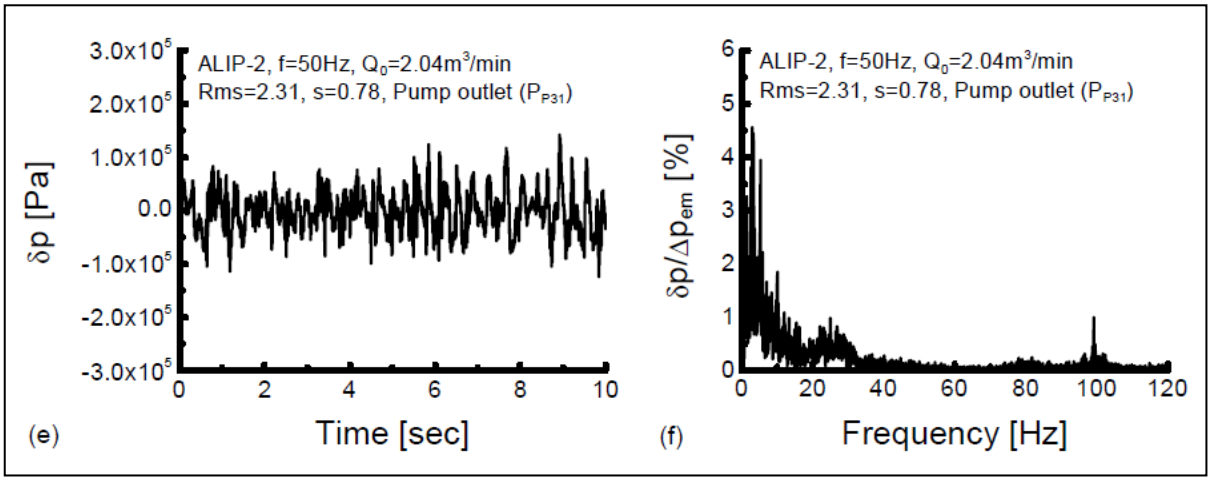

Fig. 25. Pressure pulsations and its spectrum. Rm_s = 2.31. [35]

Authors purpose DSF pulsations suppression method using linear grading off applied magnetic field in the inductor ends Fig. 26 and show efficiency of this method Fig. 27.

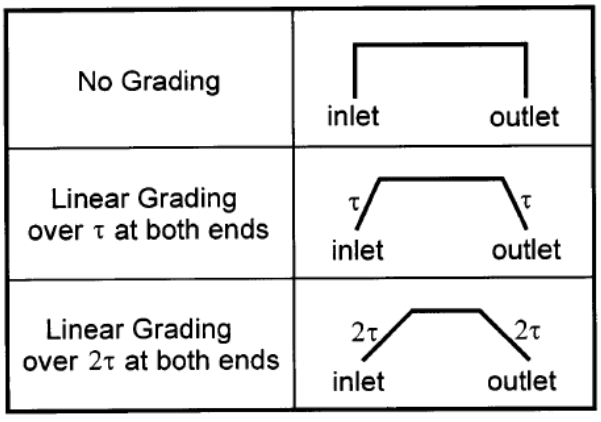

Fig. 26. Scheme of linear winding grading. [34]

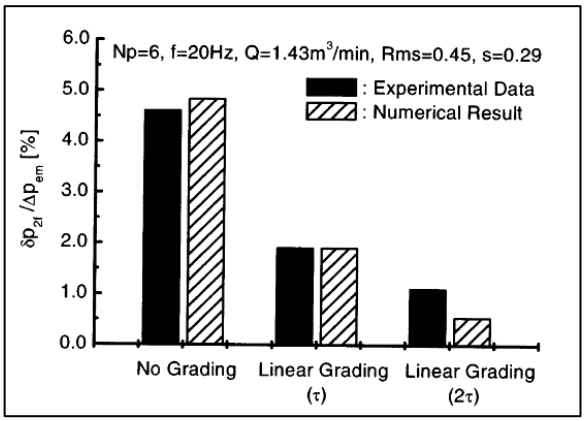

Fig. 27. Effect of linear grading f = 20 Hz. [34]

While DSF pulsation clearly appear from finite length of the ALIP and is purely electromagnetic effect, similar cannot be said about LF pulsations, appearance of which characterize MHD instability up to some extent.

In [25] authors develop and test idea already known since 1980-ies [23] to stabilize the flow and reduce LF pulsations by changing connection of coils (distribution of external current density) in the inductor by applying phase shift Fig. 28. The main goal of such change is to somehow interfere in distribution of magnetic field (and therefore developed EM forces) to reduce instability Fig. 29.

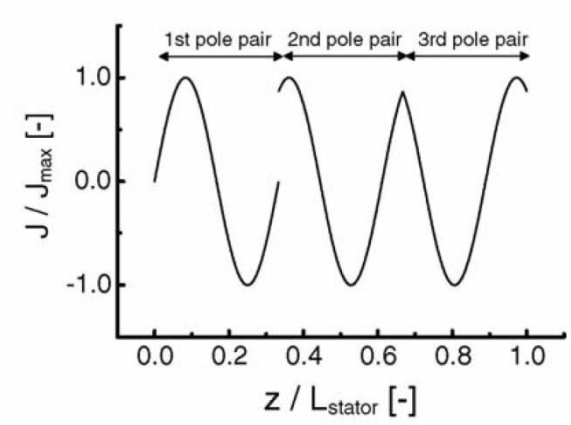

Fig. 28. Schematic drawing of phase shift. [25]

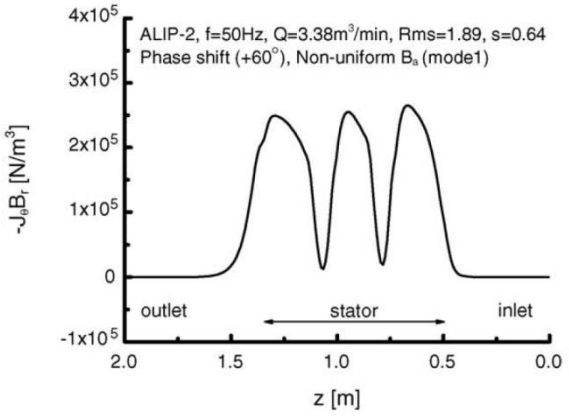

Fig. 29. EM force distribution Rms = 1.8, non-uniform B_a, mode 1, phase shift +60°. [25]

Authors are able to experimentally show evidence that using such method a positive stabilization effect of ALIP is achieved at least to some extent, which is confirmed by analysing spectrums of both – pressure (Fig. 30 and Fig. 31) and vibrations (Fig. 32 and Fig. 33), as well as efficiency has not been significantly scarified.

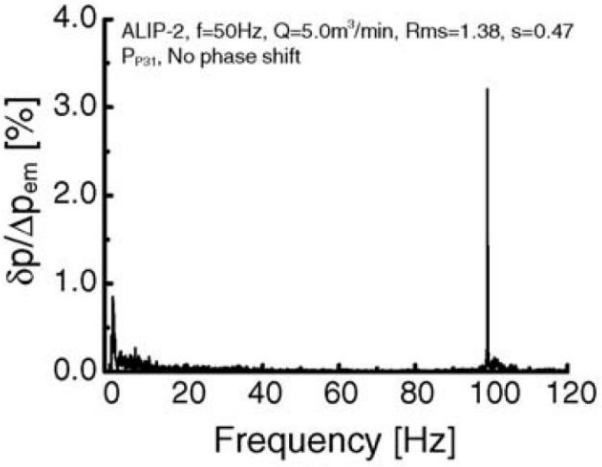

Fig. 30. Pressure pulsation spectrum: f = 50Hz, Rms = 1.38, no phase shift. [25]

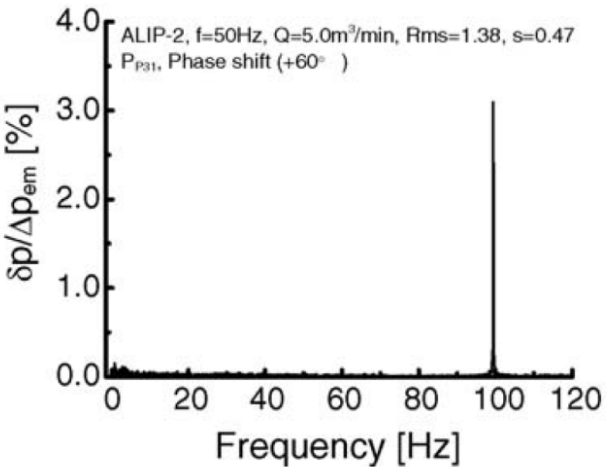

Fig. 31. Pressure pulsation spectrum: f = 50Hz, Rms = 1.38, phase shift +60°. [25]

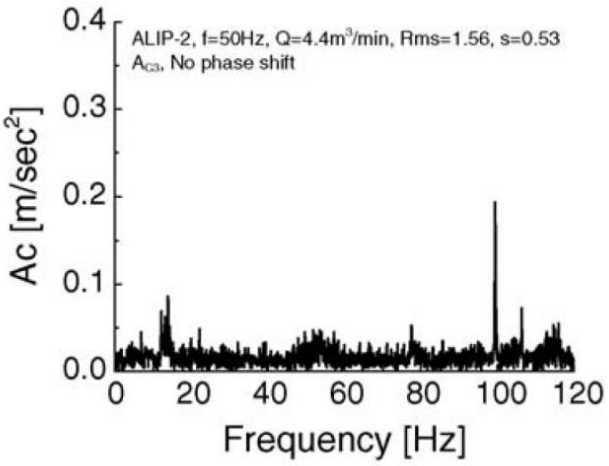

Fig. 32. Vibration spectrum: f = 50Hz, Rms = 1.56, no phase shift. [25]

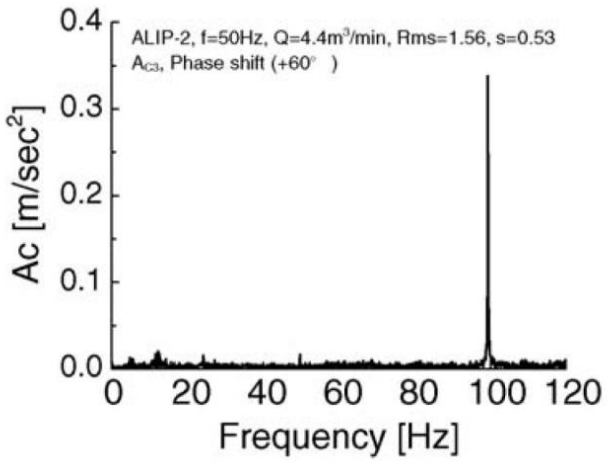

Fig. 33. Vibration spectrum: f = 50Hz, Rms = 1.56, phase shift +60°. [25]

Finally, large sodium immersed, self-cooled ALIP is experimentally analysed in work of Ota et al. [36]. A principal drawing of this rather unique machine meant for cooling of SFR is shown in Fig. 34 developing flowrate Q = 160m^3/min and pressure p = 2.8 bar.

First of all, authors show that measurements of external magnetic over azimuth deviate only within 5%.

Then global performance of this ALIP is analysed and found that instability characterized by fluctuation of pressure and flowrate appear somewhat around $Rm_s \approx$ 1.4 ... 1.5 Fig. 35.

Similarly as in previous works, it is found that these fluctuations start to rapidly increase when the point of local maximum is passed Fig. 36 and Fig. 37. Authors are able to show development of instability also with transient signal of magnetic field and pressure pulsations. They also characterize stable, transition and unstable zones of p-Q characteristic, therefore defining Area I where ALIP should nominally operate Fig. 38.

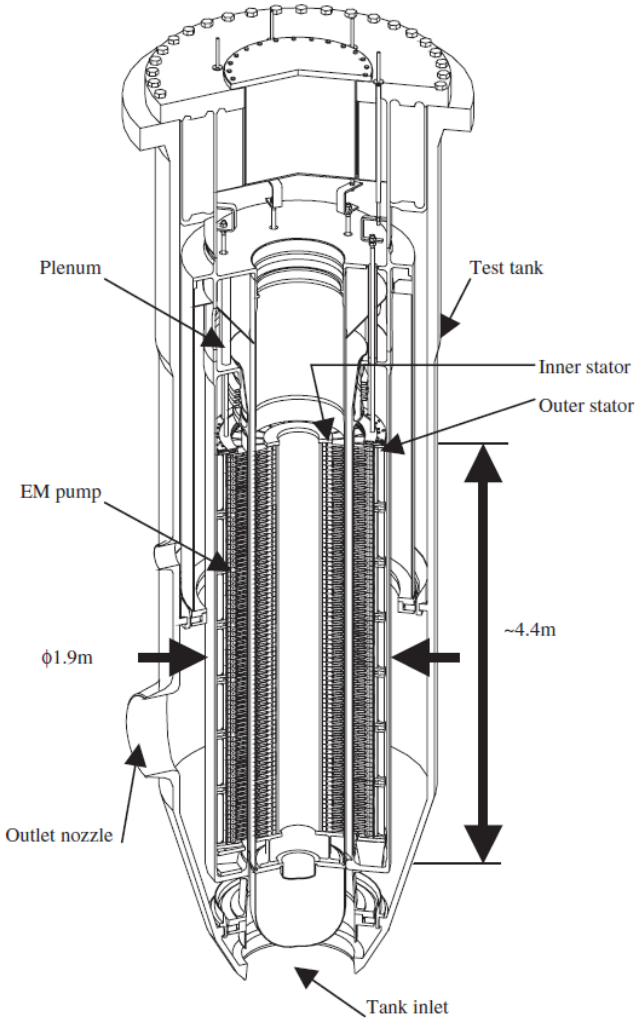

Fig. 34. Bird-eye view of EM pump. [36]

This transition is well captured by authors in Fig. 39, showing that both pressure and magnetic field start to oscillate significantly as soon as Area II is reached.

There is an interesting remark concerning transition Area II: *"The pump current, the flow rate and the head could not be controlled in this area. When the frequency and the voltage were fixed and the valve was narrowed down from Area I, it was identified that after the flow rate and the head reaching the Q–H characteristics peak, the operating point passed this Area II and transited to Area III."*

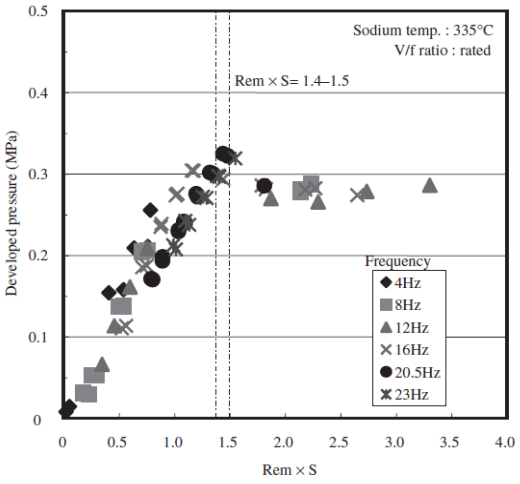

Fig. 35. Dependence of developed pressure on Rm_s. [36]

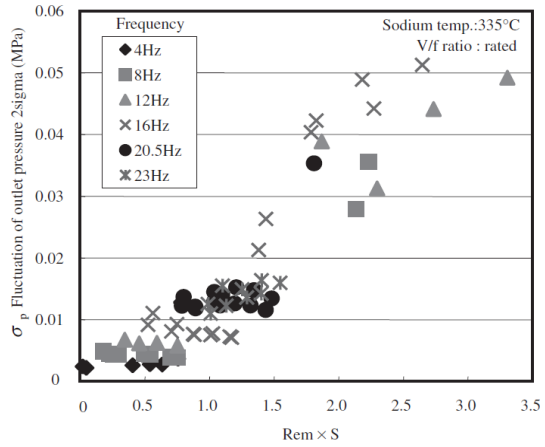

Fig. 36. Dependence of pump outlet pressure fluctuations on Rms. [36]

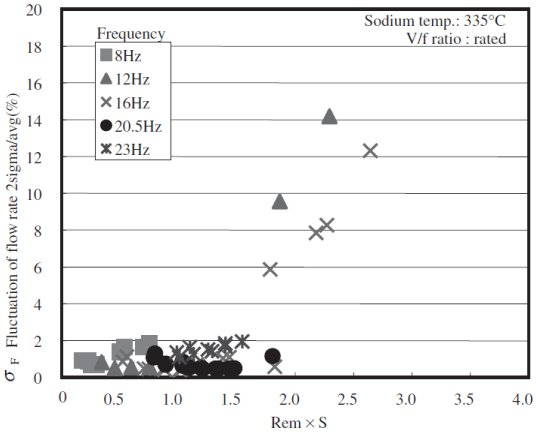

Fig. 37. Dependence of flowrate fluctuations on Rms. [36]

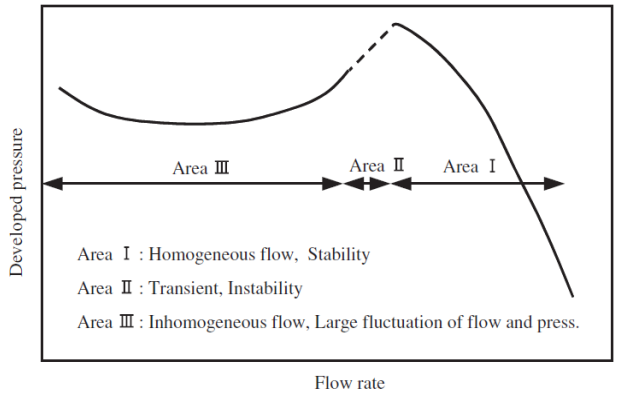

Fig. 38. Classification of features of Q-H characteristic observed [36]

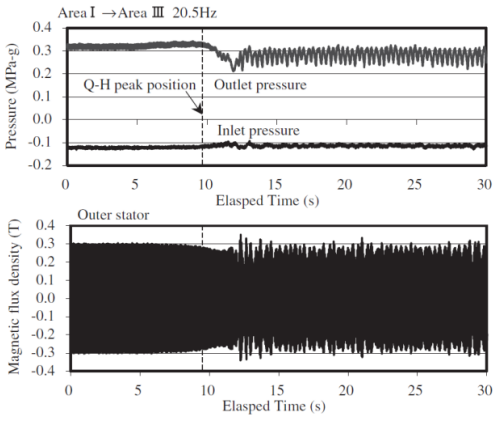

Fig. 39. Trend of magnetic flux density and pump pressure between Area I and Area III. [36]

Finally, another peculiar note can be found in the work: "*Stable operating area of this pump (in the case of constant voltage power source control):* $Na\ 200^oC\ Rm_s < 1.7$" and "$Na\ 335^oC\ Rm_s < 1.4$". Reasons why higher stability threshold should be achieved with higher conductivity of Na are not obvious.

1.3.1. Final remarks on experimental investigations

Picked reviewed works in this chapter are somewhat different for most of the literature in ALIP – with deeper inside on MHD instability characterization. However, significantly more experimental works on EMIPs can be found, which are relevant in context of large ALIP development or working with liquid Na.

Works involving 850 m^3/h flowrate ALIP operating with liquid sodium were carried out in [7] [21] and traces of MHD instability confirmed. The stabilization technique using phase shift was, first of all, experimentally tested also on this pump [23].

A number of works discussing global characteristics of vertical ALIP-3500 also have been published earlier [10] [49] showing feasibility of such pump to be implemented in SFR.

Analysis of integral behaviour of ALIP discussed in the beginning of this chapter can be found in [50].

Another paper about reviewed Na immersed large scale pump can be found which postulate that MHD instability has not been observed [51]. This contradicts to presented results in [36] and is obviously a misinterpretation. The development and experimental work on sodium immersed ALIPs can be also found in works [12] [11].

Some recent experimental activities on ALIPs have been also started in India [52] and also South Korea [38].

Experimental works on MHD phenomenon in FLIPs can be found in [20] [53] [19] [54].

1.4. Numerical investigations of MHD instability

A highly important part in modern research is use of computers and numerical models. However, MHD instability discussed in [18] is asymmetric phenomenon, which literally means, that it cannot be modelled using 2D axi-symmetric approach. Obviously, complete 3D model would be appropriate, but very time consuming solution for this task and no such study can be found in literature so far. Only reported numerical simulation capable to describing MHD instability using 2D asymmetric (θ-z) model is by Araseki et al. [35] [25]. Here concept of this model and obtained results are briefly discussed.

First of all, such model is radially (height) averaged – all fields (magnetic, velocity) are averaged over the height (similarly as in [18]). Therefore, if condition (57) is met, one can define mean radius R, cut the annular channel and unfold it thus working with planar geometry Fig. 40.

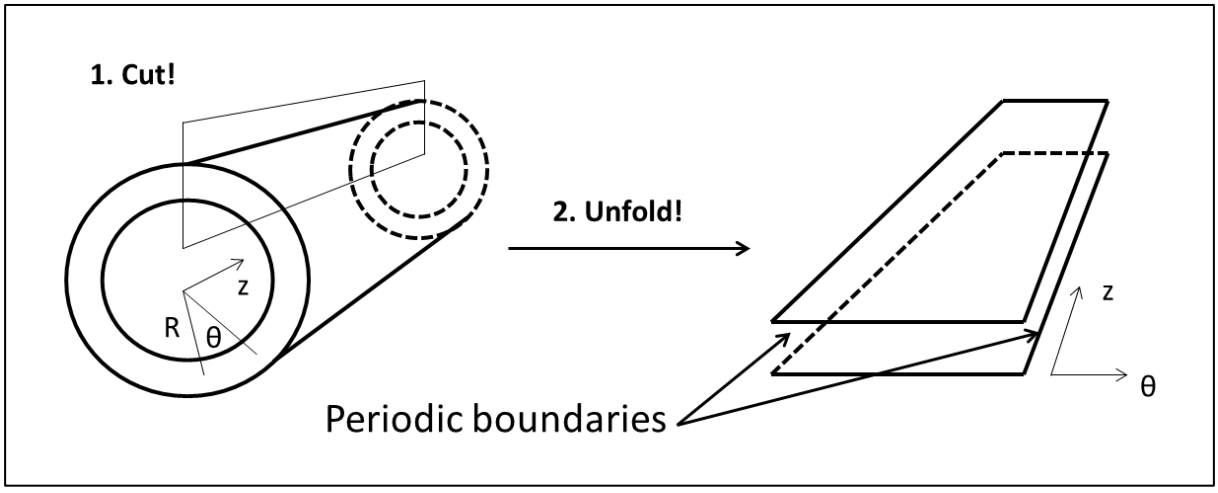

Fig. 40. Formation of 2D θ-z model geometry.

Then (since there is no derivative over radius and case is 2D) in-plane (θ-z) two component velocity field and single out-of-plane (r) component of magnetic field is considered.

The induction equation in such case must be solved using method of decomposition of magnetic field into external and induced (chapter 1.1.2). This implies that external magnetic field (field in the channel without liquid metal) has to be known (calculated) before, and used as source term in the induction equation. This also allows user defined modifications of imposed field (e.g. perturbations or simplifications). In particular authors impose following distribution of magnetic field:

$$B_{ar} = B_{a0}(1 + \beta\, sin(\gamma\theta + \varphi))sin(\omega t - \alpha z) \tag{77}$$

Where amplitude B_{a0} is found from 2D axisymmetric calculation and β, γ, φ are user input parameters. The decay of the magnetic field outside stator region is imposed by exponential law.

Another peculiar feature of this model is that there are no walls (inlet, outlet and periodic boundaries), therefore friction must be included into Navier-Stokes equation as

additional dissipative source term. This, however, was neglected and in the presented model only viscose effects were taken into account. In order to introduce velocity perturbation, inlet boundary condition was:

$$v_z = v_{z0}(1 + a\,sin(b\theta + c)) \tag{78}$$

Where amplitude v_{z0} is mean axial velocity and a, b, c are user input parameters.

The geometry of model is shown in Fig. 41. Mesh with 36 x 200 cells was used in transient calculation with time-step of 10^{-4}s.

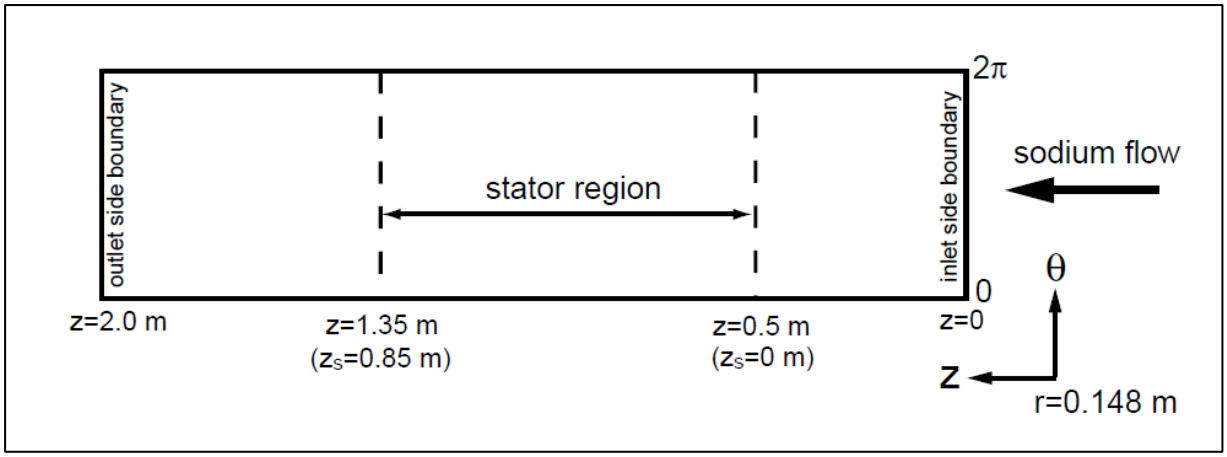

Fig. 41. Analytical model (of numerical calculation) [35]

Authors also analyse geometrical effects due to which different type of patterns or modes of perturbations may appear. In Fig. 42 they are presented and referred later as Mode 1 - 3.

First of all, a situation where solely magnetic field is perturbed with Mode 1 is studied and user input parameters are: $\beta = 0.1;\ \gamma = 1;\ \varphi = \pi/2$.

In Fig. 43 - Fig. 46 qualitative distribution of velocity vector field is shown at some time instant; it can be observed that with increase of Rm_s flow becomes more complex.

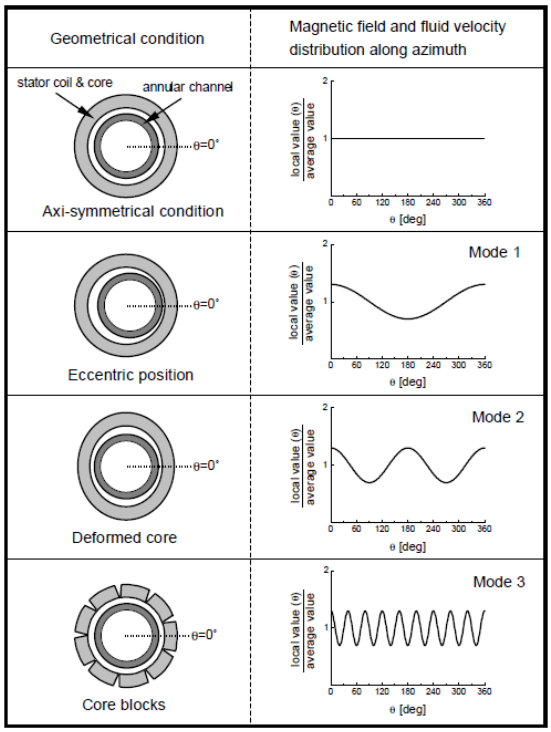

Fig. 42. Non-uniform patterns of applied field and sodium velocity. [35]

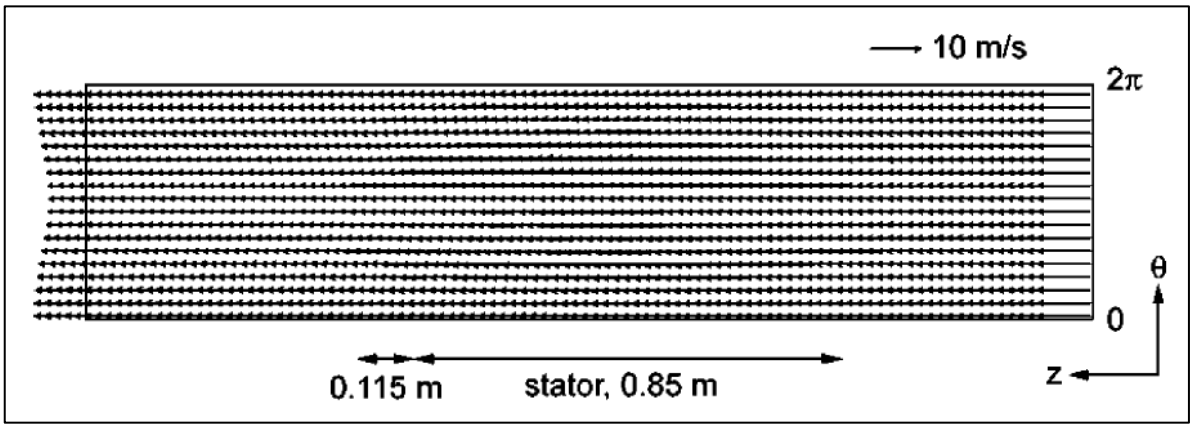

Fig. 43. Sodium flow: Rms = 0.75, non-uniform Ba, Mode 1, ±10%. [35]

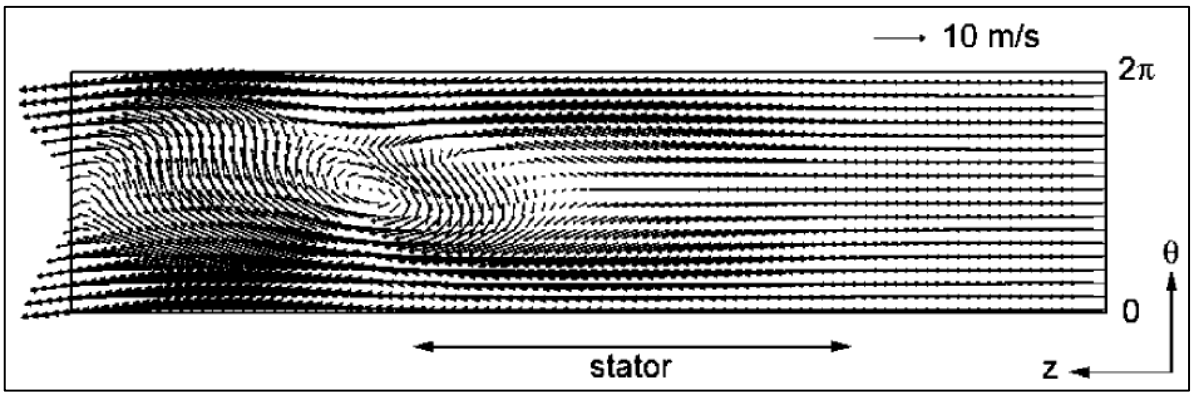

Fig. 44. Sodium flow: Rms = 1.56, non-uniform Ba, Mode 1, ±10%. [35]

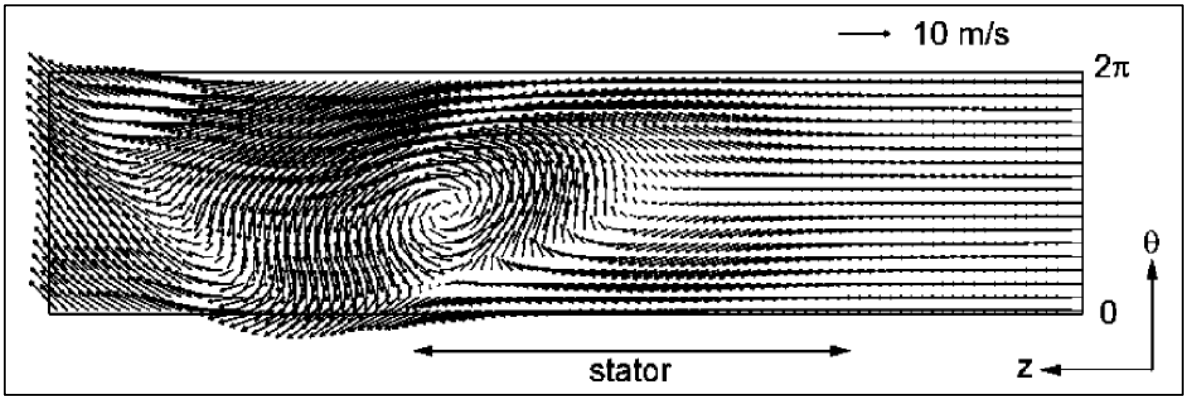

Fig. 45. Sodium flow: Rms = 1.89, non-uniform Ba, Mode 1, ±10%. [35]

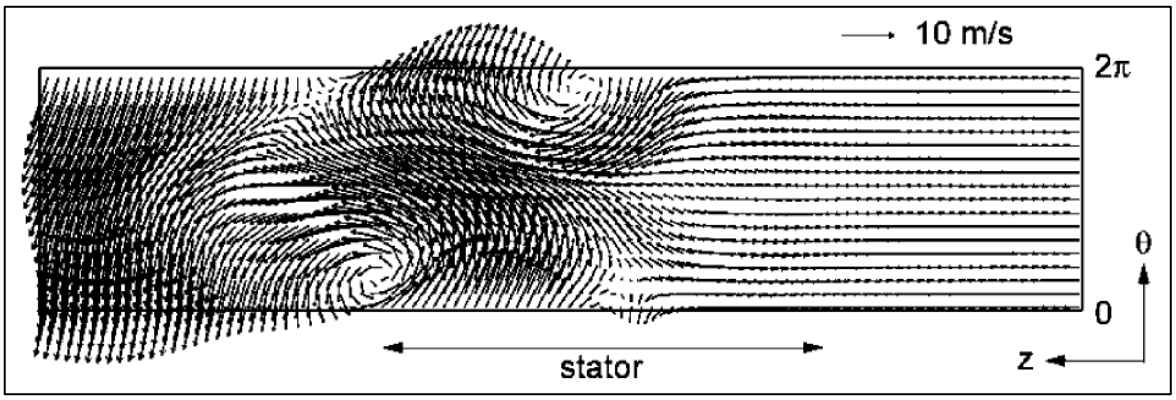

Fig. 46. Sodium flow: Rms = 2.31, non-uniform Ba, Mode 1, ±10%. [35]

Spectrum of pressure oscillations in the single cell outside the stator region is shown in Fig. 47 - Fig. 50. First of all, it can be observed that DSF pulsations decrease with increase of Rm_s, but discrete frequency LF pulsations appear. One can notice that frequency of LF pulsations is decreasing with Rm_s Fig. 48, Fig. 49 but amplitude of it increases. Finally in Fig. 50 a set of discrete LF has appeared which seem to be multiples of base frequency (in this case ~2.5 Hz).

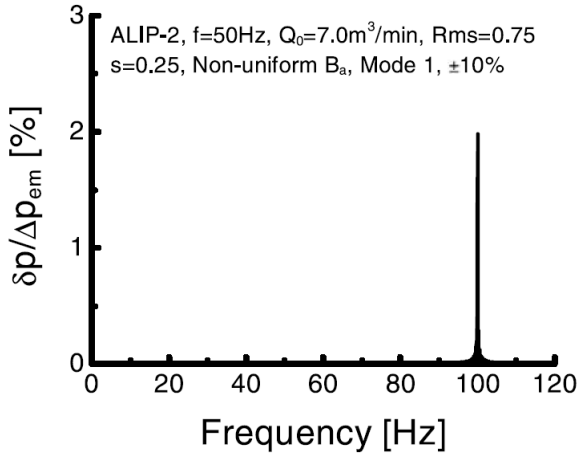

Fig. 47. Pressure pulsation spectrum: Rms = 0.75, non-uniform B_a, Mode 1, ±10%. [35]

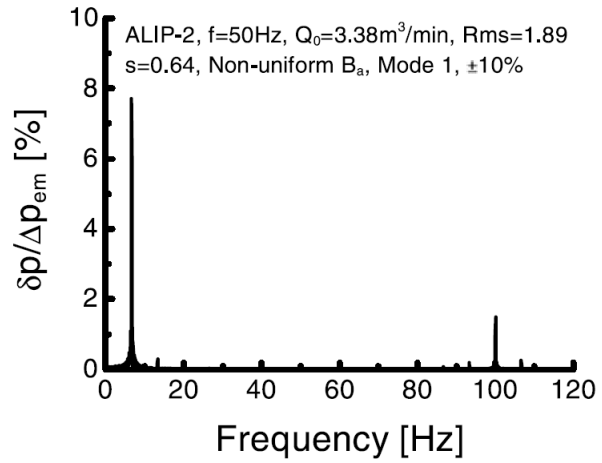

Fig. 48. Pressure pulsation spectrum: Rms = 1.89, non-uniform B_a, Mode 1, ±10%. [35]

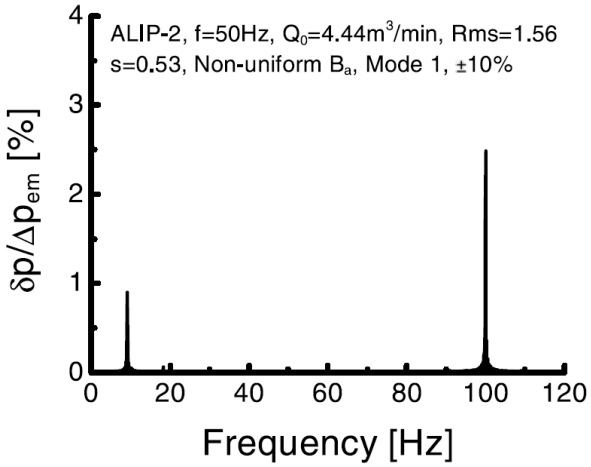

Fig. 49. Pressure pulsation spectrum: Rms = 1.56, non-uniform B_a, Mode 1, ±10%. [35]

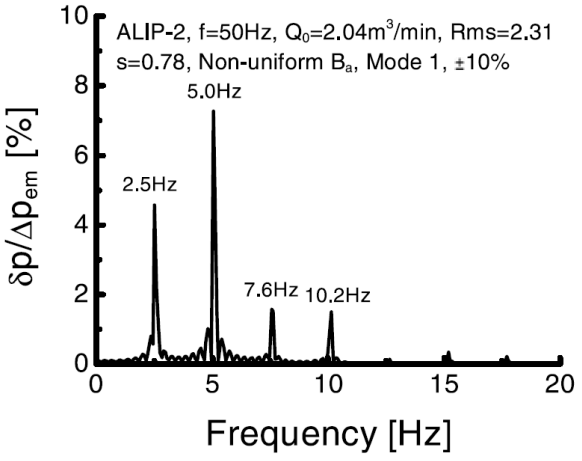

Fig. 50. Pressure pulsation spectrum: Rms = 2.31, non-uniform B_a, Mode 1, ±10%. [35]

Another interesting result is pressure pulsations obtained by perturbation of inlet velocity profile by 30%. In the case with perturbation Mode 1 Fig. 51 spectrum similar to Fig. 48 is obtained. When Mode 2 is implied additional frequencies do appear in spectrum Fig. 52 and some of them are surely interference effects – beats (e.g. additional frequencies near 100 Hz).

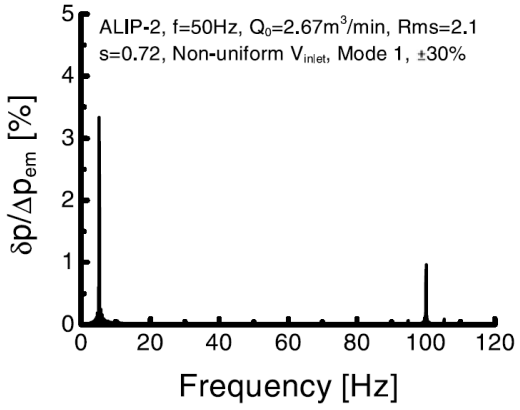

Fig. 51. Pressure pulsation spectrum: Rms = 2.1, non-uniform V_{inlet}, Mode 1, ±30%. [35]

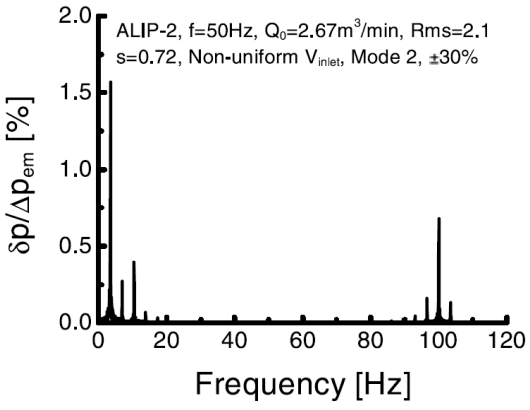

Fig. 52. Pressure pulsation spectrum: Rms = 2.1, non-uniform V_{inlet}, Mode 2, ±30%. [35]

Finally, authors are able to also numerically demonstrate suppression of LF pulsations using phase shift of applied external current (magnetic field) Fig. 53 and Fig. 54. It is shown that phase shift does not sufficiently increase DSF pulsations in the case of $Rm_s > 1$, but brings some penalty of the developed pressure.

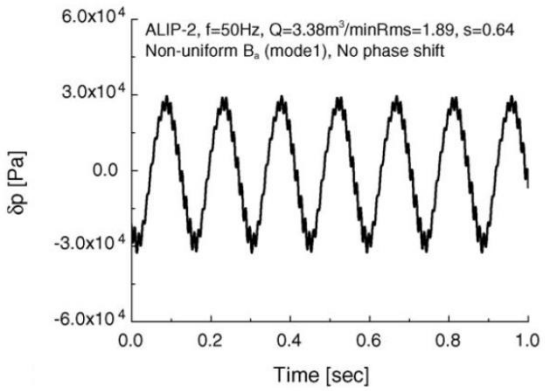

Fig. 53. Pressure pulsation at pump outlet: Rms = 1.89, non-uniform B_a, Mode 1, no phase shift. [25]

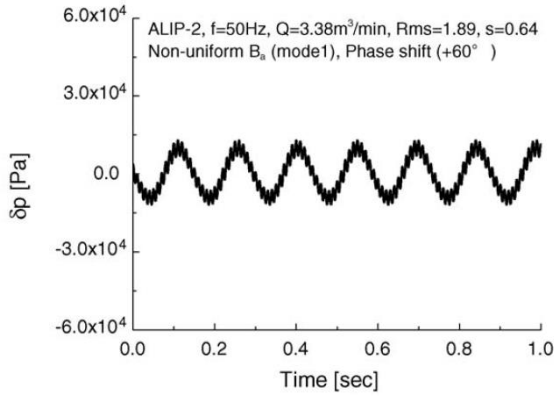

Fig. 54. Pressure pulsation at pump outlet: Rms = 1.89, non-uniform B_a, Mode 1, phase shift +60° [25]

1.4.1. Final remarks on numerical investigations

Classically ALIPs are studied in 2D axisymmetric models. A good example of such study can be found in [55]. DSF pulsations in [16] [34] are analysed by similar means.

An interesting quasi - 2D model is described in [56] which accounts also flow non-uniformity using concept of separate jets already developed in [57]. Such models comparative performance is analysed in [58] and show reasonable capabilities.

Finally, some recent work on modelling ALIPs using commercial software COMSOL can be also found [59].

1.5. Summary of bibliographical review

In reviewed bibliography conclusions and common elements of all works can be summarized:

1. Using 2D axi-symmetric models distribution of magnetic field over length and height of channel can be calculated. Solid body approximations can be used and developed pressure estimated in the case of steady flow both numerically and analytically.
2. In most of the cases of practical significance relationship (57) is met and effects can be averaged over the height. This simplifies model and offers simpler ways analysis of asymmetric flows.
3. DSF pulsations are caused by oscillating component of magnetic field which appear due to finite length of inductor and is electromagnetic effect.
4. Theoretically predicted stability threshold is verified experimentally and numerically. It is found that, when threshold is exceeded azimuthal perturbations of velocity are amplified with increase of slip (Rm_s).
5. Growth of azimuthal perturbations over channel length is experimentally observed.
6. With higher values of (Rm_s), even though decrease of perturbation amplitudes is observed, oscillations of flowrate, pressure etc. appear and rapidly increase with Rm_s.
7. This loss of stability is near the experimental local maximum of p-Q characteristic where in uncontrolled transient from stable to unstable regime may be observed.
8. 2D asymmetric (θ-z) model is capable of modelling instability. Pulsations characterizing instability are of low frequencies and are found in this numerical model.
9. Numerical results show that, after stability threshold is reached, single LF peak is observed in pressure spectrum. With increase of Rm_s multiples of base LF pulsation appear.
10. Stabilization using phase shift in winding connection is confirmed to decrease oscillations and stabilize flow up to some extent.

Nevertheless, there are some important gaps between theoretical, experimental and numerical studies which limit the full analysis and comprehension of MHD instability process:

- There is no theoretical estimation of perturbation temporal and spatial development. Therefore even amplification of perturbation is measured, there is no possibility of verify this result. Except comparison with numerical calculations.

- Presented numerical model, even though capable of modelling instability, is highly simplified. E.g. applied form of external magnetic is severely approximated and taking into account only viscose dissipation in highly turbulent flow might not hold critique. Therefore methods of MHD instability simulations should be also improved by taking into account more and more sophisticated effects.
- To proceed with developing more sophisticated tools, verification of numerical solutions in simplified MHD instability cases must be done *a priori*. This is problematic; since only theoretical estimate is threshold (74) and models of MHD instability in ideal ALIP have not been studied.
- At this point it is clear that LF pulsations do represent MHD instability phenomenon, but generation mechanisms why such pulsations appear are not well understood.
- There are also uncertainties about stabilization methods of the ALIP. E.g. there is lack of mathematical arguments why experimentally tested method works.
- From experimental point of view, it seems that pressure spectrums could be used for characterizing global behaviour of ALIP and effects of MHD instability. However, it is questionable if such comparison is quantitative.

To resolve some of these points already mentioned tasks evolve naturally, reminding that they are:

1) analyse a system of MHD equations for ideal ALIP theoretically and identify conditions when perturbations start to amplify
2) discuss the theoretical results of the thesis in the context of the existing research
3) examine theoretically the stable operation and stabilization of ideal ALIP
4) calculate and compare the theoretical and numerical perturbation growth rates for an ideal ALIP
5) develop the numerical model of realistic EMIP and elaborate potentially unstable regimes
6) conduct an experiment equivalent to the numerically developed model and compare the results.

Here bibliographical review is finished and in next chapter is realization of list above is started.

2. THEORETICAL INVESTIGATIONS

2.1.Analysis of nature of MHD instability in ideal ALIP

2.1.1. Studied dimensionless system

So far system of MHD equations was presented in dimensional form and some dimensionless groups (magnetic Reynolds number, Interaction parameter etc.) appeared in reviewed works. The one of difficulty for consistent analysis is that frequently authors use slightly different definitions and symbols for dimensionless groups. In order to clarify this question, derivation process of studied dimensionless system is shown below. The system is:

$$\Delta \boldsymbol{B} - \mu_0 \sigma \left[\frac{\partial \boldsymbol{B}}{\partial t} - (\boldsymbol{B}\nabla)\boldsymbol{v} + (\boldsymbol{v}\nabla)\boldsymbol{B} \right] = -\mu_0 \nabla \times \boldsymbol{j_e} \tag{79}$$

$$\rho \left(\frac{\partial \boldsymbol{\omega}}{\partial t} + (\boldsymbol{v}\nabla)\boldsymbol{\omega} - (\boldsymbol{\omega}\nabla)\boldsymbol{v} \right) = \nabla \times \left(\frac{(\boldsymbol{B}\nabla)\boldsymbol{B}}{\mu_0} - \frac{\lambda_h}{d_h} \cdot \rho \frac{\boldsymbol{v}|\boldsymbol{v}|}{2} - \boldsymbol{j_e} \times \boldsymbol{B} \right) \tag{80}$$

$$\nabla \boldsymbol{v} = 0 \tag{81}$$

With condition (57) it can be rather correctly assumed that the applied linear current density is evenly spread over a height of the non-magnetic gap d_m.

It is more convenient to solve induction equation using complex numbers and considering only real (physical) part of e.g. complex magnetic field. Classically, notation $Re[\dots]$ is left out by convention. However, here notation of real part is kept by sum of complex and complex conjugate part. This is necessary to avoid confusion when another group of complex terms (for stability analysis) is introduced.

$$\boldsymbol{j_e} = Re\left[\frac{\sqrt{2}J}{d_m} \cdot e^{i(\alpha z - \omega_B t)} \right] \boldsymbol{e_\varphi} = \frac{\sqrt{2}J}{d_m} \cdot \frac{1}{2} \sum_{\pm} e^{\pm i(\alpha z - \omega_B t)} \tag{82}$$

In the case of small channel height (57), only 2D axially-azimuthal flow and radial component of magnetic field can be considered:

$$\boldsymbol{v} = v_z(\varphi, z, t)\boldsymbol{e_z} + v_\varphi(\varphi, z, t)\boldsymbol{e}_\varphi \tag{83}$$

$$\boldsymbol{B} = B_r(\varphi, z, t)\boldsymbol{e_r} = \frac{1}{2} \sum_{\pm} B_0^{\pm} e^{\pm i(\alpha z - \omega_B t)} \boldsymbol{e_r} \tag{84}$$

Therefore only single radial vorticity component exists:

$$\boldsymbol{\omega} = \left(\frac{\partial v_z}{R\partial \varphi} - \frac{\partial v_\varphi}{\partial z} \right) \boldsymbol{e_r} = \omega(\varphi, z, t)\boldsymbol{e_r} \tag{85}$$

In such 2D case some terms can be simplified:

$$(\boldsymbol{B}\boldsymbol{\nabla})\boldsymbol{B} = (\boldsymbol{B}\boldsymbol{\nabla})\boldsymbol{v} = (\boldsymbol{\omega}\boldsymbol{\nabla})\boldsymbol{v} = 0 \tag{86}$$

Then MHD equation system can be rewritten:

$$\Delta \boldsymbol{B} - \mu_0 \sigma \frac{d_h}{d_m}\left(\frac{\partial \boldsymbol{B}}{\partial t} + (\boldsymbol{v}\boldsymbol{\nabla})\boldsymbol{B}\right) = -\frac{\mu_0\sqrt{2}J}{d_m} \cdot \frac{1}{2}\sum_{\pm} \boldsymbol{\nabla} \times e^{\pm i(\alpha z - \omega_B t)}\, \boldsymbol{e}_{\varphi} \tag{87}$$

$$\rho\left(\frac{\partial \boldsymbol{\omega}}{\partial t} + (\boldsymbol{v}\boldsymbol{\nabla})\boldsymbol{\omega}\right) = \boldsymbol{\nabla} \times \left(-\frac{\lambda_h}{d_h} \cdot \rho \frac{\boldsymbol{v}|\boldsymbol{v}|}{2} + \frac{\sqrt{2}J}{2d_h} \times \frac{1}{2}\sum_{\pm} B_0^{\pm}\, \boldsymbol{e_z}\right) \tag{88}$$

$$\boldsymbol{\nabla} \cdot \boldsymbol{v} = 0 \tag{89}$$

By choosing characteristic scales, the dimensionless time, coordinates, velocity and magnetic field are:

$$\tilde{z} = \alpha z \tag{90}$$

$$\tilde{R} = \alpha R \tag{91}$$

$$\tilde{t} = \omega_B t \tag{92}$$

$$\tilde{v} = \frac{v}{v_B} \tag{93}$$

$$\tilde{b} = \frac{B d_m \alpha}{\sqrt{2}\mu_0 J} \tag{94}$$

Finally the dimensionless system reads:

$$\tilde{\Delta}\widetilde{\boldsymbol{b}} - Rm\left(\frac{\partial \widetilde{\boldsymbol{b}}}{\partial \tilde{t}} + (\widetilde{\boldsymbol{v}}\widetilde{\boldsymbol{\nabla}})\widetilde{\boldsymbol{b}}\right) = -\frac{1}{2}\sum_{\pm} \widetilde{\boldsymbol{\nabla}} \times e^{\pm i(\tilde{z} - \tilde{t})}\boldsymbol{e_{\varphi}} \tag{95}$$

$$Re_{\lambda}\left(\frac{\partial \widetilde{\boldsymbol{\omega}}}{\partial \tilde{t}} + (\widetilde{\boldsymbol{v}}\widetilde{\boldsymbol{\nabla}})\widetilde{\boldsymbol{\omega}}\right) + \widetilde{\boldsymbol{\nabla}} \times (\widetilde{\boldsymbol{v}}|\widetilde{\boldsymbol{v}}|) = \frac{N_{\lambda}}{Rm} \cdot \frac{1}{2}\sum_{\pm} \widetilde{\boldsymbol{\nabla}} \times \widetilde{b_0^{\pm}}\boldsymbol{e_z} \tag{96}$$

$$\widetilde{\boldsymbol{\nabla}} \cdot \widetilde{\boldsymbol{v}} = 0 \tag{97}$$

By rewriting system in dimensionless form the set of characteristic numbers appear: magnetic Reynolds number Rm, modified interaction parameter N_{λ}, modified Reynolds number Re_{λ} and additionally interaction parameter N and be introduced:

$$Rm = \frac{\mu_0 \sigma v_B}{\alpha}\left(\frac{d_h}{d_m}\right) \tag{98}$$

$$N_{\lambda} = \frac{2\sigma d_h}{\lambda_h \rho v_B}\left(\frac{\mu_0 J}{d_m \alpha}\right)^2 \tag{99}$$

$$Re_{\lambda} = \frac{2 d_h \alpha}{\lambda_h} \tag{100}$$

$$N = \frac{\sigma}{\rho \alpha v_B}\left(\frac{\mu_0 J}{d_m \alpha}\right)^2 \tag{101}$$

These dimensionless groups are consistent with [18]. However, a small remark should be made. Here the friction factor $\lambda_h$is different from (24) due to fact that d_h is half of real hydraulic diameter. Therefore:

$$\lambda_h = \frac{0.316}{2} Re^{-0.25} \tag{102}$$

Taking this into account, definition of modified interaction parameter is consistent also with [22].

2.1.2. Linear stability analysis and dispersion relation

In a solid body approximation it is assumed that velocity has only a constant axial component (103), which leads to solution of induction equation in a harmonic form with amplitude (104).

$$\tilde{\boldsymbol{v}} = \tilde{v_z}\boldsymbol{e_z} \tag{103}$$

$$\widetilde{b_0^{\pm}} = \widetilde{b_c^{\pm}} = \frac{1}{\pm i + Rm_s} \tag{104}$$

First of all, consider base state of velocity (103) and magnetic field amplitude (104). Assume that perturbed state is:

$$\tilde{\boldsymbol{v}} = [\tilde{v_z} + \delta\tilde{v_z}(\varphi, \tilde{z}, \tilde{t})]\boldsymbol{e_z} + \delta\widetilde{v_\varphi}(\varphi, \tilde{z}, \tilde{t})\boldsymbol{e_\varphi} \tag{105}$$

$$\widetilde{b_0^{\pm}} = \widetilde{b_c^{\pm}} + \delta\widetilde{b^{\pm}}(\varphi, \tilde{z}, \tilde{t}) \tag{106}$$

Axial and azimuthal perturbations are linked through continuity equation and it is sufficient to define only one of them. Look for a solution where perturbations are complex exponential functions regarding axial direction and time (107), (108). Here n, γ are complex spatial and temporal development rates and $\delta\tilde{v}_{mk}$, $\delta\widetilde{b_{mk}^{\pm}}$ are complex amplitudes, where index mk specifies amplitude of particular azimuthally-axial mode:

$$\delta\tilde{v_z}(\varphi, \tilde{z}, \tilde{t}) = \sum_{m=1}^{\infty}\sum_{k=-\infty}^{\infty} \delta\tilde{v}_{mk}\, cos(m\varphi)\, e^{n\tilde{z}-\gamma\tilde{t}} \tag{107}$$

$$\delta\widetilde{b^{\pm}}(\varphi, \tilde{z}, \tilde{t}) = \sum_{m=1}^{\infty}\sum_{k=-\infty}^{\infty} \delta\widetilde{b_{mk}^{\pm}}\, cos(m\varphi)\, e^{n\tilde{z}-\gamma\tilde{t}} \tag{108}$$

$$|\tilde{v_z}| \gg |\delta\tilde{v}_{mk}| \tag{109}$$

$$\left|\widetilde{b_c^{\pm}}\right| \gg \left|\delta\widetilde{b_{mk}^{\pm}}\right| \tag{110}$$

Obviously, in (107), (108) beside m modes non-zero axial (in longitudal z direction) k modes as well their temporal and spatial development are considered. These axial modes are defined by imaginary part of n:

$$Im[n] = n_i = \frac{k\pi}{\tilde{L}} \tag{111}$$

Essentially k defines number of half waves over the length of the ALIP which is shown in figure below:

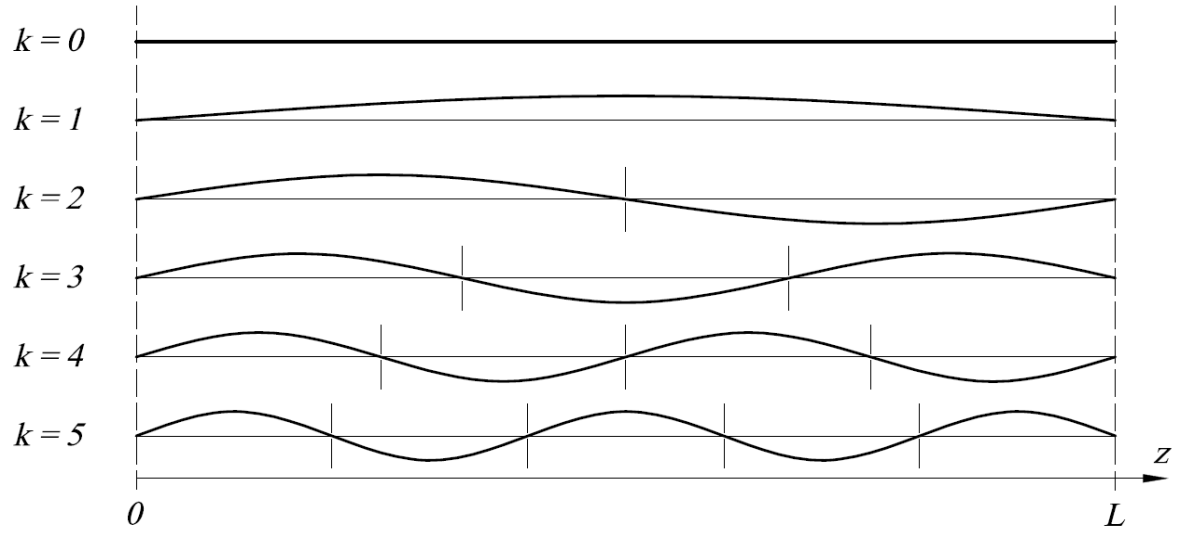

Fig. 55. A sketch of longitude k modes.

Therefore forms of perturbations in present analysis are described by two parameters m and k. In the study [18] case with $mk = m0$ is only considered.

Using (107), (108) and leaving out summation over m and k as well as complex exponent, form continuity we have:

$$\delta\widetilde{v_\varphi}(\varphi, \tilde{z}, \tilde{t})\boldsymbol{e_\varphi} = -\delta\tilde{v}_{mk} n \frac{\tilde{R}}{m} sin(m\varphi)\, \boldsymbol{e_\varphi} \tag{112}$$

Then vorticity is:

$$\widetilde{\boldsymbol{\omega}} = \widetilde{\boldsymbol{\nabla}} \times \widetilde{\boldsymbol{v}} = \delta\tilde{v}_{mk}\left(\frac{n^2}{\kappa_m} - 1\right)\frac{m}{\tilde{R}} sin(m\varphi)\, \boldsymbol{e_r} \tag{113}$$

The term responsible for inertial losses reads:

$$\widetilde{\boldsymbol{\nabla}} \times \widetilde{\boldsymbol{v}}|\widetilde{\boldsymbol{v}}| = \delta\tilde{v}_{mk}\left(\frac{n^2}{\kappa_m} - 2\right)|\tilde{v}_z|\frac{m}{\tilde{R}} sin(m\varphi)\, \boldsymbol{e_r} \tag{114}$$

And EM force term is:

$$\frac{N_\lambda}{Rm} \cdot \frac{1}{2}\sum_{\pm} \widetilde{\nabla} \times \widetilde{b_0^{\pm}}\boldsymbol{e_z} = -\frac{N_\lambda}{Rm} \cdot \frac{m}{\tilde{R}} sin(m\varphi) \cdot \frac{1}{2}\sum_{\pm} \delta\widetilde{b_{mk}^{\pm}}\, \boldsymbol{e_r} \tag{115}$$

From induction equation we have:

$$\delta\widetilde{b_{mk}^{\pm}} = \frac{\pm iRm\widetilde{b_c^{\pm}}}{\pm iRm_s - \kappa'_m + n^2 \pm 2in + Rm(\gamma - \tilde{v}_z n)} \cdot \delta\tilde{v}_{mk} \tag{116}$$

Using (116) the right hand term of (115) is expressed as:

$$\frac{N_\lambda}{Rm} \cdot \frac{1}{2} \sum_{\pm} \tilde{\nabla} \times \widetilde{b_0^{\pm}} \boldsymbol{e_z} = \frac{N_\lambda}{(1 + Rm_s^2)} \cdot \frac{(Rm_s^2 - \kappa'_m) + nRm(2 - 3\tilde{v}_z) + Rm\gamma + n^2}{\left(n^2 - \kappa'_m + Rm(\gamma - \tilde{v}_z n)\right)^2 + (2n + Rm_s)^2} \cdot \frac{m}{\tilde{R}} sin(m\varphi)\, \delta\tilde{v}_{mk} \boldsymbol{e_r} \tag{117}$$

And the left part of (96) using (112) - (114) reads:

$$Re_\lambda \left(\frac{\partial \tilde{\boldsymbol{\omega}}}{\partial \tilde{t}} + (\tilde{\boldsymbol{v}}\tilde{\nabla})\tilde{\boldsymbol{\omega}} \right) + \tilde{\nabla} \times (\tilde{\boldsymbol{v}}|\tilde{\boldsymbol{v}}|) = \left[Re_\lambda \left(\frac{n^2}{\kappa_m} - 1 \right) (\tilde{v}_z n - \gamma) + \left(\frac{n^2}{\kappa_m} - 2 \right) |\tilde{v}_z| \right] \frac{m}{\tilde{R}} sin(m\varphi)\, \delta\tilde{v}_{mk} \boldsymbol{e_r} \tag{118}$$

Combining (117) and (118) will lead to equation 7th n and 3rd γ order. In particular case consider only small development factors to study behaviour of perturbation near stability threshold (73):

$$n, \gamma \ll 1 \tag{119}$$

Thus keeping only first order γ and n terms simplified dispersion relation which couples complex spatial (n) and temporal (γ) development factors with pressure difference respect to critical pressure $\tilde{p}_m$ is obtained:

$$A_m n - B_m \gamma = \frac{N_\lambda (1 - \tilde{v}_z)}{1 + Rm_s^2} - \frac{2|\tilde{v}_z|\left(Rm_s^2 + {\kappa'_m}^2\right)(1 - \tilde{v}_z)}{(Rm_s^2 - \kappa'_m)} = \tilde{p} - \tilde{p}_m = \Delta\tilde{p}_m \tag{120}$$

Or expressing γ:

$$\gamma(n) = \frac{A_m}{B_m} n - \frac{\Delta\tilde{p}_m}{B_m} \tag{121}$$

Where coefficients are:

$$A_m = \left[4|\tilde{v}_z|(2Rm_s + Rm\kappa'_m\tilde{v}_z) + Re_\lambda \tilde{v}_z \left({\kappa'_m}^2 + Rm_s^2 \right) - \frac{N_\lambda}{(1 + Rm_s^2)} Rm(2 - 3\tilde{v}_z) \right] \frac{(1 - \tilde{v}_z)}{(Rm_s^2 - \kappa'_m)} \tag{122}$$

$$B_m = \left[\frac{N_\lambda}{(1 + Rm_s^2)} Rm + Re_\lambda \left({\kappa'_m}^2 + Rm_s^2 \right) + 4|\tilde{v}_z| Rm\, \kappa'_m \right] \frac{(1 - \tilde{v}_z)}{(Rm_s^2 - \kappa'_m)} \tag{123}$$

2.1.3. The convective and absolute instability

According to Drazin [60], convective instability is a process when sufficiently small perturbation grows at the moving point. That is - perturbation may grow while propagating downstream and eventually leaving the system.

To study such situation, first of all, randomly shaped perturbation in initial moment is given by:

$$\delta\tilde{v}_z(\varphi,\tilde{z},0)=\sum_{m=1}^{\infty}\sum_{k=-\infty}^{\infty}\delta\tilde{v}_{mk}\,cos(m\varphi)\,e^{n\tilde{z}} \tag{124}$$

The perturbation can have any constant spatial amplification, but for sake of simplicity assume:

$$Re[n]=n_R=0 \tag{125}$$

Then by using (121) and substituting it in (107) one can obtain expression for perturbation development:

$$\delta\tilde{v}_z(\varphi,\tilde{z},\tilde{t})=\sum_{m=1}^{\infty}\sum_{k=-\infty}^{\infty}\delta\tilde{v}_{mk}\,cos(m\varphi)\cdot e^{\frac{\Delta\tilde{p}_m}{B_m}\tilde{t}}\cdot e^{in_i\left(\tilde{z}-\frac{A_m}{B_m}\tilde{t}\right)} \tag{126}$$

The first exponent with real argument describes growth/decay of perturbation, while second – with imaginary argument – its transport. Apparently, this agrees with definition of convective instability.

The perturbation is transferred with phase velocity $\frac{A_m}{B_m}$ and due to the considered (linear) form of dispersion relation, in this case it is also group velocity of perturbation:

$$\tilde{v}_p=\frac{\partial\gamma}{\partial n}=\frac{A_m}{B_m} \tag{127}$$

The excitation (convective stability) threshold of any mk mode according to (126) is:

$$-\gamma_R=\frac{\Delta\tilde{p}_m}{B_m}=0 \tag{128}$$

Therefore, an arbitrary form of perturbation (as long as single azimuthal mode m is considered) in axial direction can travel over the length of pump with velocity (127), developing with exponential factor (128) and sustaining its shape Fig. 56 and Fig. 57.

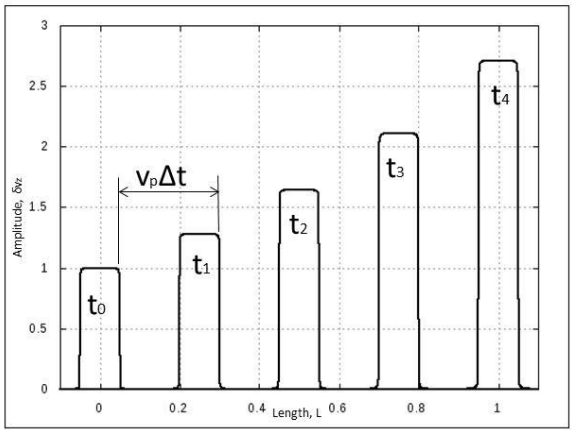

Fig. 56. Increase of perturbation in convective instability process.

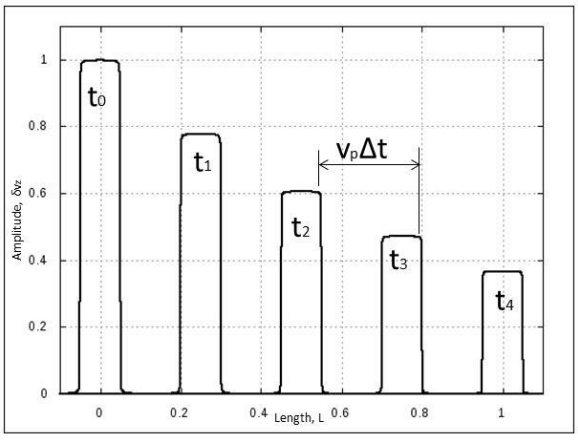

Fig. 57. Decrease of perturbation in convective instability process.

Using obtained expressions for $-\gamma_R$ and $\tilde{v}_p$ their behaviour as functions of Rm_s with different interaction parameter N and ratio of dimension are shown in Fig. 58 - Fig. 61.

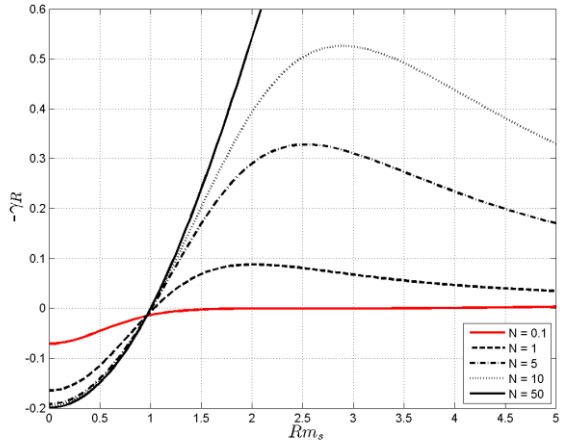

Fig. 58. Development factor $-\gamma_R(Rm_s)$ *for different* N. $\kappa_m' = 1,\ Re_\lambda = 100,\ Rm = 5.$

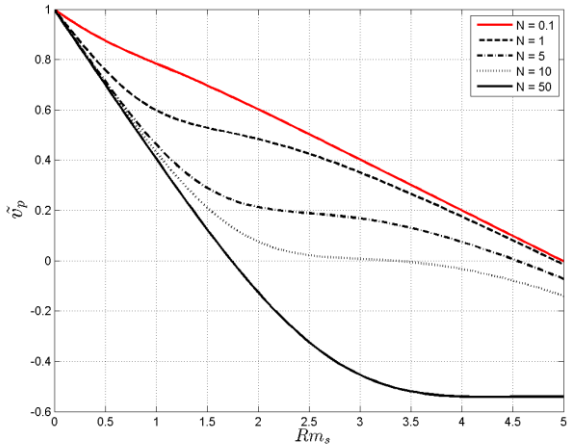

Fig. 59. Velocity $\tilde{v}_p(Rm_s)$ *for different* N. $\kappa_m' = 1,\ Re_\lambda = 100,\ Rm = 5$

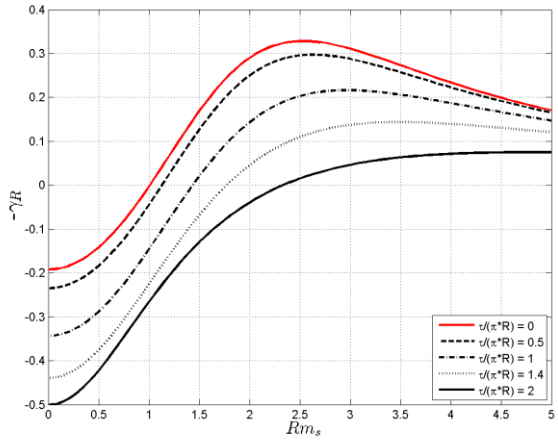

Fig. 60. Development factor $-\gamma_R(Rm_s)$ *for different* κ_m'. $N = 5,\ Re_\lambda = 100,\ Rm = 5.$

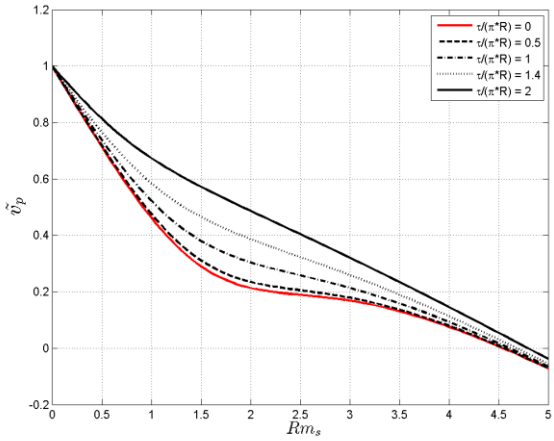

Fig. 61. Development factor $\tilde{v}_p(Rm_s)$ *for different* κ_m'. $N = 5,\ Re_\lambda = 100,\ Rm = 5.$

It can be observed in Fig. 58 - Fig. 59 that $-\gamma_R$ increases very rapidly with growth of N and only in case when $N \ll 1$ perturbation growth rate is small and stability threshold is sufficiently increased. From point of view of $\tilde{v}_p$it reaches zero faster only with sufficient increase of N. Importance of this fact will be outlined later. Obviously, it can be concluded that regimes with higher N are potentially more unstable.

Similarly form Fig. 60 - Fig. 61 it can be concluded that increment of ratio $\frac{2\tau}{2\pi R}$ (wavelength/width of the channel) not only increases convective stability threshold, but also decreases perturbation growth rate. Typically in large scale ALIP are in range $\frac{2\tau}{2\pi R} = 0 \ldots 1$.

Next, one can estimate the factor β_m with which perturbation amplified while traveling through the system. To do this, it is necessary to express time in terms of axial coordinate and perturbation velocity. Then amplification factor is:

$$\tilde{t} = \frac{\tilde{z}}{\tilde{v}_p} \quad \rightarrow \quad \frac{\Delta\tilde{p}_m}{B_m}\tilde{t} = \frac{\Delta\tilde{p}_m}{B_m \cdot \tilde{v}_p}\tilde{z} = \frac{\Delta\tilde{p}_m}{A_m}\tilde{z} = \beta_m\tilde{z} \tag{129}$$

The question what happens with system if perturbation velocity is zero, according to Drazin, is connected with term *absolute instability* [60]. That is a situation, if $\tilde{t} \to \infty$ and perturbation also infinitely amplifies at the fixed point of the flow (perturbation remains in the system).

From point of view of (126) such phenomenon can occur if two principal conditions meet:

1) ALIP is already convectively unstable. That is to say, some mode is temporally growing, which essentially is condition (74).
2) Phase velocity (127) of this mode is zero.

Praxis has shown that first condition can be frequently satisfied, especially in large ALIPs operating with liquid sodium. In the case studied in previous paragraphs, second condition from (127) requires that $A_m = 0$ and by using (122) the threshold in terms of pressure is:

$$\tilde{p}_a = \frac{4|\tilde{v}_z|(2Rm_s + Rm\kappa'_m\tilde{v}_z) + Re_\lambda\tilde{v}_z\left(\kappa'^{\,2}_m + Rm_s^2\right)}{Rm(2 - 3\tilde{v}_z)}(1 - \tilde{v}_z) - \tilde{v_z}|\tilde{v_z}| \tag{130}$$

Note, that this result suggest that in case of a pump: $\tilde{v_z} = [0 \ldots 1]$, asymptotic mean velocity for absolute instability is $\tilde{v}_z = \frac{2}{3}$.

An example of absolute stability threshold is shown in Fig. 62 .The interaction parameter N is varied by changing modified Reynolds number Re_λ.

It can be observed that with increase of N absolute stability threshold approaches its derived limit, which in this case is: $\mathrm{Rm_s} \approx \frac{Rm}{3} = 1.66$. The threshold for lower N vales remains relatively high.

In the next subchapter newly obtained results are analysed in context of experiment reported in literature.

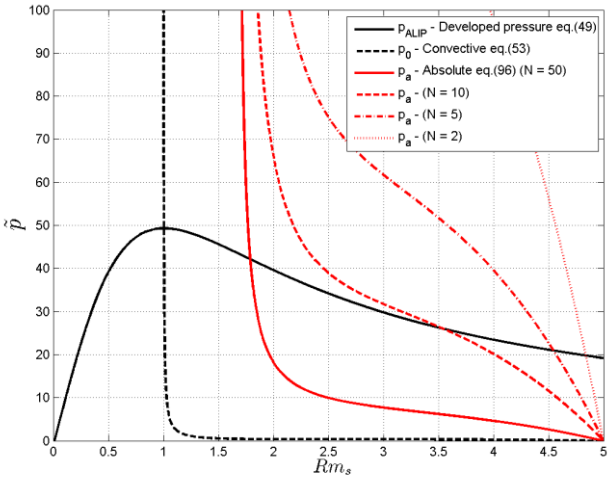

Fig. 62. Stability thresholds with different N. $\kappa'_m = 1,\ N_\lambda = 500,\ Rm = 5$

2.1.4. Qualitative comparison with existing experimental results

Consider a large scale ALIP, similar to one in experimental study [36]. To do that, it is necessary to estimate characteristic parameters from the information that can be found in the paper:

$$N_\lambda = 973; \quad Re_\lambda = 408; \quad N = 2.4; \quad Rm = 6.4; \quad \kappa'_m = 1.04; \quad \tilde{L} = 14\pi;$$

Using these parameters, the plot of equations (65), (73), (130), along with experimentally reported loss of stability $Rm_s = 1.4$ is shown in Fig. 63. The experiment suggests that stability of particular ALIP has been lost below calculated absolute stability threshold and not far from convective stability threshold.

However, one of the scenarios is that initial perturbations have been amplified over the length of the pump so significantly that non-linear behaviour of perturbations (which is out of scope of current work) lead to the loss of stability.

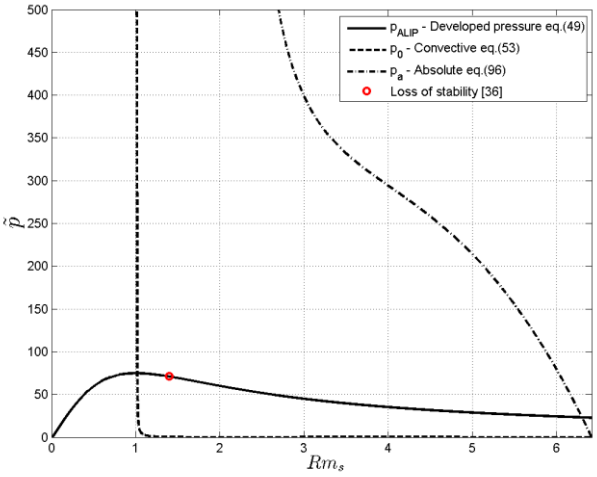

Fig. 63 Theoretical developed pressure, convective and absolute stability threshold, and experimental loss of stability of ALIP in [36].

Using (129) and characteristic dimensionless numbers it can be estimated that amplification of perturbation mode $m = 1$ over the length of pump at the critical $Rm_s = 1.4$ is about 2000 times:

$$\beta_1 \approx 0.174 \quad \rightarrow \quad e^{\beta_1 \tilde{L}} \approx 2000 \tag{131}$$

Authors state that external magnetic field "…*flux density distribution of the annular channel was uniform within 5% in the circumferential direction*… ". Therefore, in this particular case, it cannot be excluded that loss of stability might be also caused by significant amplification of initial perturbation.

Analysed case outlines that if ALIP is comparatively long (14 poles) and no measures of stabilization are considered, amplifications of perturbation over the length can reach huge numbers even near stability threshold and not necessarily reaching absolute instability.

However, it can be discussed; weather amplification rates and absolute instability threshold is well described in using presented simplifications. Partial clarification and justification of selected approach is presented later in comparison with numerical results, but undeniably there could be more rich insight solving dispersion relation of higher power.

2.2. Stable operation and stabilization of ideal ALIP

Before proposing some stabilization technique, main reason of instability in ALIP should be discussed at least qualitatively using some already developed concepts.

First of all, (65) can be also considered as a local relationship of pressure and velocity rather than global. It means that ALIP can be divided in number of jets which allow inhomogeneous distribution of velocity over azimuth.

Consider plot of function (65) p_{EM} in Fig. 64 along with two curves of external load p_{R1}, p_{R2}. The intersection points (A, B) define working regimes. Assume case of large flowrate ALIP (57) and most unstable azimuthal mode $m = 1$. Then condition of convective instability is approximately: $Rm_s > 1$.

According to [18], region in Fig. 64 is divided in two zones in the maximum of p_{EM}:

1. Stable - where azimuthal perturbations decrease
2. Unstable - where azimuthal perturbations increase

Qualitatively such behaviour can be explained by preforming following *thought experiment*. First of all, take point A in stable branch and perturb velocity over azimuth around its mean value (red line in Fig. 65, Fig. 66). The negative gradient $\frac{\partial \tilde{p}}{\partial \tilde{v}}$ defines that if velocity increases, pressure in separate jet decreases and vice versa. This stable situation is shown in Fig. 65. If point B is considered, gradient $\frac{\partial \tilde{p}}{\partial \tilde{v}}$ is positive - velocity increases, pressure also increases and vice versa. Therefore perturbation can be amplified Fig. 66.

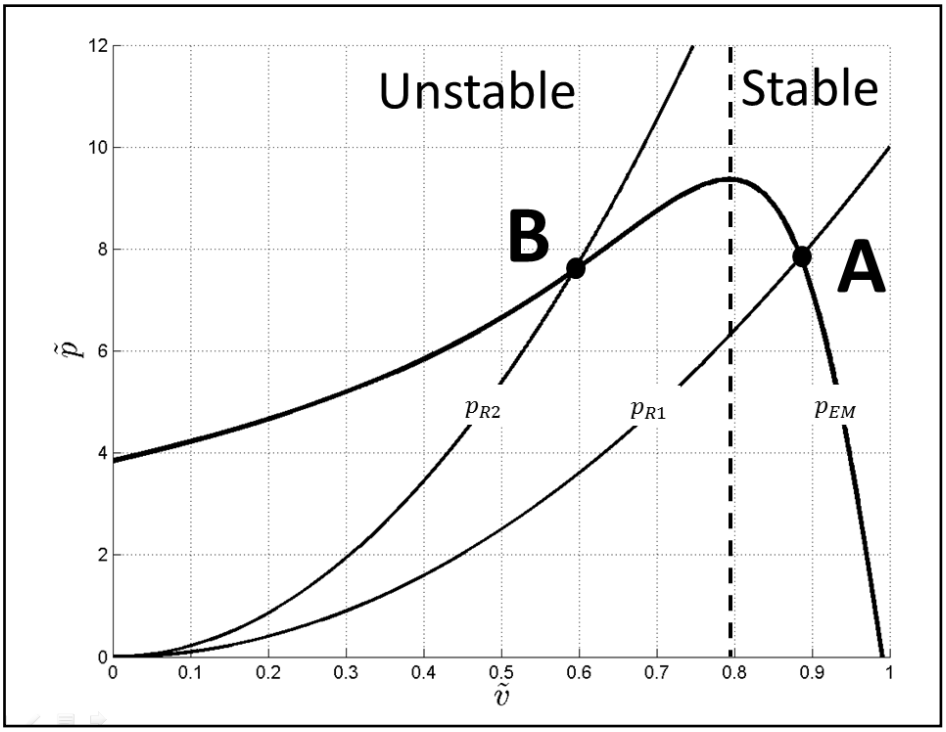

Fig. 64. Dimensionless characteristic p_{EM} coupled with two external loads p_{R1}, p_{R2}. $N_\lambda = 100$; $Rm = 5$.

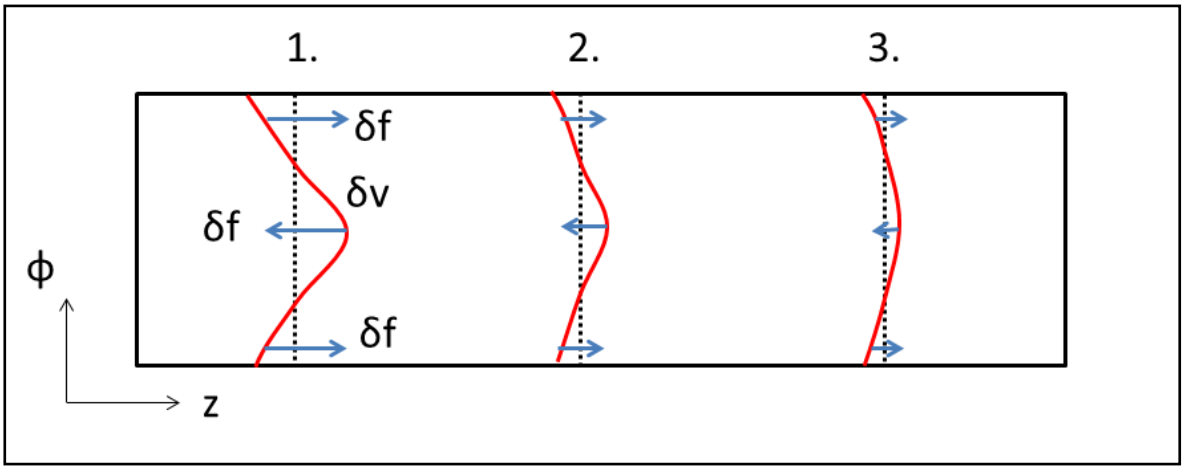

Fig. 65. A stable situation – azimuthal perturbations decrease.

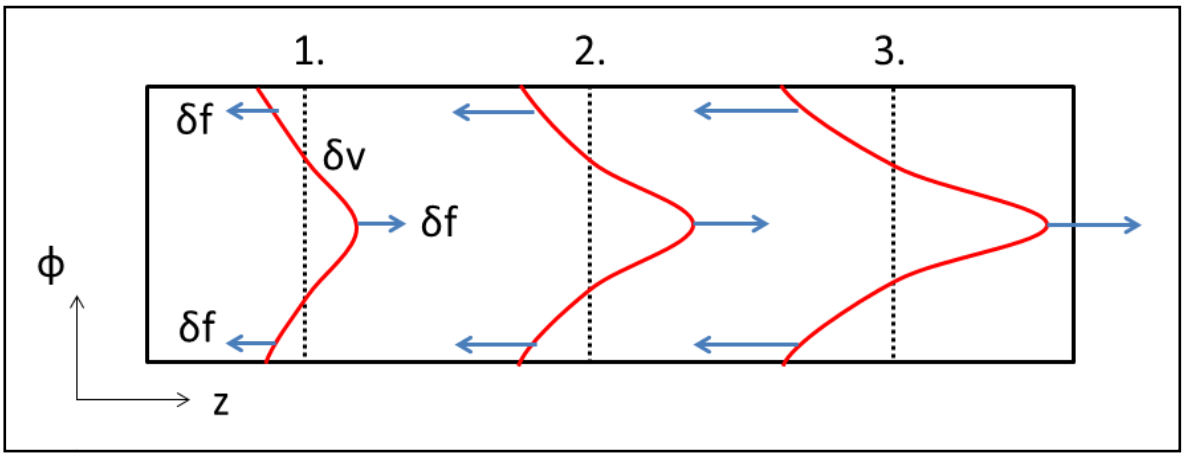

Fig. 66. An unstable situation – azimuthal perturbations increase.

Very similar discussion has been made already in [18] and above it is once again explained in marginally different manner. It should be emphasized, that in general case the stability threshold must be calculated using results from stability analysis and it is possible to have stable situation even with positive gradient $\frac{\partial \tilde{p}}{\partial \tilde{v}}$ if $\frac{\tau}{\pi R}$ is sufficiently large.

However, no opposite example has been given so far - if gradient is negative, system is stable. From this qualitative analysis at least two stabilization methods can be analysed.

2.2.1. Stabilization and stable operation by changing driving frequency/current

The stabilization by adjusting ALIPs driving supply's frequency and current is the most obvious method. It literally means changing magnetic Reynolds number to avoid condition (74) to be fulfilled.

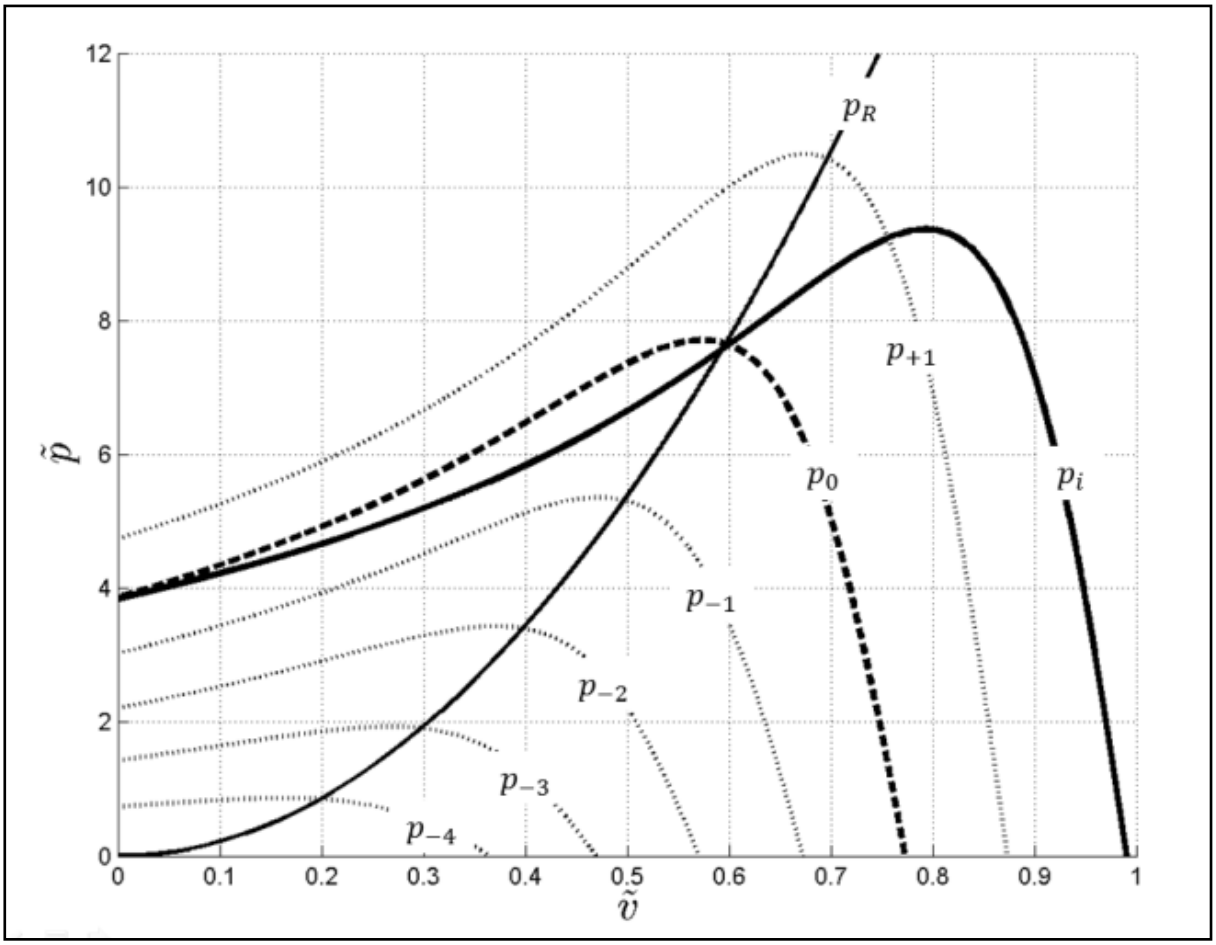

Fig. 67. Initial characteristic p_i and stabilized characteristics $p_{-4} - p_{+1}$ coupled with external load p_R. $N_\lambda = 100;\ \ Rm = 5$.

Consider case in Fig. 67. ALIP is connected to external resistance p_R and operating in the unstable zone (curve p_i). Then supply frequency and input current of pump should be corrected to have same operation point but in the stable zone of different characteristic. The first goal is to find parameters to construct curve p_0, if parameters of initial curve p_i are known.

To do this, first of all it is necessary to choose a criterion to be satisfied, that is some stable point where $\frac{\partial \tilde{p}}{\partial \tilde{v}} < 0$. For example, consider that pump should be operated in a new, stable regime using velocity of traveling magnetic field $\widetilde{v_0}$ with mean velocity $\widetilde{v_{a0}}$, that desired magnetic Reynolds number Rm_d is:

$$Rm(\widetilde{v_0} - \widetilde{v_{a0}}) = Rm_d < 1 \tag{132}$$

The new dimensionless velocity of magnetic field (factor to change frequency) is:

$$\widetilde{v_0} = \widetilde{v_{a0}} + \frac{Rm_d}{Rm} \tag{133}$$

Then in the intersection point of curves p_0, p_i:

$$J_i^2 \frac{1 - \widetilde{v_{a0}}}{1 + Rm_s^2} = J_0^2 \frac{\widetilde{v_0} - \widetilde{v_{a0}}}{1 + Rm_d^2} \tag{134}$$

From which one can find factor by which input current should be changed:

$$\frac{J_i}{J_0} = \sqrt{\frac{1 + Rm_d^2}{1 + Rm_s^2} \cdot \frac{Rm_s}{Rm_d}} \tag{135}$$

Secondly, when curve p_0 is constructed in Fig. 67 and stable operation achieved, one would like to keep it that way all over curve p_R, by changing frequency and current to maintain chosen criteria. That is - construct curves from p_{+1} to p_{-4}.

Assume that from $\widetilde{v_{a0}}$ one would like to change velocity of liquid metal to $\widetilde{v_{a1}}$, use velocity of magnetic field $\widetilde{v_1}$ and operate in stable regime according to p_{+1}. From (132) follows that frequency should be changed by factor:

$$\frac{\widetilde{v_1}}{\widetilde{v_0}} = 1 + \frac{\widetilde{v_{a1}} - \widetilde{v_{a0}}}{\widetilde{v_0}} \tag{136}$$

Since developed pressure by ALIP is quadratically proportional to applied current, but turbulent pressure loses are quadratically proportional to mean velocity, then input current should be changed proportionally to increment of velocity:

$$\frac{J_1}{J_0} = \frac{\widetilde{v_{a1}}}{\widetilde{v_{a0}}} \tag{137}$$

Using these principles all curves p_{+1} - p_{-4} in Fig. 67 are constructed operating in stable regime $Rm_d = 0.9$.

One might argue if this really is a stabilization method, since unstable regimes are simply avoided, but they do still exist. Independently how we define it, such approach indeed should significantly extend stable operating regimes of ALIP, if power supply can deliver sufficient range of frequencies and currents.

2.2.2. Stabilization of ideal ALIP using additional supply

The idea to consider the operation of ALIP with two different supplies power – driving and stabilizing - was proposed by Prof. Jānis Priede. This technique really focuses on stabilizing the pump with help of modification of magnetic field rather than escaping unstable regions.

Consider inductor with following form of applied linear current density:

$$\boldsymbol{j_{lin}} = \sqrt{2}J \cdot \left[e^{i(\alpha z - \omega t)} + \beta e^{i(\alpha z - \omega_1 t)}\right]\boldsymbol{e_\varphi} = \sqrt{2}J \cdot \left[e^{i\alpha(z - v_B t)} + \beta e^{i\alpha(z - v_1 t)}\right]\boldsymbol{e_\varphi} \qquad (138)$$

Where β is factor of applied current:

$$\beta = \frac{J_1}{J} \qquad (139)$$

Qualitatively the idea behind proposed method is following: The driving supply operates with constant current and frequency generating necessary pressure head and slip. Parameters of stabilizing supply can be changed, but in such way that it does not generate any additional pressure, it only stabilizes the flow. This can be achieved if two conditions are met:

1. Stabilizing angular frequency ω_1 is varied as function of flowrate to meet mean velocity of liquid metal
2. Amount of minimum input current depends on the gradient at operating point to compensate it

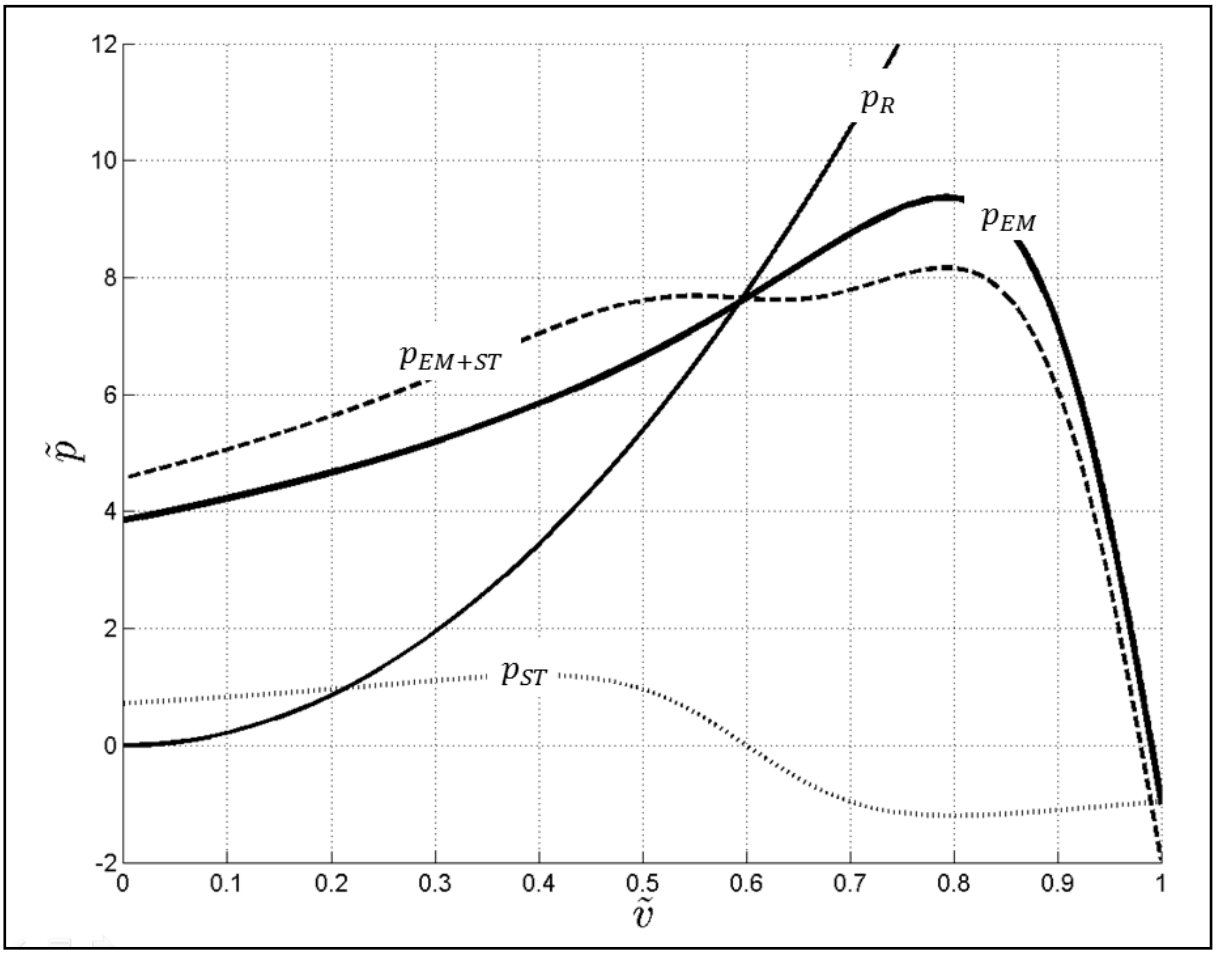

Fig. 68. p_{EM} coupled with external load p_R and stabilization of operating point using p_{ST}. $N_\lambda = 100$; $Rm = 5$; $\kappa'_m = 1$.

This principle is shown in Fig. 68. Consider pressure - velocity curve p_{EM} generated using driving power supply. The resistance of the external loop p_R is such, that operating point is in the unstable zone. Then consider another characteristic curve according to input conditions of stabilizing supply p_{ST}. The superposition of both curves p_{EM+ST} will not generate any additional force at the given point, but make gradient non-positive, therefore creating potentially stable situation.

2.2.3. Linear stability analysis of ideal ALIP with additional supply

Taking into account discussion before and form of applied current (138), dimensionless induction equation reads:

$$\tilde{\Delta}\widetilde{\boldsymbol{b}} - Rm\left[\frac{\partial\widetilde{\boldsymbol{b}}}{\partial\tilde{t}} + \left(\widetilde{\boldsymbol{v}}\widetilde{\nabla}\right)\widetilde{\boldsymbol{b}}\right] = -\widetilde{\nabla}\times\left(e^{i(\tilde{z}-\tilde{t})} + \beta e^{i(\tilde{z}-\tilde{v}_1\tilde{t})}\right)\boldsymbol{e_\varphi} \tag{140}$$

Note, that dimensionless frequency/velocity of stabilizing magnetic field $\tilde{v}_1$ here is arbitrary. By looking for steady state solution as superposition of similar harmonic forms as applied current, magnetic field reads:

$$\tilde{b} = \widetilde{b_0}e^{i(\tilde{z}-\tilde{t})} + \widetilde{b_1}e^{i(\tilde{z}-\tilde{v}_1\tilde{t})} \tag{141}$$

Where:

$$\widetilde{b_1} = \frac{\beta}{i + Rm_v} \tag{142}$$

$$Rm_v = Rm(\tilde{v}_1 - \tilde{v}_z) \tag{143}$$

Considering only quasi stationary part of electromagnetic force, steady state solution of developed pressure is:

$$\tilde{p} = \frac{N_\lambda}{Rm}\left(Re\left[\widetilde{b_0}\right] + \beta^2 Re\left[\widetilde{b_1}\right]\right) - \tilde{v}_z|\tilde{v}_z| \tag{144}$$

From which can be clearly seen that if $\tilde{v}_1 = \tilde{v}_z$ then $Re\left[\widetilde{b_1}\right] = 0$ and (144) leads to (65).

Then consider perturbed solution from is (69), (70) along with:

$$\tilde{b}_{p1} = \tilde{b}_1 + \delta\tilde{b}_{1m}\,cos(m\varphi) \tag{145}$$

From linearized induction equation and force balance one has the system:

$$\delta\tilde{b}_m = \frac{i\widetilde{b_0}}{iRm_s - \kappa'_m}\delta\tilde{v}_m \tag{146}$$

$$\delta\tilde{b}_{1m} = \frac{i\widetilde{b_1}}{iRm_v - \kappa'_m}\delta\tilde{v}_m \tag{147}$$

$$2|\tilde{v}_z|\delta\tilde{v}_m = \frac{N_\lambda}{Rm}\left(Re\left[\delta\tilde{b}_m\right] + \beta^2 Re\left[\delta\tilde{b}_{1m}\right]\right) \tag{148}$$

From which it is found that:

$$2|\tilde{v}_z| = \frac{N_\lambda}{Rm}\left(\frac{Rm_s^2 - \kappa'_m}{(1+Rm_s^2)\left({\kappa'_m}^2 + Rm_s^2\right)} + \beta^2\frac{Rm_v^2 - \kappa'_m}{(1+Rm_v^2)\left({\kappa'_m}^2 + Rm_v^2\right)}\right) \tag{149}$$

It leads to expression for ratio of applied current necessary for stable operation:

$$\beta > \sqrt{\frac{(Rm_s^2 - \kappa_m')(1 + Rm_v^2)\left(\kappa_m'^{\,2} + Rm_v^2\right)}{(\kappa_m' - Rm_v^2)(1 + Rm_s^2)\left(\kappa_m'^{\,2} + Rm_s^2\right)}} \tag{150}$$

With condition:

$$Rm_s^2 - \kappa_m' > 0 \tag{151}$$

And in particular case of our interest $\tilde{v}_1 = \tilde{v}_z$:

$$\beta > \sqrt{\frac{(Rm_s^2 - \kappa_m')\kappa_m'}{(1 + Rm_s^2)\left(\kappa_m'^{\,2} + Rm_s^2\right)}} \tag{152}$$

From expression (152) critical β is calculated and plotted as function of Rm_s in Fig. 69 for different κ_m'. One can observe that there is a maximum necessary stabilizing current which depend on κ_m'. In cases of practical significance, when $\kappa_m' = 1$, it can be found that maximum of function this function is:

$$Rm_s = \sqrt{3} \;\rightarrow\; \beta_{max} = \sqrt{\frac{1}{8}} = 0.35355\ldots \tag{153}$$

In Fig. 70 stabilization of several points on p_{EM} curve are shown and resulting characteristics p_{EM+ST}. The stabilization according to criterion (138) indeed is achieved by changing gradient of characteristic at the point of interest.

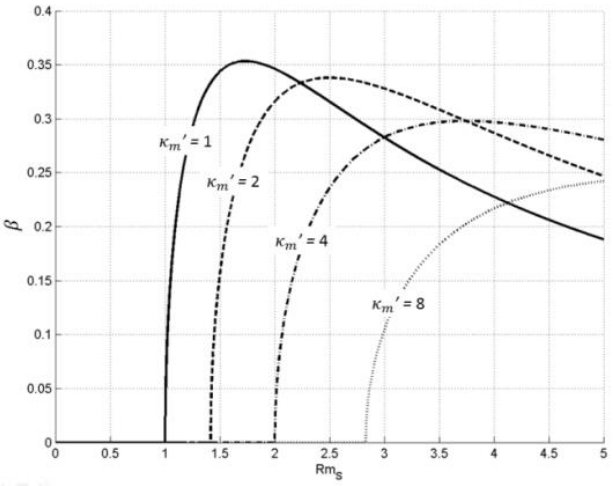

Fig. 69. Critical β as function of Rm_s with different κ_m' when $\tilde{v}_1 = \tilde{v}$.

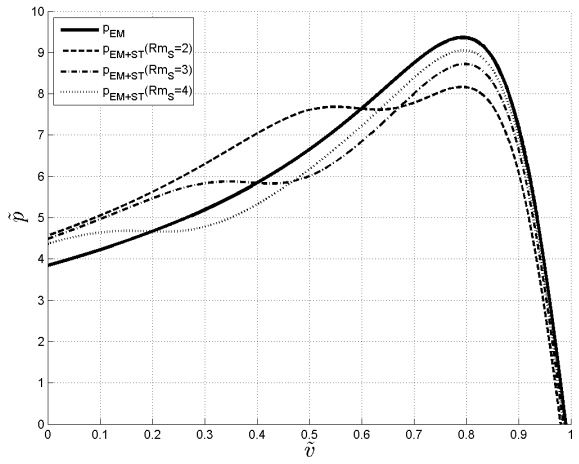

Fig. 70. Stabilization of points $\tilde{v} = [0.2, 0.4, 0.6]$ $N_\lambda = 100;\ Rm = 5;\ \kappa_m' = 1$, when $\tilde{v}_1 = \tilde{v}$.

2.3. Conclusions on theoretical investigations

In this chapter several new results have been derived which are useful in analysis of MHD instability in ALIP.

First of all, it is the estimation of perturbation spatial development in a convective type of instability (129), which gives an idea at what extent existing initial perturbation will be amplified. Such estimation requires some information about amplitudes of initial perturbations. If amplification is significant, one could expect that non-linear effects become more pronounced and eventually lead to loss of the stability. Results suggest that this might be the cause MHD instability of ALIP in some cases, even if well below threshold of absolute instability Fig. 63.

Secondly, it is the derivation of absolute stability threshold (130). Theoretical analysis suggests that in cases of high interaction parameter N absolute instability can occur when $\mathrm{Rm_s} \approx \frac{Rm}{3}$. Apparently, in such cases absolute stability will be near the convective stability threshold, if Rm is relatively small 3…4. In the same time comparison with results from literature shows that such method overestimates real stability threshold. One of the reasons of such outcome might be that used approximations of dispersion relation are not sufficient and higher order terms must be considered.

Then discussing stable operation of ALIP it is shown that, when possible, stable regimes could be obtained by tuning frequency/current of driving power supply Fig. 67. Not only this method guarantees the stability by relatively simple means, but also higher efficiency of the pump is near the maximum of $\tilde{p} - \tilde{v}$ curve.

If parameters of high power driving supply are limited and cannot cover all regimes, then stabilization with additional supply can be introduced (138), Fig. 70. Maximum required stabilization current according to (153) is around 36% of driving supply, but desirable frequency range theoretically should go down to zero depending on point to be stabilized.

It has to be outlined that in presented study of stabilization only quasi-stationary part of EM force is considered and appearance of potential low frequency beats due to interference of both applied current sources - neglected. In some cases it may limit application of later stabilization technique at least from structural mechanics point of view. Nevertheless, evidence is shown that such stabilization technique should work.

3. NUMERICAL INVESTIGATIONS

In this chapter numerical analysis of instability are discussed. Numerical models shown here are created using commercial software ANSYS FLUENT MHD module which uses formulation of external and induced field [26]. It implies that every component of external field should be user defined.

In the case of ideal EMIP such method is easy to work with, since field can be simplified to single (perpendicular) component, having constant amplitude and simple harmonic form:

$$\boldsymbol{B_e} = B_0 cos(\alpha z - \omega_B t)\boldsymbol{e_x} \tag{154}$$

For hydrodynamic part additional source term modelling turbulent dissipation is added using porous media model and friction factor:

$$\boldsymbol{f_\lambda} = -\zeta_h \cdot \rho \frac{\boldsymbol{v}|\boldsymbol{v}|}{2} \tag{155}$$

System of equations solved by ANSYS FLUENT MHD module is following:

$$\Delta \boldsymbol{B_i} - \mu_0 \sigma \left[\frac{\partial \boldsymbol{B_i}}{\partial t} - (\boldsymbol{B_i}\nabla)\boldsymbol{v} + (\boldsymbol{v}\nabla)\boldsymbol{B_i}\right] = \mu_0 \sigma \left[\frac{\partial \boldsymbol{B_e}}{\partial t} - (\boldsymbol{B_e}\nabla)\boldsymbol{v} + (\boldsymbol{v}\nabla)\boldsymbol{B_e}\right] \tag{156}$$

$$\rho \left[\frac{\partial \boldsymbol{v}}{\partial t} + (\boldsymbol{v}\nabla)\boldsymbol{v}\right] = -\nabla p - \zeta_h \cdot \rho \frac{\boldsymbol{v}|\boldsymbol{v}|}{2} + \left(\frac{\nabla \times \boldsymbol{B_i}}{\mu_0}\right) \times \boldsymbol{B} \tag{157}$$

$$\nabla \cdot \boldsymbol{v} = 0 \tag{158}$$

This is done using finite volume method, first order upwind scheme and SIMPLE algorithm [61].

In the case of *realistic* EMIP the situation is slightly more difficult since multiple harmonics of external magnetic field should be introduced and due to finite length effects it dies out eventually. This requires information about distribution of such field which can be obtained by numerical and/or theoretical means. For this purpose COMSOL Multiphysics numerical software and analytical model is used and most important harmonics of external field taken into account as well as exponential decay of field in inlet and outlet.

In COMSOL 2D distribution of magnetic field is solved using formulation of vector potential and finite element method [62].

3.1. Model of an ideal ALIP

The purpose of numerical model of ideal ALIP is to numerically calculate growth of perturbation in the simplest case possible and compare it with analytical results. Such validation is necessary to see weather analytical estimates are correct and some further conclusion can be drawn, and weather presented numerical method is capable of modelling MHD instability. Therefore a setup as close as possible to analytically studied case is necessary.

Numerical model of an ideal ALIP is rectangle geometry with $2a$ = 840 mm and 2τ = 660 mm Fig. 71. In y-z plane all opposite boundaries are periodic and mass flow rate was defined from inlet to outlet to meet necessary mean velocity. In all domain velocity was initialized with 0.5% perturbation amplitude from mean value. Such value was chosen to fulfil condition (109), (110). Cell size in y-z plane was 3mm and accordingly mesh was: n_y = 210 and n_z = 165 elements large Fig. 72.

In x direction with d_h = 48 mm there was only single cell over the height; therefore slip boundary conditions on both upper and lower walls were applied. External magnetic field was applied in a simple form as traveling wave.

Inertial friction forces were added as source term which in particular was realized in porous media model [61] with constant friction factor: ζ_h = 0.105. Molecular viscosity of sodium was decreased by factor 10^6 to neglect any viscose effects in the model. Therefore case practically identical to analytical model in Chapter 2.1 was studied.

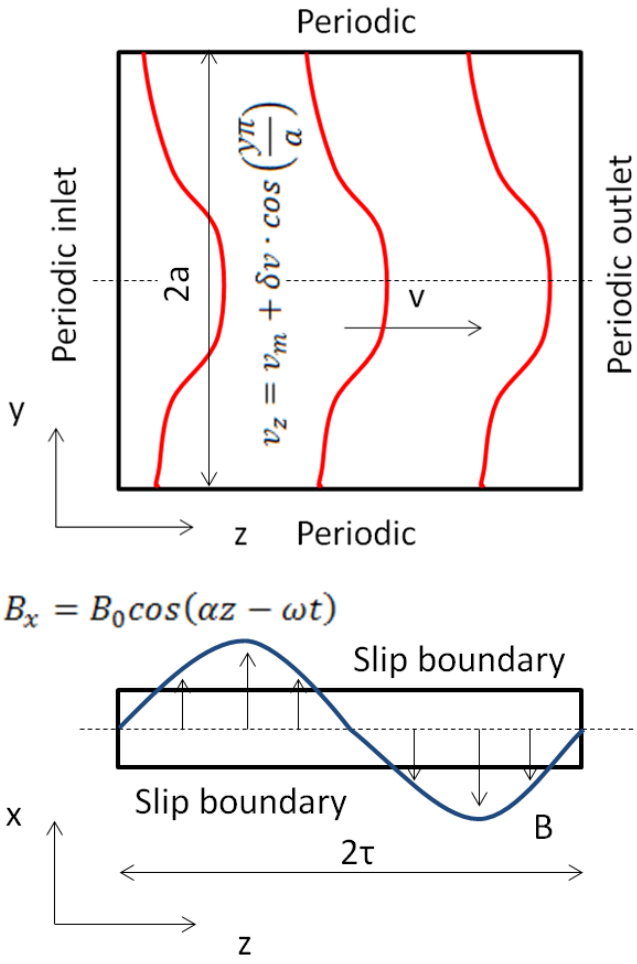

Fig. 71. The setup of numerical model of ideal ALIP.

Applied frequency in model was 10 Hz, therefore velocity of magnetic field was: v_B = 6.6 m/s. The conductivity of sodium was σ = 7.39 MS/m giving magnetic Reynolds number Rm = 6.44. Mean velocity of flow was varied to change slip magnetic Reynolds number. Also several cases with different amplitude of external magnetic field were studied to see impact of Interaction parameter.

The problem was solved transiently with timestep Δt = 10^{-4} s ensuring that CLF parameter was sufficiently low and calculation was stable from numerical point of view.

Second order upwind scheme was used for momentum and first order for magnetic field achieving convergence with residuals 10^{-6}.

All main parameters of model are summarized in tables below.

σ, [MS/m]	2τ, [m]	$2a$, [m]	d_h, [m]	f, [Hz]	v_B, [m/s]	Rm	Rm_c
7,39	0,66	0,84	0,048	10	6,6	6,44	1,34

Table 1. Parameters of the numerical model

ρ, [kg/m^3]	ζ_h	λ_h	B_0, [T]	Re_λ	N_λ	$N = N_\lambda/Re_\lambda$
903,56	0,105	0,0101	0,02	181,3	4,7	0,03
-	-	-	0,05	-	29,5	0,16
-	-	-	0,125	-	184	1,0
-	-	-	0,3	-	1062	5,9
-	-	-	0,45	-	2390	13,2

Table 2. Parameters of the numerical model

Δx, [m]	Δt, [s]	CFL_{vB}	Res	n_x	n_y	n_z	n
4 x 10^{-3}	10^{-4}	0,165	10^{-6}	1	210	165	34’500

Table 3. Parameters of the numerical model

The calculation process was following:

1. Initialization of perturbed velocity distribution and external magnetic field (e.g. Fig. 73 and Fig. 74)
2. Calculation of a steady state with *frozen* velocity distribution (0.6s)
3. MHD calculation of perturbation development (0.6 - 1.6s)

In order to analyse the results 4 monitors were created:

1. Mean z velocity in the inlet (green line)
2. Mean z velocity over the length of geometry in the centre (red line)
3. Mean z velocity over the length of geometry in the side (blue line)
4. Total developed force z component in the domain

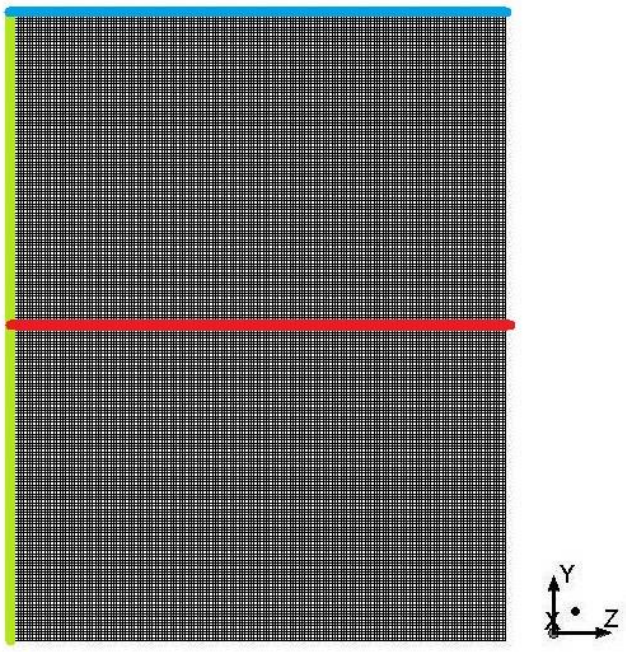

Fig. 72. Calculation mesh with 34500 rectangular elements of size 4x4mm

To cover sufficiently large range of Rm_s average velocity as varied from 4.18 – 6.58 [m/s], the corresponding Rm_s value can be found in Table 4.

v_z, [m/s]	4,18	4,38	4,58	4,78	4,98	5,18	5,38	5,58	5,78	5,98	6,18	6,38	6,58
Rm_s	2,36	2,17	1,97	1,78	1,58	1,39	1,19	1,00	0,80	0,60	0,41	0,21	0,02

Table 4. Parameters of the numerical model

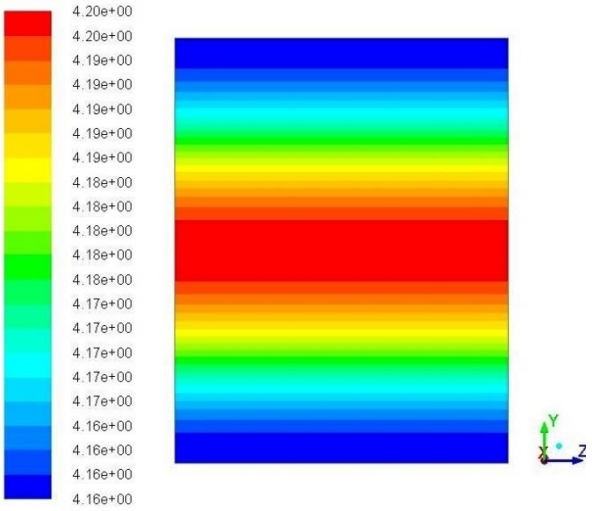

Fig. 73. Initial velocity z component distribution (vz, [m/s]): $Rm_s = 2.36;\ N = 0.16$

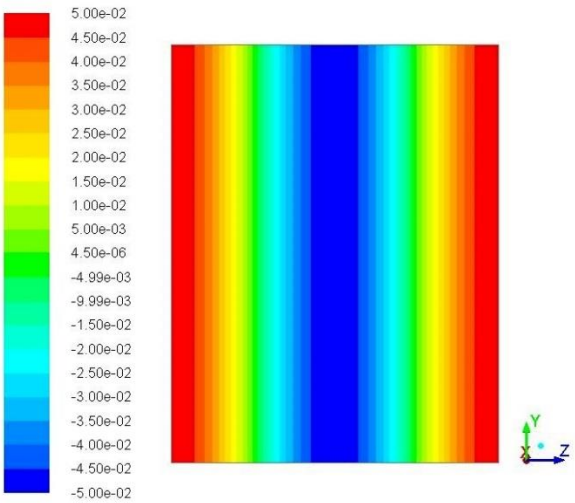

Fig. 74. Initial applied external magnetic field (B_x, [T]) $Rm_s = 2.36;\ N = 0.16$

An example of transient calculation results (monitored data) is shown in Fig. 75 - Fig. 78. In the first 0.6s of devoted for steady state calculation developed force in domain reaches its quasi-stationary value, but since velocity is *frozen* it remains constant. Then depending on regime (first of all Rm_s) ALIP is working in, initial velocity perturbation is either temporally increasing or decreasing. As long as perturbation is small or has not amplified significantly, developed EM force remains practically constant.

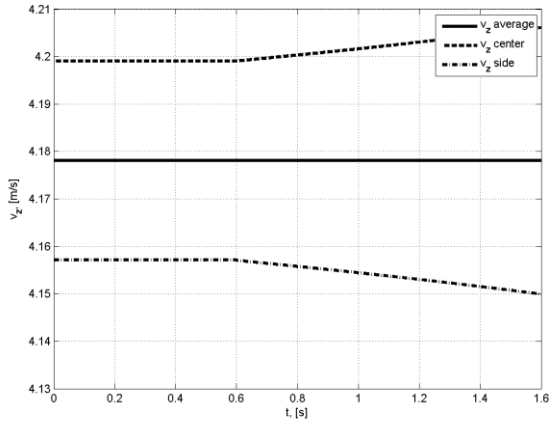

Fig. 75. Development of monitored velocity z component: $Rm_s = 2.36;\ N = 0.16$

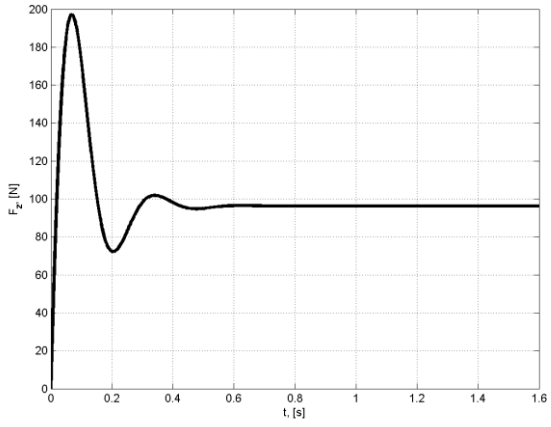

Fig. 76. Development of EM force z component: $Rm_s = 2.36;\ N = 0.16$

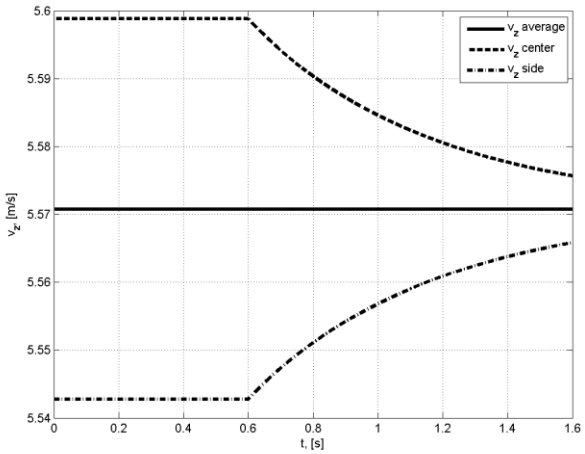

Fig. 77. Development of monitored velocity z component: $Rm_s = 1;\ N = 0.16$

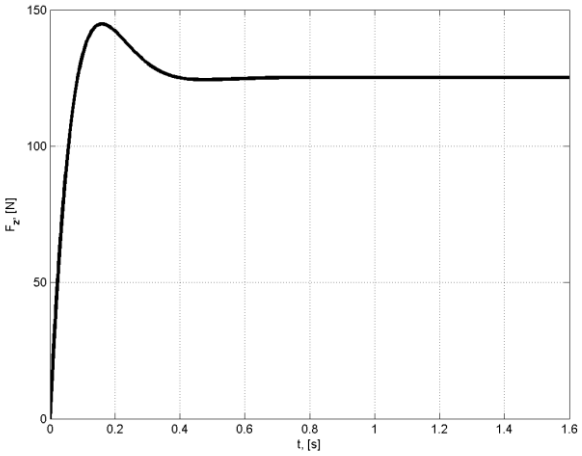

Fig. 78. Development of EM force z component: $Rm_s = 1;\ N = 0.16$

It can be observed in Fig. 75 and Fig. 77 that development of perturbation as expected follows exponential law. To find the corresponding factor, mean amplitudes of both – centre and side – monitors are normalized. Then MatLab software and optimization toolkit is used to fit the data with one of the following functions:

$$f_1 = e^{Bt} \cdot cos(Ct) \tag{159}$$

$$f_2 = Ae^{Bt} \cdot cos(Ct - D) \tag{160}$$

Where A, B, C, D coefficients being optimized to fit the data.

In the cases when numerical results have only little or none oscillatory part function (159) gives good approximation of data Fig. 79 and Fig. 80. Those are cases when perturbation is growing or in all cases with relatively low interaction parameter N. In cases with strong oscillatory part fit function (160) is used.

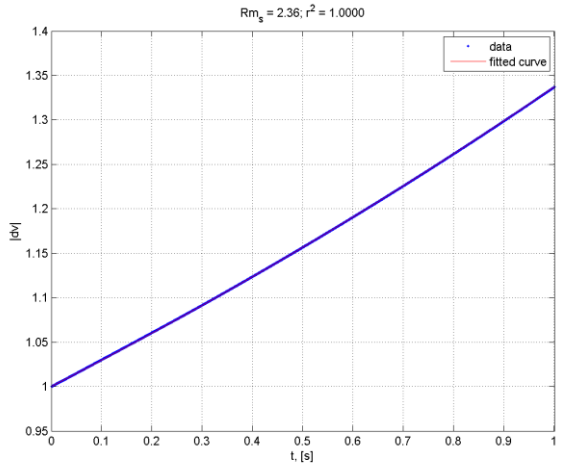

Fig. 79. Development of perturbation and numerical fit: $Rm_s = 2.36;\ N = 0.16$

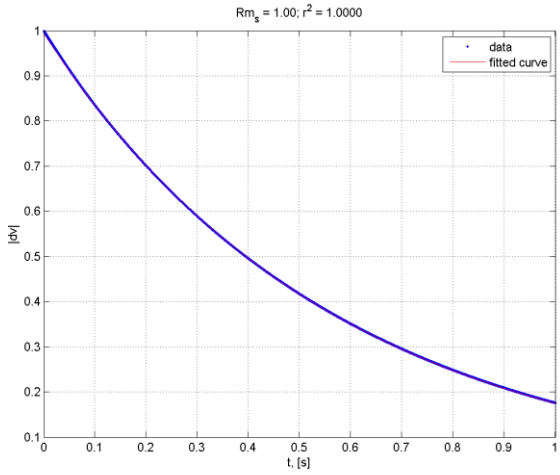

Fig. 80. Development of perturbation and numerical fit: $Rm_s = 1;\ N = 0.16$

With increase of interaction parameter N perturbation develops more rapidly. It can be observed in Fig. 81 that by the end of calculation perturbation has reached magnitude of mean flow and velocity values in centre and side zones are not symmetric anymore respect to mean velocity. Such non-linear behaviour has negative impact on developed force Fig. 82 which by the end of calculation decreases.

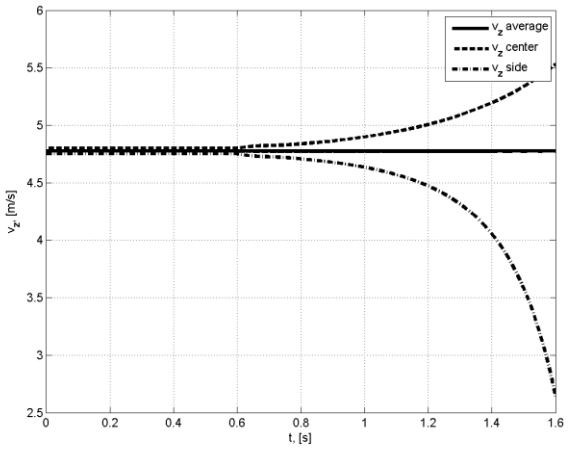

Fig. 81. Development of monitored velocity z component: $Rm_s = 1.78;\ N = 5.9.$

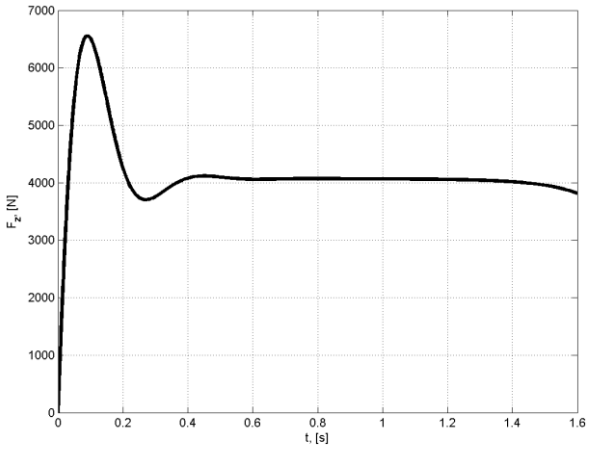

Fig. 82. Development of EM force z component: $Rm_s = 1.78;\ N = 5.9.$

On the other hand, when perturbation is decreasing, a strong oscillatory part appears, which is not always a simply damped oscillation Fig. 83. Since amplitude of perturbation is small, such oscillation does not influence developed force noticeably Fig. 84.

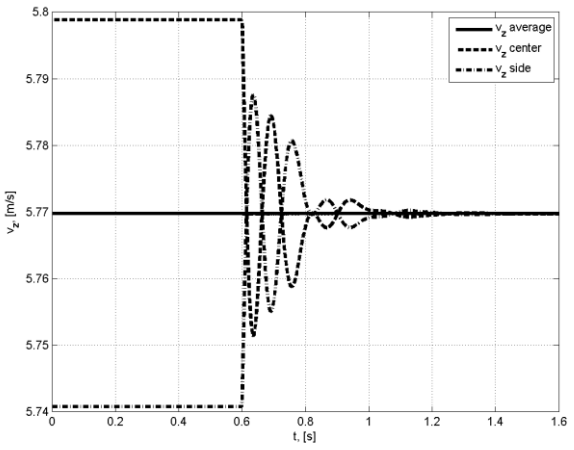

Fig. 83. Development of monitored velocity z component: $Rm_s = 0.81;\ N = 5.9.$

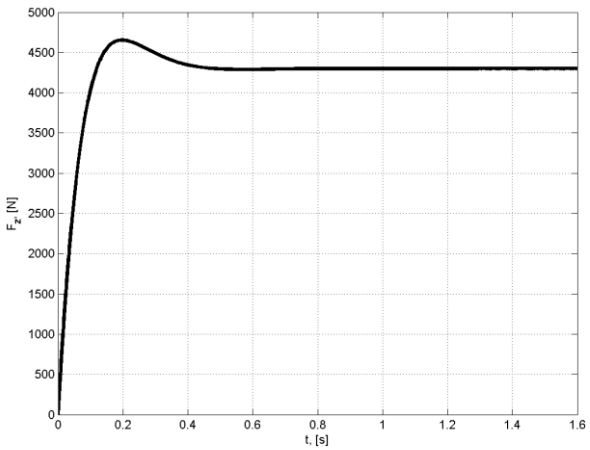

Fig. 84. Development of EM force z component: $Rm_s = 0.81;\ N = 5.9.$

Both of mentioned effects lead to necessity of selecting a smaller time range of development study where perturbations are small and obey harmonic functions. This should not influence result, since development rates are considered not be time dependent. In particular fit of presented cases data are shown in Fig. 85 and Fig. 86.

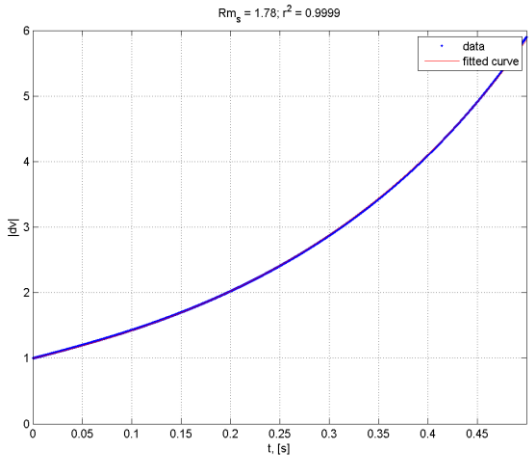

Fig. 85. Development of perturbation and numerical fit of time interval t = 0.6…1.1s: $Rm_s = 1.78;\ N = 5.9.$

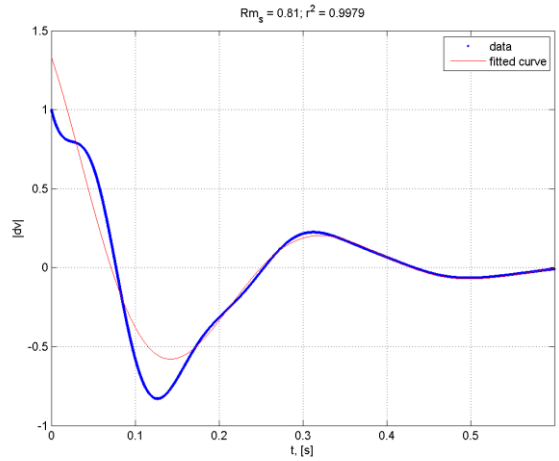

Fig. 86. Development of perturbation and numerical fit of time interval t = 1…1.6s: $Rm_s = 0.81;\ N = 5.9.$

The discussed oscillation of velocity perturbation has rather complex behaviour. Perturbation in the initial time moment Fig. 87 is defined by homogenous distribution over z. Then in Fig. 88 it can be observed that perturbation has been inverted along with the fact that certain spatial pattern is formed, likely, connected with distribution of instantaneous EM forces. Then, while decreasing perturbation has been inverted again in Fig. 89.

Precise explanation of observed phenomena is out of scope of current work.

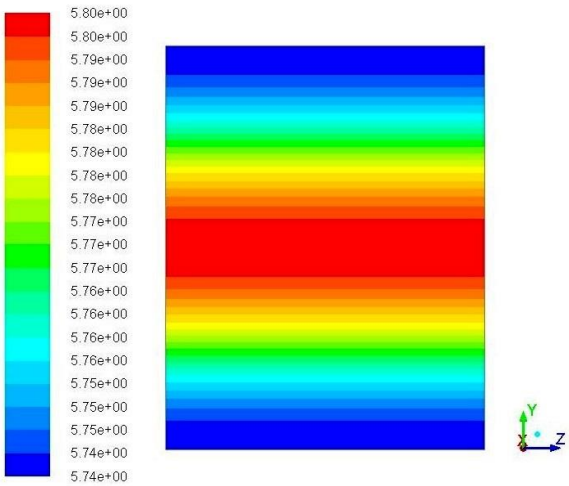

Fig. 87. Velocity z component distribution (vz, [m/s]): $Rm_s = 0.81;\ N = 5.9;\ t = 0.6s$

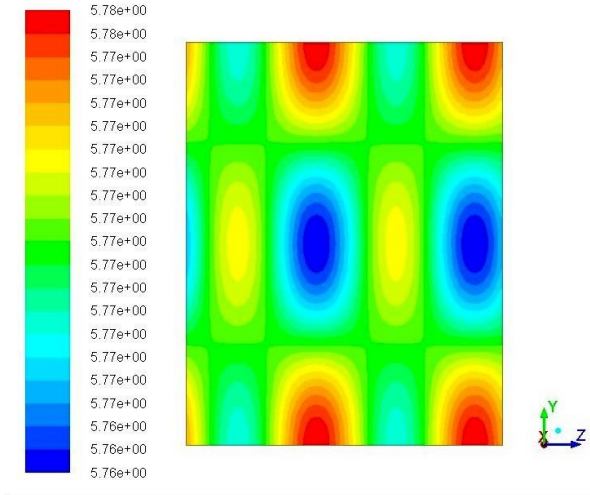

Fig. 88. Velocity z component distribution (vz, [m/s]): $Rm_s = 0.81;\ N = 5.9;\ t = 0.7s$

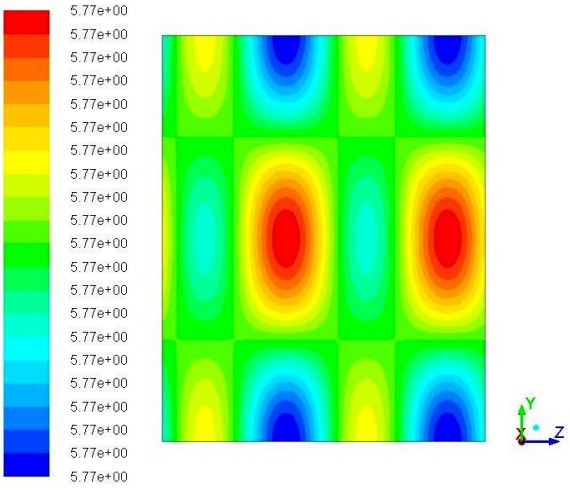

Fig. 89. Velocity z component distribution (vz, [m/s]): $Rm_s = 0.81;\ N = 5.9;\ t = 0.9s$

Finally, when all the numerical cases were post-processed and numerically estimated coefficient B in (126) found it was transformed in form of temporal perturbation growth rate $-\gamma_R$ (where minus sign is due to the form of studied perturbation). Then numerical results were compared with theoretical expression from (161):

$$-\gamma_R = \frac{\Delta\tilde{p}_m}{B_m} \tag{161}$$

The developed quasi-stationary EM force in the domain at time instant $\mathrm{t} = 0.6s$ of each case are captured and compared with theoretical formula:

$$F_z = \frac{\sigma {B_0}^2 (v_B - v_z)}{2} \cdot \frac{1}{1 + {Rm_s}^2} \cdot V \tag{162}$$

Obtained results are shown in Fig. 90 - Fig. 99.

First of all, in all cases numerically calculated EM force agrees with theoretical estimate rather well, but not perfectly Fig. 91, Fig. 93, Fig. 95, Fig. 97, Fig. 99. On the one hand one can be satisfied with such correspondence if the main interest is developed force and it can be concluded that numerical model describes EM process with sufficient precision. On the other hand, reasons of such deviation are not clear. One of the causes might be insufficient calculation time 0.6s at which numerical values are estimated and adding another 0.4s would correct this. Second cause could be insufficient spatial/temporal resolution of the model and it deviation is caused by numerical imperfections. For a one reason or another, this results in fact, that maximum of developed force is somewhat shifted and is $Rm_s > 1$. Apparently, this could lead to higher numerically obtained stability thresholds.

Secondly and most importantly, numerical results of temporal development rate $-\gamma_R$ agrees with theoretical estimates rather well, especially in cases when $N < 1$. While overall agreement in these cases is satisfactionary, the stability (perturbation growth) threshold $-\gamma_R = 0$ is not precisely estimated. This is a problem, since one should expect the best correspondence of numerical results with theory near this point where growth rates n, γ must be small. However, the slopes of theoretical curves near $-\gamma_R = 0$ correspond quite well to numerical results in all cases.

Numerical results also suggest rather bizarre behaviour of stability threshold $-\gamma_R = 0$. In the cases when $N < 1$ it is higher than theoretical estimate (73) and with increase of $N \approx 1$ it approaches (73). However, when $N > 1$, the threshold start to deviate again. It increases, which is unexpected from theoretical point of view and reasons of such behaviour are not completely clear.

In the end, it can be concluded that numerically studied model of ideal ALIP has shown reasonable results. There are number of in-depth studies that can be done using described approaches as well as fine-tuning of model could be performed to limit numerical errors to minimum. However, this is out of scope of current work, and it was decided to proceed further with development of *realistic* model of EMIP.

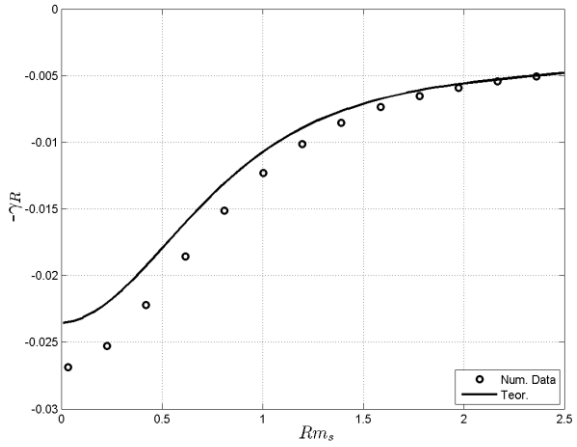

Fig. 90. Comparison of numerical and theoretical results of temporal development rate $-\gamma_R : N = 0.03$.

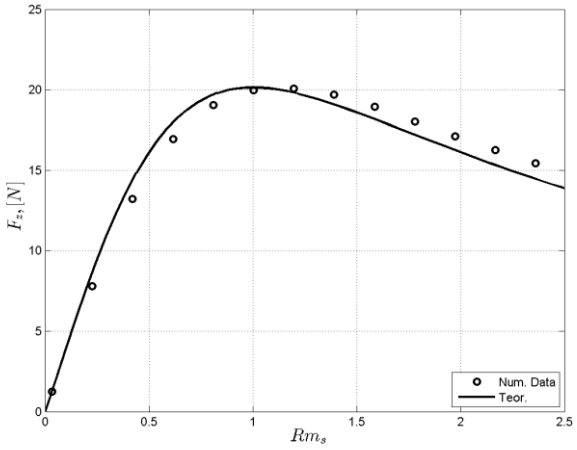

Fig. 91. Comparison of numerical and theoretical results of axial force $F_z : N = 0.03$.

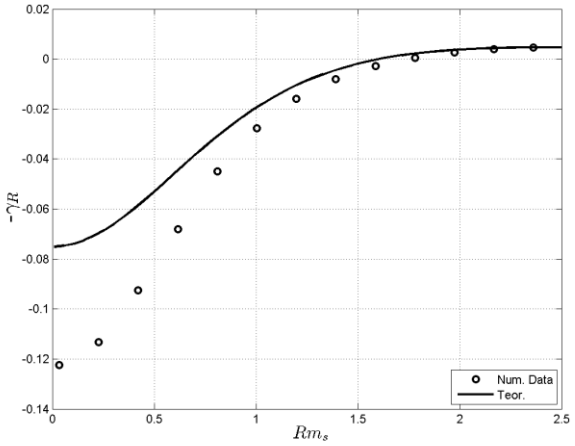

Fig. 92. Comparison of numerical and theoretical results of temporal development rate $-\gamma_R : N = 0.16$.

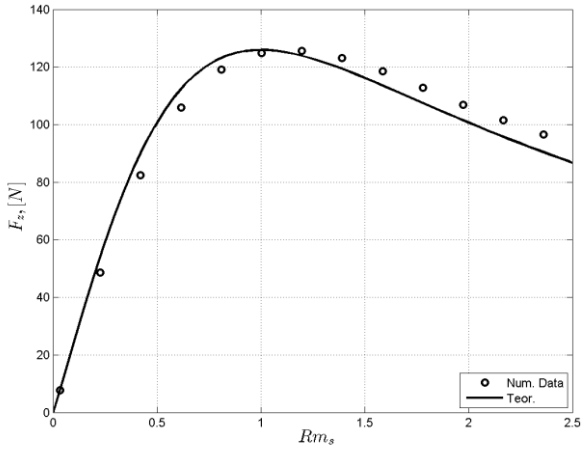

Fig. 93. Comparison of numerical and theoretical results of axial force $F_z : N = 0.16$.

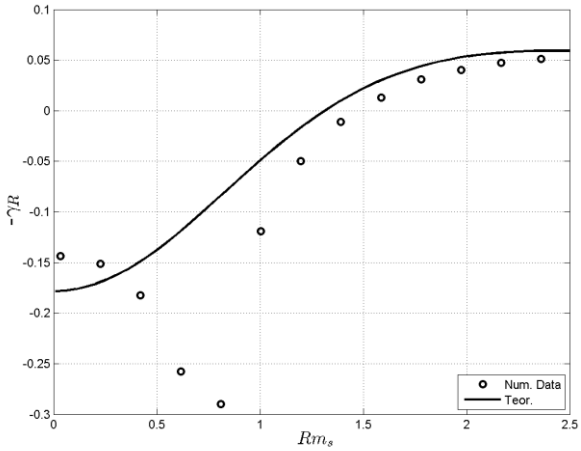

Fig. 94. Comparison of numerical and theoretical results of temporal development rate $-\gamma_R : N = 1$.

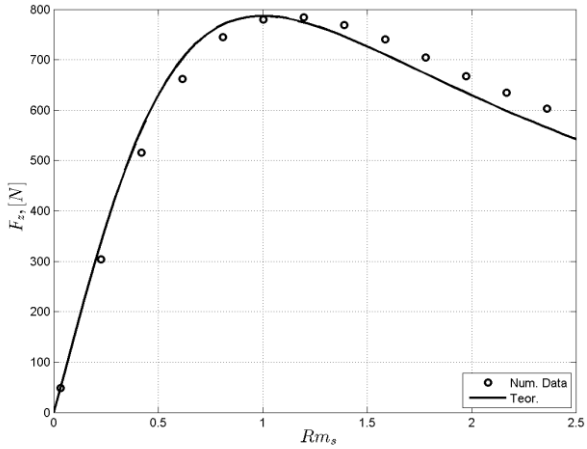

Fig. 95. Comparison of numerical and theoretical results of axial force $F_z : N = 1$.

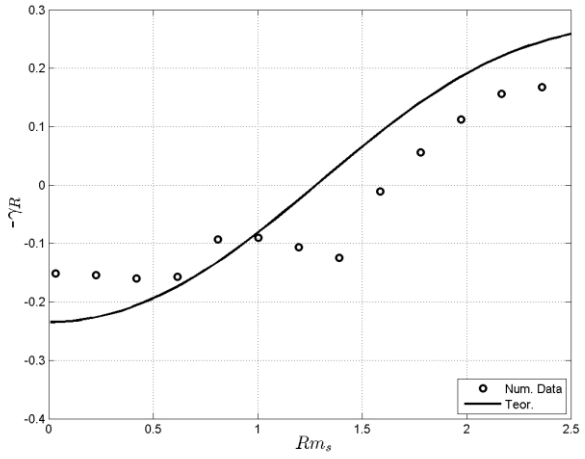

Fig. 96. Comparison of numerical and theoretical results of temporal development rate $-\gamma_R$ *:* $N = 5.9$.

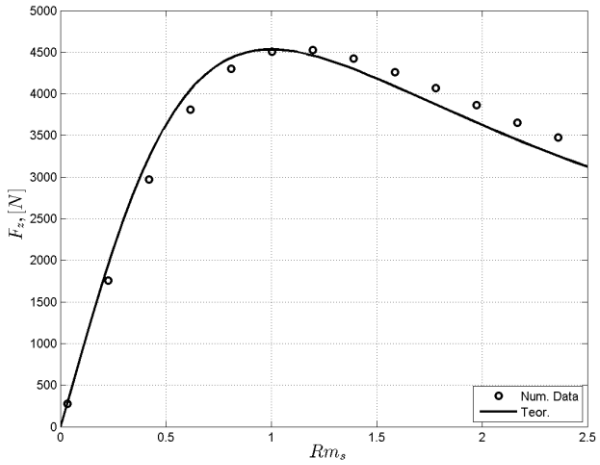

Fig. 97. Comparison of numerical and theoretical results of axial force F_z *:* $N = 5.9$.

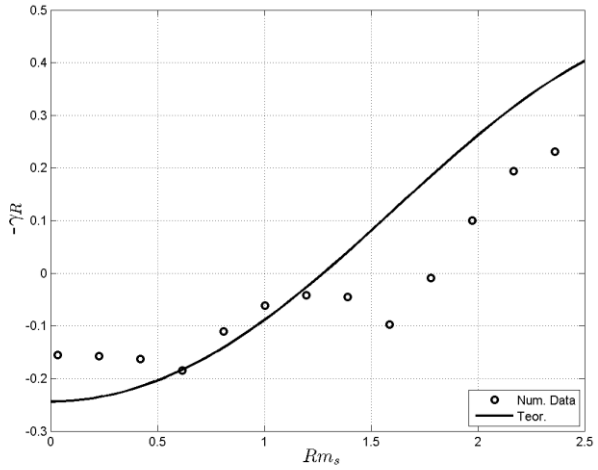

Fig. 98. Comparison of numerical and theoretical results of temporal development rate $-\gamma_R$ *:* $N = 13.2$.

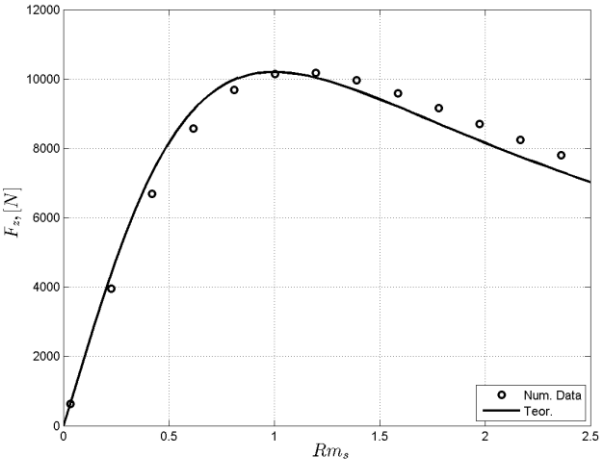

Fig. 99. Comparison of numerical and theoretical results of axial force F_z *:* $N = 13.2$.

3.2. Models of finite length FLIP with multi-harmonic magnetic field

3.2.1. Calculation of external magnetic field

In this chapter development of numerical model for finite length FLIP is discussed. MHD calculation is done as well using ANSYS FLUENT MHD module similarly as discussed before, but in a more sophisticated geometrical case. The key point here is introducing realistic distribution of external magnetic field in the model.

To do this following geometry of experimental FLIP is considered in Fig. 100

It consists of two symmetrically placed inductors with base height 110 mm and length 1100 mm (width of inductor 450 mm) creating nonmagnetic gap of 40 mm. The base is made of laminated ferromagnetic material. Each inductor consists of 36 copper coils with 28 windings which are embedded in slots of 75 mm height and 15 mm width. The ferromagnetic element between coils, frequently called *tooth*, is 15 mm width.

In the non-magnetic gap there is symmetrically placed channel of liquid Na layer 20 mm. The wall of channel is made from 4 mm thick non-magnetic stainless steel (SS). Accordingly there is 6 mm of air gap between channel and inductor on each side. Width of the channel is 420 mm. All dimensions are summarized in Table 5 and Table 6.

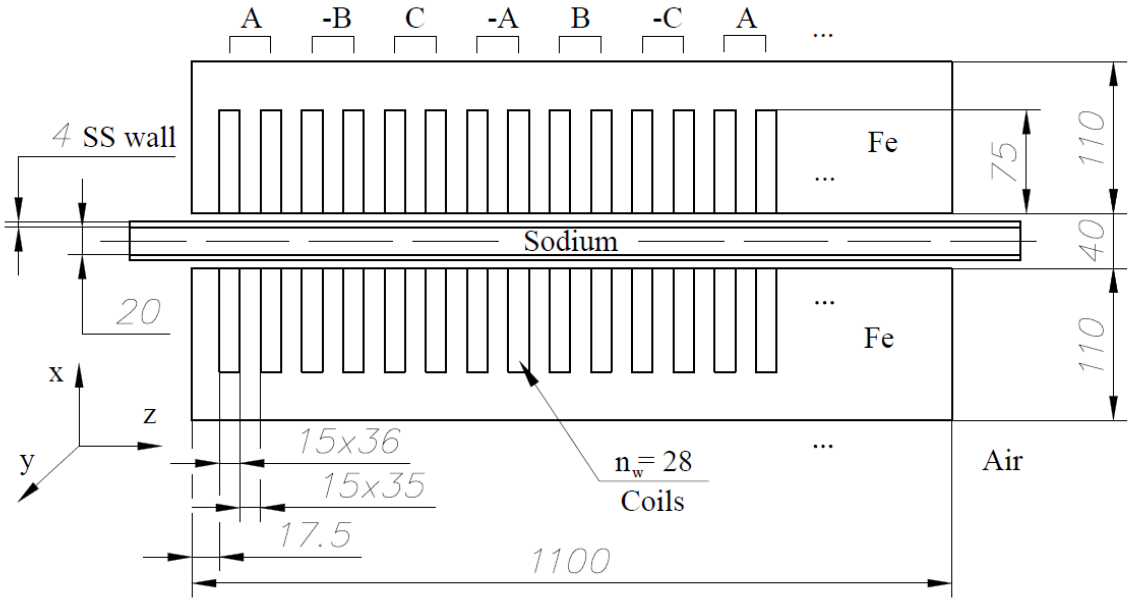

Fig. 100. Drawing of FLIP geometry.

L, [mm]	W, [mm]	H, [mm]	h_c, [mm]	w_c, [mm]	w_t, [mm]	n_c	n_w	τ, [mm]	d_m, [mm]
1100	450	110	75	15	15	36	28	180	40

Table 5. Dimensions of the model.

d_h, [mm]	w_{wall}, [mm]	W_{ch}, [mm]
20	4	420

Table 6. Dimensions of the model.

In top of Fig. 100 distribution of phases is shown. Every two coils were connected to same phase in a periodic sequence … - AA - (BB) – CC - (AA) – BB - (CC) - … where () stands for opposite direction of current in coils. In praxis this is achieved by simply winding coils in other direction (e.g. counter-clockwise instead of clockwise). Such distribution of external current density allows to rather correctly approximate it to *sin()* or *cos()* functions which is done in cases of ideal pumps. Since there are 12 slots and teeth per wavelength, then $2\tau = 0.36$ [m] and pump consists of three pole pairs (6τ).

If current in coil is known (e.g. measured), such FLIP can be modelled numerically in 2D case using COMSOL Mulitphysics and finally distribution of external magnetic field in the nonmagnetic gap obtained.

First of all, same geometry of inductors with air gap is created Fig. 101 and meshed in Fig. 102 with 181K elements. Two cut lines over centre and ¼ of channel height is made and real, imaginary and absolute value of magnetic field perpendicular (x) component monitored. Problem is solved in frequency domain, in particular case assuming 100A of measured line current. Plots of obtained magnetic field x component are shown in Fig. 103 and Fig. 104.

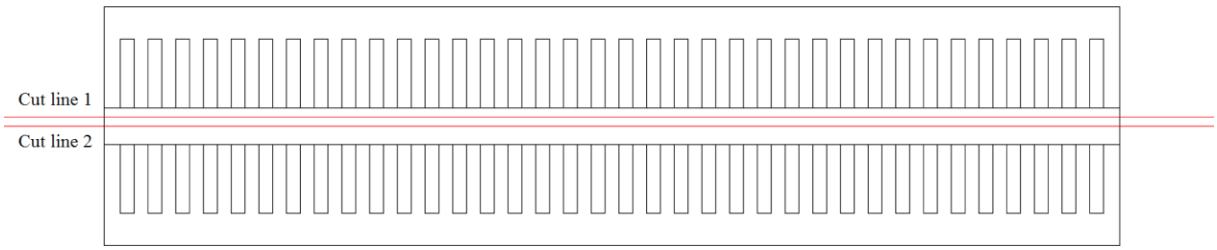

Fig. 101. An example geometry used in numerical model and cut lines.

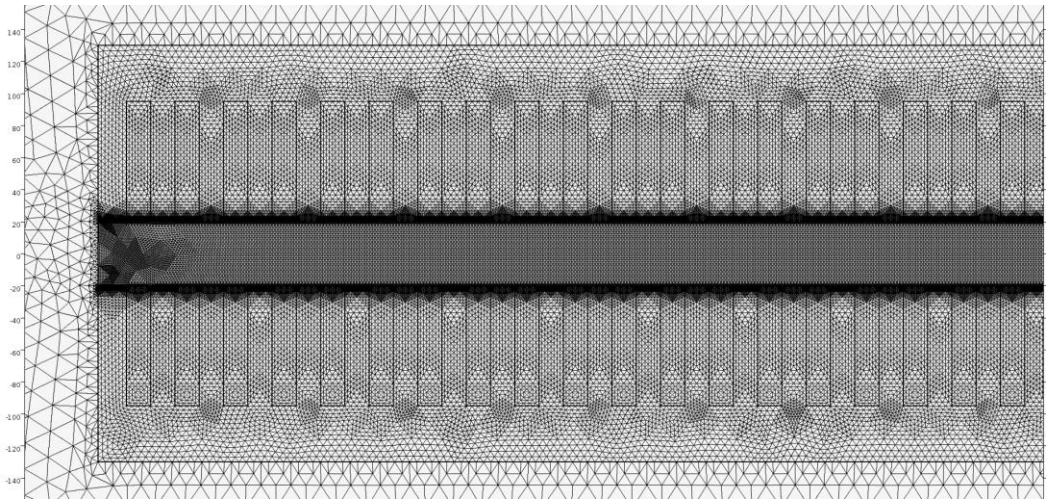

Fig. 102. An example geometry used in numerical model and cut lines.

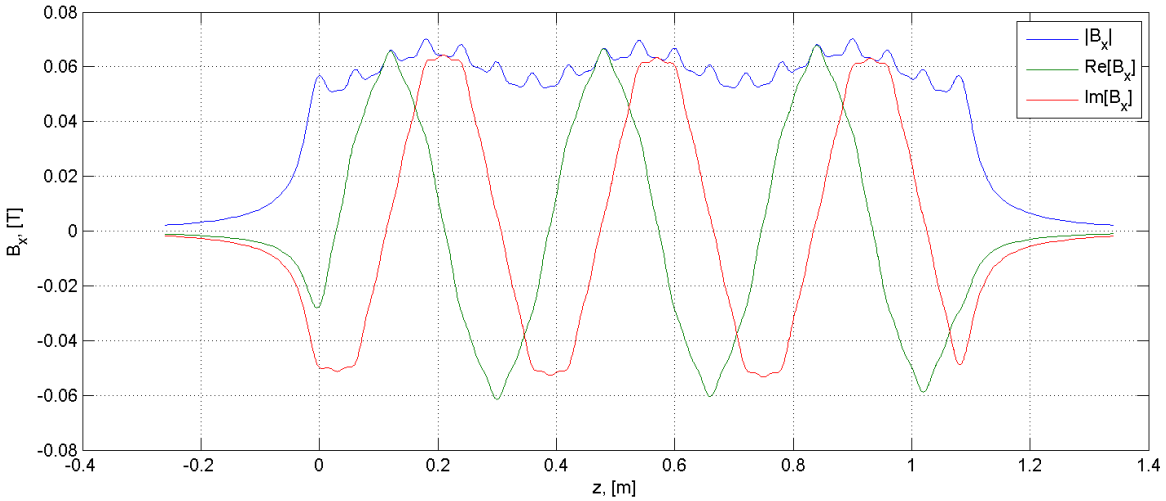

Fig. 103. Distribution of magnetic field over cut line 1. COMSOL results.

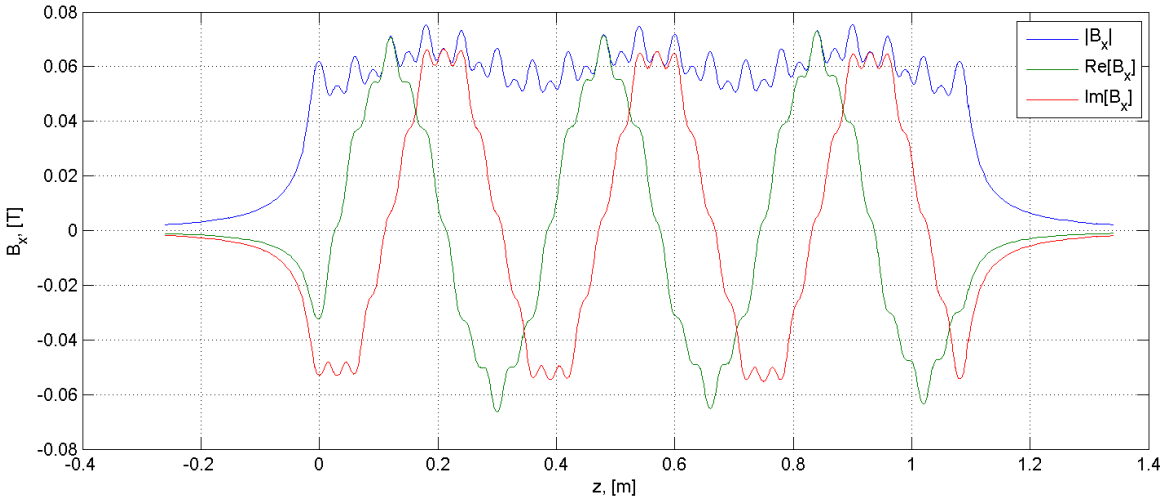

Fig. 104. Distribution of magnetic field over cut line 2. COMSOL results.

To implement distribution of obtained external magnetic field in the ANSYS FLUENT MHD module can be accomplished in two ways:

1. Use User-Defined-Functions and write known field in the appropriate data memory locations used by FLUENT
2. Use specially formatted file of magnetic field data and write data using program interface

In this work first method was used. It implies that external magnetic field should be given by mathematical functions. Also, since model in ANSYS is 2D, averaging of magnetic field over height is necessary. Both of these points suggest that analytical solution of external magnetic field in case of discrete current sources is necessary.

The solution of the periodic problem is shown in appendix, and it is found that complex distribution of external magnetic field in the gap is (see appendix for details):

$$B_x(x,z,t) = -2\mu_0\sqrt{2}I \cdot n_w \sum_{k=-\infty}^{\infty} \sum_{n=0}^{2} \frac{sin(\alpha_k w)}{\alpha_k w} \cdot \frac{cos\left(\frac{\alpha_k \tau}{12}\right)}{\tau} \cdot \frac{ch(\alpha_k x)}{sh(\alpha_k d_m)} \cdot ie^{i(\alpha_k[z-z_n-z_0]-\omega_B t+\varphi_n)} \quad (163)$$

Formula above takes into account infinite number of harmonics, however, in a good approximation it is sufficient take only 8 of them, namely:

$$k = [-5, -3, -2, 0, 1, 3, 4, 6]$$

Even though (163) gives rather good approximation of the field (Fig. 105, Fig. 106), it does not take into account two rather important details – the real slot geometry and finite length of inductor (pulsation of magnetic field and decay of the field outside the inductor). It leads to necessity to add these effects. This, of course, is done by empirical means.

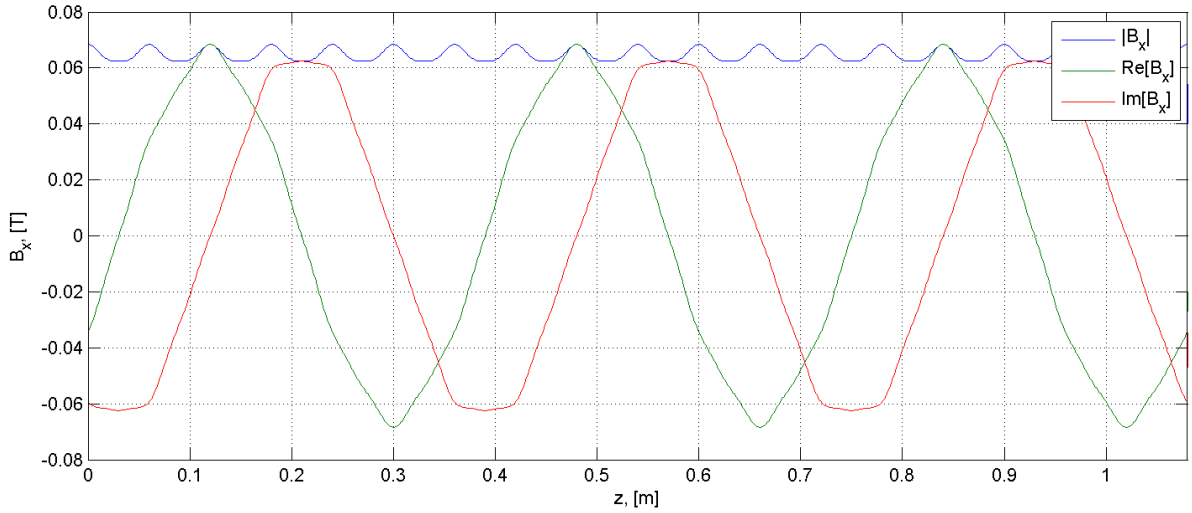

Fig. 105. Distribution of magnetic field over cut line 1. Analytical results.

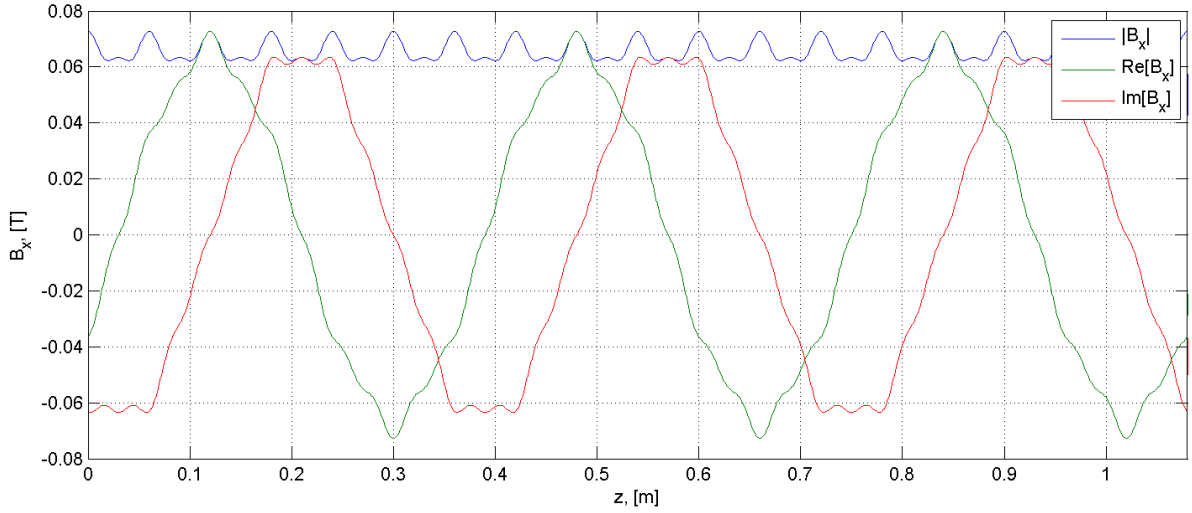

Fig. 106. Distribution of magnetic field over cut line 2. Analytical results.

First of all, correction coefficients for amplitude of each harmonic are added to better fit numerical results. They are:

$$k_c = [1.5, 1, 1, 0.925, 0.925, 1, 1, 1.5]$$

Secondly, pulsating component of magnetic field is added in form:

$$B_p = B_{p0} e^{-i\omega_B t} \tag{164}$$

Amplitude of pulsation B_{p0} is estimated of wavy-like structure of external field modulus in numerical results (Fig. 103 and Fig. 104).

Finally, decay of the field in the inlet and outlet is approximated as exponential function in from:

$$B_{in} = B_{z=0} \cdot e^{k_e z} \tag{165}$$

$$B_{out} = B_{z=6\tau} \cdot e^{k_e (6\tau - z)} \tag{166}$$

With these operations external magnetic field is fitted to numerical results with acceptable precision:

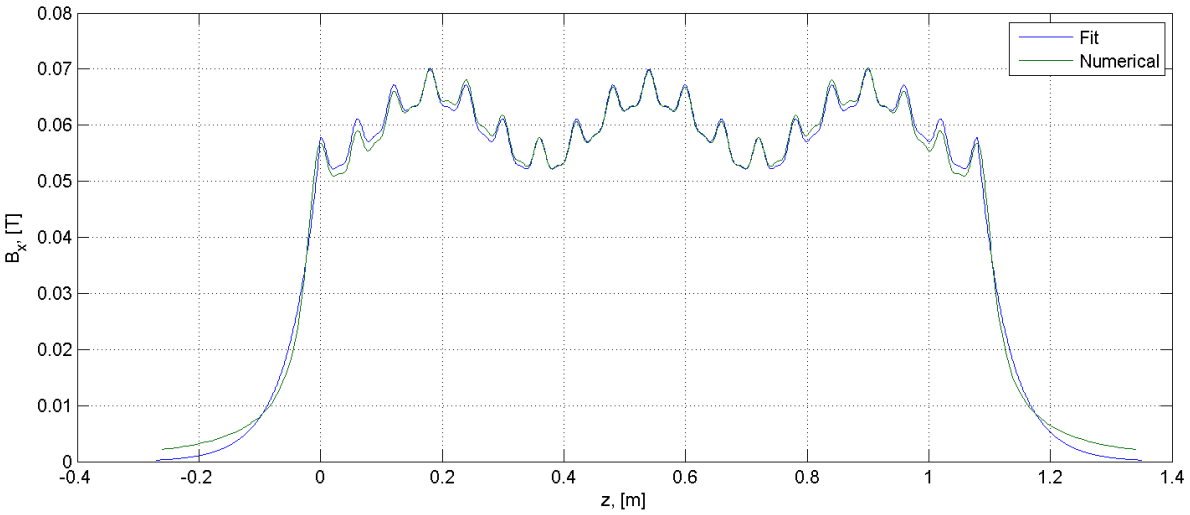

Fig. 107. Comparison of numerical and analytical results of magnetic field modulus over cut line 1.

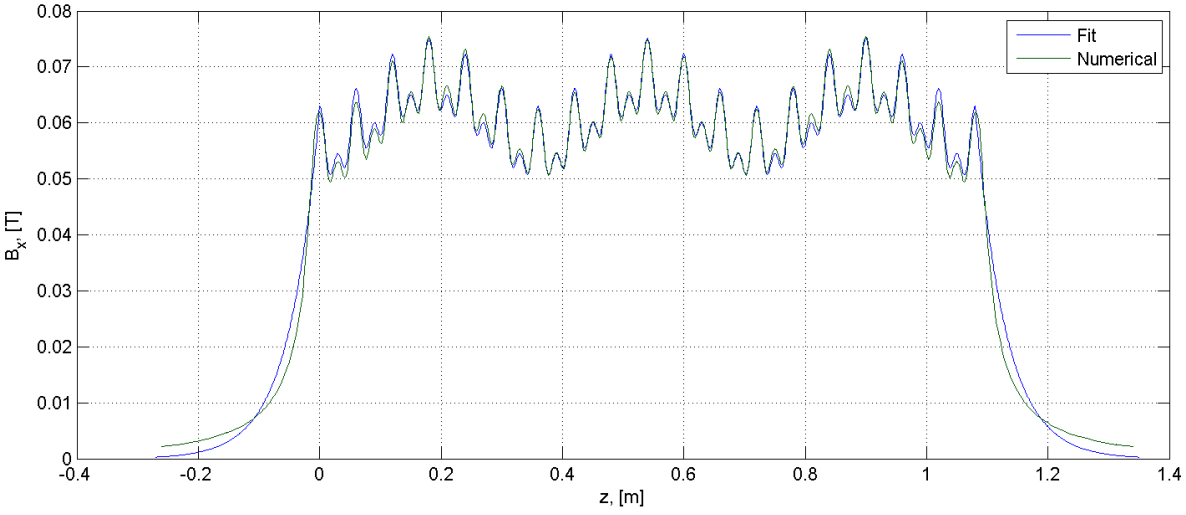

Fig. 108. Comparison of numerical and analytical results of magnetic field modulus over cut line 2.

Next (163) can be averaged over the height of the gap (167) and using fitting procedure the final distribution of height averaged field is obtained. Distribution of modulus, real and imaginary part of field is shown in Fig. 109 - Fig. 112 which represent 4 time instants of a single period. It can be observed that modulus of external field does not change in time, but instantaneous value – the real part – oscillates while moving over the axial direction. Note that only difference between distribution of real and imaginary part is time shift of ¼ of a period. This fact has high importance later in the work.

Having good description of external magnetic field, models of representing experimental setups were created.

$$B_x(z,t) = -\frac{2\mu_0\sqrt{2}I \cdot n_w}{d_m} \sum_{k=-\infty}^{\infty} \sum_{n=0}^{2} \frac{sin(\alpha_k w)}{\alpha_k w} \cdot \frac{cos\left(\frac{\alpha_k \tau}{12}\right)}{\alpha_k \tau} \cdot ie^{i(\alpha_k[z-z_n-z_0]-\omega_B t+\varphi_n)} \qquad (167)$$

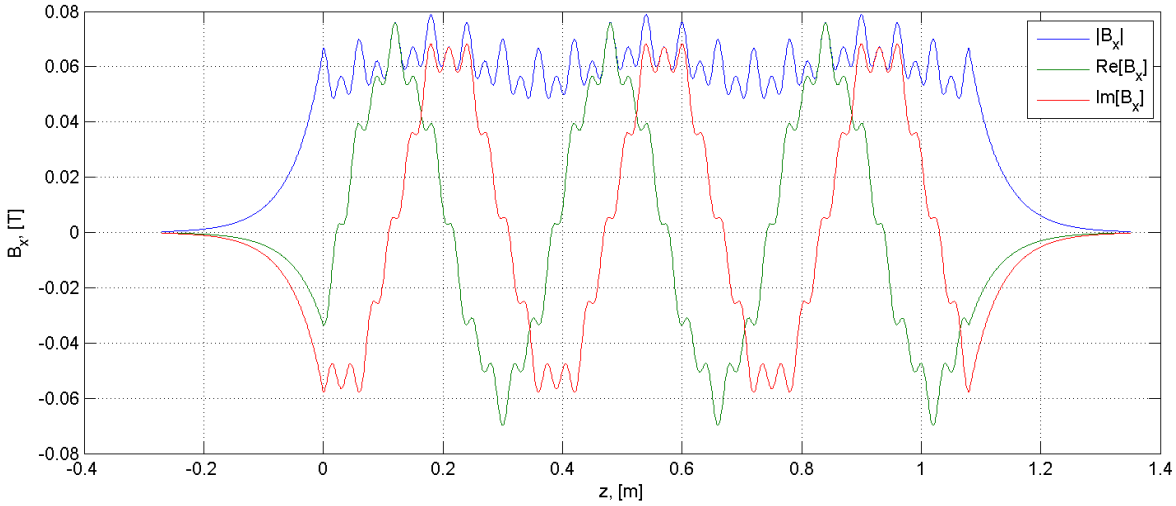

Fig. 109. Analytical magnetic field modulus over cut line 2. T = 0.

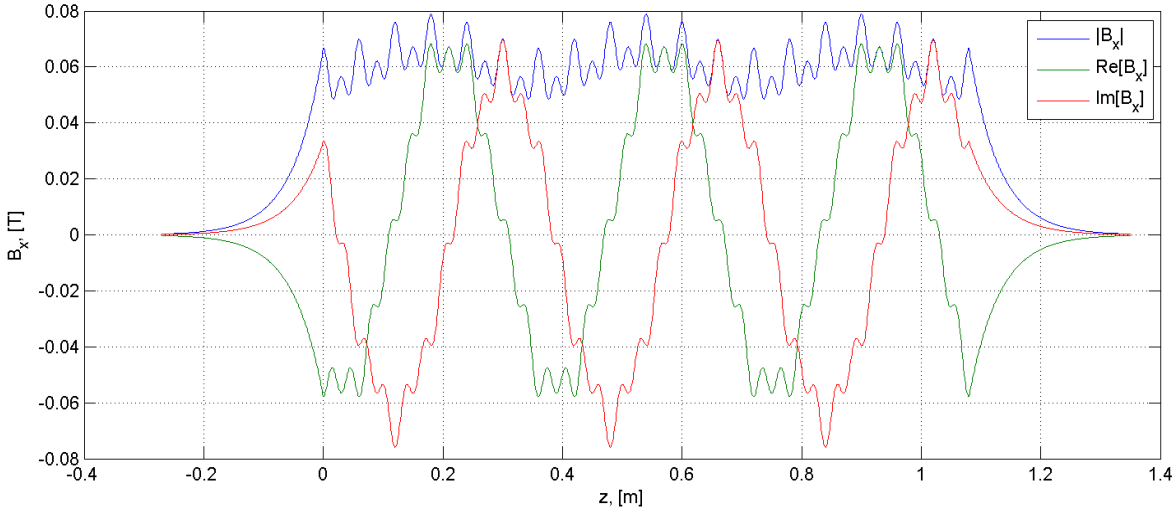

Fig. 110. Analytical magnetic field modulus over cut line 2. T = 1/4

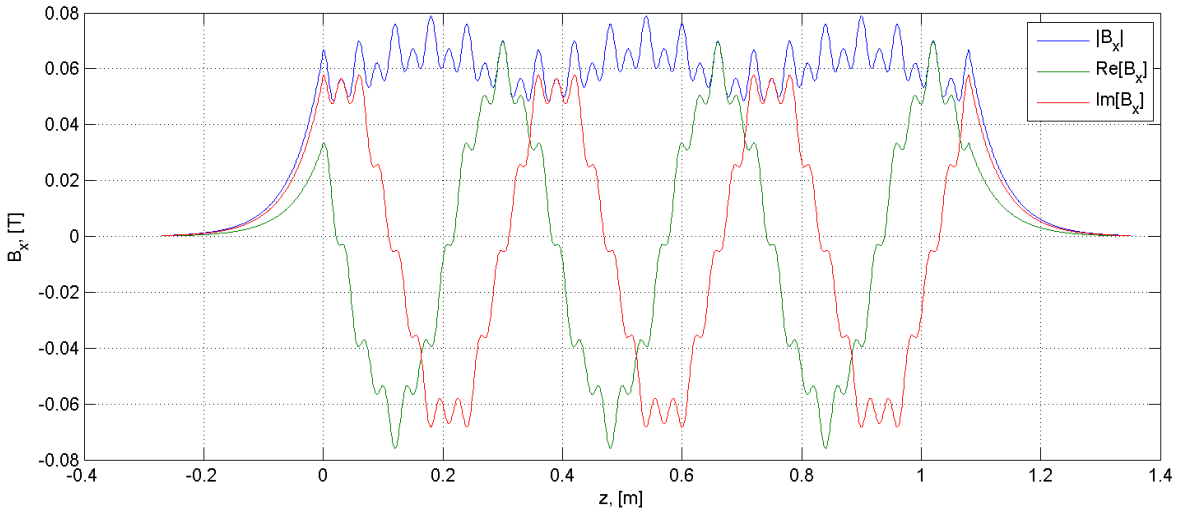

Fig. 111. Analytical magnetic field modulus over cut line 2. T = 2/4

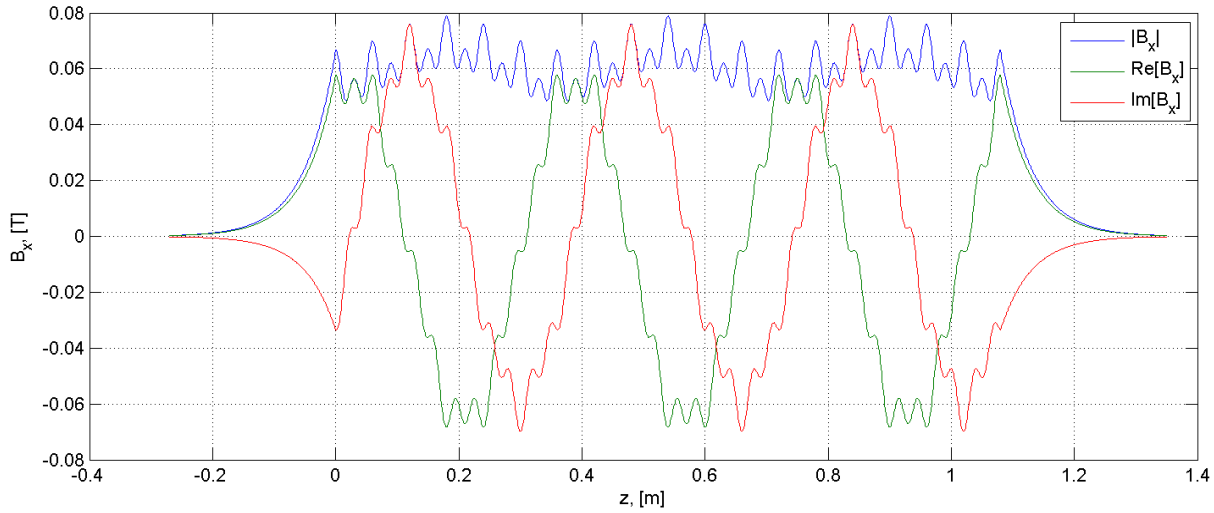

Fig. 112. Analytical magnetic field modulus over cut line 2. T = 3/4

3.2.2. Numerical model with 4 sub-channels

The 2D geometry of first studied case consisted of rectangular sodium channel with external stainless steel walls. The central zone of the channel (where actual inductor is located) is divided by additional 3 walls into 4 sub-channels. The sketch of geometry and mesh is shown in Fig. 113 and Fig. 114.

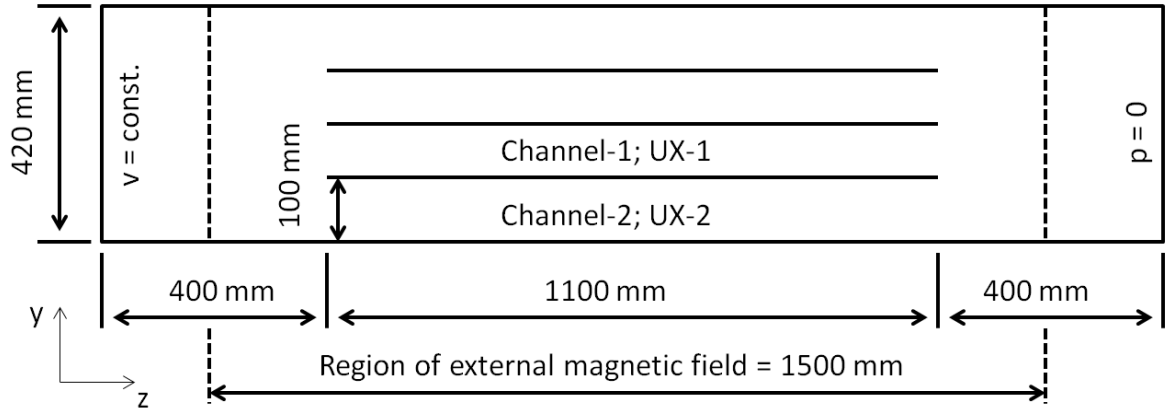

Fig. 113. A sketch of geometry.

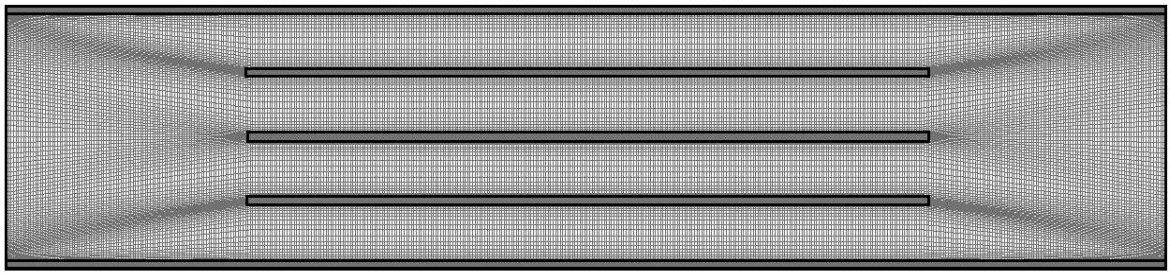

Fig. 114. Used mesh with 57K elements.

Some peculiarities of FLIP 2D model should be discussed which are significant in all similar type calculations.

First of all, one should keep in mind that all physical effects are height averaged. E.g. this is the reason why it was necessary to find good analytical approximation of external magnetic field. This also means that there is only height of liquid metal layer d_h and non-magnetic gap d_m does not exist (in the numerical model). Therefore, if the real conductivity of liquid metal is used, one will arrive to higher magnetic Reynolds number. To fix this problem, ratio d_h/d_mshould be implemented into the conductivity, therefore having the same Rm:

$$Rm = \frac{\mu_0 \sigma v_B}{\alpha}\left(\frac{d_h}{d_m}\right) \quad \rightarrow \quad Rm = \frac{\mu_0 \sigma_1 v_B}{\alpha} \quad where \quad \sigma_1 = \sigma\left(\frac{d_h}{d_m}\right) \tag{168}$$

Secondly, since conductivity has been changed, obviously modified interaction parameter will change as well. To fix this, it is necessary to change or density ρ by the same factor:

$$N_\lambda = \frac{2\sigma}{\zeta_h \rho v_B} B_0^2 \quad \rightarrow \quad N_\lambda = \frac{2\sigma_1}{\zeta_h \rho_1 v_B} B_0^2 \quad where \quad \rho_1 = \rho\left(\frac{d_h}{d_m}\right) \tag{169}$$

Finally modified Reynolds number has not been changed and set of dimensionless numbers is corrected for use in 2D model:

$$Re_\lambda = \frac{2\alpha}{\zeta_h} \tag{170}$$

There is, however, one important remark. The described changes of only material properties allow to rather easily obtaining desired set of dimensionless numbers. This set indeed should describe behaviour and nature of physical process, but absolute value of developed pressure will not be exactly comparable with the experiment, since conductivity of material has been changed by factor d_h/d_m. Apparently, division by mentioned factor is necessary.

Main parameters used in numerical model are summarized in tables below:

σ_{Na}, [MS/m]	ρ, [kg/m^3]	ζ_h	σ_{SS}, [MS/m]	f, [Hz]	B_0, [T]	Rm	N_λ	Re_λ	N
3,7	903,56	0,37	1,77	50	0,29	4,8	103,4	94,3	1,1

Table 7. Parameters of the numerical model.

Δx, [m]	Δt, [s]	CFL_{vB}	Res	n_y	n_z	n
4 x 10^{-3}	10^{-4}	0,45	10^{-6}	120	475	57K

Table 8. Parameters of the numerical model.

Q, [L/s]	0	10	20	30	45
Rm_s	4,8	4,47	4,15	3,82	3,33

Table 9. Parameters of the numerical model

Cases with 5 different flowrates Q = [0, 10, 20, 30, 45] L/s were studied. Each calculated up to 1.4s when steady state of flow was achieved. Then distribution of magnetic field over the pump was analysed and is shown in Fig. 115 in case of flowrate Q = 45 l/s and can be observed that it is symmetric.

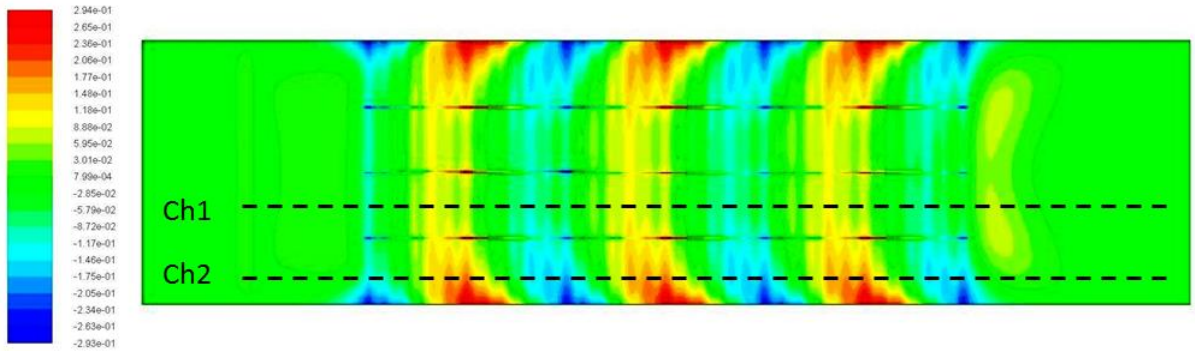

Fig. 115. Distribution of B_x [T]: Q = 45 L/s, $Rm_s = 3.3$.

An example of distribution of field over lines Ch1 and Ch2 is shown in Fig. 116. One can observe tendency that magnetic field is stronger in the outer channel, but weaker in the inner channel.

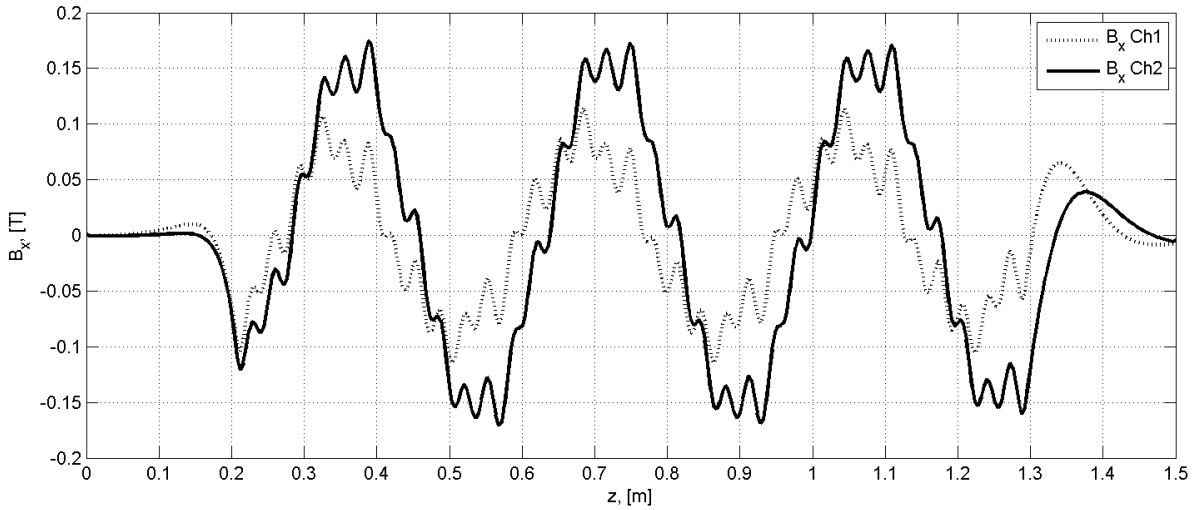

Fig. 116. Distribution of B_x [T] over cut lines: Q = 45 L/s, $Rm_s = 3.3$.

Velocity z component distribution of a particular case is shown in Fig. 117. It can be observed that overall there are higher velocity in the outer channels, but lower in the inner channel. Besides that, there is strong recirculation flow near the outer wall which is caused by closure of the current loop over the width of the channel, therefore inhomogeneous forces. The distribution of velocity is symmetric as well.

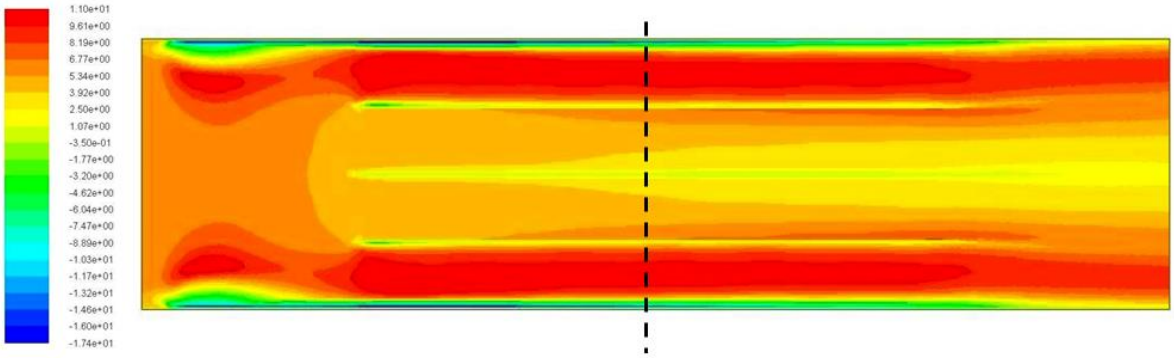

Fig. 117. Distribution of v_z [m/s]: Q = 45 L/s, $Rm_s = 3.3$..

In particular, distribution of axial velocity with different flowrates in the middle of the channel is shown in Fig. 118. Only half of it is shown due to the symmetry. It can be observed that in all cases a strong negative velocity exists near outer wall. Also in case of low flowrate, overall negative velocity is observed in the central channel, but positive in the side channel. This suggests that recirculation from side to centre is possible.

Finally, amplitude of magnetic field and axial velocity in the centre of each sub-channel is compared as function of flowrate in Fig. 119 and Fig. 120. It can be observed that changes of both of these parameters are quite similar and obviously they are correlated. E.g. lower absolute value, but higher changes of magnetic field in the Ch-1 and higher absolute value, but lower changes in Ch-2 correspond to similar velocity behaviour.

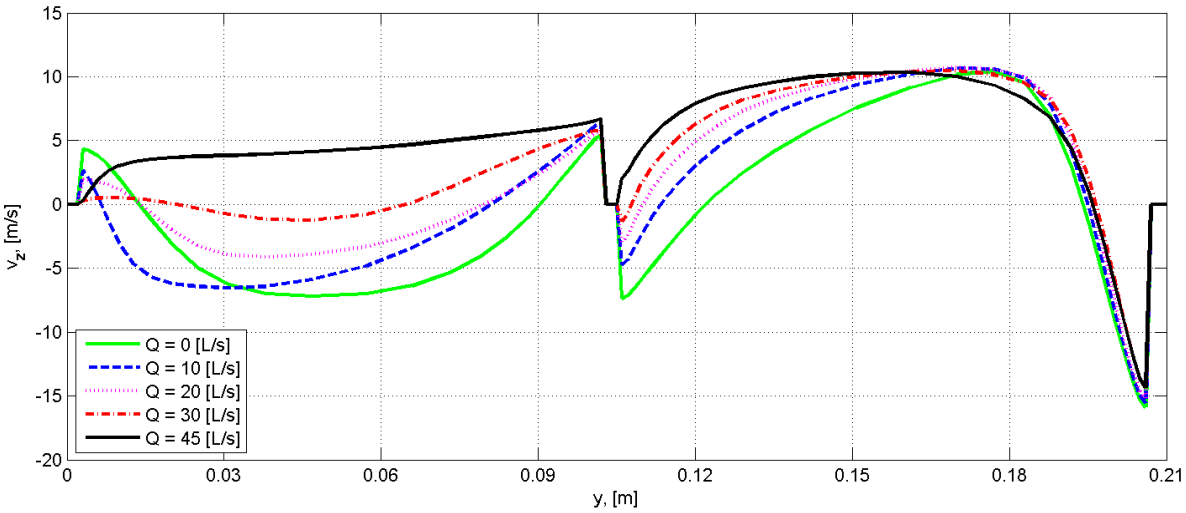

Fig. 118. Distribution of v_z [m/s] in the middle of the channel for different flowrates.

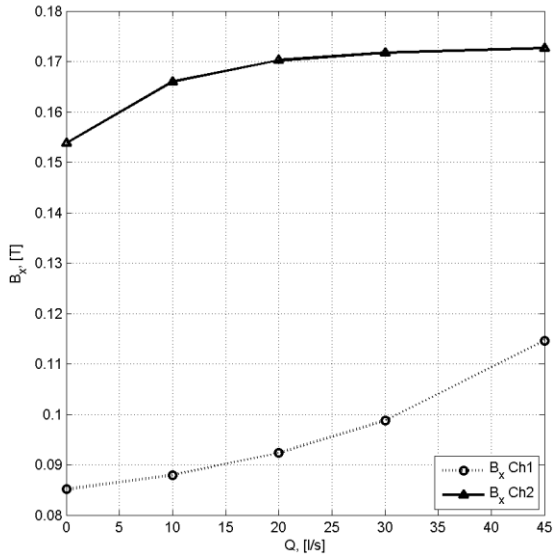

Fig. 119. Amplitude B_x [T] in the middle of the sub-channel as function of flowrate.

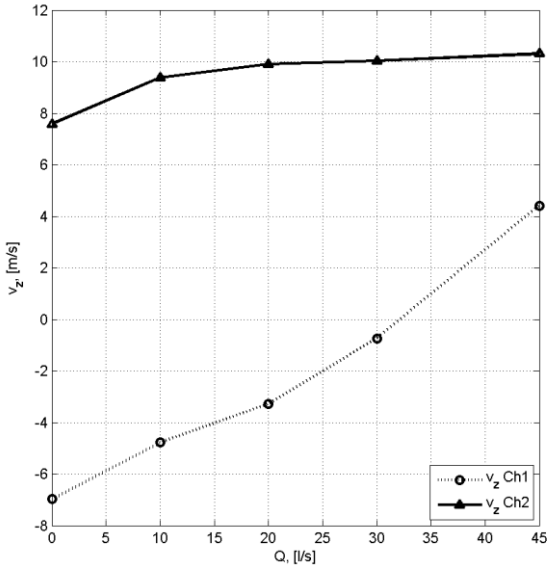

Fig. 120. v_z [m/s] in the middle of the sub-channel as function of flowrate.

It can be rather easily shown that in the case of high $Rm \gg 1$ and $s \to 1$ magnetic field should change according to:

$$B_x \approx \frac{B_e}{Rm}\left(1 + \frac{v_z}{v_B}\right) \tag{171}$$

This means that field should be a linear function of axial velocity and should increase with it, and explains obtained similarities in the figures.

Presented model with sub-channels was only first step towards to development of more detailed and realistic simulations of FLIP and EMIP in general. Further development is discussed in following chapter.

3.2.3. Numerical model without sub-channels

A significantly different model from geometry and setup point of view was created to analyse situation without sub-channels shown in Fig. 121. There are no sub-channels in inductor zone, but additional stainless steel walls are added for potential difference measurements in the inlet and outlet zones, therefore stationary magnetic field is present in this model. Also inlet velocity boundary condition is applied more precisely – depending on rather complex geometry of the loop before.

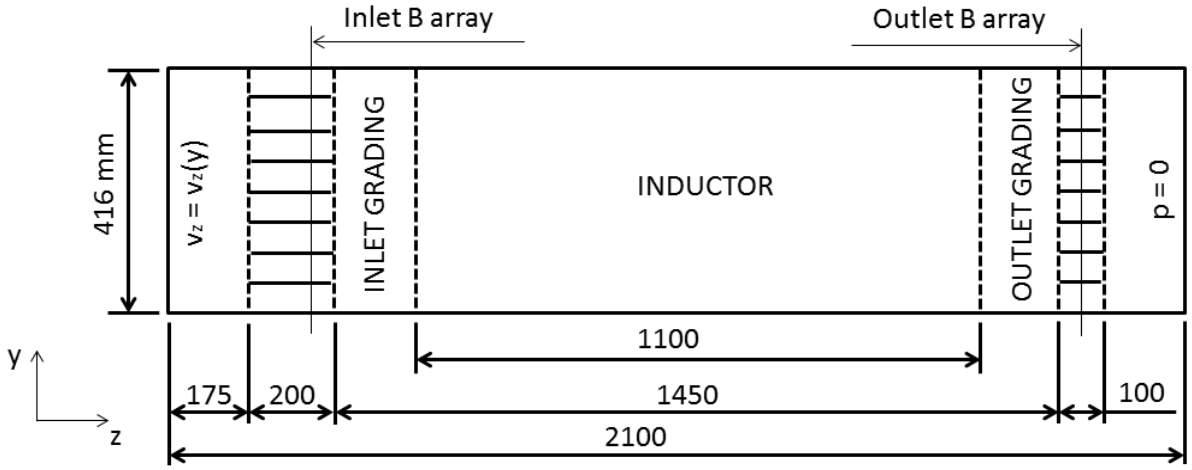

Fig. 121. Geometry and setup of numerical model without sub-channels.

Main parameters used in numerical model are summarized in tables below:

σ_{Na}, [MS/m]	ρ, [kg/m^3]	ζ_h	σ_{SS}, [MS/m]	f, [Hz]	B_0, [T]	Rm	N_λ	Re_λ	N
3,7	451,5	0,37	0,885	50	0,16	4,8	63	94	0,67

Table 10. Parameters of the numerical model

Δx, [m]	Δt, [s]	CFL_{vB}	Res	n_y	n_z	n
2 x 10^{-3}	2 x 10^{-4}	1,8	10^{-4}	350	1050	372K

Table 11. Parameters of the numerical model

Q, [L/s]	10	20	30	40
Rm_s	4,47	4,15	3,82	3,5

Table 12. Parameters of the numerical model

The inlet velocity boundary condition was obtained using separate 3D calculation and taking into account corner of the sodium loop, as well as geometry of the diffusor Fig. 122. The problem was solved stationary using k-ω SST turbulence model.

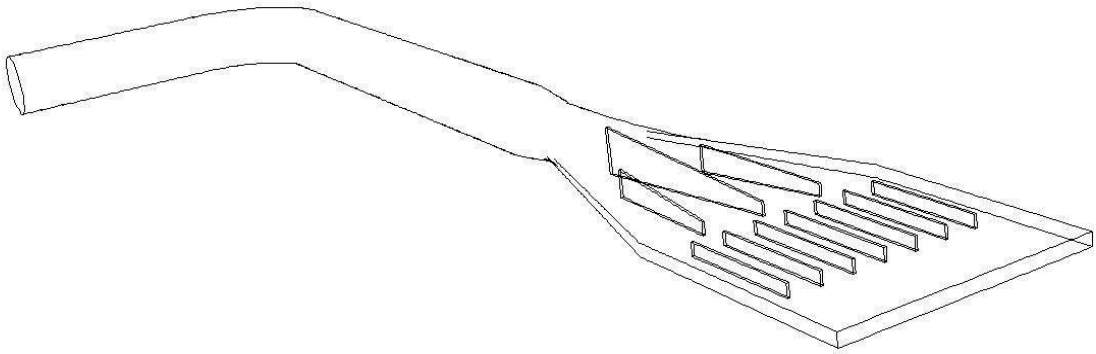

Fig. 122. The geometry of corner and diffusor for velocity profile boundary condition calculation.

By varying flowrate, velocity distribution was obtained and profile of velocity z component saved according to cut line in Fig. 123:

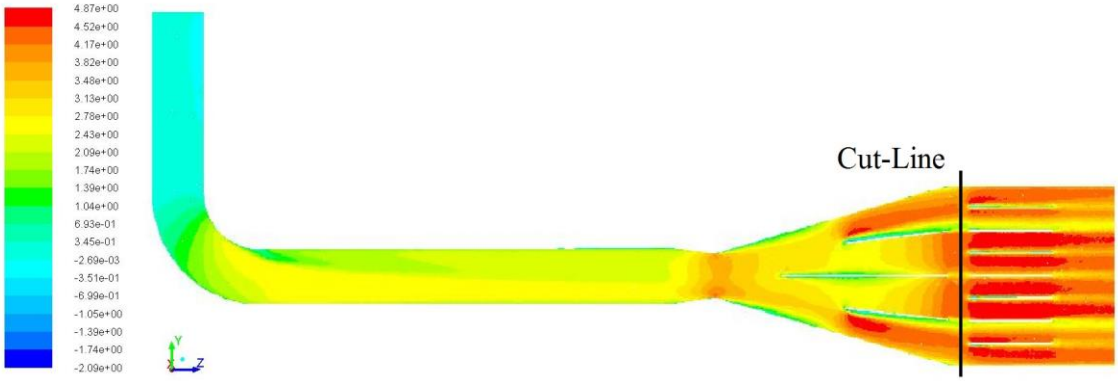

Fig. 123. Distribution of v_z [m/s], Q = 30 L/s and cut-line where velocity profile for boundary condition was registred.

Stationary magnetic field in the inlet and outlet zones was applied using simplified expression:

$$B_e = B_{Dc} \cdot sin\left(\frac{y\pi}{y_0}\right) \quad where \quad B_{Dc} = 0.26[T] \quad \& \quad y_0 = 0.0515 \quad [m] \qquad (172)$$

In Fig. 124 in plane distribution of external magnetic field is shown, where DC magnetic field in inlet and outlet zones as well as AC field in inductor zone can be distinguished. In Fig. 125 applied external field over the cut-line is shown in details.

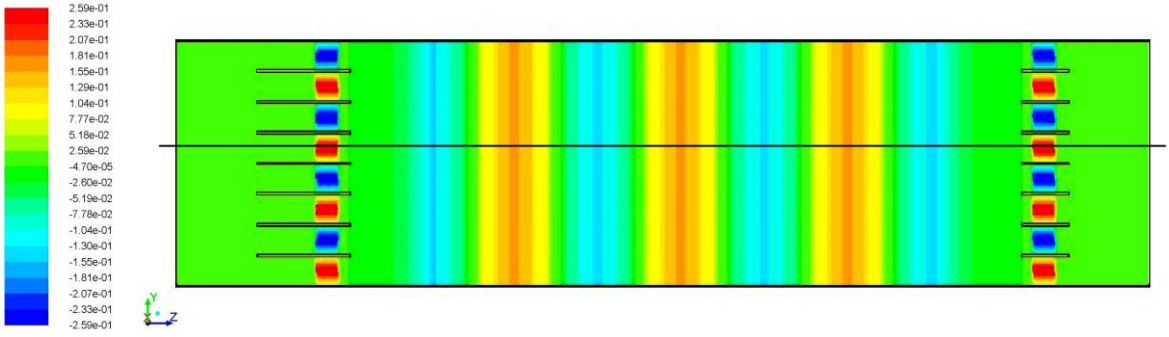

Fig. 124. Distribution of external AC magnetic field in the inductor zones, DC field between stainless steel walls and cut-line. B_{ex}, [T].

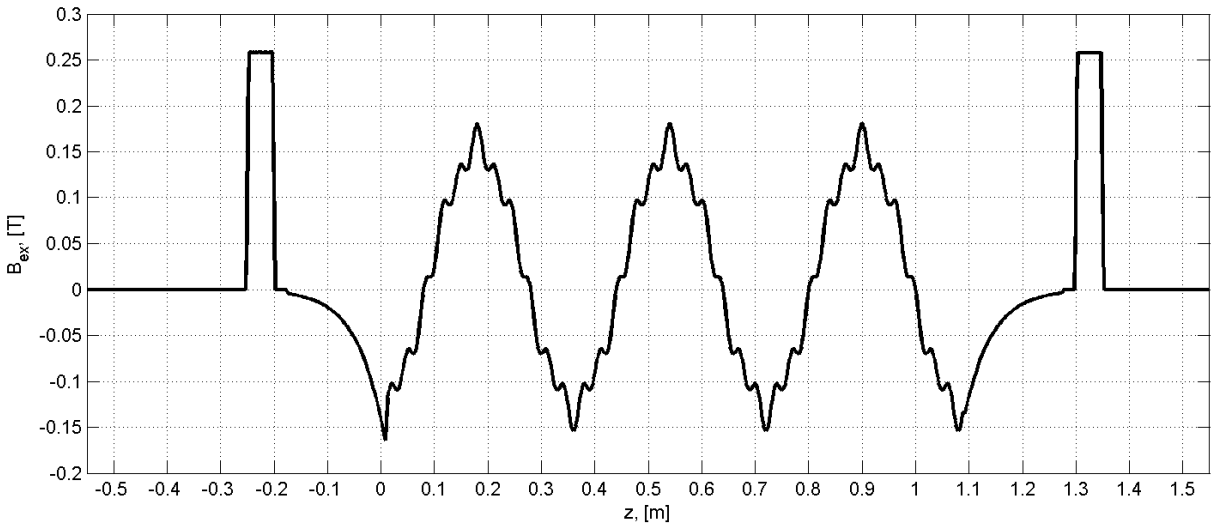

Fig. 125. Distribution of external magnetic field over the cut- line.

Calculations were carried out in several cases, with flowrates Q = [10, 20, 30, 40] L/s. In each case developed flow was calculated several seconds to obtain necessary amount of data for pressure spectrum analysis.

Different post processing method was used for magnetic field. First of all, one is interested in its modulus, since this value is measureable in experiment. However, such parameter is not available in ANSYS FLUENT MHD interface directly, moreover – it cannot be recalculated by simple means.

To solve this problem, distribution of total magnetic field is saved every quarter of the period. As shown before, using complex description, real and imaginary part are simply 90º shifted from one another Fig. 109 - Fig. 112. Therefore, if frequency of magnetic field is sufficiently high, that there are no significant flow changes during ¼ of period, it is possible to recalculate modulus of magnetic field using data of these 2 time steps. This was realized using MatLab software.

Modulus of magnetic field along with axial velocity distribution only in inductor zone is shown in Fig. 126 - *Fig.* 141. One can observe that distribution of magnetic field modulus is somewhat similar in all cases, having stronger field near side walls and lower field in the centre of channel (e.g. Fig. 126 and Fig. 128).

In the case of $Rm_s = 4.47$ (Fig. 126 - *Fig.* 129) it can be observed that nature of flow in the channel is rather unstable and large vortical structures can be observed. Moreover, these structures are not stationary but oscillating with comparatively low frequency (Fig. 127 and *Fig.* 129). Interestingly, it is possible to see that these fluctuations and therefore distribution of the flow are reflected in the modulus of magnetic field (Fig. 126 and Fig. 128). It should be noted that strong backflow exists in the near wall region, where only tangential component of currents exist.

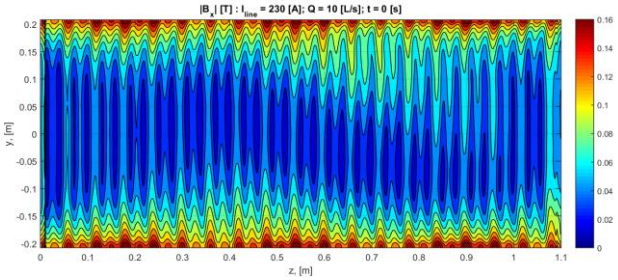

Fig. 126. $|B_x|$ *[T]:* $Rm_s = 4.47$, *t = 0 s.*

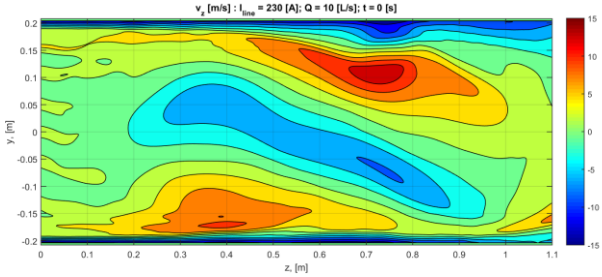

Fig. 127. v_z *[m/s]:* $Rm_s = 4.47$, *t = 0 s.*

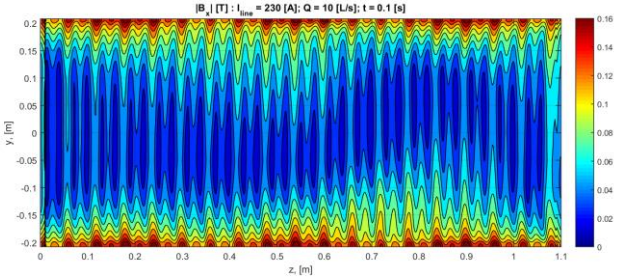

Fig. 128. $|B_x|$ *[T]:* $Rm_s = 4.47$, *t = 0.1 s.*

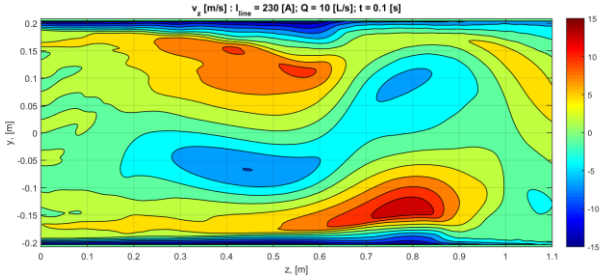

Fig. 129. vz [m/s]: $Rm_s = 4.47$, *t = 0.1 s.*

Qualitatively similar behaviour of flow and magnetic field can be observed also in case $Rm_s = 4.15$. Nevertheless, vortices of the flow are less intense (Fig. 131 and *Fig.* 133) and one can note that structures are located slightly more to the outlet of inductor zone. Even though amplitude of oscillations also is not that important as previously, it can be still rather well observed in distribution of magnetic field in Fig. 130 and *Fig.* 132.

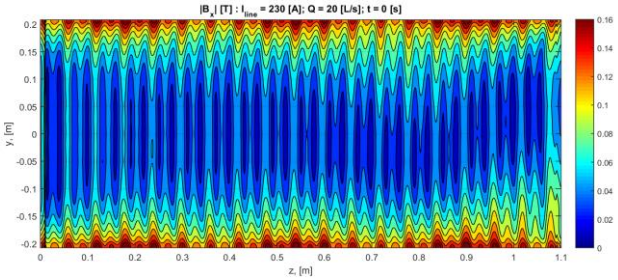

Fig. 130. $|B_x|$ *[T]:* $Rm_s = 4.15$, *t = 0s.*

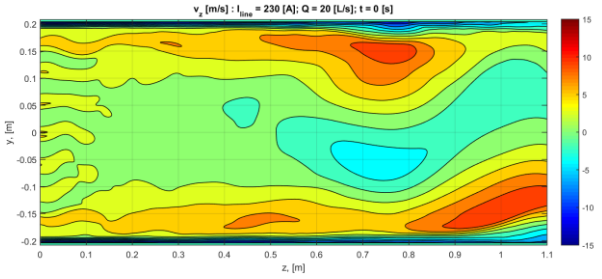

Fig. 131. v_z *[m/s]:* $Rm_s = 4.15$, *t = 0s.*

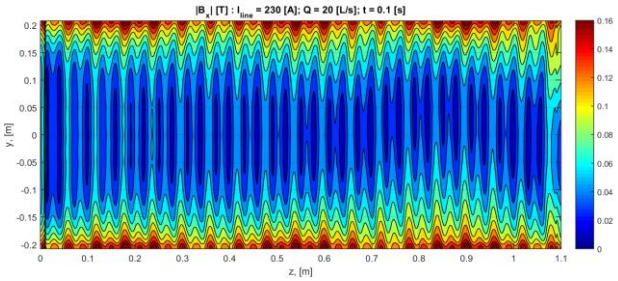

Fig. 132. $|B_x|$ *[T]:* $Rm_s = 4.15$, *t = 0.1s.*

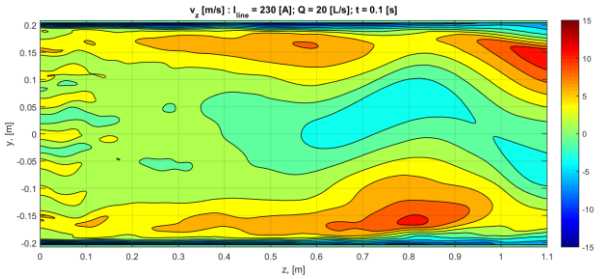

Fig. 133. v_z *[m/s]:* $Rm_s = 4.15$, *t = 0.1s.*

In following case $Rm_s = 3.82$ no strongly oscillating structures are observed, but in the outlet of inductor still important inhomogeneity of velocity is observed over width of the channel, where stronger velocity exists in side zones, but slightly negative in central zone (*Fig.* 135. and *Fig.* 137). The jet-like structures in the inlet of inductor are caused by array of permanent magnets. Even though no strong perturbations of distribution of magnetic field are observed in *Fig.* 134 and *Fig.* 136, one can note that field becomes weaker towards the outlet, however, more precise methods of analysis are necessary to discuss this case properly.

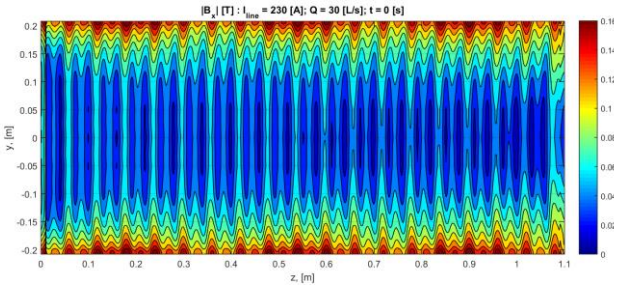

Fig. 134. $|B_x|$ *[T]:* $Rm_s = 3.82$, t *= 0s.*

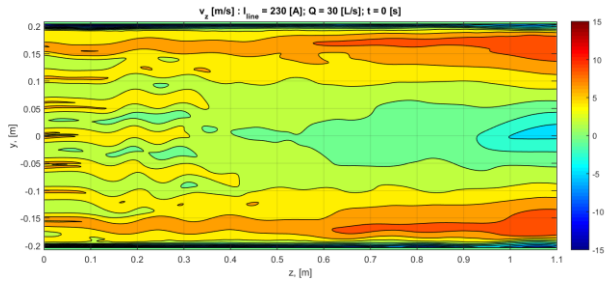

Fig. 135. v_z *[m/s]:* $Rm_s = 3.82$, t *= 0s.*

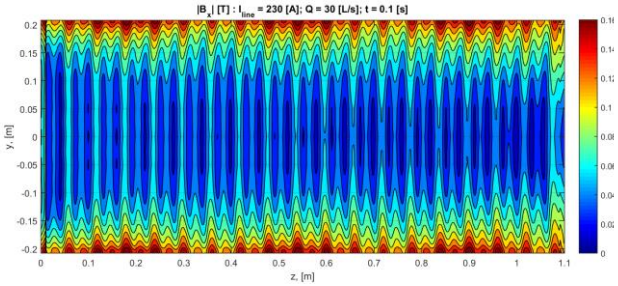

Fig. 136. $|B_x|$ *[T]:* $Rm_s = 3.82$, t *= 0.1s.*

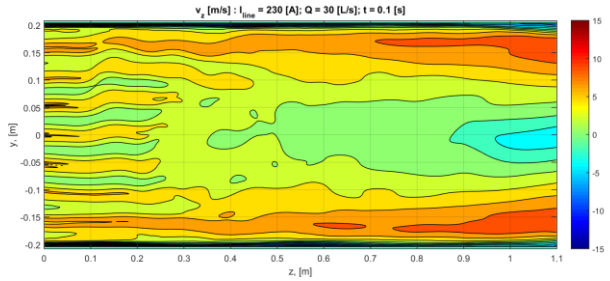

Fig. 137. v_z *[m/s]:* $Rm_s = 3.82$, t *= 0.1s.*

Finally, in the case of $Rm_s = 3.5$, jet-like flow is up to middle of the inductor zone (Fig. 139 and Fig. 141) and then forms inhomogeneous velocity distribution similar as in previous case. No obvious changes of distribution of magnetic field cannot be observed and qualitatively remains the same.

Presented numerical results give only qualitative view on phenomenon in question and observed structures of magnetic field and axial velocity distributions require more detailed treatment. E.g. it should be possible to preform 2D Fourier decomposition of fields and quantify them in terms of wavelength or similar. Such methodology of such post-treatment is necessary to develop, but is out of scope of current work.

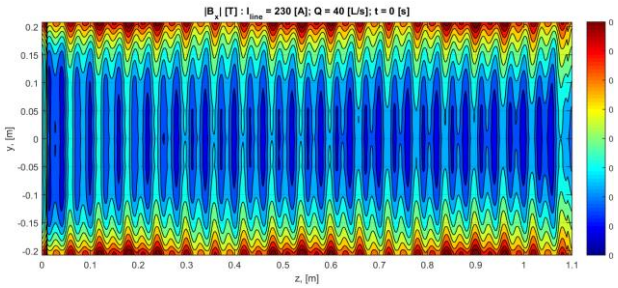

Fig. 138. $|B_x|$ *[T]:* $Rm_s = 3.5$, t *= 0s.*

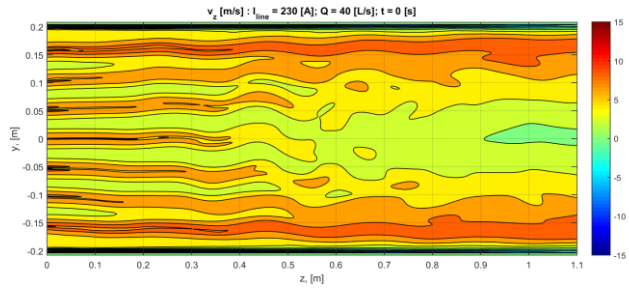

Fig. 139. v_z *[m/s]:* $Rm_s = 3.5$, t *= 0s.*

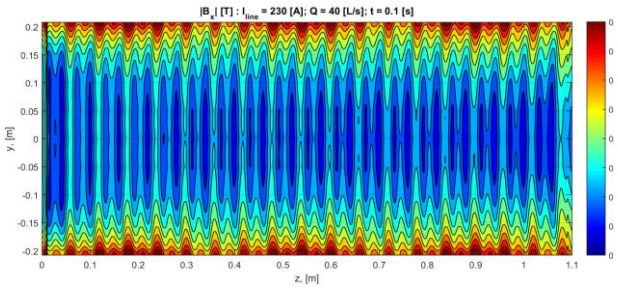

Fig. 140. $|B_x|$ *[T]:* $Rm_s = 3.5$, t *= 0.1s.*

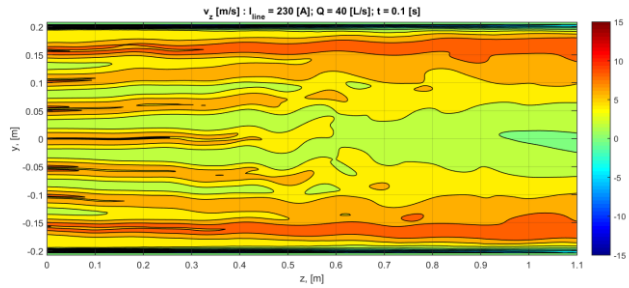

Fig. 141. v_z *[m/s]:* $Rm_s = 3.5$, t *= 0.1s.*

Next, effects of applied external DC magnetic field are analysed in the inlet and outlet zones. Since permanent magnets create velocity perturbation that is already observed in e.g. *Fig.* 141, velocity z component in zones of applied DC field is shown in *Fig.* 142:

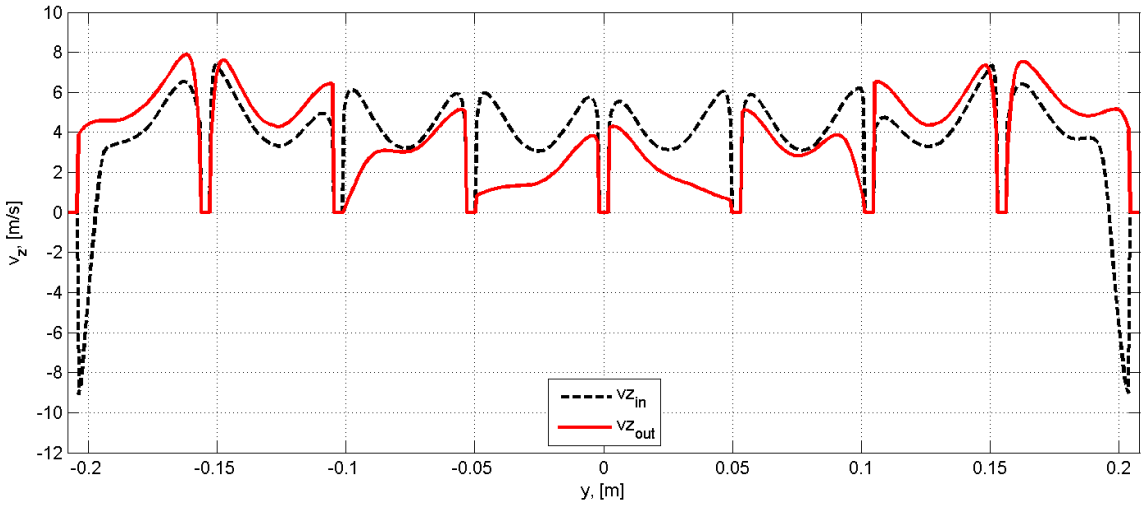

Fig. 142. Time averaged distribution of v_z [m/s]: $Rm_s = 3.82$.

The cross product of velocity z component and magnetic field x component generates electrical field y component, distribution of which is shown in Fig. 143.

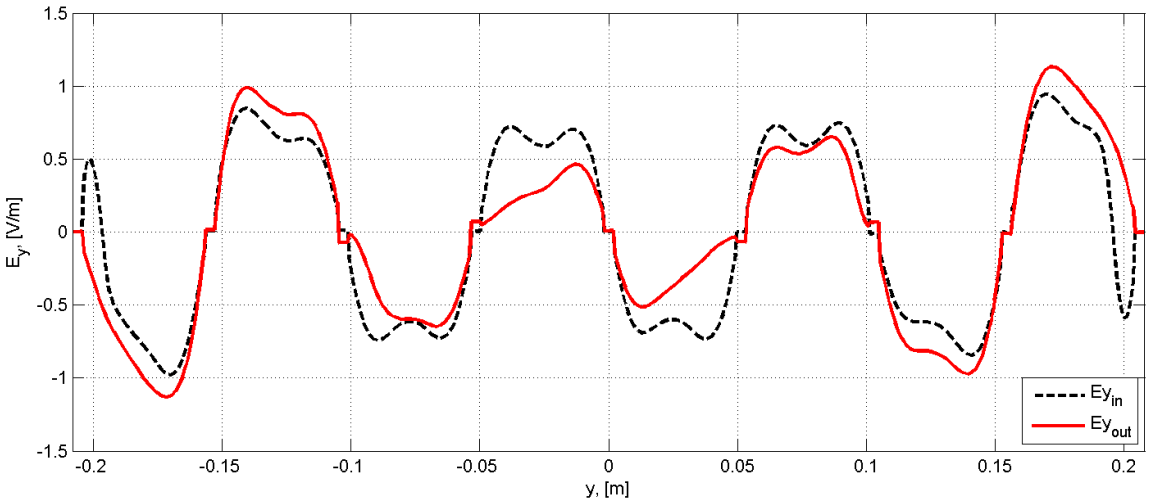

Fig. 143. Time averaged distribution of E_y [V/m]: $Rm_s = 3.82$.

Then electrical field was numerically integrated over the width from one wall to another, using MatLab software to obtain generated voltage difference between walls. Results of time averaged potential difference profiles are shown in Fig. 144 - *Fig.* 147, where error bars indicate amplitude of oscillations.

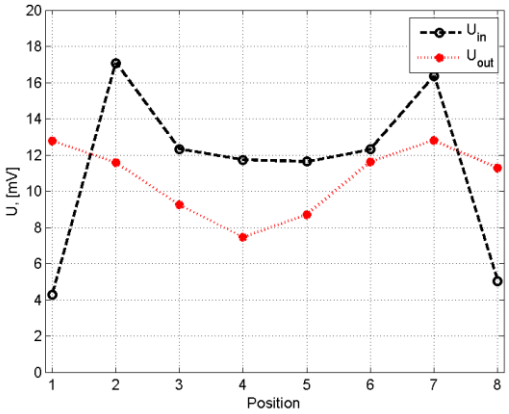

Fig. 144. Potential difference: $Rm_s = 4.47$.

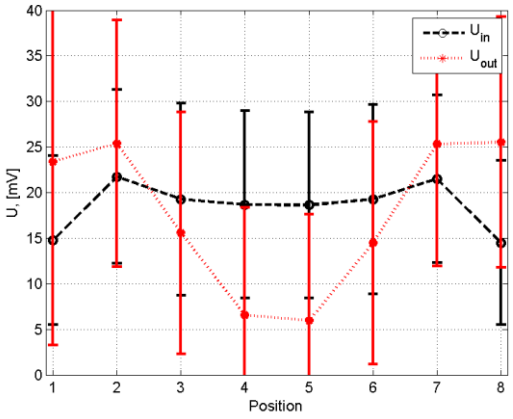

Fig. 145. Potential difference: $Rm_s = 4.15$.

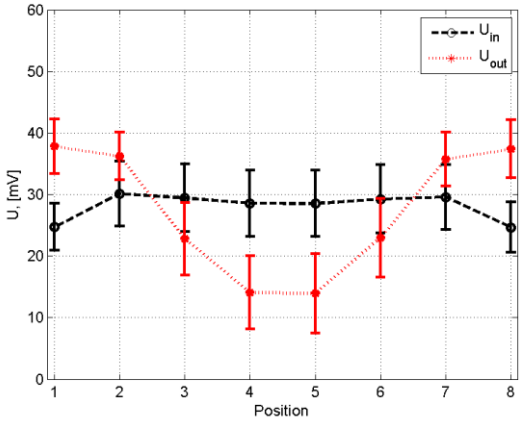

Fig. 146. Potential difference: $Rm_s = 3.82$.

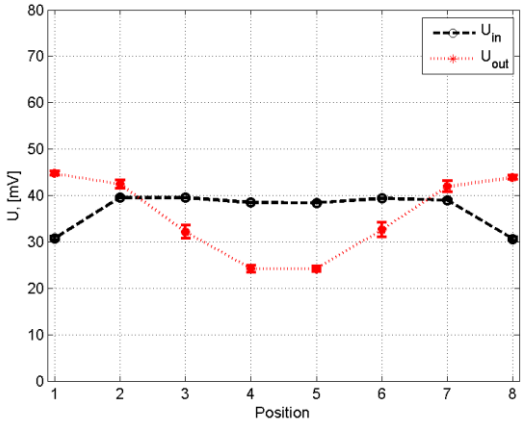

Fig. 147. Potential difference: $Rm_s = 3.5$.

For sake of simplicity amplitudes of oscillations are not shown in Fig. 144, since they are so high that figure won't be representative, situation is slightly better in Fig. 145. The overall trend is that profiles are more stable with decrease of Rm_s as well as average voltage increases with flowrate rather linearly (Fig. 146 and Fig. 147). Also the forms of profiles are rather similar from case to case and they do not change significantly, only are somewhat amplified with increase of flowrate. It can be observed that profile is more perturbed and unstable in the outlet, which is consistent with velocity distributions shown before.

Next, the developed pressure as function of flowrate is shown in *Fig.* 148. It can be observed that developed pressure decreases linearly as flowrate increases with rather good correlation. Such result could be explained by resistance of system that grows very rapidly, though it should increase quadratically. Therefore, one of the hypotheses here could be that resistance due to the systems of permanent, which should increase linearly with velocity (flowrate), dominates the process.

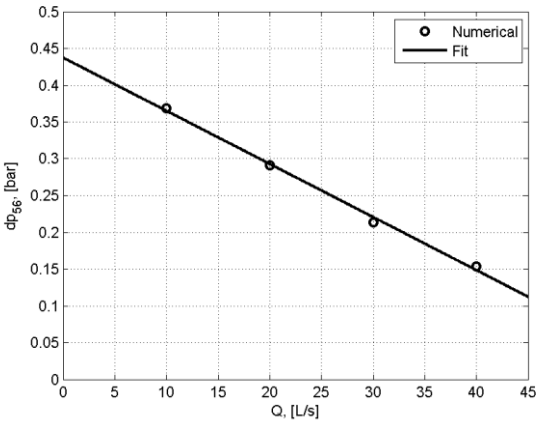

Fig. 148. Time averaged developed pressure as function of flowrate and fit with linear function.

Finally, samples of pulsations of developed pressure and their spectrums are shown in *Fig.* 149 - *Fig.* 156. Overall tendency can be observed that with higher Rm_s strong LF modes are the most dominant and with decrease o*f* Rm_s (increase of flowrate) they decrease and DSF pulsations become most dominant. Qualitatively, such behaviour of EMIP was expected from theory.

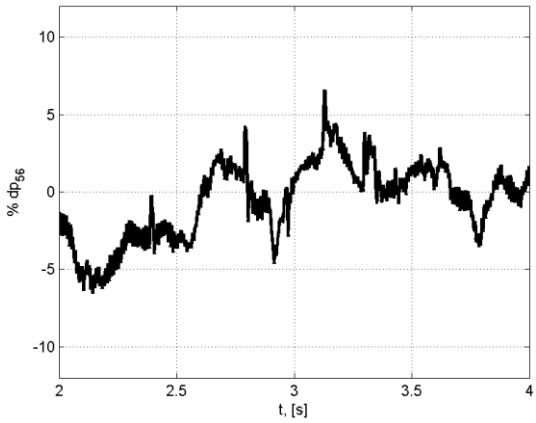

Fig. 149. Pulsations of developed pressure: $Rm_s = 4.47$.

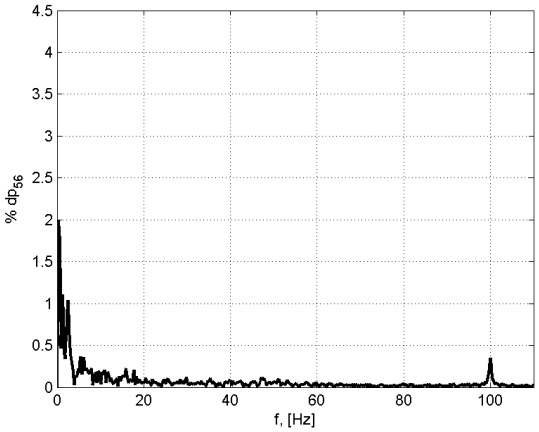

Fig. 150. Spectrum of pressure pulsations, $Rm_s = 4.47$.

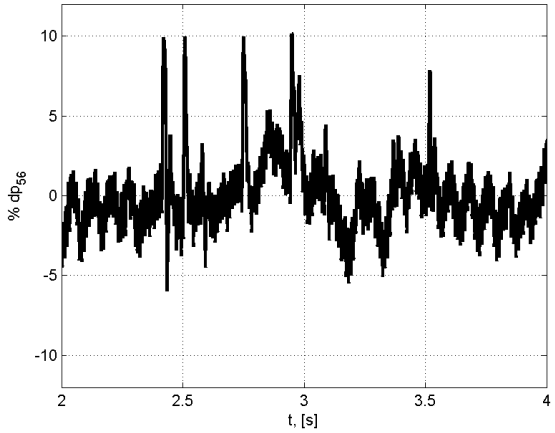

Fig. 151. Pulsations of developed pressure: $Rm_s = 4.15$.

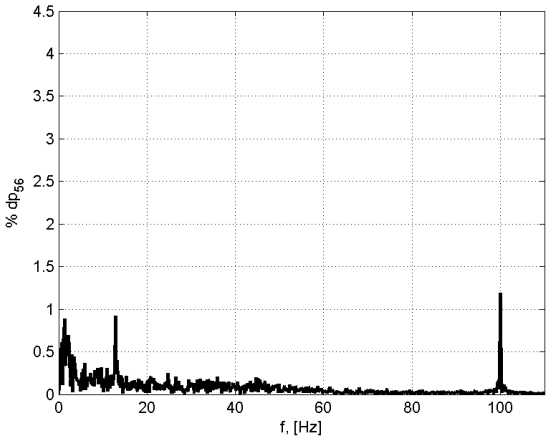

Fig. 152. Spectrum of pressure pulsations: $Rm_s = 4.15$.

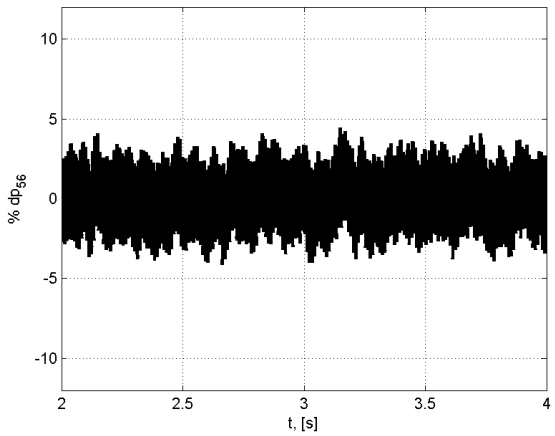

Fig. 153. Pulsations of developed pressure: $Rm_s = 3.82$.

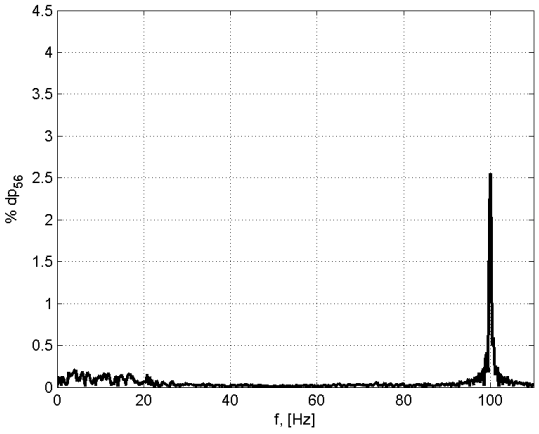

Fig. 154. Spectrum of pressure pulsations: $Rm_s = 3.82$.

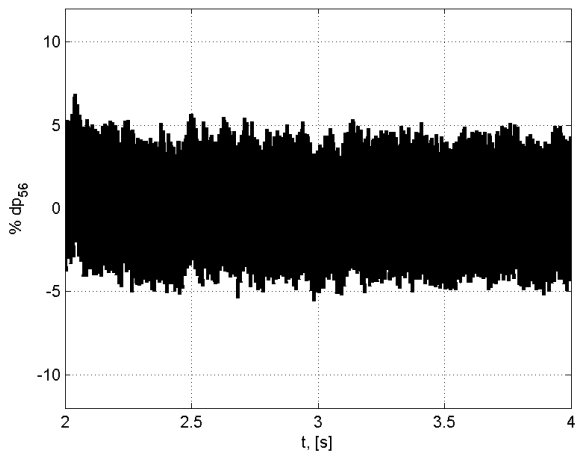

Fig. 155. Pulsations of developed pressure: $Rm_s = 3.5$.

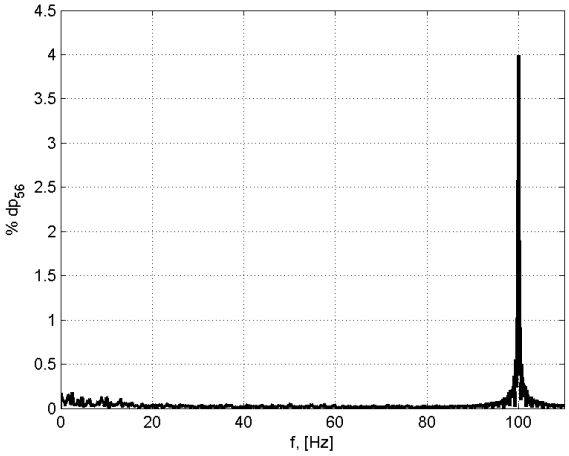

Fig. 156. Spectrum of pressure pulsations: $Rm_s = 3.5$.

3.3. Conclusions on numerical investigations

Importance and novelty of presented numerical investigations and results can be evaluated from following perspective. First of all, no similar numerical investigations concerning stability of ideal ALIP has been reported before and development of such model is first of a kind. The context of work, of course, should be considered as well, in frame of which comparison with new theoretical results was possible. Agreement between the two can be regarded at least as good or satisfactionary, since main tendencies of temporal development rate are captured and developed quasi – stationary force in all cases is represented quite well (Fig. 90 - Fig. 99). It can be also said that, by using this relatively small model capabilities of used numerical tools were tested.

However, reasons of difference between numerical and theoretical results must be eventually investigated more rigorously. This primary refers to numerical parameters – mesh size and time step, which might be in question in this analysis. Then selected 0.6s of only EM calculation might not be enough and longer periods are necessary to fully develop quasi-stationary state. Another reason that could introduce errors is method of development factor estimation which can be still improved. Finally, it should be noted, that theoretical and numerical models are not exactly the same as well from temporal point of view and degree of precision (all assumptions that are made in linear theory).

Secondly, the using derivation and fit of multi harmonic external magnetic field it was possible to create close to reality 2D models of FLIP which represents experimental setups discussed later. The peculiarities of building such 2D models are outlined, that by changing properties of material a set of necessary dimensionless numbers can be obtained.

Results showed that in case numerical model with 4 sub-channels, both magnetic field and axial velocity are stronger in the side channels and thin recirculation zone exists near outer wall (Fig. 118). With increase of the flowrate magnetic field and velocity grow more rapidly in the central channels an obviously are correlated (Fig. 119 , Fig. 120).

The second numerical model without sub-channels was created taking into account loop 3D geometry to calculate inlet boundary condition (Fig. 123). More detailed post-treatment methods were developed and used as well. Primary it is calculation of magnetic field modulus distribution and dynamics using data registration with ¼ period difference and calculation in MatLab. This allowed to clearly demonstrate influence of strong velocity perturbations of measurable field (Fig. 126 - *Fig.* 133). Then profile of potential difference between stainless steel walls in the inlet and outlet of FLIP is calculated using applied DC magnetic field and shown that significant perturbation in the outlet are expected in all studied cases (*Fig.* 144 - *Fig.* 147). Finally, analysis of the developed pressure and its pulsations showed qualitative agreement with theory and tendency of increase of LF pulsations with growth of Rm_s is shown (*Fig.* 149 - *Fig.* 156).

Still there is a necessity for development of more rigorous methods for quantitative analysis of magnetic field and velocity distributions, especially in unstable regimes.

4. EXPERIMENTAL INVESTIGATIONS

4.1. Experimental setup and equipment

All experimental activities with sodium were carried out in Institute of Physics University of Latvia (IPUL) in Salaspils in TESLA-EMP facility (Test and Experimental Sodium Loop for Analysis of ElectroMagnetic Pumps) Fig. 157 and Fig. 158. It may be divided into several parts:

1. Hydraulic liquid sodium loop
2. Electrical heating and control system
3. FLIP power supply control system
4. Gas and vacuum system
5. Measurement and data acquisition system

Hydraulic sodium loop with nominal pipe diameter DN125 is squared shaped with each side about 4m in length and is designed with possibility to operate two FLIPs in parallel or either series. Main characteristics of used FLIPs have been already shown in Fig. 100 and summarized in Table 5 and Table 6.

Electric heating system consisted of Nickel-Chromium heaters which was controlled trough “CELDUC” SO465320 phase angle controllers and “Red Lion” T16 temperature PID controllers. More than 50 1.5mm K-type thermocouples in stainless steel coating were distributed all over the loop for measurement and control purposes.

Power supply of FLIP-1 was realized using 100 kW mechanical generator and voltage controlled with electronic rheostat by changing excitation current. When FLIP-2 was added, it was supplied through power transformer. Both pumps operated with 50Hz frequency. Voltage between phases was measured using ERA EI 48/16.8 lowering transformers and line current using (E)ASK 51.4 250/5A current transformers. Windings of pumps were connected in delta (Δ) Fig. 159.

Sodium pressure was measured with piezo-electric Keller 35XHTC manometers. Developed pressure of FLIP-1 was measured in the outlet and inlet of pump (P1 and P2), but pressure of FLIP-2 with (P5 and P6). Flowrate of the loop is in clockwise direction, electrically or mechanically regulated by valve (V1) and measured by in-house made Venturi tube using manometers (P3 and P4). The side divided into two branches can be controlled by valves (2 and 3) either electrically or mechanically. During experiment valve (V3) was always in a closed position. Loop was filled from two supply tanks and pressure was monitored with electronic manometers (P10 and P11). Magnetic field measurements were carried out by specially developed samplers discussed later.

The data acquisition system consisted mainly of equipment from National Instruments: NI cDAQ – 9188, NI 9213 for temperature measurements, NI 9205 for all other measurements.

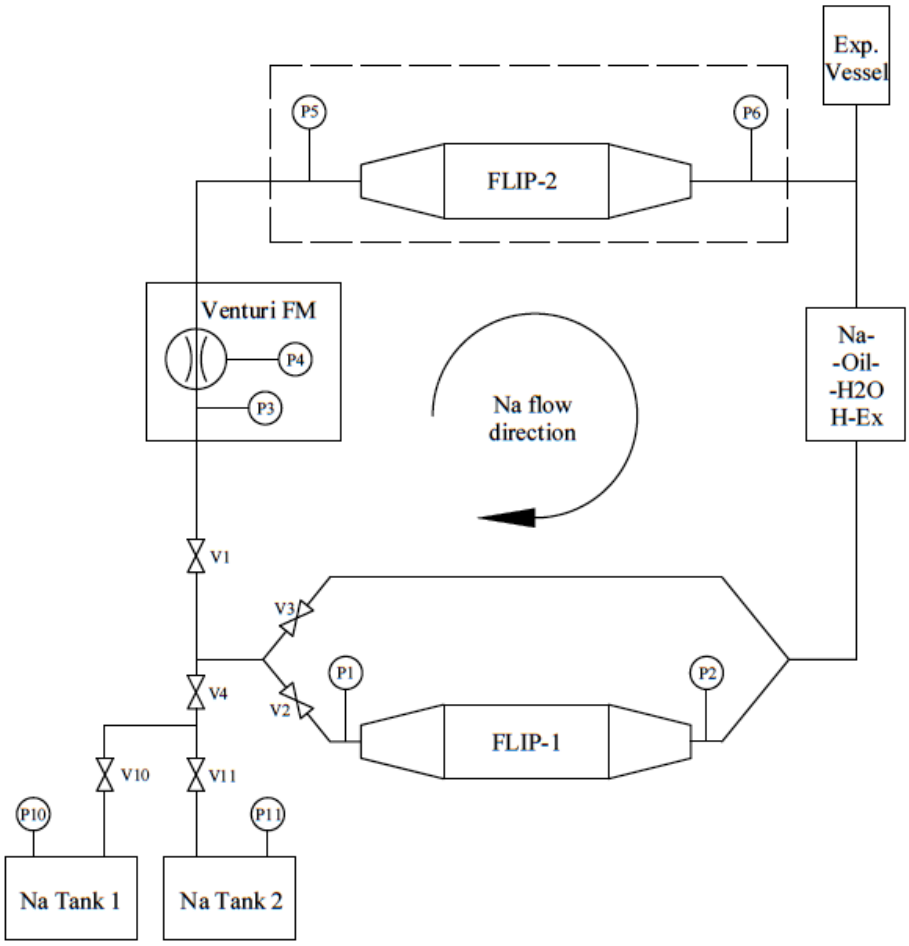

Fig. 157. Scheme of TESLA-EMP facility.

Fig. 158.Photo of TESLA-EMP facility.

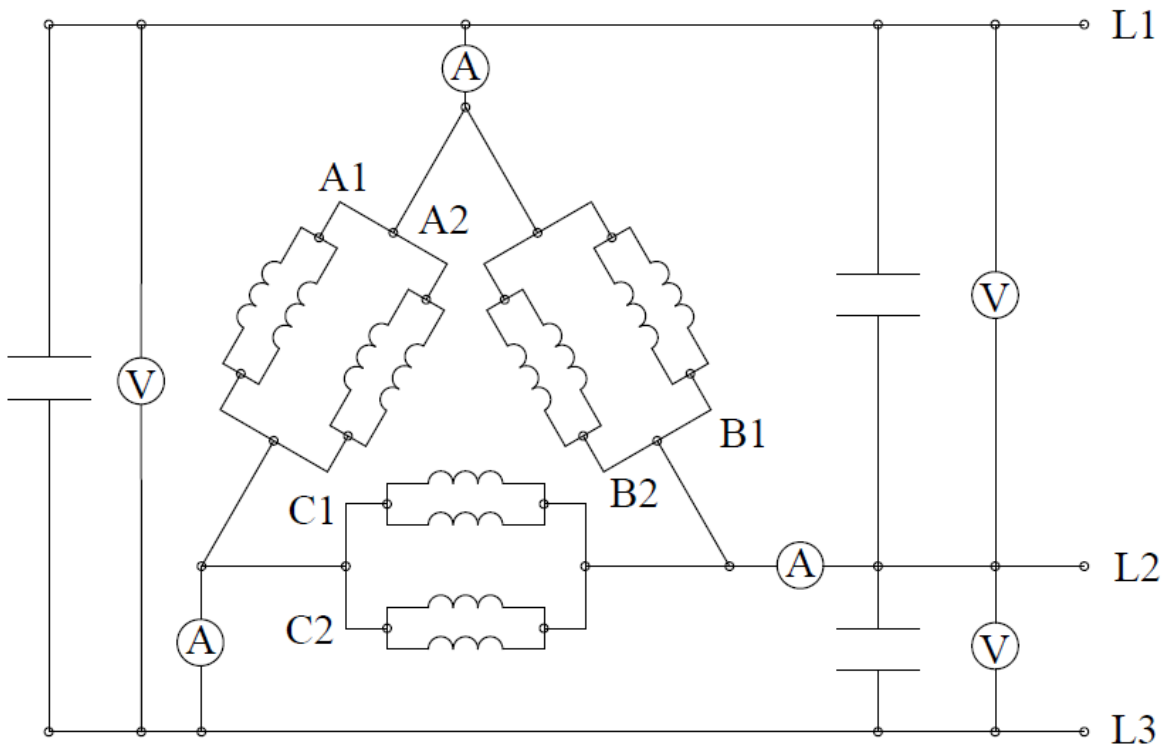

Fig. 159. Scheme of FLIP electrical connection, current and voltage measurements.

The voltage and current was measured and controlled in each phase and overall electrical connection of the loop is shown in Fig. 159. Phases of EMIPs were connected in delta (Δ) and each of inductors had 2 parallel branches per phase.

Measurements during operation were recorded using PC with LabView software interface. Input current of EMIP was controlled through digital interface, but flowrate was set by operators using electro/mechanical control. Temperature, pressure, flowrate, magnetic field and supply line current and voltage were measured.

All these measurements can be divided into two groups depending on measurement frequency:

- Fast – 1 or 2 kHz: magnetic field, current, voltage, pressure
- Slow - 75 Hz: temperature, flowrate, potential difference

Afterwards all necessary times scales for analysis are obtained by post-processing signals either in LabView directly or using external tools (particular MatLab).

Precision of measurements is considered from information of instrumentation datasheets:

- Current measurement: 1% of full scale (FS 1%) 250A. Error: ±2.5A
- Voltage: FS 2% 230V. Error: ±4.6V
- Pressure measurement: FS 0.5% 10 bar. Error: ±0.05 bar
- Flowrate: $= k\sqrt{\Delta p_{3,4}} \quad \rightarrow \quad \delta Q = \frac{k}{2}\frac{\delta p}{\sqrt{\Delta p_{3,4}}} \approx \pm 5\ [l/s]$
- Magnetic field: ±2-3% of measurement (see results in the next chapter)

4.1.1. Magnetic field measurements using EPCOS B82451N coil

For measurements of magnetic field in-house samplers were made using commercial EPCOS B82451N transponder coils with ferrite core Fig. 160.

These coils were chosen due to following important advantages:

- Small size
- High signal-to-noise ratio
- Standardized product with low price

However, problem using ferrite core coils is saturation of core material for relatively high fields. This effect deforms the shape of the signal and leads to nonlinear relationship between effective EMF and applied field.

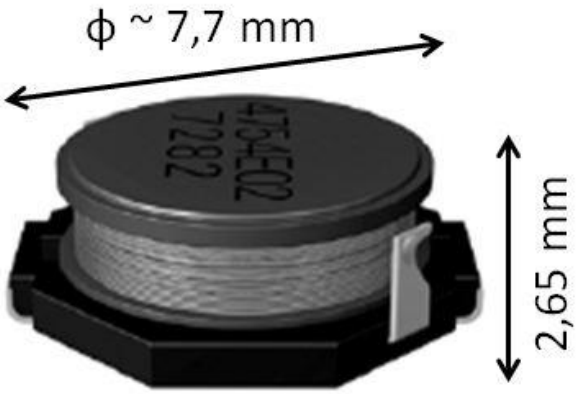

Fig. 160. EPCOS B882451N ferrite core coil.

Moreover, core material is sensitive to temperature which leads to additional non-linearity. These drawbacks are, of course, quite important and surely must be taken into account. To study impact of these effects precisely several experimental setups were created in Faculty of Physics and mathematics of University of Latvia

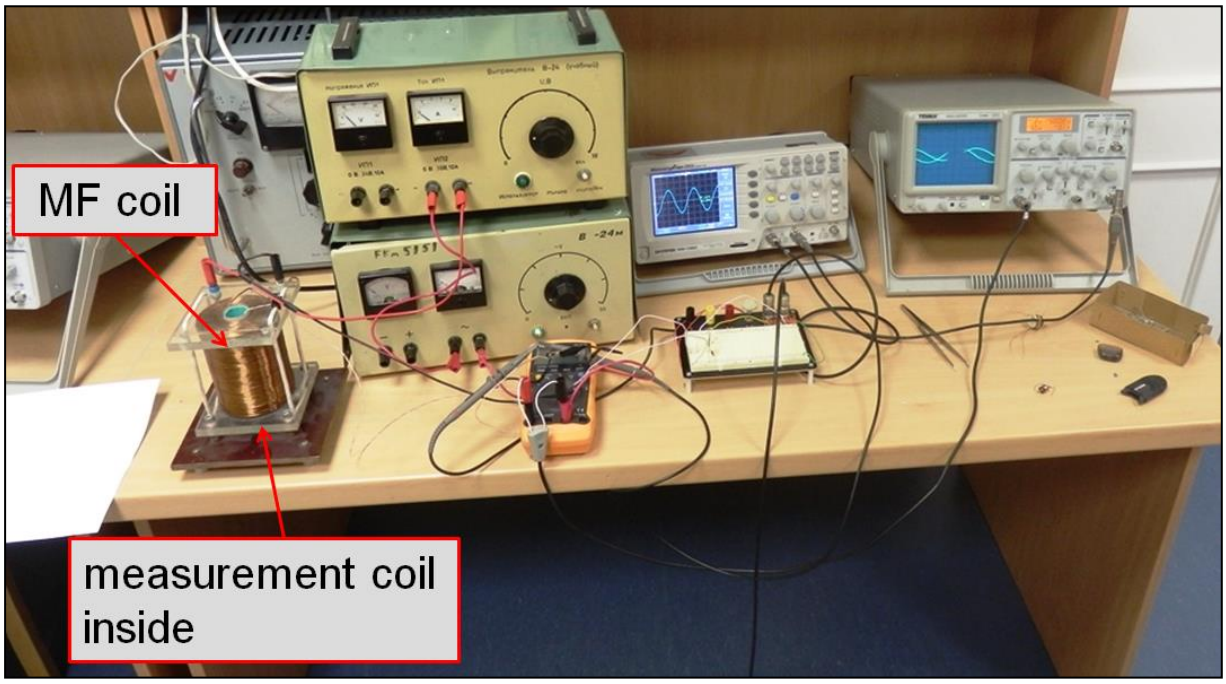

Fig. 161. Setup for signal analysis of measurement coil.

First of all, signal of measurement coils was analysed by putting it inside a known AC magnetic field (larger coil) operating with 50 Hz (Fig. 161). It was observed that the shape of the signal was deformed with increase of amplitude of magnetic field Fig. 162 - Fig. 165.

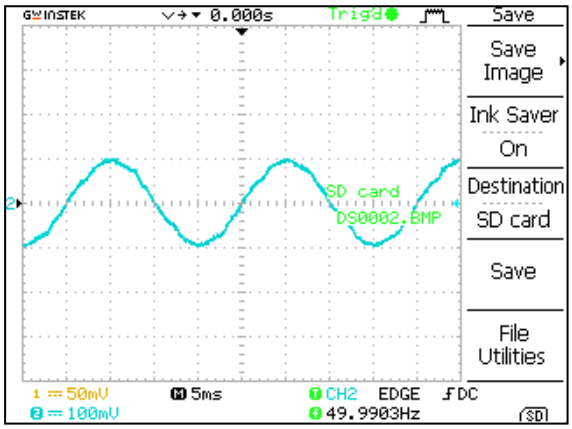

Fig. 162. Signal of measuring coil, B ≈ 0.01T

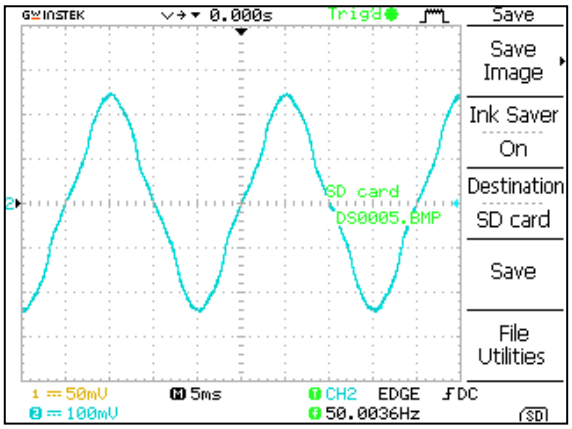

Fig. 164. Signal of measuring coil, B ≈ 0.03T

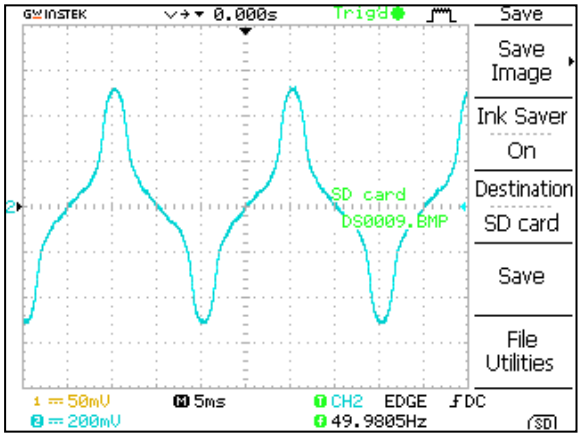

Fig. 163. Signal of measuring coil, B ≈ 0.06T.

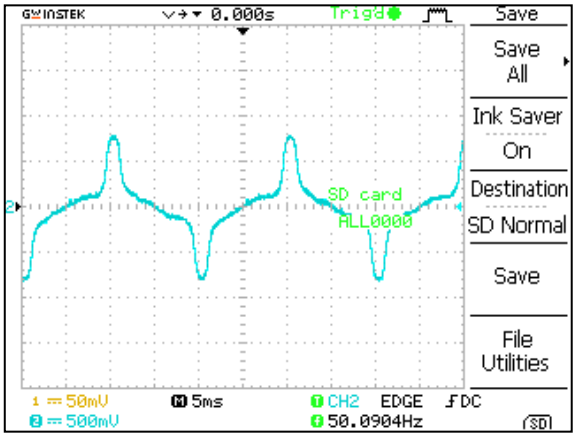

Fig. 165. Signal of measuring coil, B ≈ 0.12T.

However, attention was paid to the fact that applied field and EMF signal in measurement coil is 90° shifted. Obviously, this is result of Faradays law and peak in measured signal is obtained at the time instant when external magnetic field is actually 0 (Fig. 166). Therefore in this time instant core material cannot be saturated and value of peak must be linearly proportional to applied magnetic field.

This is indeed observed in measurements Fig. 167 where voltage effective value of RMS and peak-to-peak signals are compared.

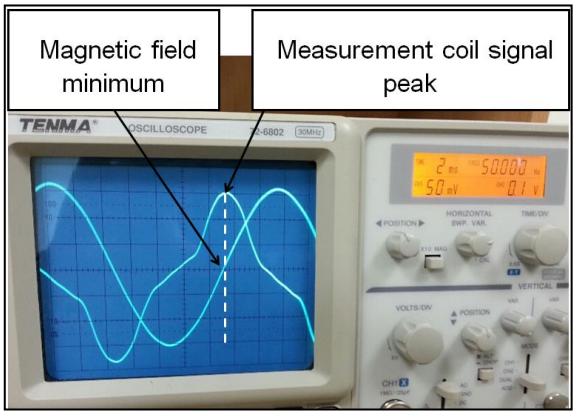

Fig. 166. Relationship between AC magnetic field and signal in coil.

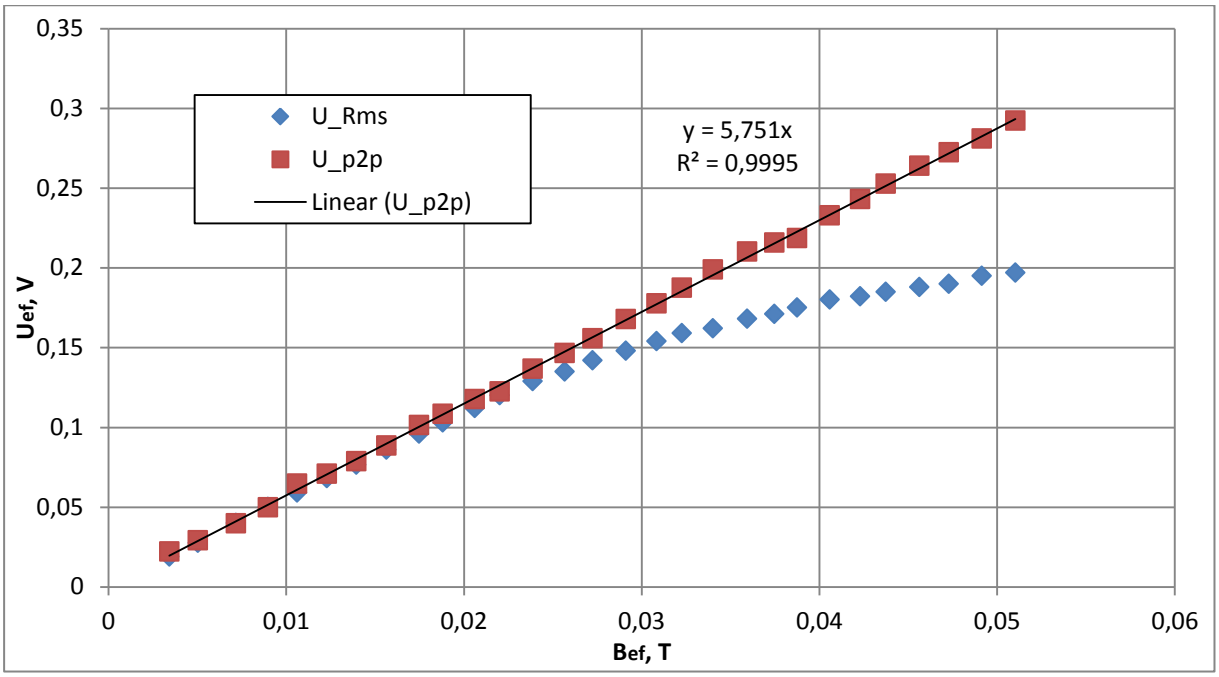

Fig. 167. Effective value of voltage as function of magnetic field. Comparison of RMS and peak-to-peak signals.

It can be said that the problem of magnetic field measurement with ferrite core coil is actually problem of finding peak values of the signal. This means that in experiment sufficiently high discretization frequency is required to describe each period in details.

In studied case relationship between peak voltage and magnetic field amplitude is:

$$B_{amp} = U_{peak}/5.751 \tag{173}$$

The next question was about influence of temperature on the measurement. To study this, first of all, the temperature of core material has to be known. This can be found quite simply for a single coil using thermocouple in well-defined lab environment, however, it might be rather complicated if inhomogeneous distribution of temperature is present and large number of measurements necessary.

Another way of finding core material temperature is measuring resistance of coil wire. Since it is closely winded around the ferrite core their temperature should be practically identical. Therefore relationship T(R) of the copper wire must be found in the first place. For this purpose following graduation setup was created (Fig. 168, Fig. 169) consisting of:

1. Digital ohm meter
2. Test coil
3. Electric heater
4. Ceramic try with water
5. Reference thermocouple

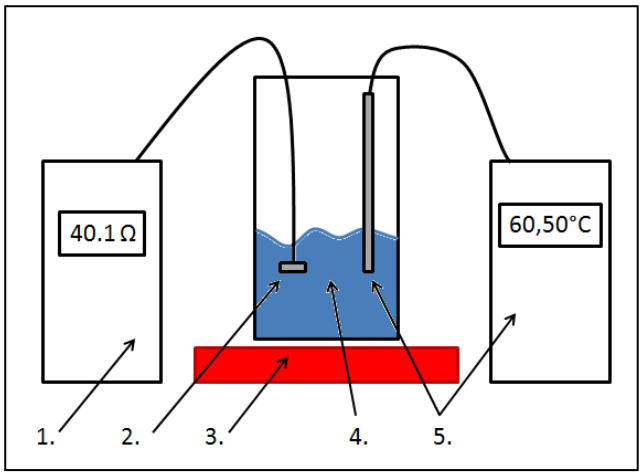

Fig. 168. Scheme of graduation setup.

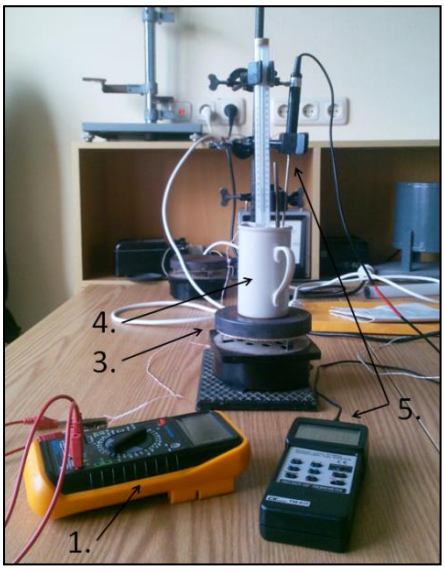

Fig. 169. Realization of graduation setup.

The water was slowly heated and cooled while registering its temperature and resistance of immersed coil. Results are shown in Fig. 170. From obtained experimental curves following relationship for temperature (in ºC) as function of resistance is found:

$$T = (R - 33.75)/0.141 \tag{174}$$

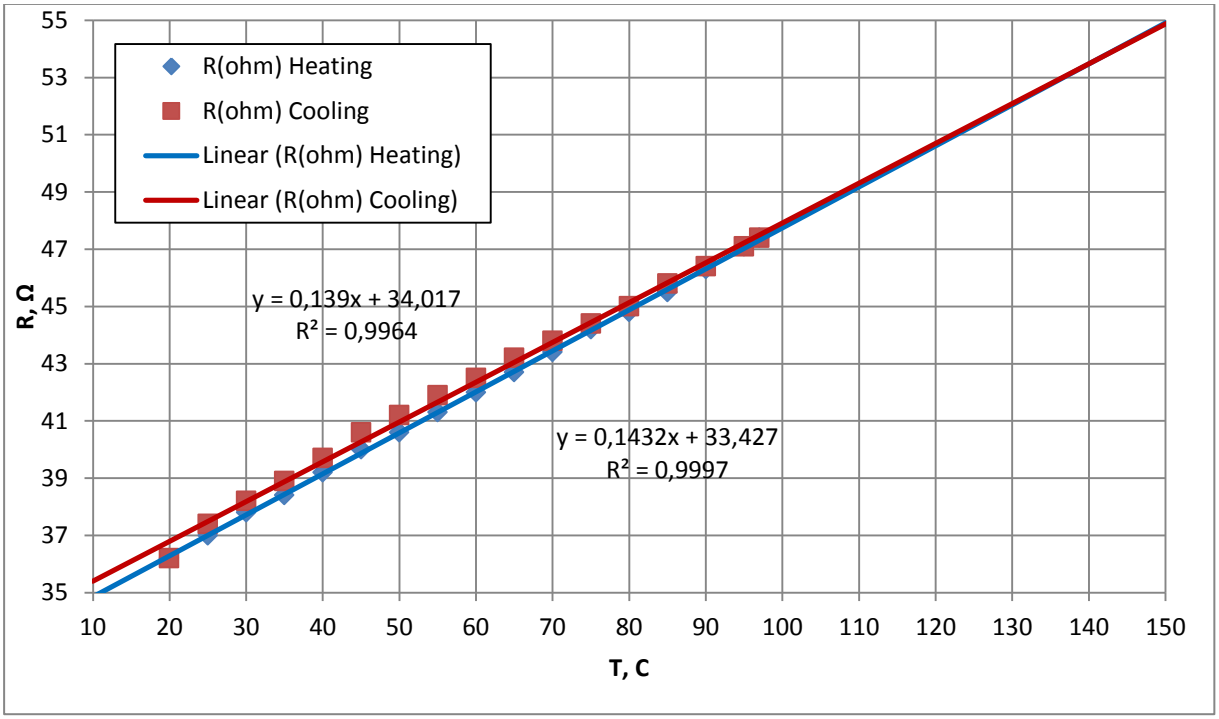

Fig. 170. Results of coils' thermal resistivity graduation.

Then following setup for analysis of temperature influence on signal was created:

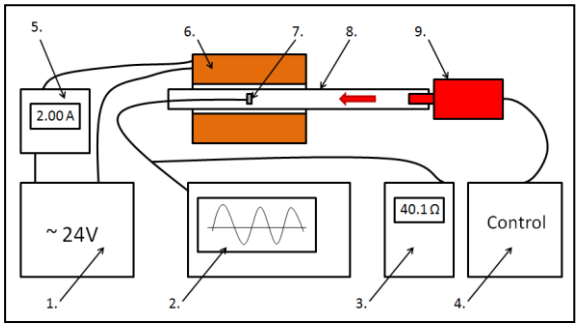

Fig. 171. Scheme of signal analysis setup.

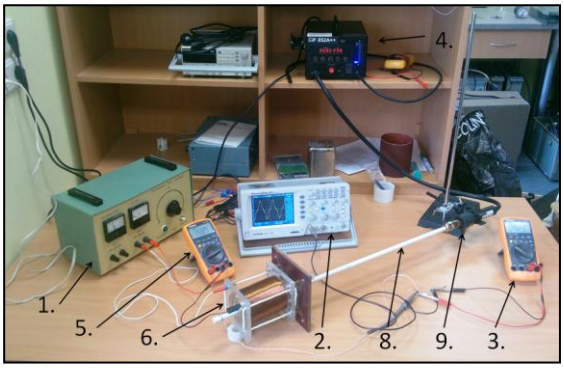

Fig. 172. Realization of signal analysis setup.

It consisted of (Fig. 171, Fig. 172):

1. Power supply (set to 2A RMS)
2. Digital oscilloscope
3. Digital ohm meter
4. Control unit of hot air gun (150°C reached on measurement coil)
5. Ampere meter
6. External field generating coil
7. Measurement coil
8. Ceramic tube
9. Hot air gun

In this case using resistance measurement of the coil winding it was possible to determine core material temperature. The shape of signal obtained by oscilloscope as function of temperature is shown in Fig. 173.

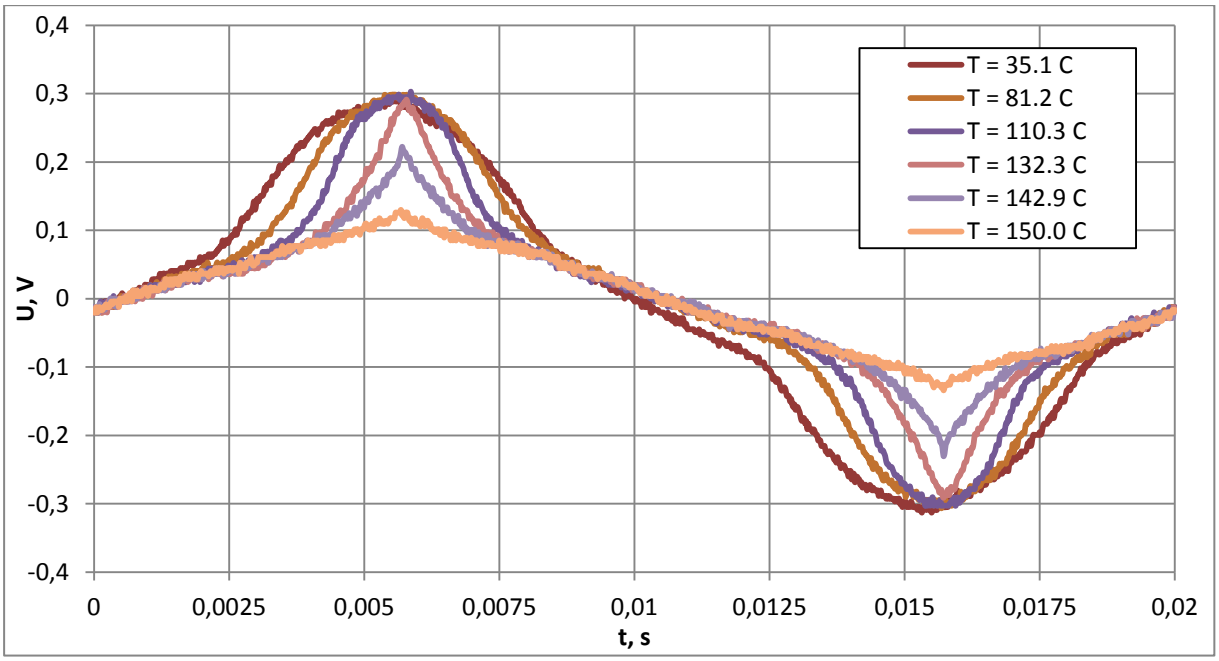

Fig. 173. Transient signal from measurement coil with different temperature normalized to 2 A current.

In Fig. 173 it can be seen that for temperature up to 130°C there is no significant changes in peak to peak measurements, but the peak of the extreme becomes narrower.

Negative effect of such narrowing is requirement of higher discretization frequency. However, above this threshold temperature core material loses its magnetic properties and peak value decreases – previously obtained relationship is not valid anymore. Therefore temperature of measurement coils should be controlled not to exceed 130 °C to sustain linearity of peak to peak measurement.

Finally, active resistances of multiple coils were measured in room temperature and deviation from mean value was calculated. It was found that active resistance deviates on average 0.8% and maximum 1.7%. in Table 13.

In the end, some conclusion about successful AC magnetic field measurements using ferrite core coils can be done:

- Peak measurements should be performed (they are linear to applied field)
- Peaks become narrower with increase of magnetic field an temperature
- High discretization frequency is required to find peak values in each period
- Temperature of coils should not exceed 130 °C
- Coil temperature can be monitored by measuring wire resistance

Being aware of and taking into account mentioned conditions, special magnetic field samplers were developed and implemented in experimental setup.

Nr. coil	R, Ω	dR%	L, mH	dL%
1	36.7	1.7%	4.826	0.7%
2	35.59	1.4%	4.801	0.2%
3	36.03	0.2%	4.761	0.6%
4	36.37	0.7%	4.831	0.9%
5	35.76	0.9%	4.824	0.7%
6	36.03	0.2%	4.725	1.4%
7	36.48	1.1%	4.79	0.0%
8	36	0.3%	4.725	1.4%
9	36.31	0.6%	4.827	0.8%
10	36.53	1.2%	4.815	0.5%
11	35.72	1.1%	4.789	0.0%
12	36.34	0.7%	4.784	0.1%
13	35.55	1.5%	4.809	0.4%
14	35.56	1.5%	4.789	0.0%
15	35.9	0.6%	4.745	0.9%
16	35.94	0.4%	4.792	0.0%
17	35.99	0.3%	4.753	0.8%
18	36.31	0.6%	4.864	1.5%
19	36.05	0.1%	4.883	1.9%
20	35.89	0.6%	4.787	0.1%
21	36.36	0.7%	4.784	0.1%
22	36.34	0.7%	4.805	0.3%
23	36.47	1.0%	4.771	0.4%
24	35.93	0.5%	4.777	0.3%
25	35.77	0.9%	4.794	0.1%
26	36.38	0.8%	4.795	0.1%
27	35.86	0.7%	4.727	1.3%
28	36.39	0.8%	4.722	1.4%
29	35.84	0.7%	4.823	0.7%
30	36.59	1.4%	4.788	0.0%
AVG	36.10	0.8%	4.790	0.6%
MAX		1.7%		1.9%

Table 13. Measurements of the active resistance and inductance of EPCOS B82451N coils.

4.2. Experimental setup with 4 sub-channels

In the first experimental session capabilities of instrumentation and the measurement system was tested, having a single technological FLIP-1 in the loop. The channel and the inductor zone of the FLIP is shown in the Fig. 174. Similarly as in presented numerical model, the channel is divided into 4 sub-channels. 8 magnetic field samplers were used in the experiment having 3 point measurement – 1 and 2 in the centre of each sub-channel and 3 outside the inductor. In each point there were two ferrite core coils in the differential connection to amplify the signal and suppress any disturbances. Realization of the sampler is shown in Fig. 175.

It was possible to manually insert and remove samplers during experiment in 3 different positions (Pos = 1…3) provided by guide in Fig. 174. Positions represent location of the sampler with respect to tooth and slot:

- Pos = 1 – in front of the tooth
- Pos = 2 – between tooth and slot
- Pos = 3 – in front of slot.

During the experiment it was found that most reasonable position is Pos = 1, since perpendicular component of field is stronger and less sensitive to errors of placement compared to other positions. For these reasons presented magnetic field measurements are in Pos = 1 except sampler U2-… which was only possible to place in Pos = 2 due to some mechanical issue.

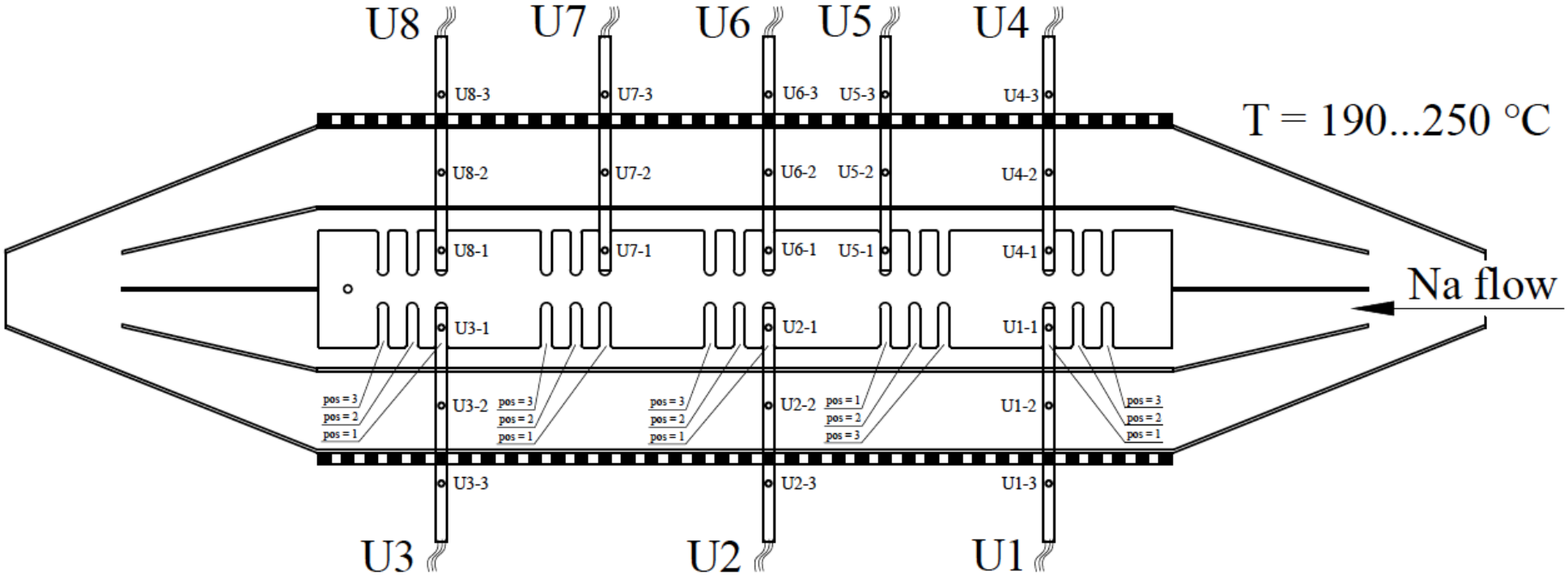

Fig. 174. A scheme of measurements in experimental setup

Fig. 175. Magnetic field sampler used in experiment.

4.2.1. Measurements of magnetic field without liquid metal

Before experimental session with liquid metal, measurements of the magnetic field with empty channel were performed in order to test samplers and be able to determine and exclude effects which are not connected with MHD nature processes in the channel. Measurement frequency was 1kHz.

First of all, raw signal of individual sampler (U8) is analysed and also spectrum of U8-1 coil signal is calculated (Fig. 176 - Fig. 183). Here voltage is normalized to the mean current of all phases. One can see that coils (U8-1 and U8-2) that are in the gap between inductor and channel give significantly higher signal than coils which are outside (U8-3). Also signal is almost identical in (U8-1 and U8-2) therefore; external magnetic field at least up to centre of each sub-channel is rather homogeneous over the width.

Secondly, the shape of signal is not simply sinusoidal due to saturation of the core; it is peak-to-peak value which is linearly proportional to applied current (magnetic field). By increasing current higher harmonics become more and more important (Fig. 177, Fig. 179, Fig. 182, Fig. 183) and must be discretized sufficiently.

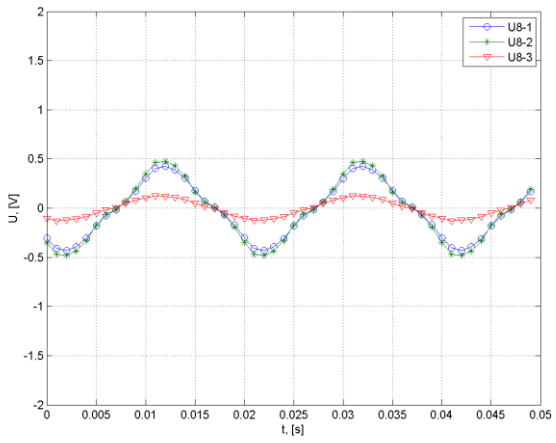

Fig. 176. Signal with sampler U8, I = 50 [A].

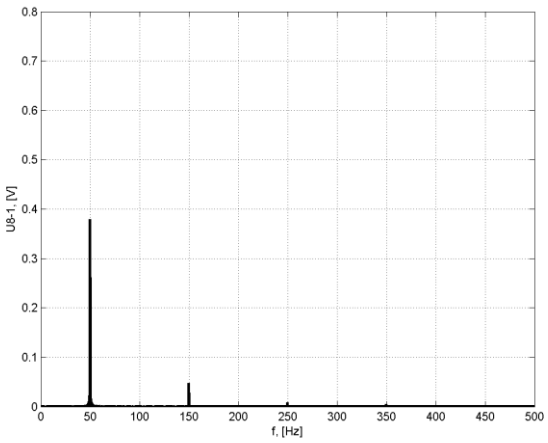

Fig. 177. Spectrum of signal U8-1, I = 50 [A]

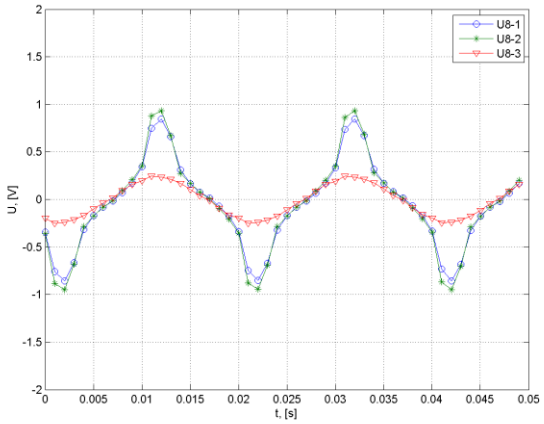

Fig. 178. Signal with sampler U8, I = 100 [A].

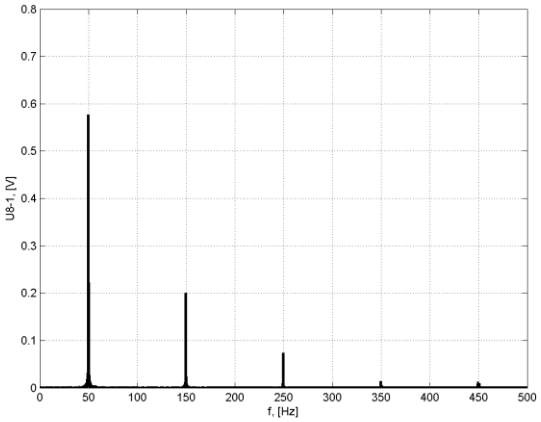

Fig. 179. Spectrum of signal U8-1, I = 100 [A].

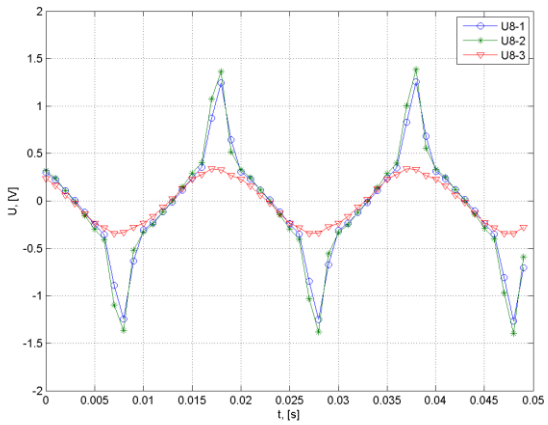

Fig. 180. Signal with sampler U8, I = 150 [A].

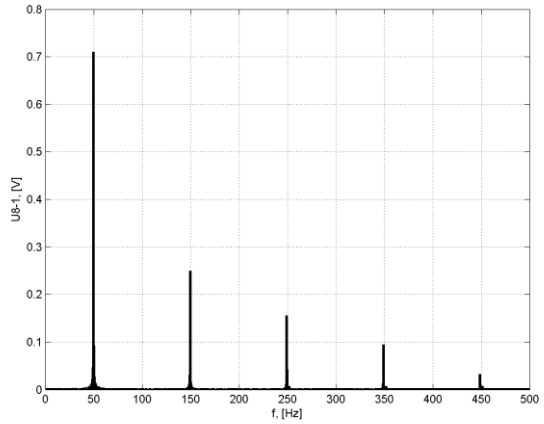

Fig. 181. Spectrum of signal U8-1, I = 150 [A].

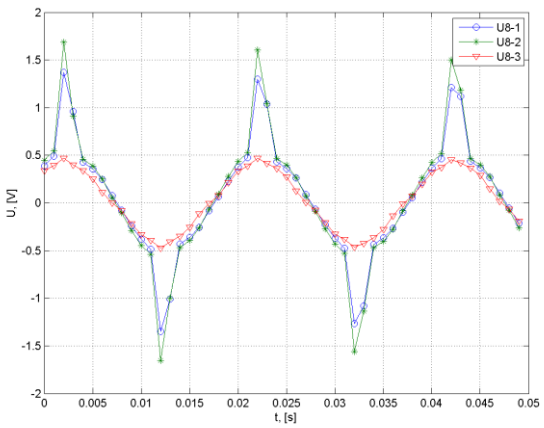

Fig. 182. Signal with sampler U8, I = 200 [A].

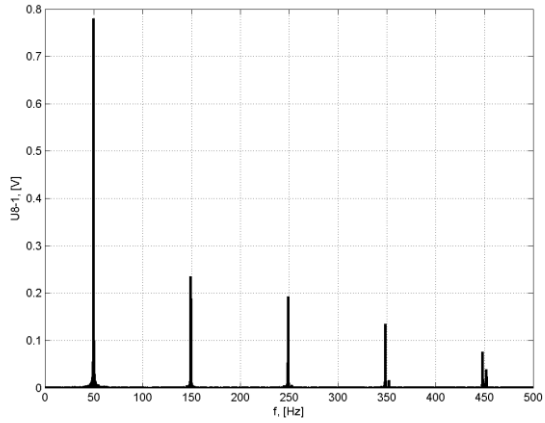

Fig. 183. Spectrum of signal U8-1, I = 200 [A].

It can be observed in Fig. 184 that for high strength of signal used discretization of single period is not enough and pulsating component appears in a longer record. This aliasing of peak-to-peak value is due to the ferrite core and leads to the problem of discretization.

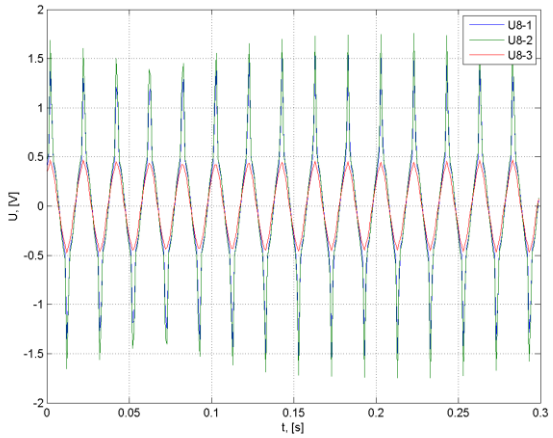

Fig. 184. Signal with sampler U8 over several periods, I = 200 [A].

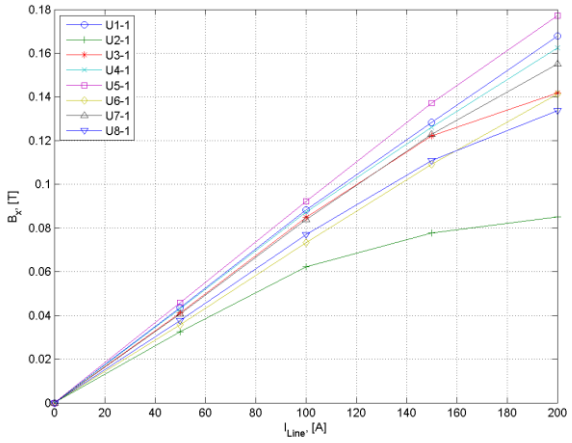

Fig. 185. $|B_x|$ as function of I_{line} for all samplers 1st coil.

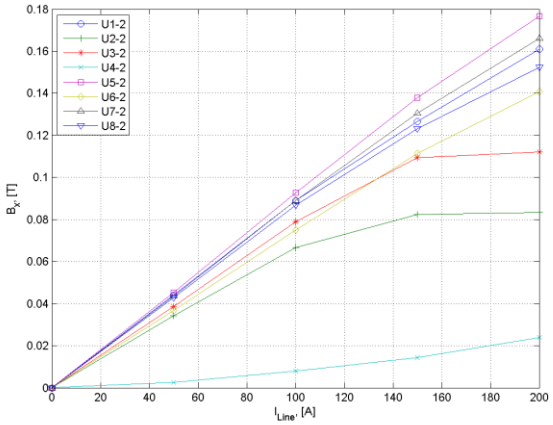

Fig. 186. $|B_x|$ as function of I_{line} for all samplers 2nd coil.

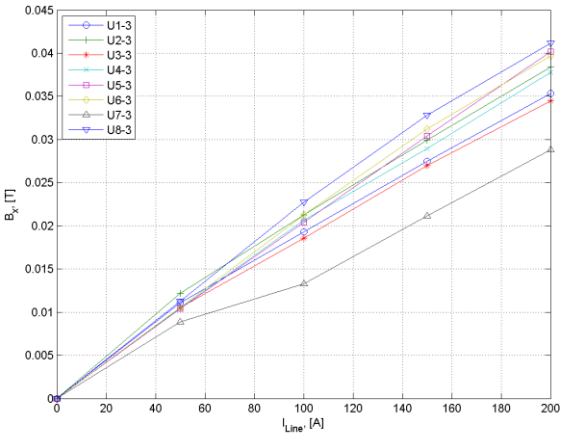

Fig. 187. $|B_x|$ as function of I_{line} for all samplers 3rd coil.

Finally, measured voltage in each point is post-processed and modulus of magnetic field as function of current is shown in Fig. 185 - Fig. 187. Except wiring issues with point U4-2 in Fig. 186 other measurements show acceptable linearity as function of current, which should be expected.

A non-linear behaviour of sampler U3 could be also explained by the imperfection of positioning system, which was manual. If the position of first coil was relatively precise with small angular deviation (U3-1 is inside the guide, Fig. 185), then it leads to larger position and therefore measurement error for the second coil (U3-2, Fig. 186).

4.2.2. Measurements with liquid Na: p-Q characteristics

Developed pressure of FLIP and flowrate in the loop is shown in Fig. 188. Maximal developed pressure reached was 1.8 bars and flowrate up to 45 l/s. The pressure loss of the whole loop is described by quadratic law (since it is turbulent flow) (Fig. 188, ---dp_{res}). Estimated relationship in this case is:

$$dp_{res} = 78 \cdot 10^{-5} Q^2 \ [bar]$$

In Table 14. and Table 15. set of dimensionless numbers with different values of line current and flowrate are summarized. Overall, there are two general issues with the discussed setup, which become obvious by analysing tables below.

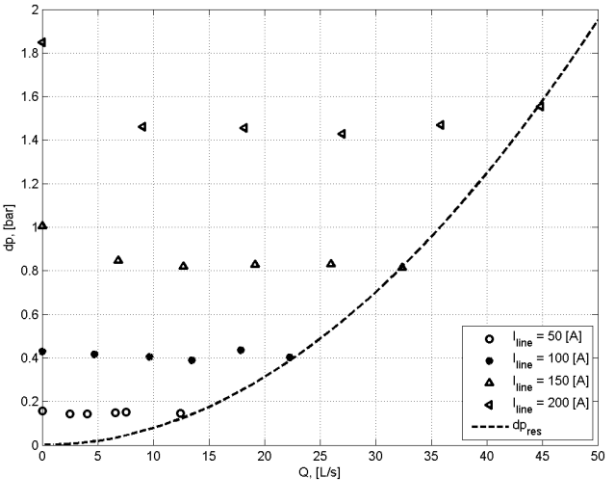

Fig. 188. p-Q characteristics for different currents

N_λ	Re_λ	N
4	94	0,04
16	-	0,17
35	-	0,38
63	-	0,67

Table 14. Estimation of interaction parameter of function of line current.

Q, [L/s]	0	5	10	15	20	25	30	35	40	45
Re, x10^4	-	4.7	9.4	14.1	18.8	23.4	28.1	32.8	37.5	42.2
Rm_s	4,80	4,63	4,47	4,31	4,15	3,98	3,82	3,66	3,50	3,33

Table 15. Estimation of Reynolds and magnetic Reynolds number as function of flowrates.

First of all, FLIP-1 is operating in the regime of high Rm_s only and even with maximum flowrate it is well above unity. Secondly, interaction parameter N in all cases is smaller than 1. Both of these results are linked with capabilities of power supply, which was limited to only 50 Hz and could not reach currents much higher than 200A.

On the one hand, to decrease Rm_s it is necessary to increase flowrate, which in this case can be done only by increasing developed pressure head of FLIP. This means increasing applied current or increasing N. This, of course, leads to injecting much more power in the system. One the other hand, it is possible to decrease Rm_s by decreasing frequency or velocity of magnetic field v_B. Also since v_B is in the denominator of N it will increase aswell. Therefore, the most optimal way to operate pump in low Rm_s and high N regime, is to decrease frequency.

However, the power supply had its limitations with which one should cope and make best use of it.

Also note that in all experimental activities the sodium flow is fully turbulent with characteristic Reynolds number ~ 10^5.

4.2.3. Measurements with liquid Na: analysis of pressure pulsations

Using piezo-electronic manometers it was possible to record pressure with high frequency. It allows analysing not only mean for very slowly changing pressure, but also have information about pressure pulsations up to 100 Hz which is the limit of stainless steel membrane in this sensor design. As discussed and shown before, by analysing the spectrum of pressure pulsations in some extent it is possible to determine whether FLIP is working in regime which can be regarded as stable or unstable.

Results only for case with the highest interaction parameter $N = 0.67$ is shown, since in cases of $N = 0.04,\ 0.17$ pulsations were minor and in case $N = 0.38$ tendencies are quite similar. This suggests, that N should be indeed comparatively high to experimentally observe

such unstable phenomenon. In other words, EM forces are not sufficiently high to dominate the process. 10s long signal of pressure pulsations were analysed.

Obtained results are shown in Fig. 189 - Fig. 200. Overall the tendency can be summarized as following – with increase of flowrate, amplitudes and band of pulsations increase. However, amplitudes of pulsations are relatively small and practically always fall in the range of measurement error, which in this case is around ±3.3 %. Since the monometer was limited to 100 Hz frequency, DSF pressure pulsations might not be represented correctly in this case, since operation is practically at the limit.

Interestingly, that for the highest flowrates in spectrums of pressure pulsations Fig. 198 and Fig. 200 certain low frequency modes become dominant around 12 and 24 Hz (therefore multiple) and tend to increase with the flowrate. Even though estimated amplitudes of pulsations are small and might subject of discussion, the appearance of these distinct frequencies cannot be result of measurement error and must be physical.

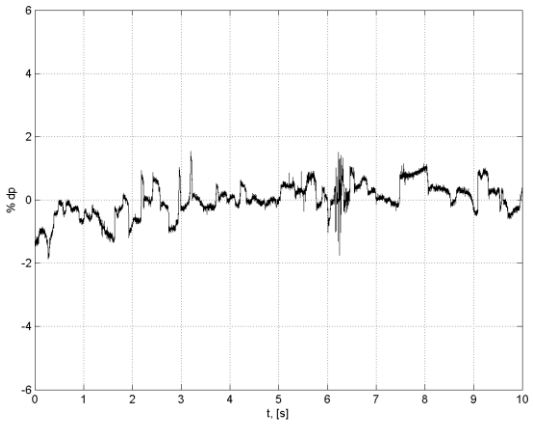

Fig. 189. Pulsations of developed pressure difference: $N = 0.67$, $Rm_s = 4.8$.

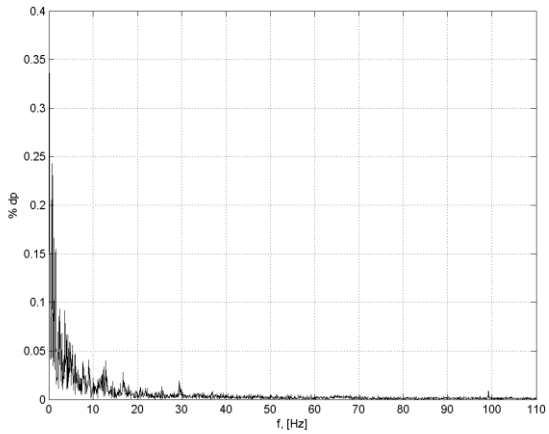

Fig. 190. Spectrum of pressure pulsations: $N = 0.67$, $Rm_s = 4.8$

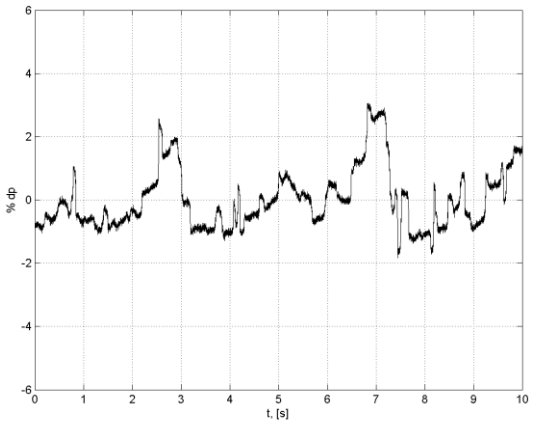

Fig. 191. Pulsations of developed pressure difference: $N = 0.67$, $Rm_s = 4.5$.

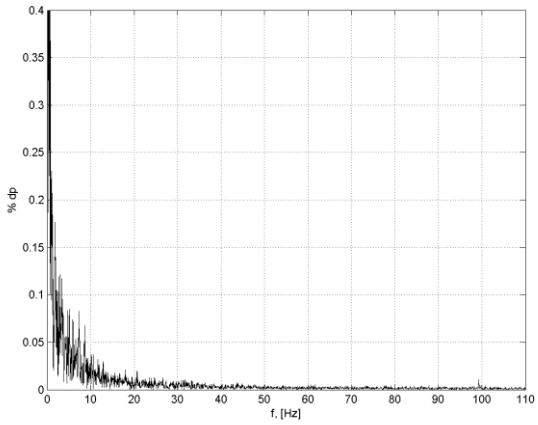

Fig. 192. Spectrum of pressure pulsations: $N = 0.67$, $Rm_s = 4.5$.

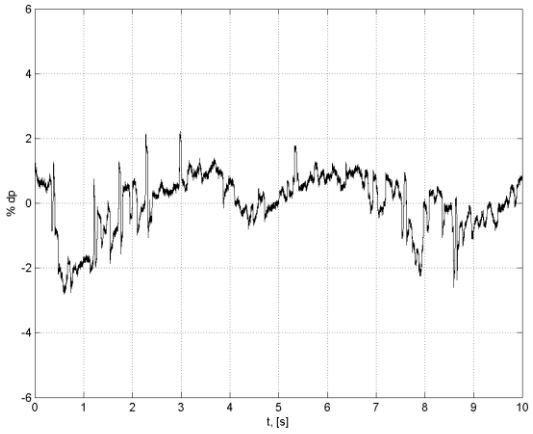

Fig. 193. Pulsations of developed pressure difference: $N = 0.67$, $Rm_s = 4.21$.

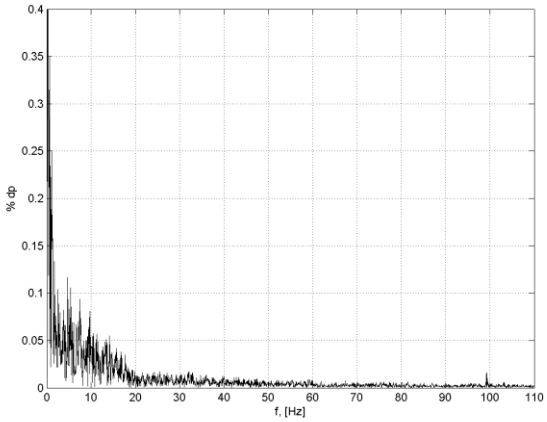

Fig. 194. Spectrum of pressure pulsations: $N = 0.67$, $Rm_s = 4.21$.

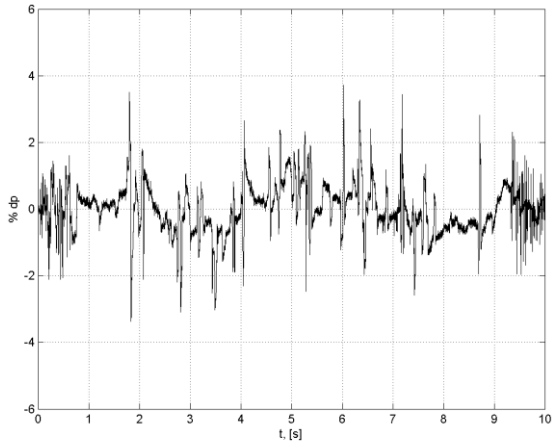

Fig. 195. Pulsations of developed pressure difference: $N = 0.67$, $Rm_s = 3.92$.

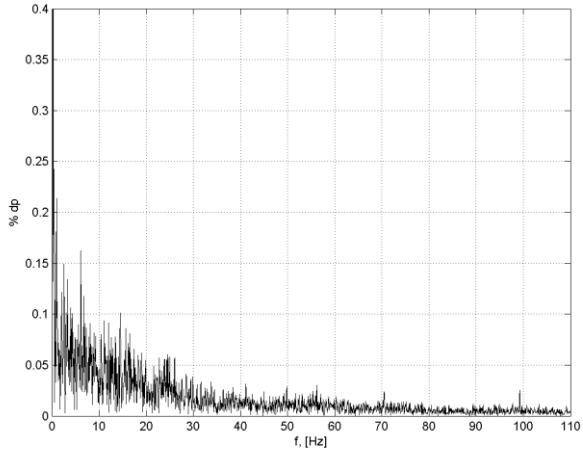

Fig. 196. Spectrum of pressure pulsations: $N = 0.67$, $Rm_s = 3.92$.

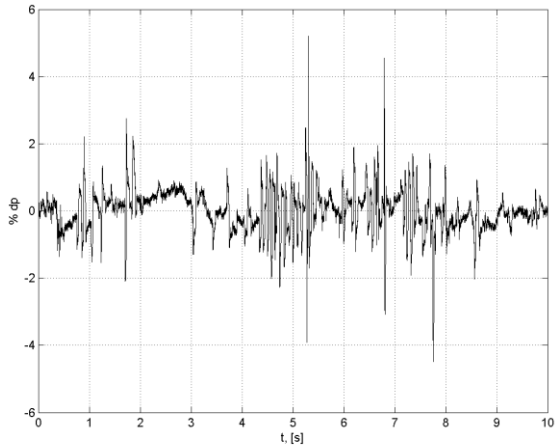

Fig. 197. Pulsations of developed pressure difference: $N = 0.67$, $Rm_s = 3.63$.

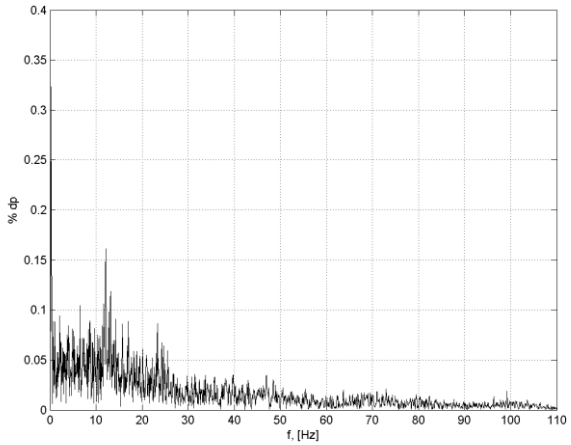

Fig. 198. Spectrum of pressure pulsations: $N = 0.67$, $Rm_s = 3.63$.

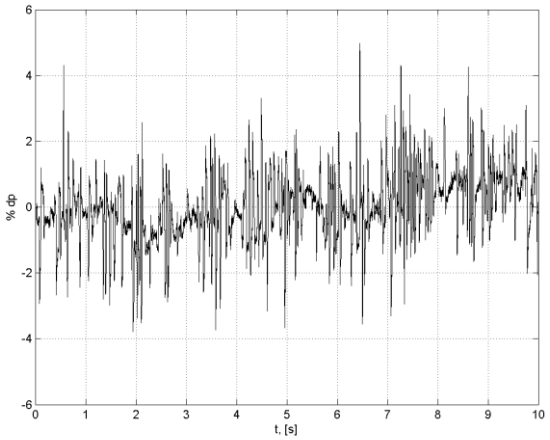

Fig. 199. Pulsations of developed pressure difference: $N = 0.67$, $Rm_s = 3.33$.

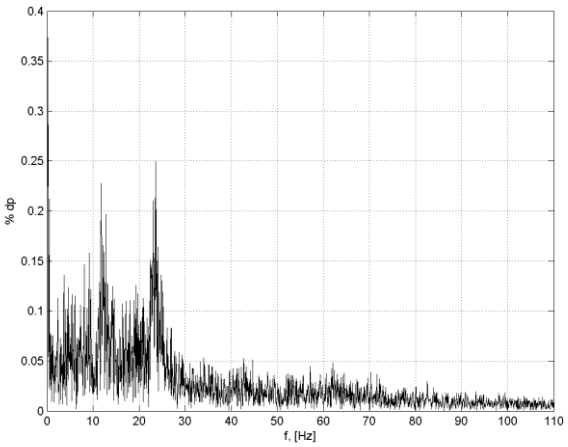

Fig. 200. Spectrum of pressure pulsations: $N = 0.67$, $Rm_s = 3.33$.

4.2.4. Measurements with liquid Na: magnetic field

In Fig. 201 - Fig. 206 measured modulus of magnetic field is shown as function of flowarate with two highest interaction parameter $N = 0.38, 0.67$. Main tendencies of these results can be summarized:

First of all, there is a global trend that in case of high $\mathrm{Rm_s}$ by increasing flowrate magnetic field increases. Secondly, there is rather significantly dispersion of results that could be caused by several reasons:

1. Inconsistent errors in positioning of samplers due to repositioning
2. Non-symmetric loading of phases
3. Temperature influence
4. Non-uniformity of flow and magnetic field caused by MHD interaction

First point is the systematic error of the experiment due to its setup and assuming that all samplers were identical is estimated using dry measurements. The second point is about taking into account current of each phase and their geometrical distribution in the analysis, since measurement coils are placed under the certain tooth. Non-symmetry of loading reached about 10% in the experiment. Importance of the third point was already discussed. Last point is the phenomenon one would like to quantify.

Thirdly, it can be observed that measured magnetic field is side sensitive. The shape of signals from samplers U1, U3 are somewhat different than from samplers U4-U8. It can be rather well observed especially in cases of Fig. 204. It suggests that flow in the channel is not symmetric by default which could be caused by peculiarities of the loop.

Forth, the magnetic field is higher in the side channels than in the central channels (e.g. see Fig. 204 and Fig. 205). Moreover, by increasing flowrate, signals increase much more in rapidly the central channels (Fig. 204), but less in the side channels (Fig. 205).

The interpretation of this result has been given already in previous chapter and is a consequence of operating FLIP with high Rm and slip, then magnetic field should be proportional to:

$$B_x \approx \frac{B_e}{Rm}\left(1 + \frac{v_z}{v_B}\right) \tag{175}$$

This, suggests, that there is a higher velocity in the side channel than in the middle and, secondly, by increasing the flowrate, velocity in the middle channel changes more importantly than in the side. Same tendency has been observed in numerical calculations Fig. 119 and Fig. 120.

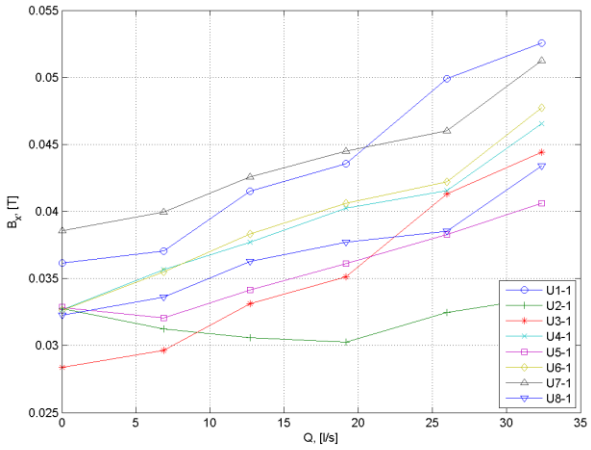

Fig. 201. $|B_x|$ *for UX-1:* $N = 0.38$.

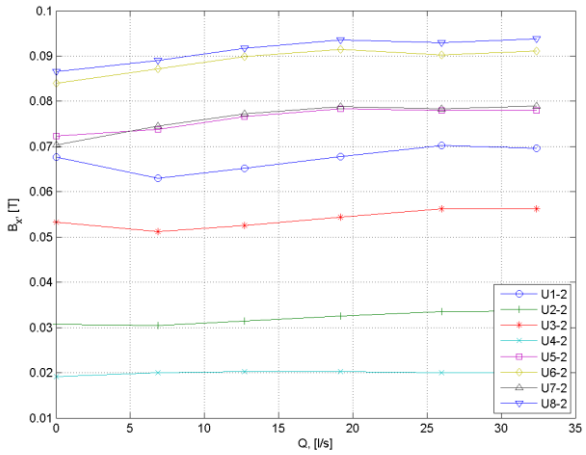

Fig. 202. $|B_x|$ *for UX-2:* $N = 0.38$.

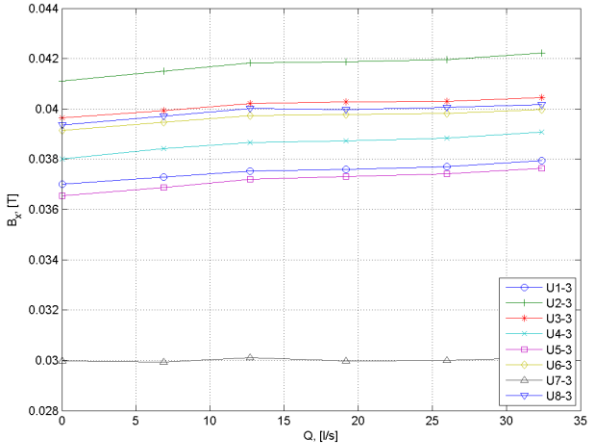

Fig. 203. $|B_x|$ *for UX-3:* $N = 0.38$.

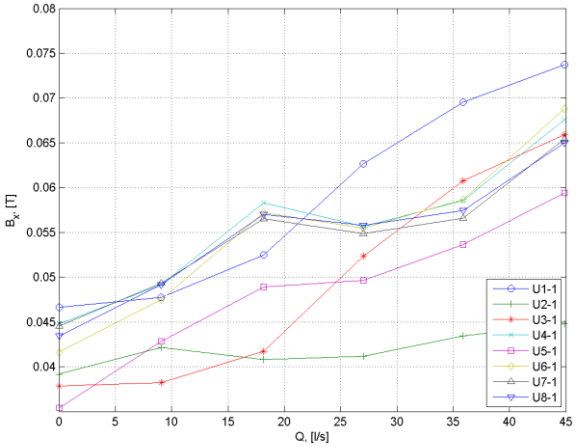

Fig. 204. $|B_x|$ *for UX-1:* $N = 0.67$.

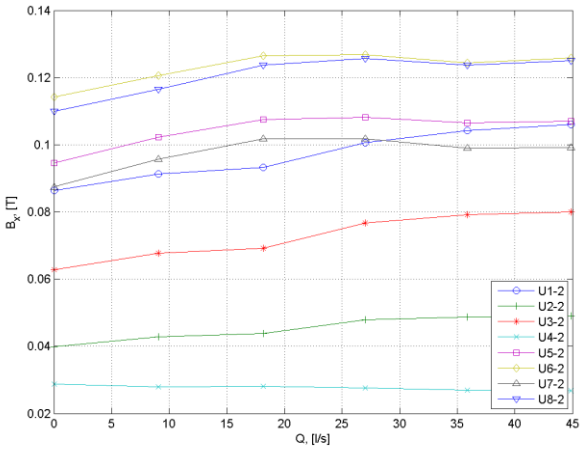

Fig. 205. $|B_x|$ for UX-2: $N = 0.67$.

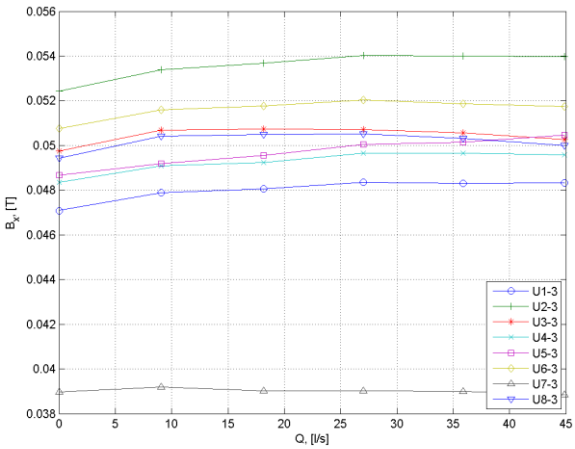

Fig. 206. $|B_x|$ for UX-3: $N = 0.67$.

4.2.5. Conclusions on experiment with 4 sub-channels

The performed experiment and obtained results allow summarizing several important points about setup of the loop, measurement techniques, instrumentation used and behaviour of physical phenomena.

First of all, global characteristics and possibilities of TESLA-EMP facility were tested. It turned out that upgrade of power supply system is necessary to operate FLIP in regime of higher N and lower Rm_s which would allow to characterize more precisely transition from stable regime to unstable. The most perspective solution would be variation of frequency.

Secondly, commercially available Keller 35 XHTC manometers (0-10 bar) proved to be rather good solution, however with its limitation. Namely, measurement frequency up to 100 Hz, which is not enough if supply frequency of 50 Hz is used in FLIP and better precision could be desirable, which theoretically lead to rather high errors of measured flowrate and poses problems with analysis of pressure pulsations, if amplitudes are small. In the same time, measured band LF pulsations should be valid (Fig. 189 - Fig. 200).

Thirdly, the chosen measurement technique of magnetic field using coils with ferrite core did prove their advantages - signal was strong (couple of V) and level of noise is not a problem in this case (Fig. 176 - Fig. 183), suggesting that single coil measurement could be done with sufficient precision.

However, the main inconvenience of such type of measurement is saturation of ferrite core at competitively low magnetic fields and need of high discretization frequency and even using 1 kHz aliasing of signal was observed (Fig. 184). Another aspect that has to be taken into account is temperature of core should not exceed 130°C (Fig. 173), therefore it must be controlled which was not done in this experiment.

Finally, important mechanical issue is fixing and positioning the magnetic field samplers. Since they were manipulated manually, measurement errors simply due to the not well defined positions can be obtained.

Overall, measurements of magnetic field showed acceptable linearity in measurements without sodium (Fig. 185 - Fig. 187). In case with liquid metal qualitatively same behaviour was observed as in numerical model (Fig. 201 - Fig. 206):

- Magnetic field is stronger in the side channel
- With increase of flowrate magnetic field increases
- The increase is more rapid in the side channel.

However, asymmetric distribution and behaviour of magnetic field was observed, which was not numerically modelled. One of the reasons for such outcome could be influence of inlet geometry and fact that velocity profile in the inlet is not homogeneous, which was assumed in numerical model. This effect was partly taken into account in later development.

In the end it can be said that preformed experiment showed also qualitative agreement with the numerical analysis done before, even if there is a certain lack of consistency between them. Perhaps most importantly, obtained experience and faced issues allowed to improve measurement techniques and data acquisition system for more detailed magnetic field measurements in the next experiment.

4.3. Experimental setup without sub-channels

In this session the philosophy of experiment was sufficiently changed. First of all, a dedicated experimental FLIP-2 was added in the loop with channel geometry without longitude walls, therefore flow was not restricted by certain *paths* and larger structures of vortices theoretically can form. FLIP-1 was kept in the loop as technological pump. Secondly, in the inlet and outlet of channel 8 zones, separated by stainless steel walls. Conductive flow meters were introduced to characterize inlet and outlet velocity distribution. This was done using array of permanent magnets of opposite polarity and measuring voltage difference on the wall. Finally, there were 144 point measurements covering surface of the inductor of magnetic field and temperature in air gap, which allowed having a 2D image of distribution.

4.3.1. An upgrade of measurement system and experimental concept

The idea obtaining magnetic field and temperature distributions by voltage measurements was proposed by prof. L. Buligins. The essence of idea is to add a small DC current in measurement circuit, therefore measured voltage consists of two parts - stationary (necessary for temperature measurement) and oscillatory (measurement of magnetic field). The circuit diagram used in measurements is shown in Fig. 207.

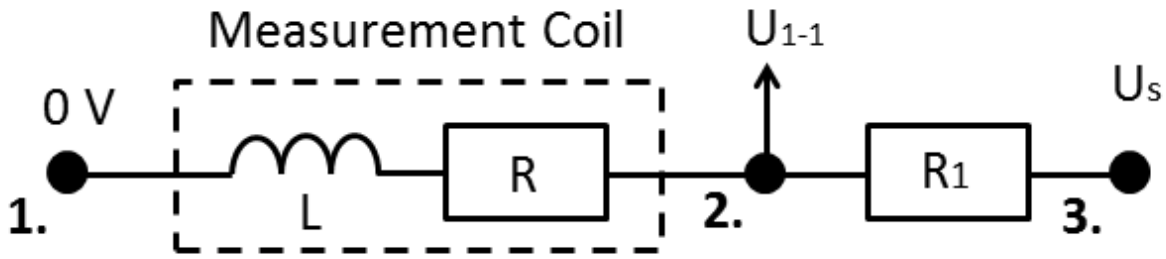

Fig. 207. Updated voltage measurement scheme.

The main difference here is added resistance R_1= 12KΩ and constant voltage source U_s = 12V. Since R<< R_1, current flowing from terminal 3 to 1 is practically 1 mA. Then resistance of coil can be calculated, by measuring mean voltage between terminals 1 and 2:

$$R \approx \frac{U_{1-1}}{U_s} R_1 \tag{176}$$

When resistance is known, temperature is recalculated using (174).

It consists of 36 samplers (U1 – 36) with 4 coils each. They are distributed in 18 rows with electrical connections on both sides. Therefore coils are evenly distributed in array of 18 x 8 and distances between coils 60 mm x 51.5 mm, covering practically all surface of inductor. Since sufficiently strong signal was obtained in previous experiment, it was decided to use single coil per point instead of differential connection. Also magnetic field measurement frequency was increased to 2 kHz. Global view on measurement system is shown in Fig. 209. Example of newly designed sampler is shown in Fig. 210. The realization of measurement system is shown in Fig. 208.

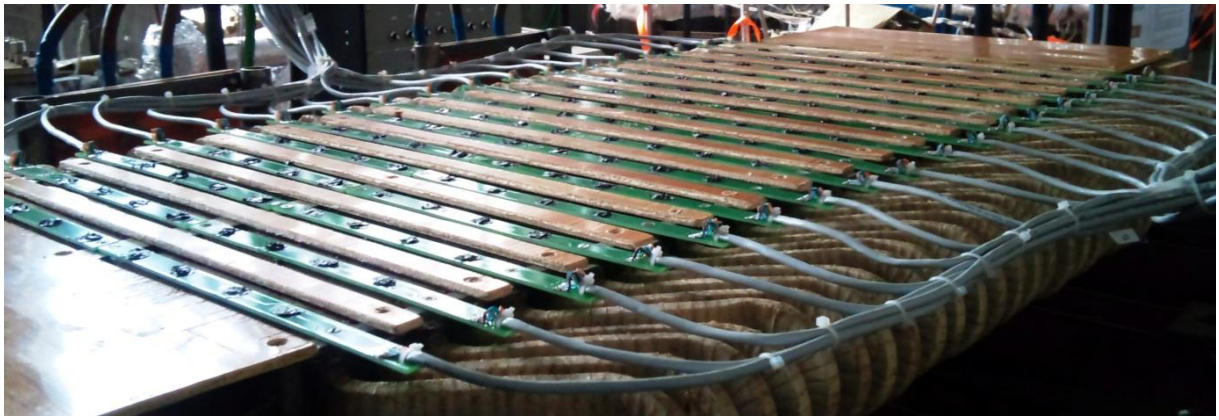

Fig. 208. Magnetic field measurement system on the surface of inductor.

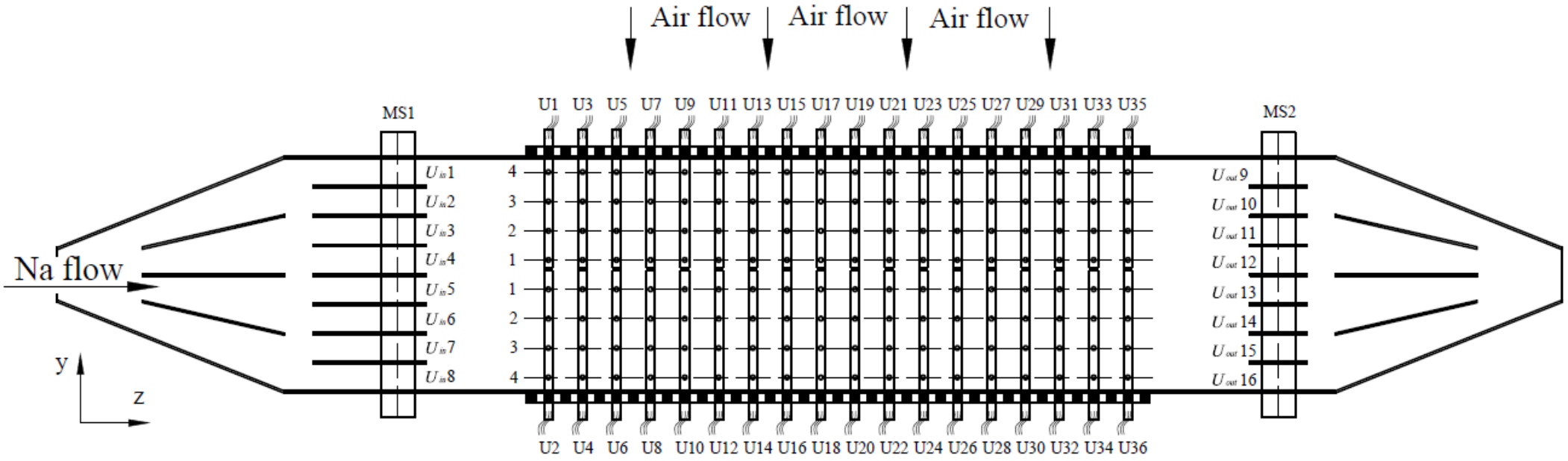

Fig. 209. A measurement scheme in experiment without sub channels.

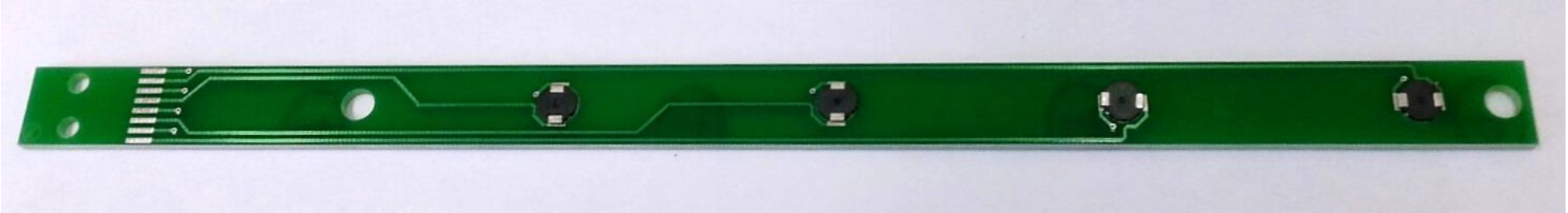

Fig. 210. Magnetic field sampler.

Magnetic field samplers were only 4 mm thick and above them air gap of 8 mm was created to apply convective cooling with air. After system was assembled magnetic field measurements with empty channel were carried out and then compared with calculation of 2D COMSOL model, showing good agreement Fig. 211.

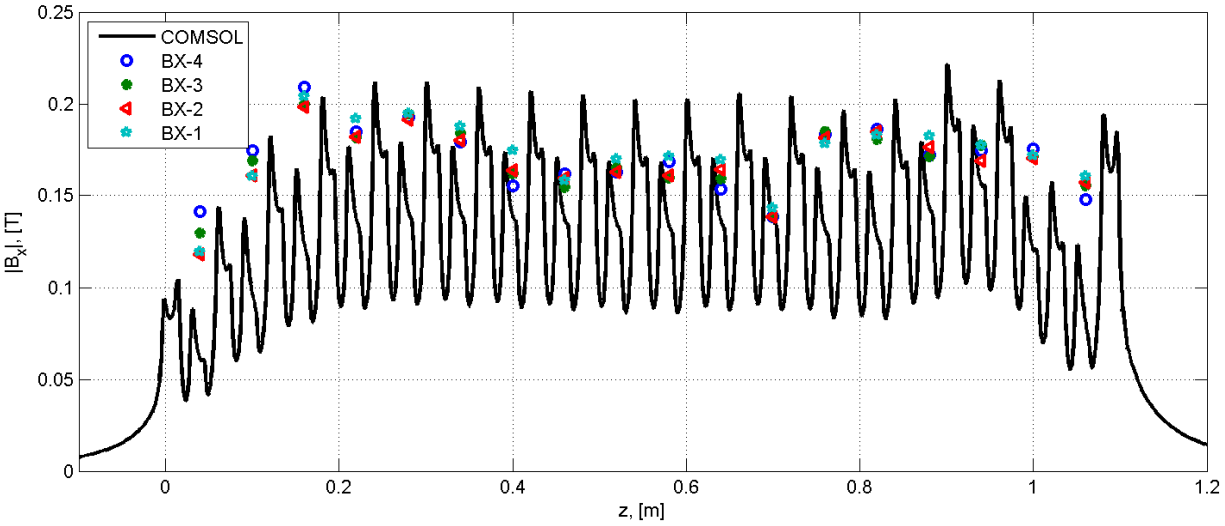

Fig. 211. Experimental and numerical results of $|B_x|$ of empty channel.

In the inlet and outlet zones pins for potential measurements were added as shown in Fig. 212. There is a single pin in the centre of external wall and two pins on both sides of inner walls. Between pins over width of the channel a system of permanent magnets of varying polarity are placed from both sides creating necessary field for potential measurement. Location of pins is shown in details in Fig. 213 ($\varphi_{1,2}$ … etc.) allowing to measure potential differences ($U_{in}1, 2\ldots$) .

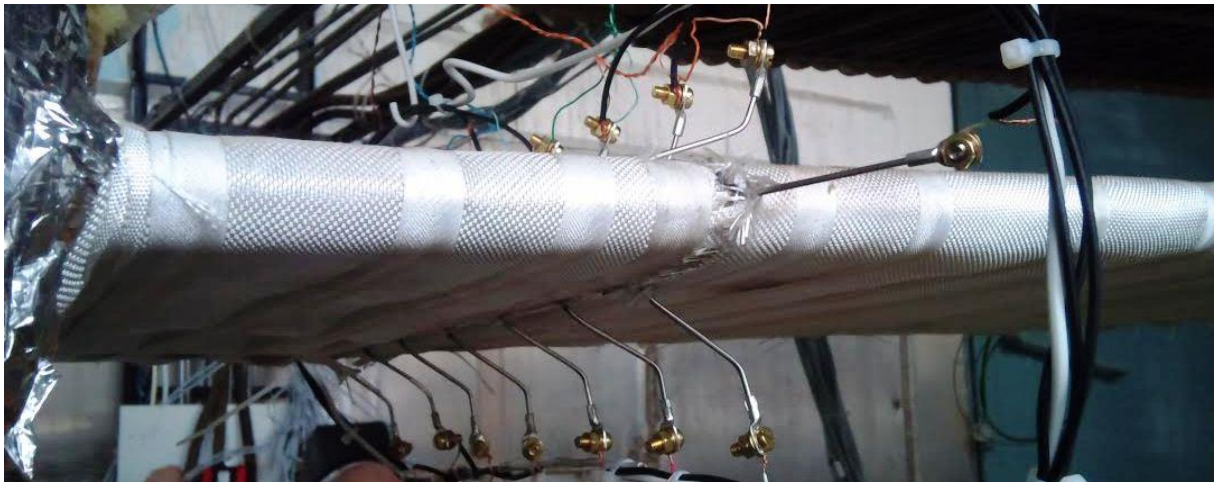

Fig. 212. Potential pins (inlet).

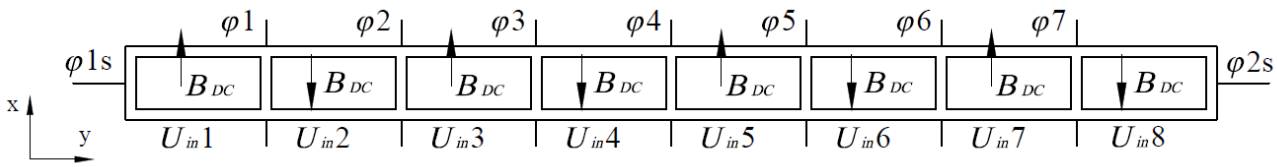

Fig. 213. A scheme of location of potential pins (inlet), applied magnetic field and measured voltage.

The idea behind such comparatively detailed measurements is primary to find how perturbations of the Na flow are reflected in distribution and temporal behaviour of magnetic field. It is also possible to analyse their spatial and temporal development.

When first step is achieved, it must be possible to invert the problem and find corresponding velocity distribution in the channel. This, would be a great advancement in experimental methods of EMIP, but unfortunately is out-of-reach in current work.

Experiment was carried out with several interaction parameters; however, they all are smaller than unity. In upcoming chapters case only with highest of them is presented. Dimensionless numbers of experiment are collected in tables above and are quite similar to the previous experiment:

N_λ	Re_λ	N
63	94	0,67

Q, [L/s]	10	20	30	42
Re, x10^4	9.4	18.8	28.1	39.4
Rm_s	4,47	4,15	3,82	3,43

Table 16. Estimation of dimensionless parameters in the experiment.

4.3.2. Measurements of magnetic field with liquid metal

In this chapter measurement results of 2D distribution of magnetic field in the inductor zone are presented. Since estimation technique of magnetic field is based on peak values of the signal obtained from coils, the minimum time discretization was 2.5 periods - 0.05 s of AC current used in the inductor. In principal precise estimation of peak value could allow achieving discretization up to ½ periods, however, this again meets problem of high acquisition frequency.

The relatively small measurement time step allows capturing dynamics of unstable structures over the channel. It can be estimated that with 60 mm x 51.5 mm mesh of sensors and times step of 0.05 s it is possible to precisely capture motion of structures with velocity ~1 m/s. In case if structures move with higher velocities, it is still possible to capture them, even though they might cross several cell elements during one time step.

All obtained data was post processed using MatLab software by also adding extrapolated points between the grid of measurements to smoothen the contour plots. The program as written in a way, that it was possible to change time step in which magnetic field was calculated.

First of all distribution dynamics of magnetic field in case of $Rm_s = 4.47$ is shown in *Fig.* 214 - *Fig.* 217. It can be observed that distribution of magnetic field is asymmetric and oscillating modes exists over z axis.

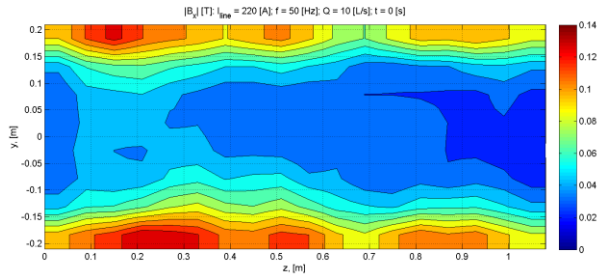

Fig. 214. $|B_x|$ *[T]:* $Rm_s = 4.47$*,* $t = 0$ *s.*

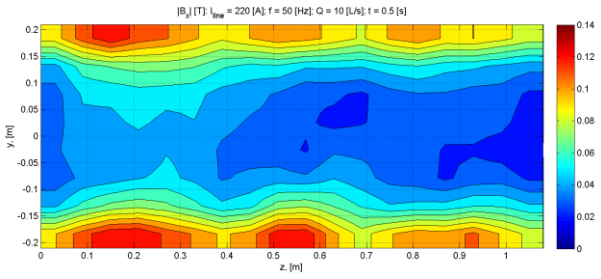

Fig. 215. $|B_x|$ *[T]:* $Rm_s = 4.47$*,* $t = 0.5$ *s.*

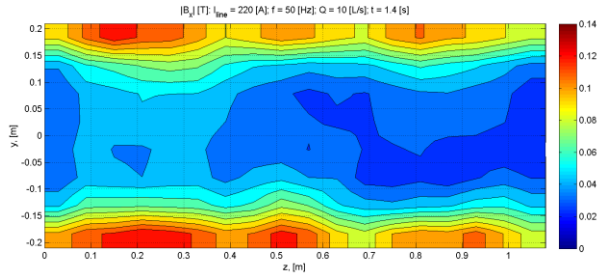

Fig. 216. $|B_x|$ *[T]:* $Rm_s = 4.47$*,* $t = 1.4$ *s.*

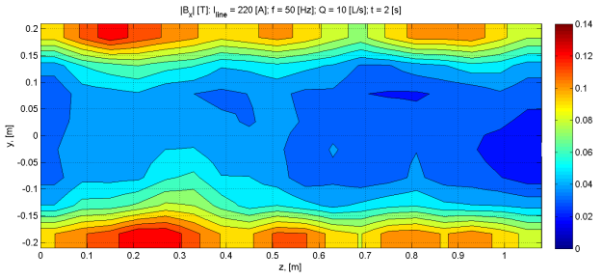

Fig. 217. $|B_x|$ *[T]:* $Rm_s = 4.47$*,* $t = 2$ *s.*

In case of $Rm_s = 4.15$ similar behavior can be observed *Fig.* 218 - *Fig.* 221. Nevertheless oscillations of field are less pronounced as before.

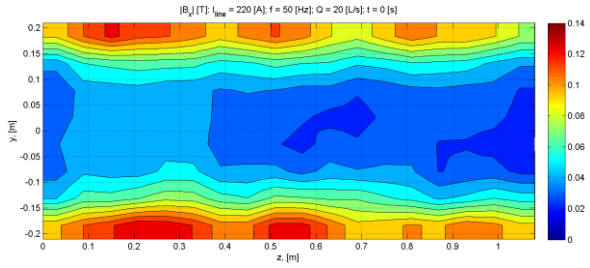

Fig. 218. $|B_x|$ *[T]:* $Rm_s = 4.15$, $t = 0$ *s.*

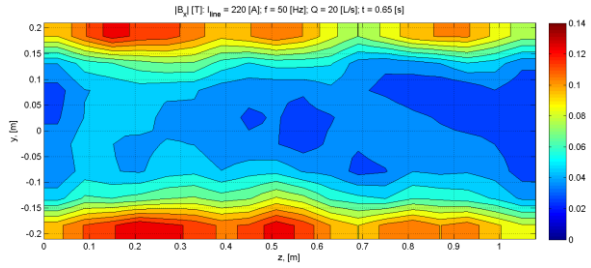

Fig. 219. $|B_x|$ *[T]:* $Rm_s = 4.15$, $t = 0.5$ *s.*

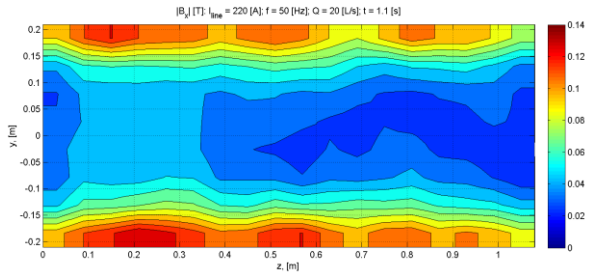

Fig. 220. $|B_x|$ *[T]:*, $Rm_s = 4.15$, $t = 1.1$ *s.*

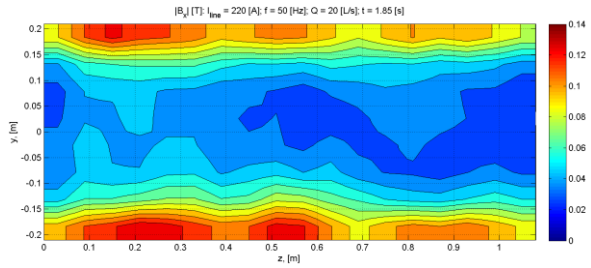

Fig. 221. $|B_x|$ *[T]:* $Rm_s = 4.15$, $t = 1.85$ *s.*

In the cases $\mathrm{Rm_s} = 3.82$ (*Fig.* 222 - *Fig.* 223) and $\mathrm{Rm_s} = 3.43$ (*Fig.* 224 - *Fig.* 225) only minor oscillations of field can be found and its distribution is relatively symmetrical.

Overall distribution of magnetic field again, strongly resembles to what was foreseen by numerical calculations – field is sufficiently weaker in central part and stronger in sides. Also pronounced oscillations of magnetic field in cases of higher Rm_s predicted by numeric were observed.

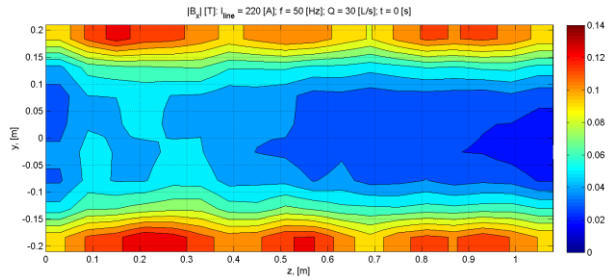

Fig. 222. $|B_x|$ *[T]:* $Rm_s = 3.82$, $t = 0$ *s.*

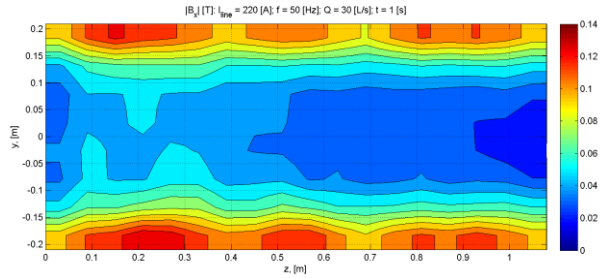

Fig. 223. $|B_x|$ *[T]:* $Rm_s = 3.82$, $t = 1$ *s.*

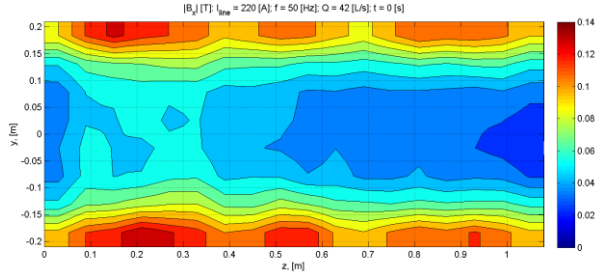

Fig. 224. $|B_x|$ *[T]:* $Rm_s = 3.43$, $t = 0$ *s.*

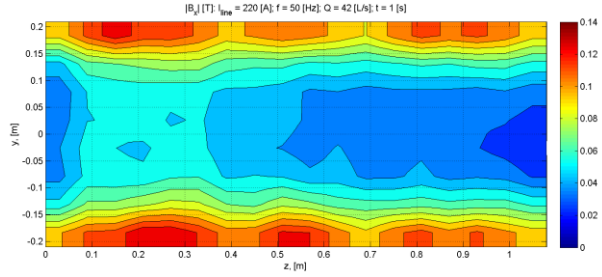

Fig. 225. $|B_x|$ *[T]:* $Rm_s = 3.43$, $t = 1$ *s.*

4.3.3. Measurements of potentials difference in the inlet and outlet

Time averaged potential difference measurements in the inlet and outlet of the FLIP in cases of different Rm_s are shown *Fig.* 226 - *Fig.* 229, where error bars indicate oscillations of the profile over the mean value.

First of all, it can be observed that measured signal increase as with flowrate precisely linearly. Secondly, in all cases measurements show that profile in inlet is more perturbed than in outlet, with higher signal in sides and lower - in the middle. Finally, oscillations of profiles tend to increase with Rm_s and vice-versa.

All the observed trends seem to be rather coherent with numerical results except of fact that profiles are more perturbed in the inlet, weather it was expected that it will be in the outlet. Such outcome is not obvious and suggests either rather important influence of e.g. real channel geometry, either error in the data acquisition.

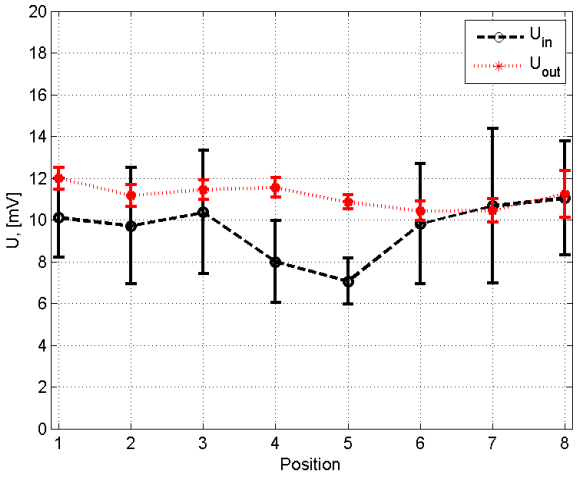

Fig. 226. Profiles of potential difference: $Q = 10\ [L/s];\ Rm_s = 4.47$

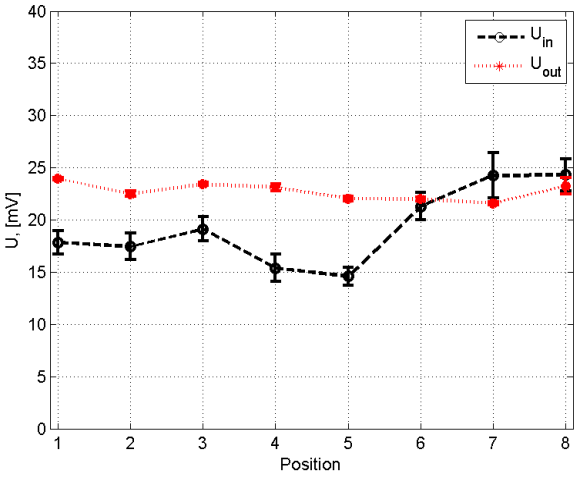

Fig. 227. Profiles of potential difference: $Q = 20\ [L/s];\ Rm_s = 4.15$

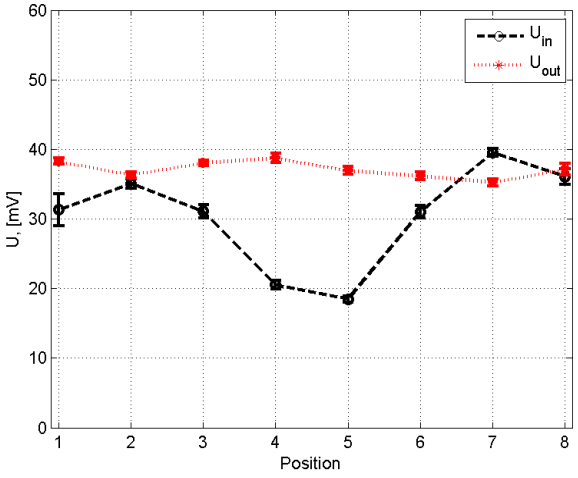

Fig. 228. Profiles of potential difference: $Q = 30\ [L/s];\ Rm_s = 3.82$

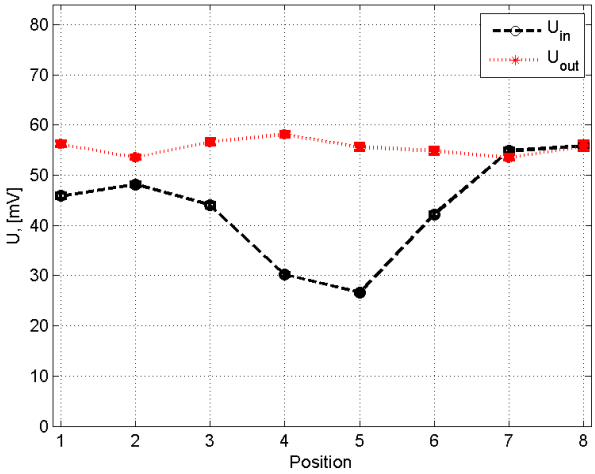

Fig. 229. Profiles of potential difference: $Q = 42\ [L/s];\ Rm_s = 3.43$

4.3.4. Pressure difference and pulsation measurements

Pressure difference of manometers P6 and P5 as function of flowrate is shown in *Fig.* 230. It can be observed that, developed pressure becomes negative around 30 L/s, these regimes were obtained using technological as another pressure source. As discussed before, the main source of resistance are systems of strong permanent magnet which are necessary for potential difference measurements.

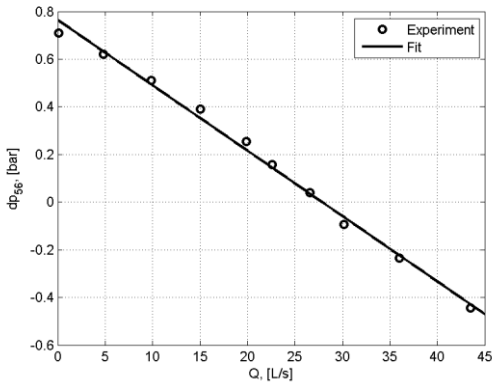

Fig. 230. Pressure difference of FLIP-2 as function of flowrate.

In this case a good relationship signal/pressure loss was not found, which has resulted in unnecessary high resistance of the channel. However similar tendency has been observed also in numerical calculations. Oscillations of developed pressure and according spectrums for different Rm_s values are shown in *Fig.* 231 - *Fig.* 238.

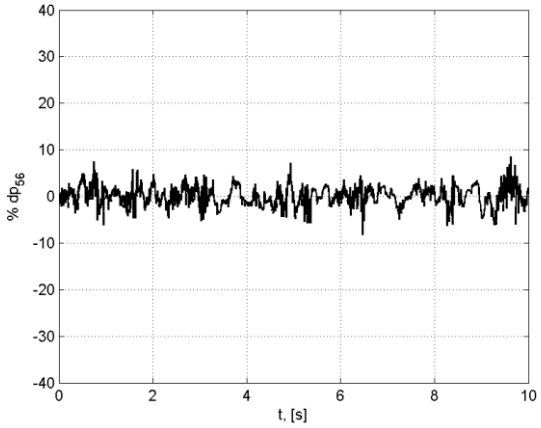

Fig. 231. Oscillations of developed pressure: $Q = 10\ [L/s];\ Rm_s = 4.47$

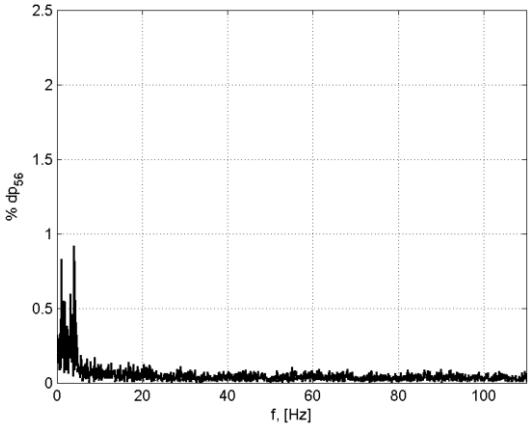

Fig. 232. Spectrum of oscillations: $Q = 10\ [L/s];\ Rm_s = 4.47$

It can be observed that amplitude of osculation tend to increase with flowrate. Practically in all cases LF oscillations are the most dominant but still relatively small, except of case $Rm_s = 3.43$ where equally strong peaks near DSF are observed in *Fig.* 238. However, obtained signal in this case *Fig.* 237 is unexpected with sequence of bursts and possible noise, which would require additional verification in similar regimes. Unfortunately, this was the highest obtainable flowrate.

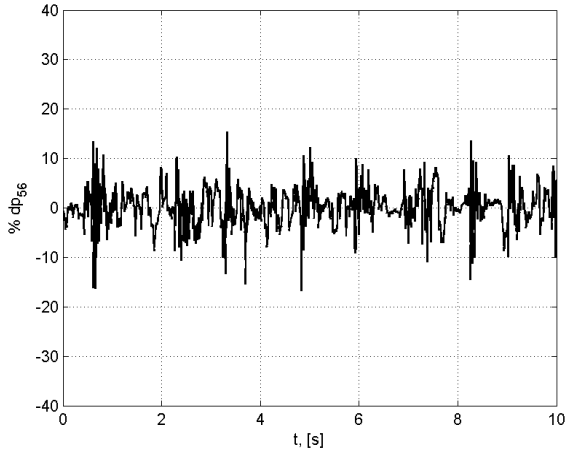

Fig. 233. Oscillations of developed pressure: $Q = 20\ [L/s];\ Rm_s = 4.15$

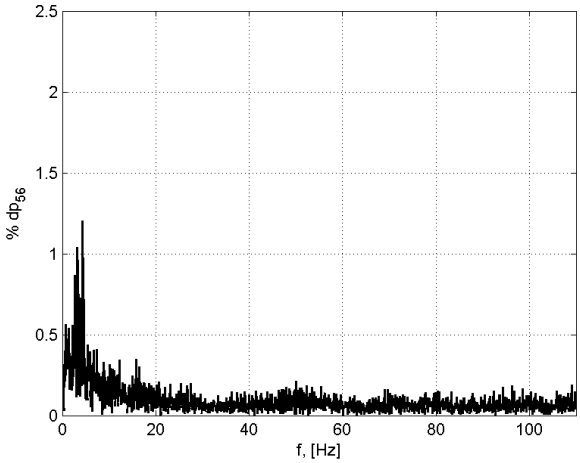

Fig. 234. Spectrum of oscillations: $Q = 20\ [L/s];\ Rm_s = 4.15$

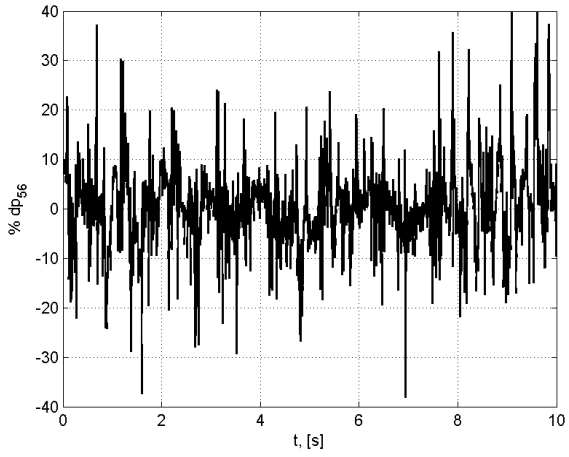

Fig. 235. Oscillations of developed pressure: $Q = 30\ [L/s];\ Rm_s = 3.82$

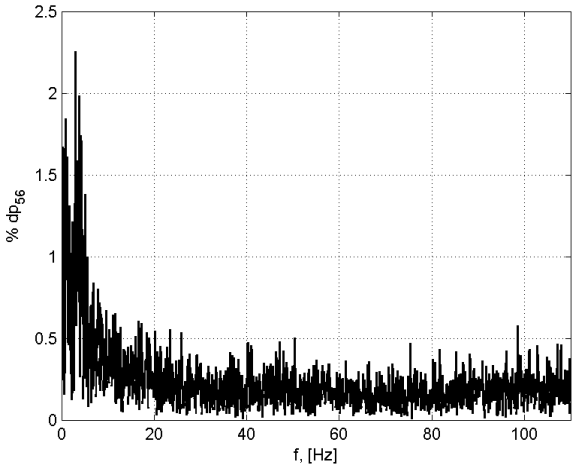

Fig. 236. Spectrum of oscillations: $Q = 30\ [L/s];\ Rm_s = 3.82$

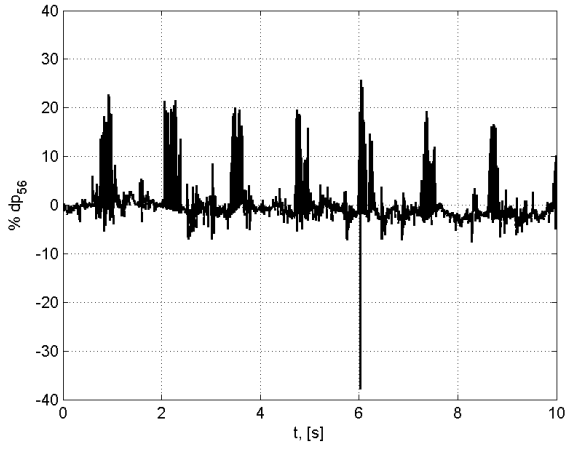

Fig. 237. Oscillations of developed pressure: $Q = 42\ [L/s];\ Rm_s = 3.43$

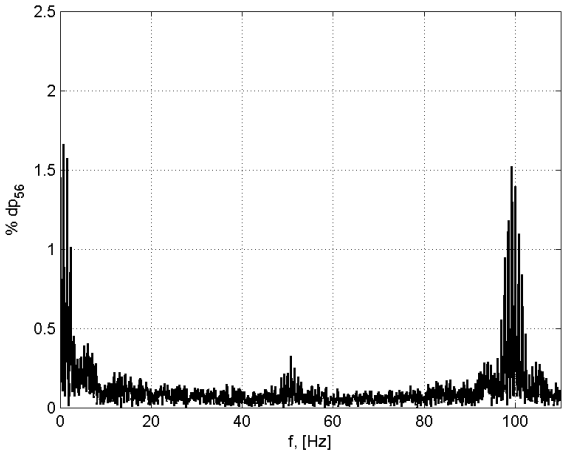

Fig. 238. Spectrum of oscillations: $Q = 42\ [L/s];\ Rm_s = 3.43$

Power of pressure oscillations in the inlet and outlet of FLIP-2 are compared with Kolmogorov -5/3 law for inertial regime of turbulent flow [2] in *Fig. 239 - Fig. 246*. In most cases qualitative agreement is obtained in frequency band 5 – 100 Hz, therefore flow is dominated by turbulence and LF oscillations due to MHD effects are too weak to be clearly distinguishable from rest of the spectrum. The most probable cause of such result is low interaction parameter N, outlining its importance.

It should be noted that in all cases pressure oscillations (also LF ones) are stronger in the inlet of pump being more pronounced with lower flowrate. This is in a good accordance with fluctuation of profiles in *Fig.* 226 - *Fig.* 229, while causes of such effect are still unclear.

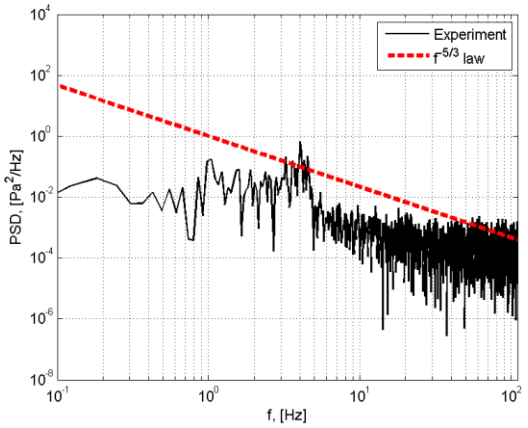

Fig. 239. Inlet log pressure power spectrum: $Q = 10\ [L/s];\ Rm_s = 4.47$

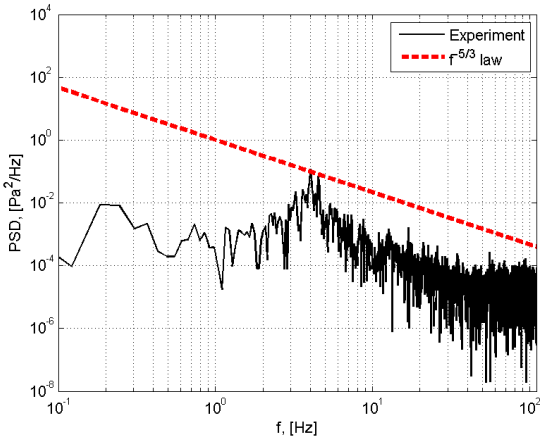

Fig. 240. Outlet log pressure power spectrum $Q = 10\ [L/s];\ Rm_s = 4.47$

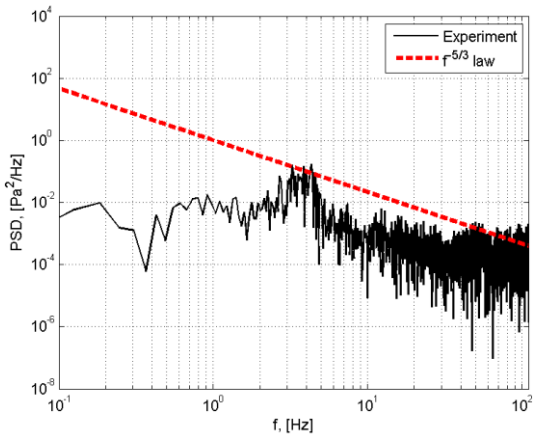

Fig. 241. Inlet log pressure power spectrum: $Q = 20\ [L/s];\ Rm_s = 4.15$

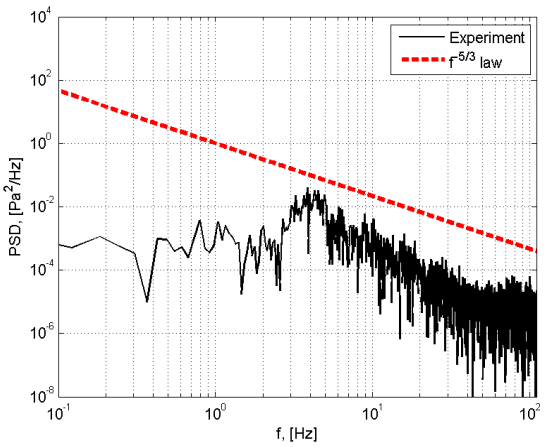

Fig. 242. Outlet log pressure power spectrum: $Q = 20\ [L/s];\ Rm_s = 4.15$

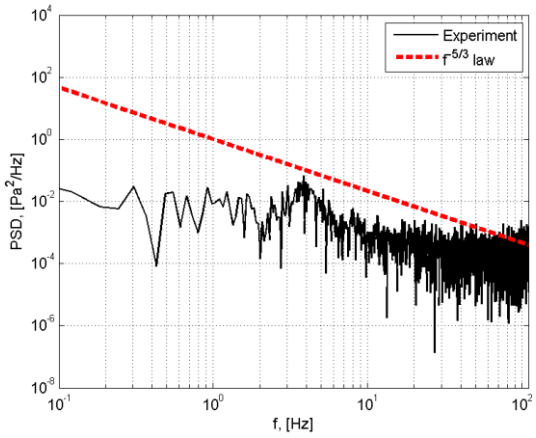

Fig. 243. Inlet log pressure power spectrum: $Q = 30\ [L/s];\ Rm_s = 3.82$

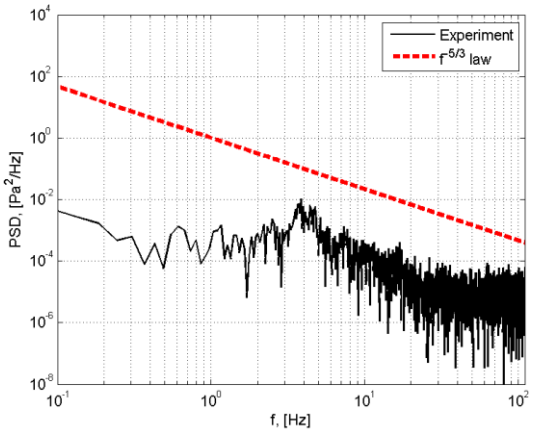

Fig. 244. Outlet log pressure power spectrum: $Q = 30\ [L/s];\ Rm_s = 3.82$

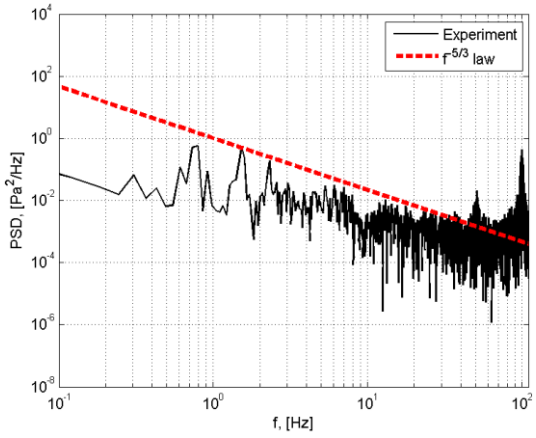

Fig. 245. Inlet log pressure power spectrum: $Q = 42\ [L/s];\ Rm_s = 3.43$

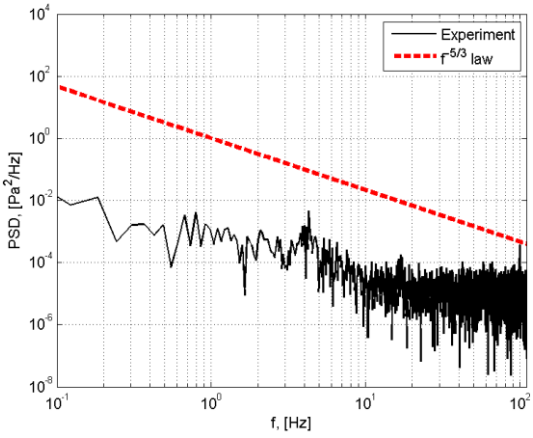

Fig. 246. Outlet log pressure power spectrum: $Q = 42\ [L/s];\ Rm_s = 3.43$

4.3.5. Measurements of the coil temperature in the air gap

The main purpose of the temperature measurement was to monitor and not overheating the coils. As shown in Fig. 209, forced air cooling was realized using 4 ventilators from one side of the channel. This effect can be very well observed in presented results of time averaged temperature distribution in *Fig.* 247 - *Fig.* 250. Results show that, in all cases temperature has been stabilized and well controlled not exceeding 80 - 90 ºC.

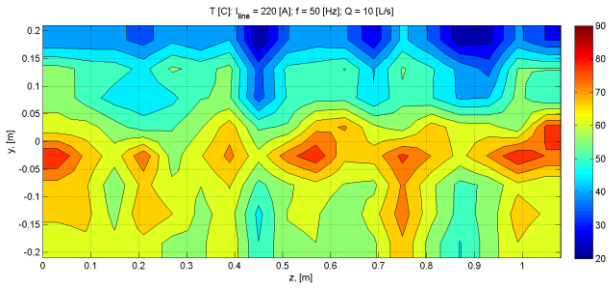

Fig. 247. T [C], $Rm_s = 4.47.$

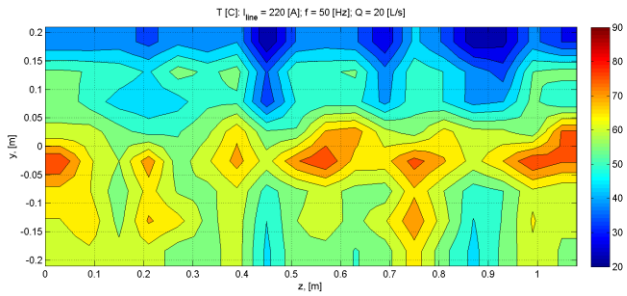

Fig. 248. T [C], $Rm_s = 4.15$

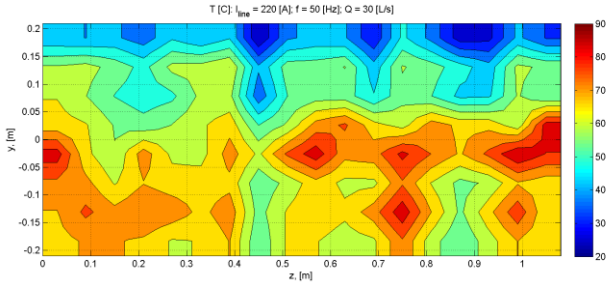

Fig. 249. T [C], $Rm_s = 3.82$.

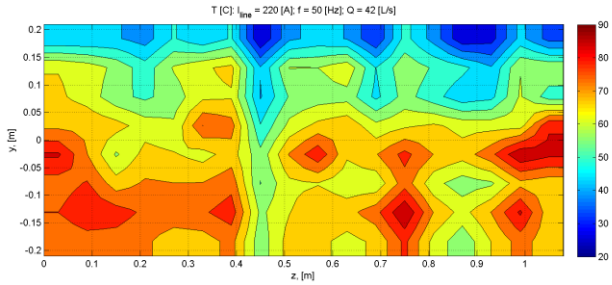

Fig. 250. T [C], $Rm_s = 3.43$

4.3.6. Conclusions on experiment with without sub-channels

Experimental session without sub-channels was successful at least for several reasons. First of all, newly designed magnetic field sampler and updated measurement technique which allowed resolving some of the faced problems in previous experiment. Positions of samplers were fixed and well known, as well as temperature of coils was controlled in a well-defined manner. With increase of measurement frequency, precision of data was improved.

All this effort resulted in a possibility to capture the dynamics of magnetic field distribution over the surface of the channel. Periodic, oscillating structures are as well as asymmetry of the field observed in case of higher Rm_s (*Fig.* 214 - *Fig.* 221). For lower values of Rm_s such strong oscillations are not observed and distribution of field is relatively symmetric (*Fig.* 222 - *Fig.* 225). This corresponds well to numerical predictions.

Measured potential differences in the inlet and outlet surprisingly showed higher perturbation of the profiles and higher oscillations in the inlet of FLIP-2 (*Fig.* 226 - *Fig.* 229). This unexpected result is necessary to verify, since numerical results suggest the opposite. Otherwise, the shape of the profiles and the behaviour (oscillations decrease with the decrease of Rm_s) agrees with numerical estimates very well.

The developed pressure and pulsations also qualitatively resemble to numerical calculations. The pressure flowrate relationship seems to be quite linear as well, which is cause by pressure losses due to the potential measurement system (*Fig.* 230). Then LF pressure oscillations are observed in all cases with order of magnitude around 1-2% (*Fig.* 231 - *Fig.* 236). DSF pulsations were also registered in case of $Rm_s = 3.43$ (*Fig.* 237 - *Fig.* 238), but seems to be subject of noise. Overall, due to rather low interaction parameter spectrum of flow is mainly turbulent (Fig. 239 - Fig. 246) and magnitude of LF pulsation caused by MHD process - small.

Lastly, introduced control of temperature showed, that coil are not overheated (*Fig.* 247 - *Fig.* 250).

In the end, it can be concluded that in these experimental activities a number of new approaches and methods of analysis were introduced to capture instability process. Such detailed measurements of field dynamics have never been done or reported before. This novel nature of the work has also brought some unnecessary and errors in the development of experimental and numerical investigation which led to comparison difficulties in some cases. Therefore high level of attention to the details is required in this precision demanding work.

5. CONCLUSIONS AND PERSPECTIVES

Partly conclusions of each principal part of the work has been already given, however, it is necessary to summarize all main results as well as discuss them in context in future work.

First of all, **in the chapter 2. of theoretical investigations** nature of MHD instability process in ideal ALIP has been studied in more general case than before. A simplified dispersion relation is considered in linear stability analysis, taking into account only linear terms.

Obtained equation (126) for perturbation development in convective instability process showed behaviour of perturbation in convective instability process and allowed to estimate perturbation growth rate (128) and phase velocity (127). From that, estimation of perturbation spatial development (129) can be found, which gives an idea at what extent existing initial perturbation will be amplified. Such estimation requires some information about amplitudes of initial perturbations. If amplification is significant, one could expect that non-linear effects become more pronounced and eventually lead to loss of the stability. Results suggest that this might be the cause MHD instability of ALIP in some cases, even if well below threshold of absolute instability Fig. 63.

Theoretically found absolute instability threshold (130) suggests, that in case of high interaction parameter N absolute instability can occur when $\mathrm{Rm}_s \approx \frac{Rm}{3}$. Therefore if Rm is relatively small (3..4) in principle it is possible to arrive at the threshold of absolute instability. However, in a detailed comparison with experimental results found in literature, theory does not predict loss of stability (Fig. 63). Apparently, it still does not capture phenomenon completely and some improvements are necessary. One of the future tasks is constructing absolute instability threshold by numerically solving full dispersion relation.

Stable operation and stabilization methods of ideal ALIP are discussed further. It is shown that if ALIP has possibility to control frequency and current in sufficiently wide range, a stable operation regime can be easily found depending on desired operating conditions (Fig. 67). The stabilization technique proposed by prof. J. Priede involves operation with another frequency that is equals with mean velocity of liquid metal. It has been shown in Fig. 69 using linear stability analysis that maximal stabilization current does not exceed 36 % of driving current (153). Importantly, it has been illustrated that, stabilization of ALIP is essentially correction of the gradient of force-velocity relationship in the considered point (Fig. 70).

The most intriguing part is to test the discussed stabilization technique and verify if estimates of necessary current presented in this work are correct. It should be also taken into account that in presented analysed only quasi stationary parts of EM force were considered, however, situation is more complicated in general case and pulsating part of force governed by the frequency difference may introduce unwanted oscillations. A possible experimental setup could consist of pump with two inductors where one of them is supplied by driving, other by stabilizing source.

Next, in **chapter 3. of numerical investigations**, first of all, study of MHD instability in ideal ALIP was carried out. The periodic model of a single period of ideal ALIP was

compared with theory and showed reasonable results, even though some indications that spatial and/or temporal discretization could be improved. The comparison of numerically estimated perturbation temporal development rate with theory showed that it is strongly dependent on interaction parameter N and good agreement is not obtained in all cases even though qualitatively phenomenon is well captured. In all cases numerically estimated stability threshold is higher than theoretically predicted, especially with high N (Fig. 98).

In the cases of low interaction parameter, when the temporal growth rate of perturbation is small, the overall agreement is better (Fig. 90, Fig. 92). Reasons for this are twofold. First of all, only exponential growth rate is observed in numerical calculations (exponent with real argument) and it is much easier to precisely fit it (than complex exponent). Secondly, linear stability analysis discusses only small growth rates, therefore it should be expected that the best agreement between the two is in cases of low interaction parameter and near stability threshold. One should also consider that numerical and theoretical cases are slightly, but different. Numerical is purely transient, while theoretically quasi-stationary case is studied. Also higher longitude mode exist in numerical model.

These deviations and uncertainties define scope of possible future work, which are waiting for answers. The complexity in this case is also connected with still existing necessity to improve theory (as mentioned before), while refining numerical models. Nevertheless, some serious first steps have been made mastering theoretical and numerical methods of this analysis, which requires high precision.

In second part of the chapter 3. 2D models of realistic FLIPs were created – geometries with and without 4 sub-channels. The word *realistic* mainly implies that distribution of magnetic field is not idealized, taking into account distribution of discrete phases and finite length. Since models are 2D in φ-z plane, all effects by default are height averaged.

The first model – with 4 sub-channels, was a kind of test mainly due to the lack of experience working with such problems. The obtained results indicated that velocity and magnetic field is stronger in the side channels (Fig. 116, Fig. 118), but in centre back flow is possible especially in cases of low flowrate. With increase of flowrate distribution tends to homogenize, since higher increase of the velocity and magnetic field in central channel is observed (Fig. 119, Fig. 120). Similar trends were expected from experiment, therefore overall agreement is satisfactionary.

Second numerical model without sub-channels was more refined. The necessary set of dimensionless numbers was obtained by change of material properties. A realistic velocity distribution boundary condition in the inlet was added using dedicated 3D model taking into account geometry of the loop (Fig. 123). The results of analysed cases show that rather strong oscillating vortical structures of the flow and modulus of magnetic field are present for highest values of $Rm_s = 4.47,\ 4.15$ (Fig. 126 - *Fig.* 133). LF oscillations are also observed in profiles of potential difference and pressure spectrums with magnitude 1-2% (*Fig.* 144, *Fig.* 145, *Fig.* 149 - *Fig.* 152).

On the other hand for $Rm_s = 3.82,\ 3.5$ development of velocity inhomogeneity over the length of channel is found, while being comparatively stable (*Fig.* 134 - *Fig.* 141). More

sophisticated analysis methods are necessary to track these perturbations in distribution of magnetic field. No important oscillations of potential difference profiles are observed (*Fig.* 146, *Fig.* 147) and DSF dominate with amplitude up to 4% (*Fig.* 153 - *Fig.* 156).

Even though overall numerical results share many trends and details with experiment, the comparison of results is still quite complicated, mainly due to the lack of consistent quantitative analysis methods and therefore is not done in this work.

There are number of possible improvements of numerical study, but the discussion about future development of more detailed models will eventually turn into the question about 3D simulations. A number of uncertainties arise at this point – is it sufficient to model 3D only hydrodynamic part, or is it necessary to extend it to whole domain including electromagnetics as well (e.g. air domain outside the inductor etc.)? In the first case validity of boundary conditions for magnetic field should be concerned, in the other – size of the mesh. Then the question about complexity of the simulation – what turbulence model to use, is it important to consider all components of external field, how real geometry of the loop is taken into account? From temporal point of view simulation must be transient and most likely to meet the numerical stability criterion time step must be sufficiently small, therefore fully transient formulation of the MHD problem should be used. Many additional numerical studies are still necessary to properly answer these questions and find an optimal simulation approach.

However, the calculation itself is only one part, obtained data has to be post processed into results in the proper and efficient manner. This, of course, is directly connected also with the experimental possibilities in terms of comparison. In this work it is clearly shown that to characterize observed complex structures either in numeric or experiment results more quantitative methods are necessary. One of the possible ways would be to decompose the spatial distribution of the field into longitude and transverse modes using Fourier transform.

The chapter 4. is based on results obtained in two experimental activities in IPUL on TESLA-EMP loop. The first of them concerns only technological FLIP-1 which had 4 sub-channels in the second experimental pump FLIP-2 with much more detailed measurement system was introduced.

The newly introduced method magnetic field measurements using ferrite core coil played a highly important role and is one of the main reasons why experimental activities are considered to be successful. The key using such method is to have good temporal discretization of the voltage to capture the peak values of the signal, which are linearly proportional to the field (Fig. 167). Temperature of coils should be also controlled not to exceed 130º C (Fig. 173).

The first experiment measurement equipment was tested for the first time on TESLA-EMP loop and showed good capabilities. It was possible to operate loop with flowrate up to 45 [l/s] with developed pressure around 1.5 [bar] (Fig. 188). Observed pressure pulsations were small in this case, but they tend to increase with the flowrate, for the highest of which multiples of LF pulsations can be found (Fig. 189 - Fig. 200). Measurements of magnetic field indicated that there is asymmetry of the flow over the width of the channel, since increase of

the field with increase of flowrate was side sensitive (Fig. 201 - Fig. 206). Overall trends are the same as expected numerically.

More detailed measurements were carried out in the final experimental session where dedicated FLIP-2 was introduced. The obtained distribution of magnetic field indeed showed that in case of higher $Rm_s = 4.47, 4.15$ oscillations of field appear (*Fig.* 214 - *Fig.* 221) and decreased with further decrease of $Rm_s = 3.82, 3.5$ (*Fig.* 222 - *Fig.* 225), resulting in comparatively stable situation. Such behaviour and overall distribution of the field resembles to numerical prediction acceptably. Temperature control showed that none of the coils were overheated (*Fig.* 247 - *Fig.* 250).

Situation is slightly different with profiles of potential difference, even though the same tendency is observed - profiles are less oscillating and overall signal grows with decrease of Rm_s, less perturbed profile is obtained in the outlet, more perturbed – in the inlet (*Fig.* 226 - *Fig.* 229). This is exactly opposite in the numerical simulations. Reasons of such result are unclear – one of the possibilities is that there has been human error in the program of the data acquisition system, other – some unexpected physical phenomenon which is not taken into account in the numeric.

Finally, measurements of developed pressure of FLIP-2 has shown that pressure decreases linearly with flowrate, which is explained by applied strong DC magnetic field for potential difference measurements (*Fig.* 230). Amplitudes of oscillations of developed pressure tend to increase with flowrate not exceeding 1-2% (*Fig.* 231 - *Fig.* 234). Finally, strong DSF pulsations are observed in spectrums with the highest flowrate (*Fig.* 235 - *Fig.* 238), but these regimes should be studied in more details. All these trends agree qualitatively well to the obtained numerical results.

Possible future improvements of experimental setup mainly concerns power supply system. The regimes of low interaction parameter N and high slip magnetic Reynolds number Rm_s are mainly limited possible maximal current provided by supply and lack of frequency change. It is discussed that, if frequency could be varied (decreased) this would allow to study regimes in the transition of (theoretically) stable to unstable regime. Unfortunately, this was not possible in current work.

Another drawback in the current setup turned out to be strength of DC field for potential measurements, which guaranteed a sufficiently strong signal, but resulted in unnecessary high pressure drop. This point definitely can be optimized.

Already mentioned post treatment methods should be improved. However, one of the questions with highest interest is possibility to recalculate flow distribution in the channel based on measurements of the magnetic field. The task is not straight forward and would require clear idea of required methods such as correlation functions to be successful. Nevertheless, with proper amount of effort this seems to be realizable and would lift importance of presented magnetic field measurements in the new level.

In the end, author would like to conclude that with this work problem of MHD instability in ALIP (and for that matter in FLIP), is not yet solved and neither completely studied, since it is too profound to be finished in a single PhD work. Nevertheless, author

would like to think that a decent amount of light has been shed on the problematic and this work can serve at least as a reference to any further activities in this topic, as number of important questions has been discussed and some of encountered problems resolved. The nature of results in the work is still qualitative one even though big amount of effort has been put to approach the requirements of quantitative study. Author hopes that in the near future such goal will be possible to achieve.

This final remark ends the presented study.

ACKNOWLEDGMENTS

I would like to acknowledge the help of all people who had direct impact on this PhD work and participated in its creation.

First of all, I would like to thank my supervisors Leonīds Buligins, Yves Fautrelle and Christine Biscarrat for the support facing scientific and administrative problems along whole thesis process.

It is necessary to specially outline the large involvement of prof. Buligins in development of magnetic field measurement technique and also supervising experimental activities in IPUL.

Separately I would like to thank Christian Latge for the organizing the framework of this international thesis.

Secondly, I would like to thank all the team of IPUL who made the experiment to be possible: Ēriks Platacis, Alberts Romančuks, Aleksejs Fļorovs and many other. Special thanks to team which accompanied me in the first experimental session: Jānis Peintbergs, Kalvis Kravalis and Raimonds Nikoluškins.

Thirdly, the theoretical part of the work would be practically impossible without tutoring and help of Agris Gailītis from IPUL. His high scientific standards, mathematical skills, depth of understanding and work ethics will remain for me as a reference for physicist.

Forth, I would like to thank prof. Jānis Priede, for fruitful conversation during dinner in Bad Honnef seminar on MHD and sharing his view on stabilization of ALIP.

Finally, I would like to thank my close friend and soul mate Kristīne Krumberga always being besides me both physically and in my heart during this whole process.

In the end, I would like to acknowledge help of all the organizations without which, this PhD thesis would not be possible:

Embassy of France in Latvia

Grenoble Institute of Technology

Commissariat à l'énergie atomique et aux énergies alternatives (CEA) Cadarache

University of Latvia and faculty of Physics and Mathematics

European Social Fund within the project «Support for Doctoral Studies at University of Latvia».

Thank you,

Linards Goldšteins

BIBLIOGRAPHY

[1] J. A. SHERCLIFF, A textbook of magnetohydrodynamics, Oxford: Pergamon Press, 1965.

[2] P. A. DAVIDSON, An introduction to magnetohydrodynamics, Cambridge: Cambridge University Press, 2001.

[3] F. GAUCHE et al., "French SFR R&D Program and Design Activities for SFR Prototype ASTRID," *Anisan Nuclear Prospects 2010,* pp. 314 - 316, 2011.

[4] S. VITRY et al., "Development of large flow ALIP EMP for application in ASTRID sodium cooled fast reactor and future plant reactors," *8th PAMIR International Conference September 5-9,* vol. 2, pp. 551 - 556, 2011.

[5] G. RODRIGUEZ et al., "Development of experimental facility platform in support of the ASTRID program," *Intl. Conf on FAST REACTOR AND RELATED FUEL CYCLES,* 2013.

[6] "Wikipedia," 2015. [Online]. Available: https://en.wikipedia.org/wiki/Sodium-cooled_fast_reactor#/media/File:Sodium-Cooled_Fast_Reactor_Schemata.svg.

[7] A. M. ANDREEV et al., "Results of an exprimental investigation of electromagnetic pumps for the BOR-60 facility," *Magnetohydrodynamics,* no. 4, pp. 93 - 100, 1978.

[8] A. M. ANDREEV et al., "Choice of constructional Schemes of electromagnetic pumps for atomic energy stations with fast reactors," *Magnetohydrodynamics,* no. 1, pp. 101 - 105, 1982.

[9] I. R. KIRILLOV, "Electromagnetic pumps for Nuclear Energy power," *Magnetohydrodynamics,* no. 3, pp. 87 - 97, 1982.

[10] A. M. ANDREEV et al., "Electromagnetic pump CLIN-3/3500," *Magnetohydrodynamics,* no. 1, pp. 61 - 68, 1988.

[11] A. OTO et al., "Sodium-immersed self-cooled electromagnetic pump design and development of a large-scale coil for high temperature," *Nuclear technology,* vol. 110, no. 2, pp. 159 - 167, 1994.

[12] W. KWANT et al., "In-sodium testing and preformance of a 43.5 m3/min electromagnetic pump for LMR application," in *5th International Conference onn Nuclear Energy*, Nice, 1997.

[13] J. LIELPETERS, MHD machines using liquid metals, Riga: Zinatne, 1969.

[14] A. I. VOLDEK, Induction magnetohydrodynamic machines using liquid metal as working medium, Leningrad: Energia, 1970.

[15] G. A. BARANOV et al., Calculation and Design of Liquid-Metal MHD Induction Machines, Moscow: Atomizdat Publishers, 1978.

[16] H. ARASEKI et al., "Double - supply - frequency pressure pulsation in annular linear induction pump. Part I: Measurment and numerical analysis," *Nuclear Engineering and Design,* pp. 85 - 100, 2000.

[17] A. GAILITIS et al., "Internal hydraulics of magnetohydrodynamic machine with nonhomogenous distribution of forces," *Magnetohydrodynamics,* no. 2, pp. 123 - 127, 1971.

[18] A. GAILITIS et al., "Instability of homogeneous velocity distribution in an induction-type MHD machine," *Magnetohydrodynamics,* no. 1, pp. 87 - 101, 1975.

[19] R. R. KRISHBERG et al., "Experimental study of instability in plane-linear MHD induction machines," *Magnetohydrodynamics,* no. 3, pp. 75 - 78, 1977.

[20] R. A. VALDMANE et al., "Local characteristics of the flow in the channel of an induction MHD machine at large electromagnetic-interaction parameters," *Magnetohydrodynamics,* no. 1, pp. 99 - 104, 1977.

[21] I. R. KIRILLOV et al., "Experimental investigation of flow nonuniformity in a cylindrical linear induction pump," *Magnetohydrodynamics,* no. 2, pp. 107-113, 1980.

[22] I. R. KIRILLOV et al., "Local characteristics of a Cylindrical induction pump for Rms > 1," *Magnetohydrodynamics,* no. 2, pp. 95 - 102, 1987.

[23] I. R. KIRILLOV et al., "Suppression of instability in linear induction pumps for Rms > 1 by modifying the external magnetic field," *Magnetohydrodynamics,* no. 4, pp. 105 - 109, 1981.

[24] A. GAILITIS, "Electrical stabilization of azimuthal mode in large electromagnetic induction pumps," *Magnetohydrodynamics,* no. 4, pp. 3 - 7, 1993.

[25] H. ARASEKI et al., "Manetohydrodynamic instability in annular linear induction pump. Part II. Suppression of instability by phase shift.," *Nuclear Engineering and Design,* pp. 965 - 974, 2006.

[26] ANSYS Inc., ANSYS FLUENT magnetohydrodynamics (MHD) module manual, 2011.

[27] G. K. BATCHELOR, An introduction to fluid dynamics, Cambridge: Cambridge University Press, 2000.

[28] The Clay Mathematics Institute, 2015. [Online]. Available:

http://www.claymath.org/millennium-problems/navier%E2%80%93stokes-equation.

[29] J. H. FERZIGER et al., Computational methods for fluid dynamics, Berlin: Springer, 2002.

[30] I. E. IDELCHIK, Handbook of hydraulic resistance, Moscow: Masinostroienie, 1992.

[31] N. M. OKHREMENKO, "Experimental determination of the channel resistance coefficient for a turbulent MHD flow in a traveling magnetic field," *Magnetohydrodynamics,* vol. 3, no. 3, pp. 119 - 126, 1967.

[32] J. J. VALDMANIS et al., "On theory of longitudal finite length effect in linear induction magnetohydrodynamic machine," *Magnetohydrodynamics,* pp. 101 - 106, 1966.

[33] I. R. KIRILLOV, "Londitudal end effects in cylindrical induction MHD machines," *Magnetohydrodynamics,* no. 2, pp. 109 - 116, 1972.

[34] H. ARASEKI et al., "Double - supply - frequency pressure pulsation in annular linear induction pump. Part II: Reduction of pulsation by linear winding grading at both stator ends.," *Nuclear Engineering and Design,* pp. 397 - 406, 2000.

[35] H. ARASEKI et al., "Magnetohydrodynamic instability in annular linear induction pump. Part I. Experiment and numerical analysis.," *Nuclear Engineering and Design,* pp. 29 - 50, 2004.

[36] H. OTA et al., "Development of 160 m3/min Large Capacity Sodium-Immersed Self-Cooled Electromagnetic Pump," *Journal of NUCLEAR SCIENCE and TECHNOLOGY,* vol. 41, pp. 511-523, 2004.

[37] H. R. KIM, "Design and Experimental Characterization of an EM Pump," *Journal od the Korean Physical Society,* no. 4, pp. 309 - 314, 1999.

[38] H. R. KIM et al., "A design and characteristic experiment of the small annular linear induction electromagnetic pump," *Annals of Nuclear Energy,* no. 38, pp. 1046 - 1052, 2011.

[39] R. E. SCHWIRIAN, "Analysis of linear-induction or travveling-wave electromagnetic pump of annular design," National Aeronautics and Space Administration, Washingtion, 1965.

[40] C. MAIDANA et al., "Design of an Annular Linear Induction Pump for Nuclear Space Applications," in *Proceedings of Nuclear Engineering Technologies for Space 2011*, Albuquerque, 2011.

[41] H. R. KIM, "The theoretical approach for viscose and end effects on a MHD pump for sodium circulation," *Annals of Nuclear Energy,* no. 62, pp. 103 - 108, 2013.

[42] R. R. KRISHBERG et al., “Shunting effect of channel walls on external characteristics of plane-linear induction pump.,” *Magnetohydrodynamics,* no. 1, pp. 142 - 145, 1989.

[43] R. R. KRISHBERG, "Limit of formation of counterparallel flows in plane-parallel induction MHD machines," *Magnetohydrodynamics,* no. 4, pp. 112 - 116, 1978.

[44] L. LEBOUCHER et al., "Channel shape optimization of elecromagnetic pumps," *IEEE transactions on magnetics,* vol. 31, no. 3, pp. 2142 - 2145, 1995.

[45] L. LEBOUCHER et al., “Slot design of optimized electromagnetic pump,” *IEEE transactons on magnetics,* vol. 29, no. 6, pp. 2953 - 2955, 1993.

[46] H. R. KIM et al., "MHD instability analysis of a liquid sodium flow a the annular gap of an EM pump," *Annals of Nuclear Physics,* no. 43, pp. 8 - 12, 2012.

[47] F. WERKHOFF, "Finite - length effects and stability of electromagnetic pumps," *Experimental theral and fluid science,* no. 4, pp. 166 - 170, 1991.

[48] L. GOLDSTEINS et al., “Numerical quasi stationary and transient analysis of annular linear electromagnetic induction pump,” in *COMSOL CONFERANCE ROTERDAM2013*, Rotterdam, 2013.

[49] B. G. KARASEV et al., "3500 m3/h MHD pump for fast breeder reactor," in *In: LIELPETERS. J. and MOREAU R. "Liquid Metal Magnetohydrodynamics"*, Dordrecht, Kluwer Academic Publishers, 1989, pp. 333 - 338.

[50] I. R. KIRILLOV et al., "Integral caracteristics of cylindrical induction pump in case of Rms >1," *Magnetohydrodynamics,* no. 3, pp. 115 - 119, 1987.

[51] A. FANNING et al., "Giant Electromagnetic Pump for Sodium Cooled Reactor Applications," *Electric Machines and Drives Conference,* no. 1, pp. 477 - 482, 2003.

[52] B. K. NASHINE et al., "Design, in-soduim testing and preformance evaluation of annular linear induction pump for a sodium cooled fast reactor," *Annals of Nuclear Energy,* no. 73, pp. 527 - 536, 2014.

[53] R. VALDMANE et al., "Integral characteristics of induction-type MHD machines with large electromagnetic-interaction parameters," *Magnetohydrodynamics,* no. 4, pp. 107 - 109, 1977.

[54] R. R. KRISHBERG et al., "An experimental investigation of MHD flow at high magnetic Reynolds numbers in induction pump having side-wall busbars," *Magnetohydrodynamics,* no. 2, pp. 144 - 146, 1978.

[55] S.-. H. SEONG et al., "Analyses of annular linear inductionn pump characteristics using a time-harmonic finite difference analysis," *Nuclear Engineering and Technology,* vol. 40, no. 3, pp. 213 - 224, 2008.

[56] I. R. KIRILLOV et al., "Two dimensional model of analysis of cylindrical linear induction pump characteristics: model description and numerical analysis," *Energy Conversion and Manegement,* vol. 44, pp. 2687 - 2697, 2003.

[57] R. VALDMANE et al., "Calculation of the characteristics of an induction type MHD pump for Rms > 1 with allowance for the nonuniform distribution of external magnetic field," *Magnetohydrodynamics,* no. 3, pp. 98 - 104, 1982.

[58] I. R. KIRILLOV et al., "Comparison of computer codesfor evaluation of double-supply-frequency pulsation in linear induction pumps," *Nuclear Enginering and Design,* no. 231, pp. 177 - 185, 2004.

[59] J. Kilbane et al., "Multiphysical modeling of an Annular Linear Induction Pump with Applications to Space Nuclear Pwer Systems," National Aeronautics and Space Administartion, Washington, 2014.

[60] P. G. DRAZIN, Introduction to Hydrodynamic Stability, Cambridge: Cambridge University Press, 2002.

[61] ANSYS Inc., ANSYS FLUENT 12.0 User's Guide, 2009.

[62] COMSOL, AC/DC Module User's Guide, 2012.

[63] Y. POLOVKO et al., "Contrast structures and rotating stall in MHD flows," *Transfer Phenomena in Magnetohydrodynamics and Electrocunductive Fows,* no. 51, pp. 395 - 408, 1999.

[64] C. C. YANG et al., “A large electro-magnetic pump for high temperature LMFBR aplications,” *Nuclear Enigineering and Design,* no. 44, pp. 383 - 395, 1977.

[65] H. ARASEKI et al., "Sodium flowrate measurment method of annular linear induction pumps," *Nuclear Engineering and Design,* no. 243, pp. 111 - 119, 2012.

APPENDIX

Analytic solution of external magnetic field distribution in FLIP with discrete current layers of 3 phases in "two coils per phase" configuration.

In this chapter distribution of external magnetic field in air gap of infinitely long FLIP created by discrete sources of linear current is analysed.

First of all, consider problem of periodic single phase setup in Fig. 251:

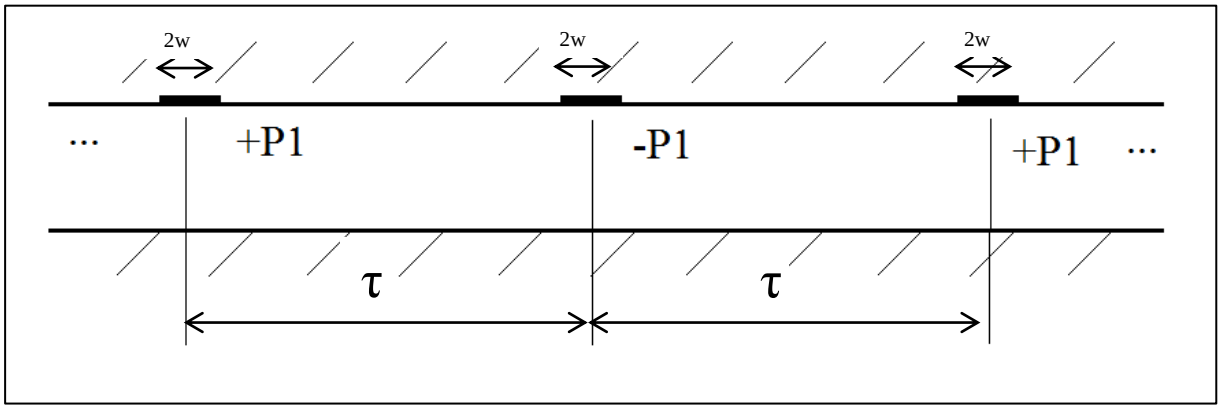

Fig. 251. Schematic of single phase system.

As problem is periodic, only fragment of it can be studied (Fig. 252).

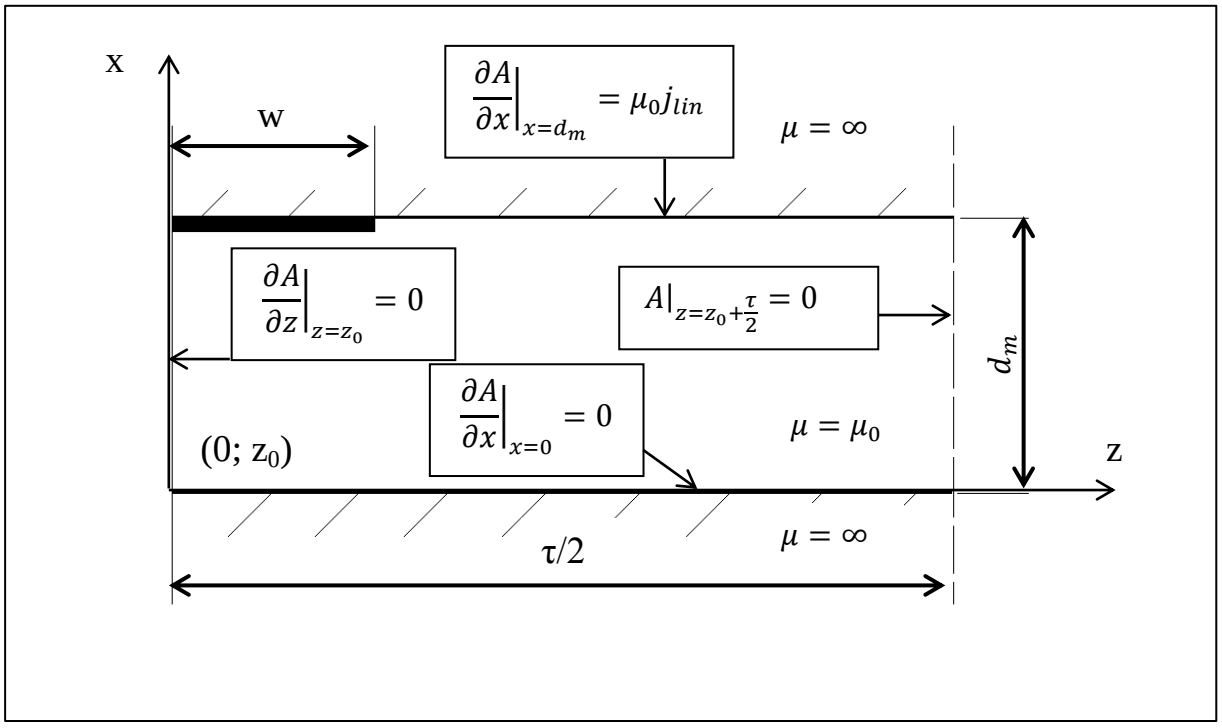

Fig. 252. Schematic of a periodic problem.

Distribution of vector potential in the (non-conductive) air gap is governed by Laplace equation:

$$\Delta A(x,z) = 0 \tag{177}$$

On boundaries over x axis boundary conditions are applied as shown in figure before:

$$\left.\frac{\partial A}{\partial x}\right|_{x=d_m} = \mu_0 j_{lin} \tag{178}$$

$$\left.\frac{\partial A}{\partial x}\right|_{x=0} = 0 \tag{179}$$

External linear current density is applied only in zone $z = [z_0 : z_0 + w]$. Mathematically, such distribution can be described using Heaviside step function:

$$j_{lin} = \frac{I}{2w} \cdot (1 - H(z - [z_0 + w])\,) \tag{180}$$

Where $\frac{I}{2w}$ is effective applied linear current density in the discrete segment.

On boundaries over z axis boundary conditions are following:

$$B_x = \left.\frac{\partial A}{\partial z}\right|_{z=z_0} = 0 \tag{181}$$

$$B_z = A|_{z=z_0+\frac{\tau}{2}} = 0 \tag{182}$$

Using standard method of separation of variables (7)

$$A(x,z) = X(x) \cdot Z(z) \tag{183}$$

One has equation for function *Z(z):*

$$Z''(z) + \alpha_k^2 Z(z) = 0 \tag{184}$$

Which is satisfied with a solution:

$$Z(z) = \sum_{k=0}^{\infty} A_k\, cos(\alpha_k[z - z_0]) + \sum_{k=0}^{\infty} B_k\, sin(\alpha_k[z - z_0]) \tag{185}$$

Using boundary conditions it can be estimated that:

$$\begin{cases} B_k\, cos(\alpha_k 0) - A_k\, sin(\alpha_k 0) = 0 \\ A_k\, cos\left(\alpha_k \frac{\tau}{2}\right) + B_k\, sin\left(\alpha_k \frac{\tau}{2}\right) = 0 \end{cases} \rightarrow \begin{cases} B_k = 0 \\ A_k\, cos\left(\alpha_k \frac{\tau}{2}\right) = 0 \end{cases} \rightarrow$$

$$\alpha_k = \frac{\pi}{\tau}(2k - 1); \quad k = 1{,}2 \ldots \infty \tag{186}$$

Merging unknown constant A_k and function of $X(x)$ into $A_k(x)$ it follows that solution of Laplace equation in particular case should be in from:

$$A(x,z) = \sum_{k=1}^{\infty} A_k(x) \cdot cos(\alpha_k[z - z_0]) \tag{187}$$

In order to successfully apply boundary conditions over x axis, distribution of linear current should have similar form as distribution of vector potential, therefore it should be transformed using Fourier series:

$$j_{lin} = \frac{I}{2w} \cdot (1 - H(z - [z_0 + w])\,) = \sum_{k=1}^{\infty} C_k \cdot cos(\alpha_k[z - z_0]) \tag{188}$$

Norm of series in this case is:

$$\|Z_k\| = \int_{z_0}^{z_0+\frac{\tau}{2}} cos^2(\alpha_k[z - z_0])\, dz = \frac{1}{4\alpha_k} \int_{z_0}^{z_0+\frac{\tau}{2}} 1 + cos(2\alpha_k[z - z_0])\, d(2\alpha_k[z - z_0]) = \frac{\tau}{4} \tag{189}$$

Therefore coefficient C_k:

$$C_k = \frac{I}{2w} \cdot \frac{4}{\tau} \int_{z_0}^{z_0+\frac{\tau}{2}} \big(1 - H(z - [z_0 + w])\big)\, cos(\alpha_k[z - z_0])\, dz = \frac{2I}{\tau} \cdot \frac{sin(\alpha_k w)}{\alpha_k w} \tag{190}$$

Considering that in the discrete element, effective current I is applied with angular frequency ω_B and phase shift φ_0, and coil has n_w number of windings, distribution of linear current by adding time dependent part with specific phase shift for a single phase is:

$$j_{lin} = \frac{2\sqrt{2}I \cdot n_w}{\tau} \sum_{k=1}^{\infty} \frac{sin(\alpha_k w)}{\alpha_k w} \cdot cos(\alpha_k[z - z_0])\, cos(\varphi_0 - \omega_B t) \tag{191}$$

It should be noted, that main goal of detailed discussion was to find form of j_{lin} and show that if in this periodic case distribution of linear current density is known, vector potential can be found by just by finding $A_k(x)$. This is exactly what is done in case of ideal ALIP, by simplifying form of linear current distribution. It is easier to work with complex form of linear current density (148) is transformed to:

$$j_{lin} = \frac{\sqrt{2}I \cdot n_w}{\tau} \sum_{k=-\infty}^{\infty} \frac{sin(\alpha_k w)}{\alpha_k w} \cdot e^{i(\alpha_k[z - z_0] - \omega_B t + \varphi_0)} \tag{192}$$

Now consider a periodic set of three phase discrete linear current elements which are spatially and temporally shifted according to Fig. 253.

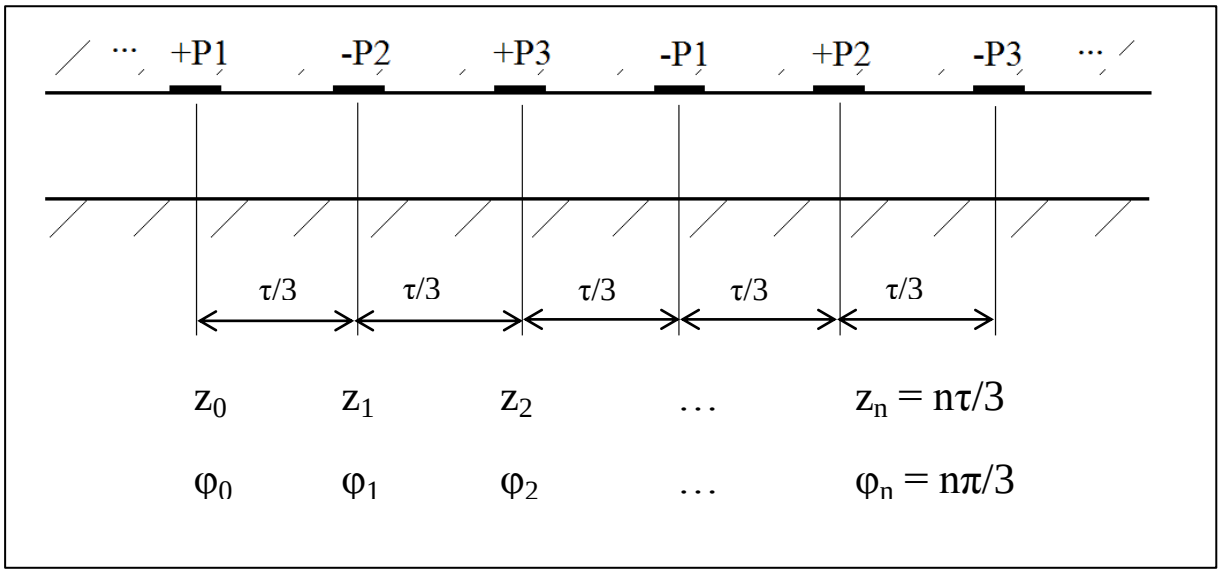

Fig. 253. Schematic of a three phase system.

Apparently, distribution of surface current in such case must be sum of the three:

$$j_{lin} = \frac{\sqrt{2}I \cdot n_w}{\tau} \sum_{k=-\infty}^{\infty} \sum_{n=0}^{2} \frac{sin(\alpha_k w)}{\alpha_k w} \cdot e^{i(\alpha_k[z-z_n]-\omega_B t+\varphi_n)} \tag{193}$$

Where:

$$z_n = \frac{n\tau}{3}; \qquad \varphi_n = \frac{n\pi}{3}; \qquad n = 0,1,2;$$

If so, to have double coil per phase configuration it is possible to simply add another set of same *coils* which are spatially shifted by τ/6:

$$j_{lin} = \frac{\sqrt{2}I \cdot n_w}{\tau} \sum_{k=-\infty}^{\infty} \sum_{n=0}^{2} \frac{sin(\alpha_k w)}{\alpha_k w} \cdot \left[e^{i(\alpha_k[z-z_n]-\omega_B t+\varphi_n)} + e^{i\left(\alpha_k\left[z-z_n-\frac{\tau}{6}\right]-\omega_B t+\varphi_n\right)}\right] \tag{194}$$

This can be rewritten in slightly more comfortable form:

$$j_{lin} = \frac{2\sqrt{2}I \cdot n_w}{\tau} \sum_{k=-\infty}^{\infty} \sum_{n=0}^{2} \frac{sin(\alpha_k w)}{\alpha_k w} \cdot cos\left(\frac{\alpha_k \tau}{12}\right) \cdot e^{i\left(\alpha_k\left[z-z_n-\frac{\tau}{12}\right]-\omega_B t+\varphi_n\right)} \tag{195}$$

Note that constant $-\frac{\tau}{12}$ which appeared in exponent, adds only spatial shift to the distribution of current. If the current distribution is somewhat different (e. g. in other reference frame), this constant can be changed depending on it. Therefore instead of $-\frac{\tau}{12}$ other symbol - z_0 is used.

It is left only to find $A_k(x)$. By looking for the solution in form corresponding to:

$$A(x,z) = \sum_{k=-\infty}^{\infty} \sum_{n=0}^{2} A_k(x) \cdot e^{i(\alpha_k[z-z_n-z_0]-\omega_B t+\varphi_n)} \tag{196}$$

Inserting in into Laplace equation it follows:

$$\frac{\partial^2 A_k(x)}{\partial x^2} - \alpha_k^2 A_k(x) = 0 \tag{197}$$

Solution of which is:

$$A_k(x) = C_k sh(\alpha_k x) + D_k ch(\alpha_k x) \tag{198}$$

Using boundary conditions it is obtained:

$$\begin{cases} \alpha_k C_k ch(\alpha_k 0) + \alpha_k D_k sh(\alpha_k 0) = 0 \quad \rightarrow \quad C_k = 0 \\ \alpha_k D_k sh(\alpha_k d_m) = \dfrac{2\mu_0\sqrt{2}I \cdot n_w}{\tau} \cdot \dfrac{sin(\alpha_k w)}{\alpha_k w} \cdot cos\left(\dfrac{\alpha_k \tau}{12}\right) \end{cases} \rightarrow$$

Therefore amplitude $A_k(x)$ is:

$$A_k(x) = 2\mu_0\sqrt{2}I \cdot n_w \cdot \frac{sin(\alpha_k w)}{\alpha_k w} \cdot \frac{cos\left(\frac{\alpha_k \tau}{12}\right)}{\alpha_k \tau} \cdot \frac{ch(\alpha_k x)}{sh(\alpha_k d_m)} \tag{199}$$

And distribution of vector potential:

$$A(x,z,t) = 2\mu_0\sqrt{2}I \cdot n_w \sum_{k=-\infty}^{\infty} \sum_{n=0}^{2} \frac{sin(\alpha_k w)}{\alpha_k w} \cdot \frac{cos\left(\frac{\alpha_k \tau}{12}\right)}{\alpha_k \tau} \cdot \frac{ch(\alpha_k x)}{sh(\alpha_k d_m)} \cdot e^{i(\alpha_k[z-z_n-z_0]-\omega_B t+\varphi_n)} \tag{200}$$

Finally by considering definition of vector potential:

$$\boldsymbol{B} = \nabla \times \boldsymbol{A} = \frac{\partial A}{\partial x}\boldsymbol{e_z} - \frac{\partial A}{\partial z}\boldsymbol{e_x} \tag{201}$$

Complex forms of magnetic field distribution components are:

$$B_x(x,z,t) = -2\mu_0\sqrt{2}I \cdot n_w \sum_{k=-\infty}^{\infty} \sum_{n=0}^{2} \frac{sin(\alpha_k w)}{\alpha_k w} \cdot \frac{cos\left(\frac{\alpha_k \tau}{12}\right)}{\tau} \cdot \frac{ch(\alpha_k x)}{sh(\alpha_k d_m)} \cdot ie^{i(\alpha_k[z-z_n-z_0]-\omega_B t+\varphi_n)} \tag{202}$$

$$B_z(x,z,t) = 2\mu_0\sqrt{2}I \cdot n_w \sum_{k=-\infty}^{\infty} \sum_{n=0}^{2} \frac{sin(\alpha_k w)}{\alpha_k w} \cdot \frac{cos\left(\frac{\alpha_k \tau}{12}\right)}{\tau} \cdot \frac{sh(\alpha_k x)}{sh(\alpha_k d_m)} \cdot e^{i(\alpha_k[z-z_n-z_0]-\omega_B t+\varphi_n)} \tag{203}$$

In the case one is interested in only height averaged solution of B_x, it reads:

$$B_x(z,t) = -\frac{2\mu_0\sqrt{2}I \cdot n_w}{d_m} \sum_{k=-\infty}^{\infty} \sum_{n=0}^{2} \frac{sin(\alpha_k w)}{\alpha_k w} \cdot \frac{cos\left(\frac{\alpha_k \tau}{12}\right)}{\alpha_k \tau} \cdot ie^{i(\alpha_k[z-z_n-z_0]-\omega_B t+\varphi_n)} \tag{204}$$

Deviation of dispersion relation for model of ideal ALIP

Principal sketch of problem is shown in Fig. 9. Analyse induction equation considering only radial component of magnetic field:

$$\Delta \boldsymbol{B} - \mu_0 \sigma \left(\frac{d_h}{d_m}\right)\left[\frac{\partial \boldsymbol{B}}{\partial t} + (\boldsymbol{v}\nabla)\boldsymbol{B}\right] = -\mu_0 \nabla \times \boldsymbol{j} \tag{205}$$

Assume that current density is evenly spread across non-magnetic gap d_m, one can write:

$$\boldsymbol{j} = \frac{J\sqrt{2}}{d_m} \cdot \frac{1}{2} \sum_{\pm} e^{\pm i(\alpha z - \omega_B t)} \boldsymbol{e_\varphi} \tag{206}$$

Choosing following length and time scales dimensionless coordinates, time and velocity can be introduced:

$$\tilde{z} = \alpha z \tag{207}$$

$$\tilde{R} = \alpha R \tag{208}$$

$$\tilde{z} = \alpha \tilde{t} = \alpha v_B t = \omega_B t z \tag{209}$$

$$\tilde{\boldsymbol{v}} = \frac{\boldsymbol{v}}{v_B} \tag{210}$$

It follows that dimensionless operators are:

$$\frac{\partial}{\partial \tilde{t}} = \frac{\partial}{\omega_B \partial t} \tag{211}$$

$$\tilde{\nabla} = \frac{1}{\alpha}\nabla \;\rightarrow\; \frac{\partial}{\tilde{R}\partial\varphi}\boldsymbol{e_\varphi} + \frac{\partial}{\partial \tilde{z}}\boldsymbol{e_z} = \frac{1}{\alpha}\left(\frac{\partial}{R\partial\varphi}\boldsymbol{e_\varphi} + \frac{\partial}{\partial z}\boldsymbol{e_z}\right) \tag{212}$$

$$\tilde{\Delta} = \frac{1}{\alpha^2}\Delta \;\rightarrow\; \frac{\partial^2}{\tilde{R}^2\partial\varphi^2} + \frac{\partial^2}{\partial \tilde{z}^2} = \frac{1}{\alpha^2}\left(\frac{\partial}{R^2\partial\varphi^2} + \frac{\partial^2}{\partial z^2}\right) \tag{213}$$

Rewriting induction equation:

$$\tilde{\Delta}\boldsymbol{B} - \frac{\mu_0 \sigma \omega_B}{\alpha^2}\left(\frac{d_h}{d_m}\right)\left[\frac{\partial \boldsymbol{B}}{\partial \tilde{t}} + (\tilde{\boldsymbol{v}}\tilde{\nabla})\boldsymbol{B}\right] = -\frac{\sqrt{2}\mu_0 J}{d_m \alpha}\tilde{\nabla} \times \frac{1}{2}\sum_{\pm} e^{\pm i(\tilde{z} - \tilde{t})}\boldsymbol{e_\varphi} \tag{214}$$

Introducing magnetic Reynolds number and choosing scale of magnetic field:

$$Rm = \frac{\mu_0 \sigma \omega_B}{\alpha^2} = \frac{\mu_0 \sigma v_B}{\alpha}\left(\frac{d_h}{d_m}\right) \tag{215}$$

$$\tilde{\boldsymbol{b}} = \frac{\boldsymbol{B} d_m \alpha}{\mu_0 \sqrt{2} J} \tag{216}$$

$$\tilde{\Delta}\tilde{\boldsymbol{b}} - Rm\left[\frac{\partial \tilde{\boldsymbol{b}}}{\partial \tilde{t}} + (\tilde{\boldsymbol{v}}\tilde{\nabla})\tilde{\boldsymbol{b}}\right] = -\frac{1}{2}\sum_{\pm} \tilde{\boldsymbol{\nabla}} \times e^{\pm i(\tilde{z} - \tilde{t})}\boldsymbol{e_\varphi} \tag{217}$$

By estimating RHT equation above, it is rewritten as scalar equation for magnetic field radial component:

$$-\tilde{\nabla}\times\frac{1}{2}\sum_{\pm}e^{\pm i(\tilde{z}-\tilde{t})}\,\boldsymbol{e_\varphi}=\begin{bmatrix}\boldsymbol{e_r} & \boldsymbol{e_\varphi} & \boldsymbol{e_z}\\ 0 & \frac{\partial}{\tilde{R}\partial\varphi} & \frac{\partial}{\partial\tilde{z}}\\ 0 & e^{i(\tilde{z}-\tilde{t})} & 0\end{bmatrix}=\frac{1}{2}\sum_{\pm}\pm ie^{\pm i(\tilde{z}-\tilde{t})}\,\boldsymbol{e_r} \tag{218}$$

It follows:

$$\tilde{\Delta}\tilde{b}-\ Rm\left[\frac{\partial\tilde{b}}{\partial\tilde{t}}+(\tilde{\boldsymbol{v}}\tilde{\boldsymbol{\nabla}})\tilde{b}\right]=\frac{1}{2}\sum_{\pm}\pm ie^{\pm i(\tilde{z}-\tilde{t})} \tag{219}$$

Assuming that in this particular 2D case:

$$\tilde{\boldsymbol{b}}=\frac{1}{2}\sum_{\pm}\widetilde{b_0^{\pm}}(\tilde{\varphi},\tilde{z},\tilde{t})e^{\pm i(\tilde{z}-\tilde{t})}\,\boldsymbol{e_r} \tag{220}$$

$$\tilde{\boldsymbol{v}}=\widetilde{v_z}(\tilde{\varphi},\tilde{z},\tilde{t})\boldsymbol{e_z}+\widetilde{v_\varphi}(\tilde{\varphi},\tilde{z},\tilde{t})\boldsymbol{e_\varphi} \tag{221}$$

Induction equation for magnetic field amplitude is:

$$\left[\frac{\partial^2}{\tilde{R}^2\partial\varphi^2}-1\pm iRm(1-\widetilde{v_z})\right]\widetilde{b_0^{\pm}}+\left[\frac{\partial^2}{\partial\tilde{z}^2}\pm 2i\frac{\partial}{\partial\tilde{z}}-Rm\left(\frac{\partial}{\partial\tilde{t}}+\widetilde{v_z}\frac{\partial}{\partial\tilde{z}}+\widetilde{v_\varphi}\frac{\partial}{\tilde{R}\partial\varphi}\right)\right]\widetilde{b_0^{\pm}}=\pm i \tag{222}$$

Next, instead of Navier-Stokes equation, it is more useful to study vorticity equation since in studied 2D flow there should be single (radial) vorticity component:

$$\rho\left(\frac{\partial\boldsymbol{\omega}}{\partial t}+(\boldsymbol{v}\boldsymbol{\nabla})\boldsymbol{\omega}\right)=\boldsymbol{\nabla}\times\left(-\frac{\lambda_h}{d_h}\cdot\rho\frac{\boldsymbol{v}|\boldsymbol{v}|}{2}+\boldsymbol{f_{EM}}\right) \tag{223}$$

However, it is necessary to estimate EM force contribution:

$$\boldsymbol{\nabla}\times\boldsymbol{f_{EM}}=\boldsymbol{\nabla}\times\left[\left(\frac{\nabla\times\boldsymbol{B}}{\mu_0}-\boldsymbol{j}\right)\times\boldsymbol{B}\right]=\boldsymbol{\nabla}\times\left[\frac{(\boldsymbol{B}\nabla)\boldsymbol{B}}{\mu_0}-\nabla\left(\frac{\boldsymbol{B^2}}{2\mu_0}\right)-\boldsymbol{j}\times\boldsymbol{B}\right] \tag{224}$$

There is zero contribution of first two RHS terms and rotational contribution is expressed only by the cross product of applied current and magnetic field:

$$-\boldsymbol{j}\times\boldsymbol{B}=\frac{\sqrt{2}J}{2d_h}\sum_{\pm}e^{\pm i(\alpha z-\omega t)}\cdot\frac{\mu_0 J\sqrt{2}}{d_m\alpha}\cdot\frac{1}{2}\sum_{\pm}\widetilde{b_0^{\pm}}e^{\pm i(\alpha z-\omega t)}\,\boldsymbol{e_z} \tag{225}$$

Considering only quasi-stationary part, rotor of the EM force reads:

$$\boldsymbol{\nabla}\times\boldsymbol{f_{EM}}=\boldsymbol{\nabla}\times\left(\frac{\sigma v_B}{Rm}\left(\frac{\mu_0 J}{d_m\alpha}\right)^2\cdot\frac{1}{2}\sum_{\pm}\widetilde{b_0^{\pm}}\ \boldsymbol{e_z}\right) \tag{226}$$

Then using dimensionless forms:

$$\rho\alpha^2v_B^2\left(\frac{\partial\tilde{\boldsymbol{\omega}}}{\partial t}+(\tilde{\boldsymbol{v}}\tilde{\boldsymbol{\nabla}})\tilde{\boldsymbol{\omega}}\right)=\alpha\tilde{\boldsymbol{\nabla}}\times\left(-\frac{\lambda_h}{d_h}\frac{\rho v_B^2}{2}\tilde{\boldsymbol{v}}|\tilde{\boldsymbol{v}}|+\frac{\sigma v_B}{Rm}\left(\frac{\mu_0 A}{d_m\alpha}\right)^2\cdot\frac{1}{2}\sum_{\pm}\widetilde{b_0^{\pm}}\,\boldsymbol{e_z}\right) \tag{227}$$

One arrives to dimensionless vorticity equation:

$$Re_\lambda\left(\frac{\partial\tilde{\boldsymbol{\omega}}}{\partial t}+(\tilde{\boldsymbol{v}}\tilde{\boldsymbol{\nabla}})\tilde{\boldsymbol{\omega}}\right)+\tilde{\boldsymbol{\nabla}}\times\tilde{\boldsymbol{v}}|\tilde{\boldsymbol{v}}|=\frac{N_\lambda}{Rm}\cdot\frac{1}{2}\sum_{\pm}\tilde{\boldsymbol{\nabla}}\times\widetilde{b_0^{\pm}}\,\boldsymbol{e_z} \tag{228}$$

Continuity equation is:

$$\frac{1}{\tilde{R}}\frac{\partial\tilde{v}_\varphi}{\partial\varphi}=-\frac{\partial\tilde{v}_z}{\partial\tilde{z}} \tag{229}$$

In a solid body approximation it is assumed that velocity has only a constant axial component (103), which leads to solution of induction equation in a harmonic form with amplitude (104).

$$\tilde{\boldsymbol{v}}=\widetilde{v_z}\boldsymbol{e_z} \tag{230}$$

$$\widetilde{b_0^{\pm}}=\widetilde{b_c^{\pm}}=\frac{1}{\pm i+Rm_s} \tag{231}$$

Assume that in this particular case:

$$\tilde{\boldsymbol{b}}=\frac{1}{2}\sum_{\pm}\widetilde{b_0^{\pm}}(\tilde{\varphi},\tilde{z},\tilde{t})e^{\pm i(\tilde{z}-\tilde{t})}\,\boldsymbol{e_r} \quad (4.66) \qquad \tilde{\boldsymbol{v}}=\widetilde{v_z}(\tilde{\varphi},\tilde{z},\tilde{t})\boldsymbol{e_z}+\widetilde{v_\varphi}(\tilde{\varphi},\tilde{z},\tilde{t})\boldsymbol{e_\varphi} \quad (4.67)$$

First of all, consider base state of velocity (103) and magnetic field amplitude (104). Assume that perturbed state is:

$$\tilde{\boldsymbol{v}}=[\widetilde{v_z}+\delta\widetilde{v_z}(\varphi,\tilde{z},\tilde{t})]\boldsymbol{e_z}+\delta\widetilde{v_\varphi}(\varphi,\tilde{z},\tilde{t})\boldsymbol{e_\varphi} \tag{232}$$

$$\widetilde{b_0^{\pm}}=\widetilde{b_c^{\pm}}+\delta\widetilde{b^{\pm}}(\varphi,\tilde{z},\tilde{t}) \tag{233}$$

Axial and azimuthal perturbations are linked through continuity equation and it is sufficient to define only one of them. Look for a solution where perturbations are complex exponential functions regarding axial direction and time (107), (108). Here n, γ are complex spatial and temporal development rates and $\delta\tilde{v}_{mk}$, $\delta\widetilde{b_{mk}^{\pm}}$ are complex amplitudes:

$$\delta\widetilde{v_z}(\varphi,\tilde{z},\tilde{t})=\sum_{m=1}^{\infty}\sum_{k=-\infty}^{\infty}\delta\tilde{v}_{mk}\,cos(m\varphi)\,e^{n\tilde{z}-\gamma\tilde{t}} \tag{234}$$

$$\delta\widetilde{b^{\pm}}(\varphi,\tilde{z},\tilde{t})=\sum_{m=1}^{\infty}\sum_{k=-\infty}^{\infty}\delta\widetilde{b_{mk}^{\pm}}\,cos(m\varphi)\,e^{n\tilde{z}-\gamma\tilde{t}} \tag{235}$$

$$|\widetilde{v_z}|\gg|\delta\tilde{v}_{mk}| \tag{236}$$

$$\left|\widetilde{b_c^{\pm}}\right|\gg\left|\delta\widetilde{b_{mk}^{\pm}}\right| \tag{237}$$

From continuity it follows:

$$\tilde{v}_\varphi \boldsymbol{e_\varphi} = \delta\widetilde{v_\varphi}(\varphi,\tilde{z},\tilde{t})\boldsymbol{e_\varphi} = -\delta\tilde{v}_{mk} n\frac{\tilde{R}}{m} sin(m\varphi)\, e^{n\tilde{z}-\gamma\tilde{t}}\boldsymbol{e_\varphi} \tag{238}$$

By expanding following equations:

$$\widetilde{\boldsymbol{\omega}} = \widetilde{\nabla}\times\widetilde{\boldsymbol{v}} = \left(\frac{\partial\tilde{v}_z}{\tilde{R}\partial\varphi} - \frac{\partial\tilde{v}_\varphi}{\partial\tilde{z}}\right)\boldsymbol{e_r} = \delta\tilde{v}_{mk}\left(\frac{n^2}{\kappa_m}-1\right)\frac{m}{\tilde{R}} sin(m\varphi)\, e^{n\tilde{z}-\gamma\tilde{t}}\boldsymbol{e_r} \tag{239}$$

$$\widetilde{\nabla}\times\widetilde{b_0^\pm}\boldsymbol{e_z} = \begin{bmatrix} \boldsymbol{e_r} & \boldsymbol{e_\varphi} & \boldsymbol{e_z} \\ 0 & \dfrac{\partial}{\tilde{R}\partial\varphi} & \dfrac{\partial}{\partial\tilde{z}} \\ 0 & 0 & b_0^\pm \end{bmatrix} = \frac{\partial\widetilde{b_0^\pm}}{\tilde{R}\partial\varphi}\boldsymbol{e_r} = -\frac{m}{\tilde{R}}\delta\widetilde{b_{mk}^\pm}\, sin(m\varphi)\, e^{n\tilde{z}-\gamma\tilde{t}}\boldsymbol{e_r} \tag{240}$$

$$\widetilde{\boldsymbol{v}}|\widetilde{\boldsymbol{v}}| \approx \left([\tilde{v}_z + \delta\tilde{v}_z e^{n\cdots}]\boldsymbol{e_z} + \delta\tilde{v}_\varphi e^{n\cdots}\boldsymbol{e_\varphi}\right)|\tilde{v}_z + \delta\tilde{v}_z e^{n\cdots}| \tag{241}$$

$$\widetilde{\boldsymbol{v}}|\widetilde{\boldsymbol{v}}| \approx \left(\tilde{v}_z|\tilde{v}_z| + 2\delta\tilde{v}_{mk}|\tilde{v}_z|\, cos(m\varphi)\, e^{n\tilde{z}-\gamma\tilde{t}}\right)\boldsymbol{e_z} - \delta\tilde{v}_{mk}|\tilde{v}_z| n\frac{\tilde{R}}{m} sin(m\varphi)\, e^{n\tilde{z}-\gamma\tilde{t}}\boldsymbol{e_\varphi} \tag{242}$$

$$\widetilde{\nabla}\times\widetilde{\boldsymbol{v}}|\widetilde{\boldsymbol{v}}| = \begin{bmatrix} \boldsymbol{e_r} & \boldsymbol{e_\varphi} & \boldsymbol{e_z} \\ 0 & \dfrac{\partial}{\tilde{R}\partial\varphi} & \dfrac{\partial}{\partial\tilde{z}} \\ 0 & -n\dfrac{\tilde{R}}{m}|\tilde{v}_z|\delta\tilde{v}_{mk}\, sin(m\varphi) & 2\delta\tilde{v}_{mk}|\tilde{v}_z| e^{(n\tilde{z}-\gamma\tilde{t})}\, cos(m\varphi) \end{bmatrix} e^{n\tilde{z}-\gamma\tilde{t}} \tag{243}$$

$$\widetilde{\nabla}\times\widetilde{\boldsymbol{v}}|\widetilde{\boldsymbol{v}}| = \delta\tilde{v}_{mk}\left(\frac{n^2}{\kappa_m}-2\right)\frac{m}{\tilde{R}}|\tilde{v}_z| e^{n\tilde{z}-\gamma\tilde{t}}\, sin(m\varphi)\, \boldsymbol{e_r} \tag{244}$$

Linearized vorticity equation reads:

$$\left[Re_\lambda\left(\frac{n^2}{\kappa_m}-1\right)(\tilde{v}_z n-\gamma) + \left(\frac{n^2}{\kappa_m}-2\right)|\tilde{v}_z|\right]\delta\tilde{v}_{mk} = -\frac{N_\lambda}{Rm}\cdot\frac{1}{2}\sum_\pm \delta\widetilde{b_{mk}^\pm} \tag{245}$$

Perturbation amplitude $\delta\widetilde{b_{mk}^\pm}$ can be estimated from linearized induction equation:

$$-\frac{m^2}{\tilde{R}^2} - 1 \pm iRm_s + [n^2 \pm 2in - Rm(-\gamma+\tilde{v_z}n)]\delta\widetilde{b_{mk}^\pm} = \pm iRm\delta\tilde{v_z}\widetilde{b_c^\pm} \tag{246}$$

From which:

$$\delta\widetilde{b_{mk}^\pm} = \frac{\pm iRm\widetilde{b_c^\pm}}{\pm iRm_s - \kappa_m' + n^2 \pm 2in + Rm(\gamma-\tilde{v}_z n)}\cdot\delta\tilde{v}_{mk} \tag{247}$$

Then the sum is:

$$\frac{1}{2}\sum_\pm \delta\widetilde{b_{mk}^\pm} = \frac{1}{2}\left[\frac{iRm\left(n^2-\kappa_m'+Rm(\gamma-\tilde{v}_z n) - i(2n+Rm_s)\right)(Rm_s - i)}{-iRm\left(n^2-\kappa_m'+Rm(\gamma-\tilde{v}_z n) + i(2n+Rm_s)\right)(Rm_s + i)}\cdot\frac{1}{\left(n^2-\kappa_m'+Rm(\gamma-\tilde{v}_z n)\right)^2 + (2n+Rm_s)^2}\cdot\frac{1}{1+Rm_s^2}\right] \tag{248}$$

Or:

$$\frac{1}{2}\sum_{\pm}\delta\widetilde{b_{mk}^{\pm}} = \frac{Rm}{1+Rm_s^2}\cdot\frac{n^2-\kappa_m'+Rm(\gamma-\tilde{v}_z n)+(2n+Rm_s)Rm_s}{\left(n^2-\kappa_m'+Rm(\gamma-\tilde{v}_z n)\right)^2+(2n+Rm_s)^2} \tag{249}$$

Dispersion relation of 7th order for n and 3rd order for γ is obtained:

$$Re_\lambda\left(\frac{n^2}{\kappa_m}-1\right)(\tilde{v}_z n-\gamma)+\left(\frac{n^2}{\kappa_m}-2\right)|\tilde{v}_z| = -\frac{N_\lambda}{1+Rm_s^2}\cdot\frac{n^2-\kappa_m'+Rm(\gamma-\tilde{v}_z n)+(2n+Rm_s)Rm_s}{\left(n^2-\kappa_m'+Rm(\gamma-\tilde{v}_z n)\right)^2+(2n+Rm_s)^2} \tag{250}$$

In particular case consider only small development factors to study behaviour of perturbation near stability threshold:

$$n,\gamma \ll 1$$

Then only first order n and γ terms are kept:

$$Re_\lambda(\gamma-\tilde{v}_z n)-2|\tilde{v}_z| = -\frac{N_\lambda}{1+Rm_s^2}\cdot\frac{(Rm_s^2-\kappa_m')+nRm(2-3\tilde{v}_z)+Rm\gamma}{\left(\kappa_m'^{\,2}+Rm_s^2\right)+2n(2Rm_s+Rm\kappa_m'\tilde{v}_z)-2Rm\,\gamma\kappa_m'} \tag{251}$$

By multiplication LHS with denominator of RHS and considering only first order terms:

$$n\left[\frac{N_\lambda Rm(2-3\tilde{v}_z)}{1+Rm_s^2}-4|\tilde{v}_z|(2Rm_s+Rm\kappa_m'\tilde{v}_z)-Re_\lambda\tilde{v}_z\left(\kappa_m'^{\,2}+Rm_s^2\right)\right]-$$

$$-\gamma\left[-\frac{N_\lambda Rm}{1+Rm_s^2}-4|\tilde{v}_z|Rm\kappa_m'-Re_\lambda\left(\kappa_m'^{\,2}+Rm_s^2\right)\right]=$$

$$=2|\tilde{v}_z|\left(\kappa_m'^{\,2}+Rm_s^2\right)-\frac{N_\lambda(Rm_s^2-\kappa_m')}{1+Rm_s^2} \tag{252}$$

Finally, dispersion relation can be rewritten in comfortable form:

$$A_m n - B_m\gamma = \tilde{p}-\tilde{p}_m = \Delta\tilde{p}_m \tag{253}$$

Where:

$$\Delta\tilde{p}_m = \frac{N_\lambda(1-\tilde{v}_z)}{1+Rm_s^2}-\frac{2|\tilde{v}_z|\left(\kappa_m'^{\,2}+Rm_s^2\right)(1-\tilde{v}_z)}{Rm_s^2-\kappa_m'}$$

And coefficients are:

$$A_m = \left[4|\tilde{v}_z|(2Rm_s+Rm\kappa_m'\tilde{v}_z)+Re_\lambda\tilde{v}_z\left(\kappa_m'^{\,2}+Rm_s^2\right)-\frac{N_\lambda}{(1+Rm_s^2)}Rm(2-3\tilde{v}_z)\right]\frac{(1-\tilde{v}_z)}{(Rm_s^2-\kappa_m')} \tag{254}$$

$$B_m = \left[\frac{N_\lambda}{(1+Rm_s^2)}Rm+Re_\lambda\left(\kappa_m'^{\,2}+Rm_s^2\right)+4|\tilde{v}_z|Rm\,\kappa_m'\right]\frac{(1-\tilde{v}_z)}{(Rm_s^2-\kappa_m')} \tag{255}$$

RESUME COMPLET

Le transport des métaux liquides pause habituellement un challenge significatif dû à la nature chimiquement active (corrosion, oxydation) des métaux et à la haute température d'utilisation. Grâce à leur conductivité électrique, la mise en mouvement des métaux liquides peut être réalisée en utilisant le champ magnétique. Pour comprendre les phénomènes mis en jeu, les lois de l'électromagnétisme et de l'hydrodynamique sont couplées dans le domaine d'études appelé la MagnétoHydroDynamique (MHD).

Les études sur la MHD, menées alors comme un sujet à part entière, a connu son début vers la fin des années 1930. Ces études se concentrent sur l'interaction des fluides (métaux liquides, électrolytes et gaz ionisés) conducteurs électriques mais non magnétiques (de perméabilité magnétique relative égale à 1) avec un champ magnétique. Le premier domaine d'études est relatif à l'astrophysique, aux phénomènes géophysiques et à l'auto-excitation de champ magnétique [1]. Vers 1960, le développement de la MHD dans l'ingénierie est devenu plus répandu grâce aux questions de la production d'électricité dans le réacteur thermonucléaire : comme par exemple le problème de confinement de plasma et du refroidissement des surrégénérateurs rapides (SFR) avec du sodium dont la mise en mouvement est assurée par des pompes ElectroMagnétiques (EM) [2]. Ce dernier est toujours un sujet réel complexe abordé dans les études de l'ingénierie et scientifiques actuelles y compris dans ce travail présenté ici.

Dans le cadre du programme français de recherche et développement de la GEN IV SFR, une étude de faisabilité d'implanter des pompes linéaires annulaires à induction de hauts débits (ALIPs) dans les boucles secondaires a été lancée pour le démonstrateur ASTRID (Advanced Sodium Technological Reactor for Industrial Demonstration) [3] [4] [5] (Fig. R 1). Dans le cadre de ces activités, une ALIP de grande taille, PEMDyn, a été conçue et réalisée par le CEA Cadarache avec le débit unitaire maximum de 1800m^3/h (416 L/s) et pour une pression développée de 2.5bar (Fig. R 2).

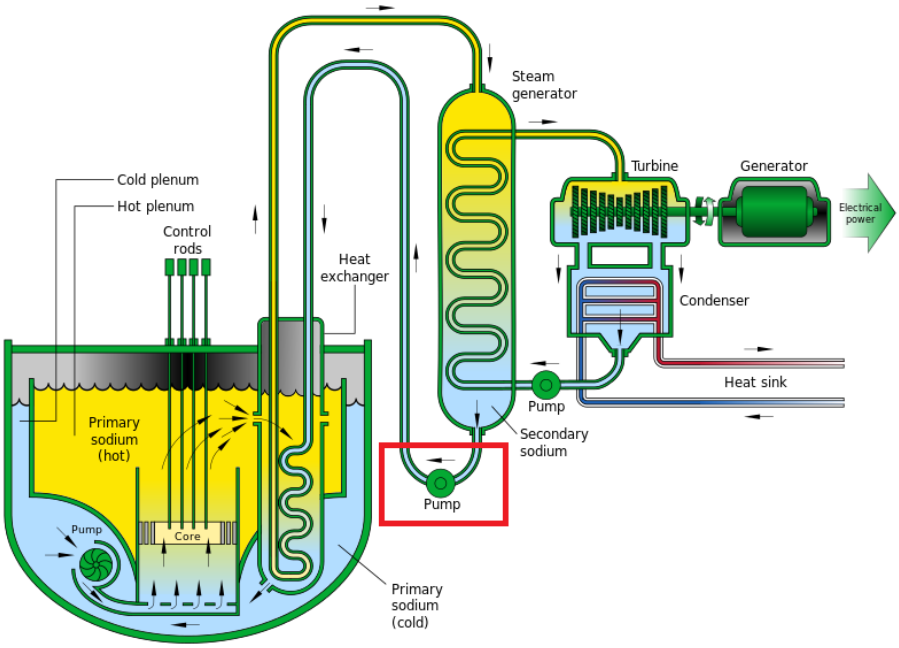

Fig. R 1. Schéma de SFR [6]. La pompe secondaire est marqué par un rectangle rouge.

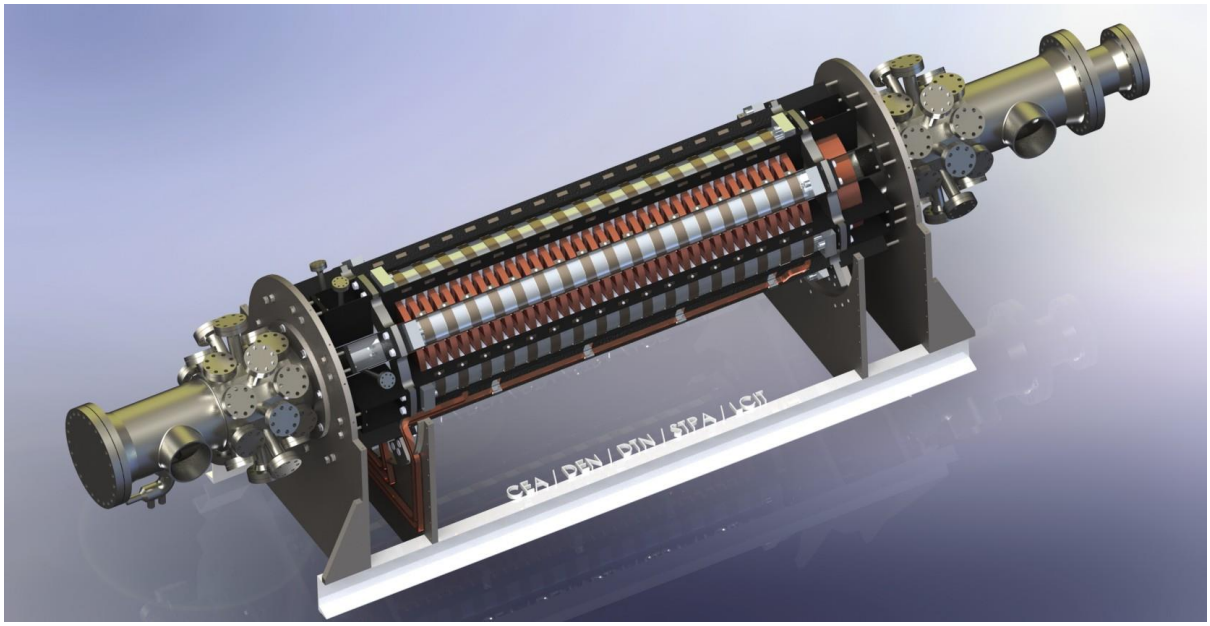

Fig. R 2. PEMDYN ALIP.

Une pompe est positionnée dans la section d'essai de cette boucle PEMDyn relativement compacte ayant tous les composants principaux, tels que les échangeurs de chaleur, un débitmètre et la vanne de commande du débit. Le circuit sodium (réservoir, système de purification) est situé sous la charpente de la section d'essai. La pompe est équipée de 24 piquages en entrée et en sortie de pompes pour implanter une instrumentation spécifique développée pour PEMDyn. Le noyau interne instrumenté de la pompe peut être enlevé et modifié sans nuire à l'intégrité de l'étanchéité du circuit sodium. Le démarrage du programme expérimental de PEMDYN est prévu pour le 4^{ième} trimestre 2015.

L'utilisation d'ALIP dans un SFR a été un souci continu depuis les années 1980 [7] [8] [9]. Actuellement, il existe deux exemples d'ALIP utilisés dans des SFRs ainsi que des installations expérimentales avec des pompes d'échelle semblable confirmant qu'une telle technologie est viable [10] [11] [12].

ALIP est une famille de pompes d'induction électromagnétique (EMIPs) qui sont très utilisées pour le transport du métal liquide dans une grande variété de processus technologiques. Le principal avantage de ces dispositifs est le pompage sans contact du métal liquide utilisant la force électromagnétique et l'absence de pièces tournantes, donc l'étanchéité absolue assure une sécurité absolue par rapport aux pompes mécaniques tout en compromettant l'efficacité. Une technologie telle que développée dans une ALIP est préférable que celle d'une pompe d'induction linéaire plate (FLIP) d'un point de vue de la conception et de l'efficacité. La géométrie des enroulements est considérablement plus simple et les effets de bord transversaux ne s'y produisent pas [13] [14] [15].

La conception d'une ALIP se compose (1) au moins d'un inducteur où des bobines sont intégrées dans le noyau ferromagnétique stratifié, (2) un canal annulaire dans lequel le métal liquide circule dans la direction du champ magnétique glissant et (3) un noyau ferromagnétique interne ou un inducteur secondaire. Cela permet de produire une composante (radiale) perpendiculaire du champ magnétique glissant en appliquant un courant triphasé aux

bobines. La forme du champ magnétique induira des courants dans le métal liquide et le croix-produit créé produit une force EM dans la direction du champ glissant.

En général, une EMIP est un moteur asynchrone linéaire conduit par un courant alternatif (AC) avec un circuit secondaire liquide. Fréquemment, ils partagent des caractéristiques semblables et une grande partie de la théorie sur les EMIPs publiée en 1960 provient de la théorie de ce type de moteurs en considérant l'écoulement bloc du métal liquide et en appliquant une approximation de corps solide [13] [14]. Cette hypothèse simplifie le problème théorique de la MHD à l'électrodynamique. Cependant, les résultats expérimentaux et théoriques supplémentaires ont montré que l'hypothèse du corps solide fournit des résultats fiables pour un nombre de Reynolds magnétique de glissement (Rm_s) autour de 1 et la liquidité du métal fondu ne peut pas toujours être négligée [17] [18] [19] [20]. Cela est dû à l'inhomogénéité de l'écoulement, aux fluctuations des basses fréquences des paramètres électriques et de la pression, aux vibrations et aux pertes de pression supplémentaires qui ont été observées dans une ALIP de haut débit en sodium lorsque Rm_s est relativement élevé [21].

Cette problématique est connue depuis les années 1970 comme phénomène d'instabilité de la MHD par Gailītis et al. [18] mettant en lumière les principaux mécanismes physiques avec un modèle idéal d'ALIP. Le résultat le plus important de ce travail est la dérivation du critère pour des modes azimutaux stables - le seuil d'une instabilité convective étant expérimentalement confirmée dans de nombreux travaux [7] [21] [22]. Quelques méthodes de stabilisation ont été proposées au cours des dernières décennies [23] [24] et en montrant que la stabilisation de l'écoulement peut être réalisée [25], néanmoins en ne résolvant pas le problème entièrement.

Par conséquent, cette problématique est abordée du point de vue académique ou appliquée de façon importante. Du point de vue applicatif, les méthodes de stabilisation sont nécessaires, tandis que du point de vue académique, une analyse théorique plus détaillée des phénomènes d'instabilité et une vérification expérimentale de ces résultats devraient être développées. Il est indéniable que l'échelle et la complexité des phénomènes mis en jeu font que les prospections de cette étude sont trop grandes pour traiter tous les problèmes et pour résoudre toutes les questions immédiatement car elle n'a pas été faite pendant les 30 dernières années. Cependant, le problème est toujours valeur pour aborder présumer cela avec une compréhension plus profonde gagnée par un travail plus prolongé et plus intensifié qu'elle pourrait être par la suite résolue.

Dans ce cadre, les principaux objectifs de cette thèse sont :

- ✓ d'élaborer les conditions et paramètres qui caractérisent les instabilités MHD dans une ALIP idéale et de les vérifier,
- ✓ de développer un modèle numérique réaliste et de confronter les résultats numériques et expérimentaux

Par conséquent, les principales questions du chercheur portent sur :

1) les conditions d'une ALIP idéale pour devenir unstable,
2) la façon d'éviter ces conditions,

3) la vérification des résultats théoriques d'une ALIP idéale,
4) le développement d'un modèle numérique réaliste,
5) les paramètres à analyser dans le modèle numérique et à comparer avec les paramètres mesurés,
6) les méthodes de mesures des paramètres nécessaires,
7) les méthodes de traitement des données expérimentales.

En conséquence, les différentes tâches du travail ont consisté à :

1) analyser un système d'équations de MHD pour une ALIP idéale théorique et identifier les conditions pour lesquelles les perturbations commencent à s'amplifier,
2) confronter les résultats théoriques de la thèse dans le cadre de la recherche existante,
3) examiner théoriquement l'opération et la stabilisation stables d'une ALIP idéale,
4) calculer et comparer les taux de croissance théoriques et numériques de perturbation pour une ALIP idéale,
5) développer le modèle numérique d'une EMIP réaliste et élaborer régimes potentiellement instables,
6) entreprendre une expérience équivalente au modèle numériquement développé et comparer les résultats.

Méthodologies et approches

L'approche de la recherche est double appliquant les deux méthodes quantitatives pour l'analyse théorique, numérique et d'expérimentale et l'interprétation qualitative des résultats obtenus. En conséquence, l'étude se concentre sur la concordance entre chacun des trois aspects des recherches avec un intérêt particulier pour deux aspects importants :

- Comparaison des investigations théoriques et numériques d'une ALIP idéale,
- Analyse des investigations numériques et expérimentales dans une EMIP réelle.

Cette approche est due au fait qu'il est difficile dans le cadre d'un travail théorique de prendre en considération tous les effets réels, par exemple la géométrie finie, la répartition discrète des courants. Cela peut être également considéré comme la vérification d'un modèle numérique (ou théorique). D'autre part, il est pratiquement impossible de créer un EMIP idéal expérimentalement.

L'étude théorique en grande partie est basée sur l'analyse de la stabilité linéaire des vortex (ou Navier-Charge), de l'induction et des équations de continuité du cas en 2D (dans le plan φ-z).

Pour les études numériques, le logiciel commercial FLUENT ANSYS avec le module MHD est utilisé pour résoudre un système instable des équations MHD numériquement en utilisant la méthode des volumes finis et l'algorithme SIMPLE pour la correction de pression. Un schéma de pas de temps implicite est utilisé au deuxième ordre pour l'équation de la quantité de mouvement et au premier ordre pour le champ magnétique.

Pour quelques calculs de champ magnétique dans le domaine de fréquence, le logiciel commercial COMSOL Multiphysics basé sur la méthode d'élément fini a été utilisé.

Les données expérimentales ont été enregistrées au format numérique à l'aide du logiciel de National Intruments et du logiciel LabView.

La majeure partie du travail de post-traitement est effectuée en utilisant le logiciel commercial MatLab où les fonctions, telles que la transformée de Fourrier, ajustement, visualisation sont mises en application. Une grande partie des images dans ce travail est obtenue par l'intermédiaire de MatLab.

CHAPITRE 1 : EXAMEN BIBLIOGRAPHIQUE

Les principales conclusions de l'étude bibliographique peut être résumé en:

1. En utilisant des modèles axisymétriques 2D, la distribution du champ magnétique dans la longueur et dans la hauteur du canal de pompage peut être calculée. Des approximations de corps solide peuvent être utilisées et la pression développée peut être estimée dans le cas d'un flux stationnaire numériquement et analytiquement.
2. Dans la plupart des cas, l'équation (57) est appliquée et des effets peuvent être moyennés dans la hauteur. Ceci simplifie le problème et permet l'analyse simplifiée des écoulements asymétriques.
3. Des pulsations DSF sont provoquées par l'oscillation de la composante du champ magnétique qui semble dues à la longueur finie de l'inducteur et sont effet électromagnétique.
4. Le seuil de stabilité prédit théoriquement est vérifié expérimentalement et numériquement. On constate que, quand le seuil est dépassé, les perturbations azimutales de la vitesse sont amplifiées avec l'augmentation du glissement (Rm_s).
5. On observe expérimentalement la croissance des perturbations azimutales le long du canal de pompage.
6. Avec des valeurs élevées de Rm_s, bien que la diminution des amplitudes de perturbation est observée, des oscillations de débit, de la pression etc… apparaissent et augmentent rapidement avec Rm_s.
7. Cette perte de stabilité est près du maximum local expérimental de la caractéristique p-q (cartes de performances) où dans le régime de transition incontrôlé de l'état stable à instable peut être observé.
8. Le modèle 2D asymétrique (θ-z) est représentatif de l'instabilité. Les pulsations caractérisant l'instabilité sont de basses fréquences et sont trouvées dans les résultats de ce modèle numérique.
9. Les résultats numériques prouvent que, après le seuil de stabilité atteint, on observe le pic de basses fréquences dans le spectre de pression. Avec l'augmentation de Rm_s , des multiples de la pulsation en basse fréquence apparaissent.
10. La stabilisation utilisant le déphasage dans la connexion d'enroulement est confirmée pour diminuer des oscillations et pour stabiliser l'écoulement au-delà.

Néanmoins, il y a quelques différences importantes entre les études théoriques, expérimentales et numériques qui limitent la pleine analyse et la compréhension du processus d'instabilité MHD:

- Il n'y a aucune évaluation théorique de la perturbation temporelle et du développement spatial. Par conséquent même l'amplification de la perturbation est mesurée, il n'existe aucune possibilité de vérifier ce résultat, sauf par comparaison avec des calculs numériques.
- Le modèle numérique présenté, quoique capable de représenter les instabilités, est fortement simplifié. Par exemple la forme appliquée du magnétique externe est sévèrement approximée et prendre en considération seulement la dissipation visqueuse dans l'écoulement fortement turbulent ne pourrait pas tenir la critique. Par conséquent, des méthodes de simulations d'instabilités MHD devraient être également améliorées en prenant en considération de plus en plus les phénomènes complexes.
- Pour continuer de développer des outils plus évolués, la vérification des solutions numériques dans des cas simplifiés d'instabilité MHD doit être faite a priori. C'est problématique ; depuis seulement l'évaluation théorique est le seuil (74) et des modèles de l'instabilité MHD dans une ALIP idéale n'ont pas été étudiés.
- En ce moment il est clair que les pulsations basses fréquences représentent le phénomène d'instabilité MHD, mais les mécanismes de génératifs de telles pulsations ne sont pas bons compris.
- Il y a également des incertitudes au sujet des méthodes de stabilisation d'une ALIP. Par exemple, la méthode expérimentale présentée fonctionne mais les méthodes mathématiques ne permettent pas d'argumenter ces observations.
- Du point de vue expérimental, il semble que des spectres de pression pourraient être utilisés pour caractériser le comportement global d'une ALIP et les effets d'instabilités MHD. Cependant, il est incertain qu'une telle comparaison soit quantitative.

Évidemment, les points présentés dans cette étude sont directement corrélés avec les questions encore existantes et les études concernant les instabilités dans une ALIP.

CHAPITRE 2 : INVESTIGATIONS THÉORIQUES

La première partie de ce chapitre est basée sur l'analyse linéaire de la stabilité des vortex, induction et l'équation de continuité pour, tout d'abord, analyser la nature des instabilités MHD dans une ALIP idéale. Les effets sont ramenés à une moyenne dans l'épaisseur du canal de pompage ; donc un écoulement 2D (φ, z) est considéré (donc composant simple des vortex) avec la composante radiale simple du champ magnétique. Des effets globaux de la dissipation turbulente sont pris en considération par des moyens semi-empiriques utilisant le facteur de frottement (relation de Blasius).

Le système d'équations est écrit à l'aide de nombres sans dimension, perturbé de la solution d'équilibre (écoulement homogène) et linéarisé. La relation de dispersion simplifiée est obtenue, prenant seulement en considération des termes purement diffusifs du second degré du développement spatial. Puis en utilisant la relation de dispersion, la nature du développement de la perturbation est analysée dans le processus d'instabilité convectrice (les perturbations s'amplifient, mais partent du système) et des conditions pour l'instabilité absolue (les perturbations s'amplifient et restent dans le système) sont étudiées.

Les principaux résultats peuvent être récapitulés comme suit:

L’équation obtenue (92) pour le développement de la perturbation met en évidence le comportement dans un système d’instabilités convectives et permet d’estimer le taux de croissance (94) et la vitesse de phase (93) Tout d'abord, l'évaluation du développement spatial de la perturbation dans un type d'instabilité convective est obtenue (94), et donne une idée comment la perturbation initiale existante sera amplifiée. Une telle évaluation exige quelques informations sur des amplitudes des perturbations initiales. Si l'amplification atteint l'ordre de grandeur de l'écoulement moyen, on pourrait compter que les effets non linéaires deviennent plus prononcés et mènent par la suite à la perte de la stabilité. Les résultats suggèrent que ceci pourrait être l'instabilité MHD en cause dans une ALIP dans certains cas, même si bien au-dessous du seuil de l'instabilité absolue de Fig. R 3. Théoriquement, le seuil d’instabilité absolue trouvé (96) qui, dans le cas d’un parameter d’intéraction élevé N, l’instabilité absolue peut se produire quand $Rm_s \approx \frac{Rm}{3}$.. Par conséquent, si Rm est relativement faible (3…4) en principe, il est possible d’atteindre ce seuil d’instabilité absolue.

D'autre part, le résultat présenté surestime la stabilité décrite dans les études expérimentales existantes (Fig. R 3) dans la littérature. Une des raisons d'un tel résultat pourrait être que les approximations utilisées dans la relation de dispersion ne sont pas suffisamment précises et des termes d’ordre supérieur qui doivent être considérés.

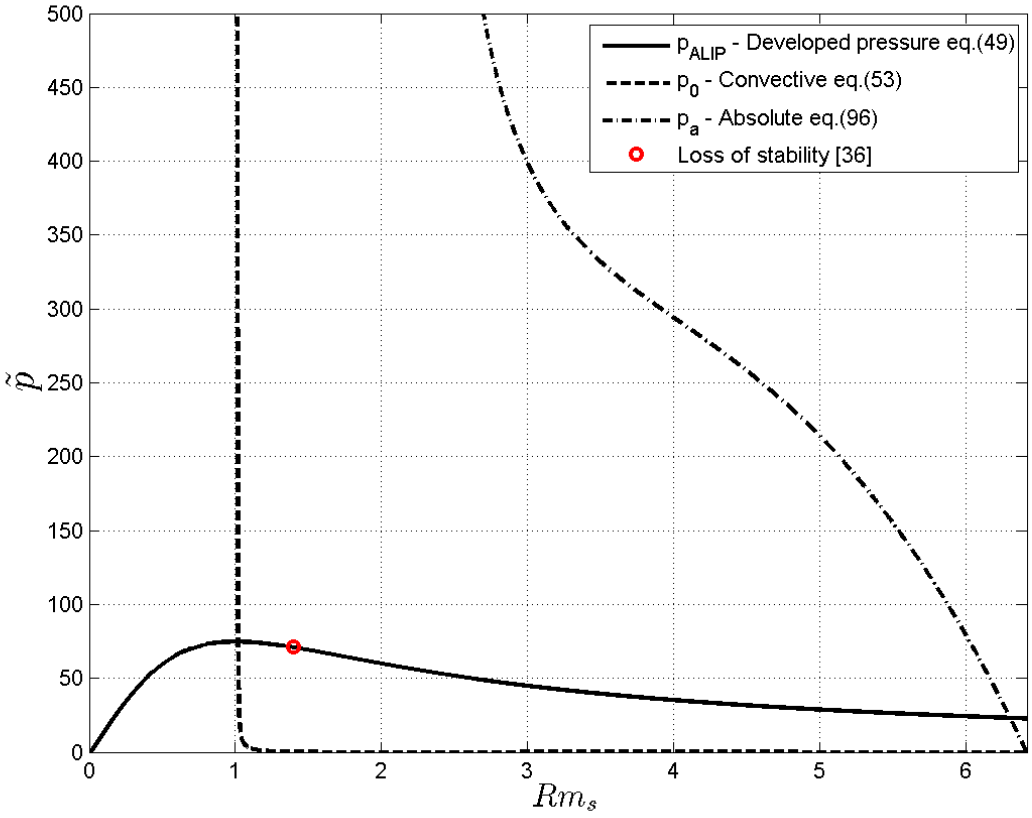

Fig. R 3. La pression théorique développé, seuil de stabilité convective et de stabilité absolue, et la perte expérimentale de stabilité ALIP dans [36].

Dans la deuxième partie de ce chapitre, des techniques d'opération de stabilisation d'ALIP idéale sont discutés. On montre sur un exemple intuitif que la croissance de la perturbation de vitesse peut être expliquée avec la forme de la pression (force) -

caractéristique de la vitesse. Si le gradient de cette courbe est positif la perturbation pourrait augmenter, s'il devient négatif une diminution est observée.

Puis on montre que, en choisissant un régime de fonctionnement stable en termes de nombre de Reynolds magnétique de glissement, ces régimes peuvent être relativement facilement obtenus par l'alimentation électrique conduite en jouant sur le couple fréquence/courant Fig. R 4. Non seulement cette méthode garantit la stabilité par des moyens relativement simples, mais également un rendement élevé de la pompe près du maximum de la courbe.

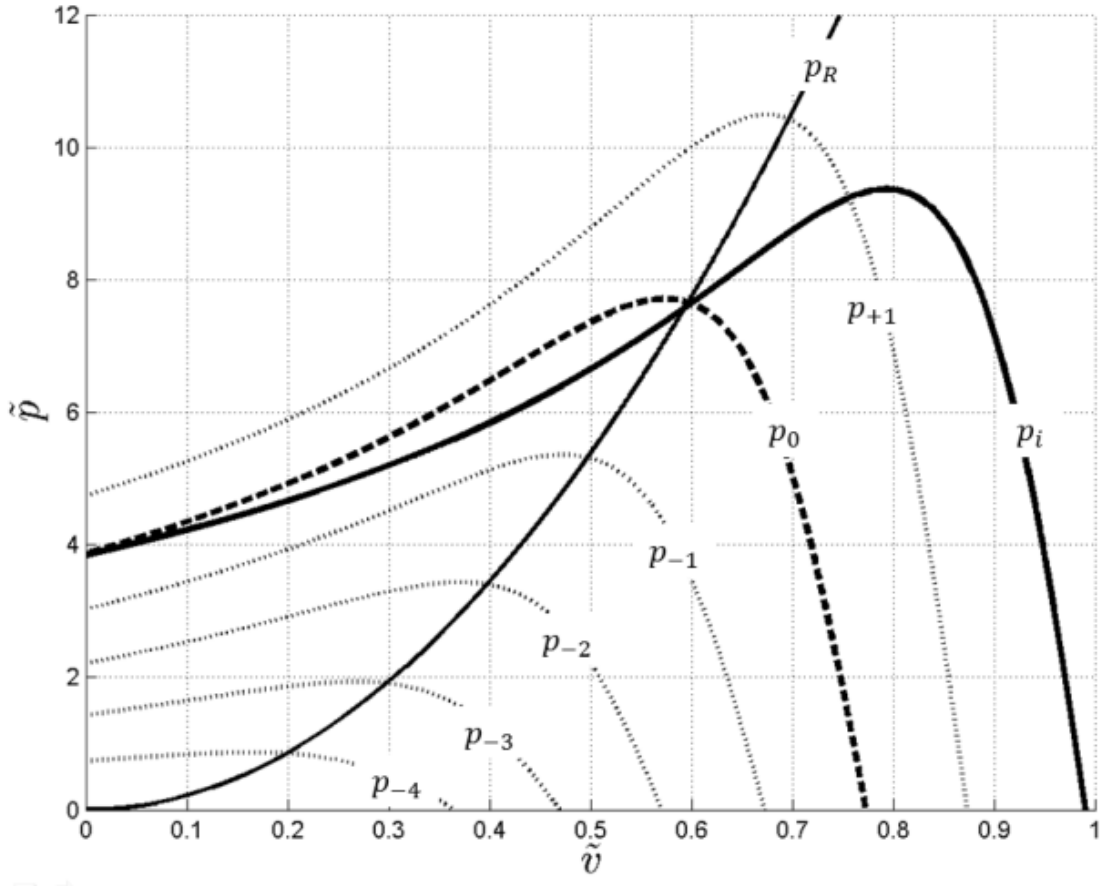

Fig. R 4. Caractéristique initiale p_i *et les caractéristiques stabilisée* $p_{-4} - p_{+1}$ *couplé avec charge externe* p_R. $N_\lambda = 100;\ \ Rm = 5.$

Cependant, il peut y avoir la situation qui les paramètres de la puissance élevée conduisant l'approvisionnement sont limités et ne peuvent pas couvrir tous les régimes, puis la stabilisation avec l'approvisionnement supplémentaire peut être présentée (138), Fig. R 5. Prof. J. Priede a proposé une telle idée.

En utilisant l'analyse de stabilité linéaire simplifiée, on montre que si la vitesse de stabilisation du champ magnétique est égale à la vitesse moyenne du fluide, une telle technique corrige simplement le gradient autour du point de fonctionnement (le tournant de positif au négatif). On montre que le maximum exige un courant de stabilisation selon (153) qui est d'environ 36% de l'alimentation (Fig. R 6), mais la plage de fréquence souhaitable théoriquement devrait descendre à zéro selon le point à stabiliser.

Nous soulignons que dans la présente étude sur la stabilisation, seule la part quasi-stationnaire de la force EM est considérée et l'aspect des battements basse fréquence potentiels dus à l'interférence des deux sources appliquées sont négligées. Dans certains cas, il se peut de limiter l'application de la technique postérieure de stabilisation au moins du point de vue du comportement mécanique des structures. Néanmoins, des preuves sont montrées qu'une telle technique de stabilisation devrait fonctionner.

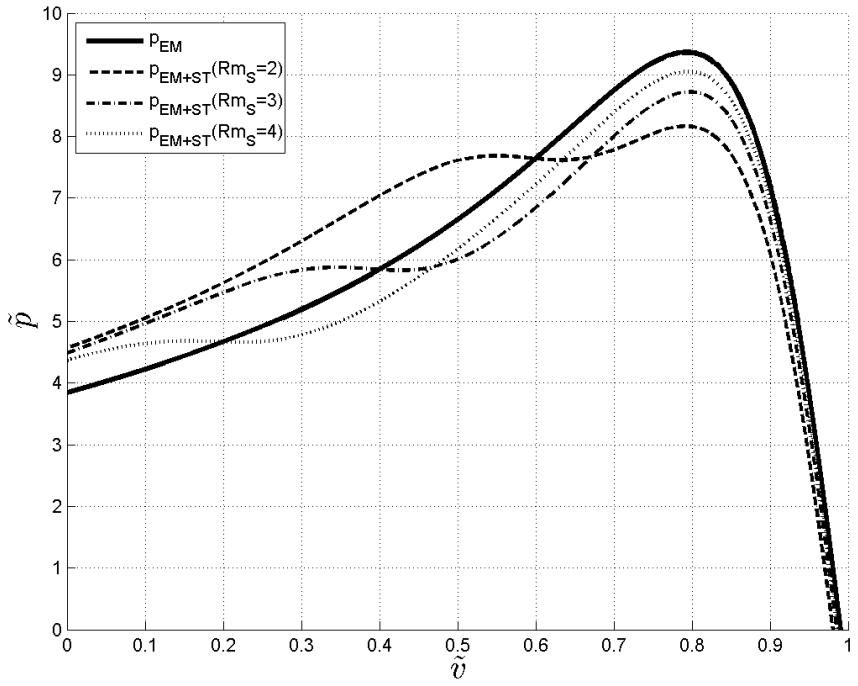

Fig. R 5. Stabilisation des régimes $\tilde{v} = [0.2, 0.4, 0.6]$ $N_\lambda = 100$; $Rm = 5$; $\kappa_m' = 1$, *when* $\tilde{v}_1 = \tilde{v}$.

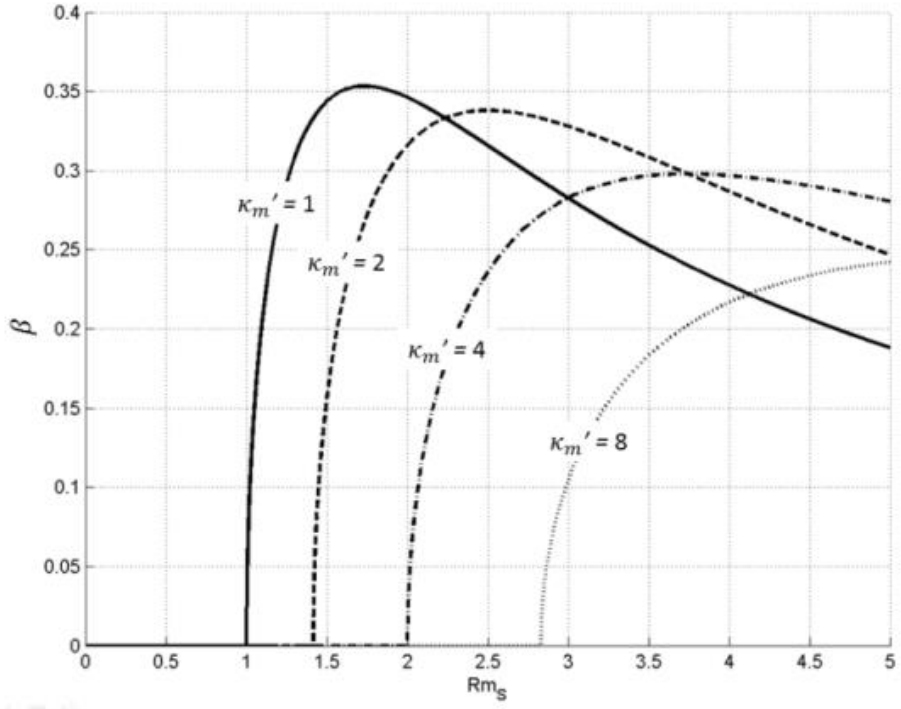

Fig. R 6. Crucial β *en fonction de*Rm_s *avec différents* κ_m' *quand* $\tilde{v}_1 = \tilde{v}$.

CHAPITRE 3 : INVESTIGATIONS NUMÉRIQUES

Dans la première partie de ce chapitre, un modèle numérique d'ALIP idéale est créé utilisant le logiciel ANSYS FLUENT MHD. C'est une première d'une étude appliquée à une ALIP idéale. De telles investigations n'ont pas été réalisées auparavant

Le modèle numérique étudié est 2D (avec une seule cellule dans la direction perpendiculaire au plan) et périodique dans le sens de la longueur et de la largeur. Dans le sens de la longueur, la géométrie comporte une seule longueur d'onde. Elle a été intentionnellement simplifiée pour être aussi proche que possible du modèle théorique pour permettre la comparaison. Cependant, la principale différence entre le modèle et la théorie réside dans le fait que la procédure numérique est entièrement transitoire, tandis que le modèle théorique ne prend en compte que les forces stationnaires.

Le calcul est effectué de la manière suivante :

1. calcul de la distribution de vitesse avec 0,5% d'amplitude de perturbation de vitesse moyenne lors de l'initialisation
2. la force électromagnétique est ensuite calculée en transitoire (la vitesse étant fixée) sur un temps de 0.6s pour avoir une force suffisamment développée
3. le calcul de magnétohydrodynamique est effectué pendant 1s, le développement de la perturbation de vitesse et de la force intégrale étant enregistrés.

A partir des données temporelles sauvées il est possible de trouver numériquement le facteur de développement de la perturbation qui peut avoir un comportement exponentiel et oscillant. Ceci est réalisé avec le logiciel MatLab.

Cinq études avec différents paramètres d'interaction sont effectuées et les résultats numériques obtenus sont comparés aux évaluations théoriques. L'accord entre les deux peut être considéré à tout le moins comme satisfaisant, puisque les tendances principales du taux temporel de développement sont capturées et la force quasi-stationnaire développée dans tous les cas est très bien représentée (Fig. R 7- Fig. R 11). On peut également dire que, en employant ce modèle aux capacités relativement modérées, plusieurs outils numériques ont été mis en oeuvre.

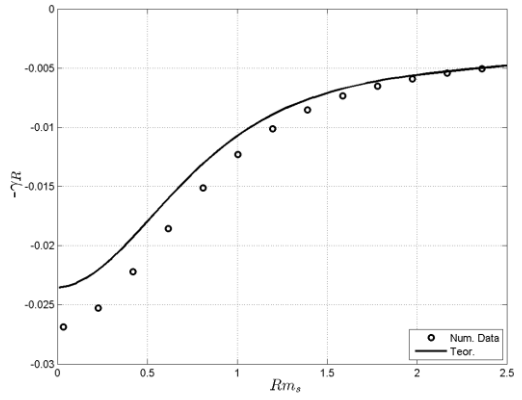

Fig. R 7. Comparaison des résultats numériques et théoriques de taux d'évolution temporelle$-\gamma_R$: $N = 0.03$.

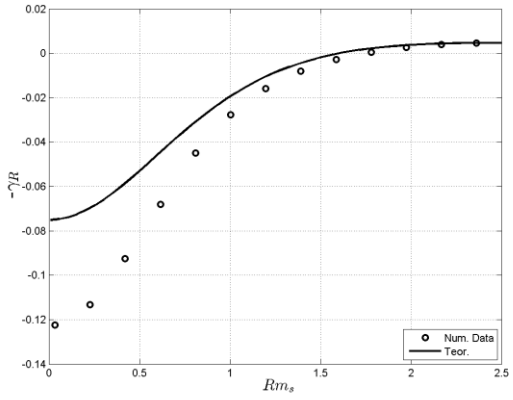

Fig. R 8. Comparaison des résultats numériques et théoriques de taux d'évolution temporelle $-\gamma_R$: $N = 0.16$.

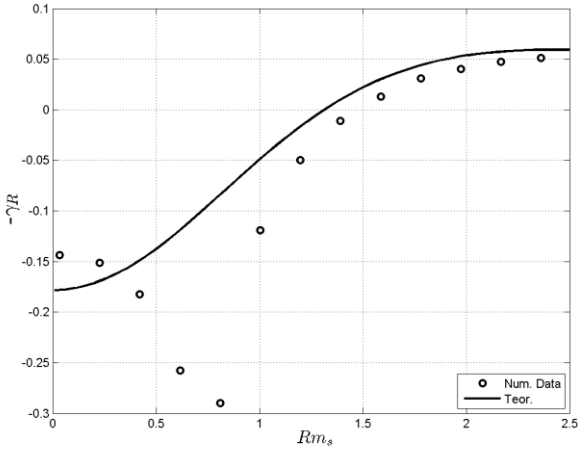

Fig. R 9. Comparaison des résultats numériques et théoriques de taux d'évolution temporelle $-\gamma_R$: $N = 1$.

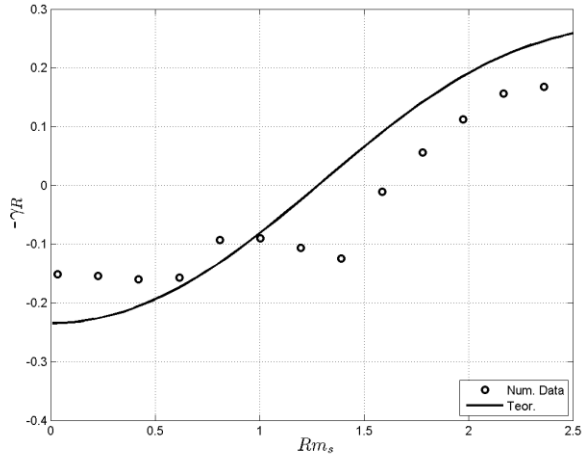

Fig. R 10. Comparaison des résultats numériques et théoriques de taux d'évolution temporelle $-\gamma_R$: $N = 5.9$.

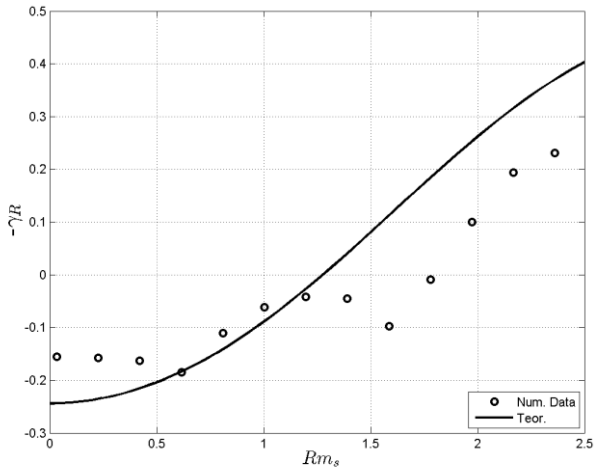

Fig. R 11. Comparaison des résultats numériques et théoriques de taux d'évolution temporelle $-\gamma_R$: $N = 13.2$.

Cependant, on observe quelques déviations entre les résultats numériques et théoriques et les raisons de ces différences devront être étudiées plus rigoureusement par la suite. Tout d'abord, ces différences peuvent se rapporter aux choix des paramètres numériques – valeurs des pas de temps d'espace et de temps. Ensuite le temps calcul de 0.6s choisi pourrait ne pas être suffisant et de plus longues périodes pourraient être nécessaires pour développer entièrement l'état quasi stationnaire. Une autre raison qui pourrait présenter des erreurs est la méthode d'évaluation du facteur de développement qui peut être encore améliorée. En conclusion, il convient aussi de noter que ces modèles théoriques et numériques ne sont pas exactement identiques, de même en ce qui concerne le degré de précision temporelle (toutes les hypothèses faites dans la théorie linéaire).

En se basant sur des résultats raisonnables obtenus dans le cas d'une étude d'ALIP idéale, nous avons réalisés un développement ultérieur du modèle 2D plus réaliste. Pour ce faire, tout d'abord il est nécessaire de prendre en compte une distribution du champ

magnétique réaliste. En particulier, ceci est réalisé par des moyens semi-analytiques, en déterminant la distribution du champ dans le cas de la géométrie périodique et prenant en considération la plupart des harmoniques importantes. Ainsi, la distribution est ajustée à la solution numérique utilisant le logiciel de COMSOL, en ajoutant la partie oscillante et le déclin du champ près des extrémités de l'inducteur (Fig. R 12). En conclusion, le champ magnétique est moyenné dans l'épaisseur du canal.

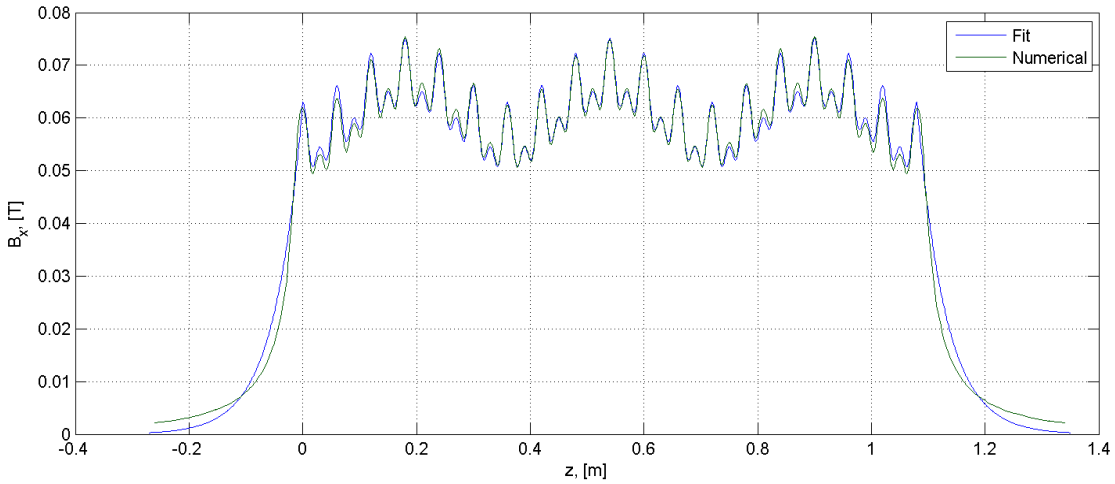

Fig. R 12. Comparaison des résultats numériques et analytiques de magnétique module de champ.

Un autre aspect important dans un tel genre de modèle est la nécessité de conserver les valeurs de l'ensemble de nombres sans dimensions, puisque le phénomène est moyenné dans la hauteur. On montre que toutes les manipulations nécessaires peuvent être faites en changeant des propriétés (conductivité et densité) de matériel (sodium).

En conclusion, dans la construction du modèle plusieurs types de vitesse d'alimentation réaliste peuvent être mis en application en utilisant des études séparées. Deux modèles légèrement différents avec et sans la présence de sous-canaux ont été étudiées, les deux ayant un rapport avec des cas expérimentalement étudiés par la suite.

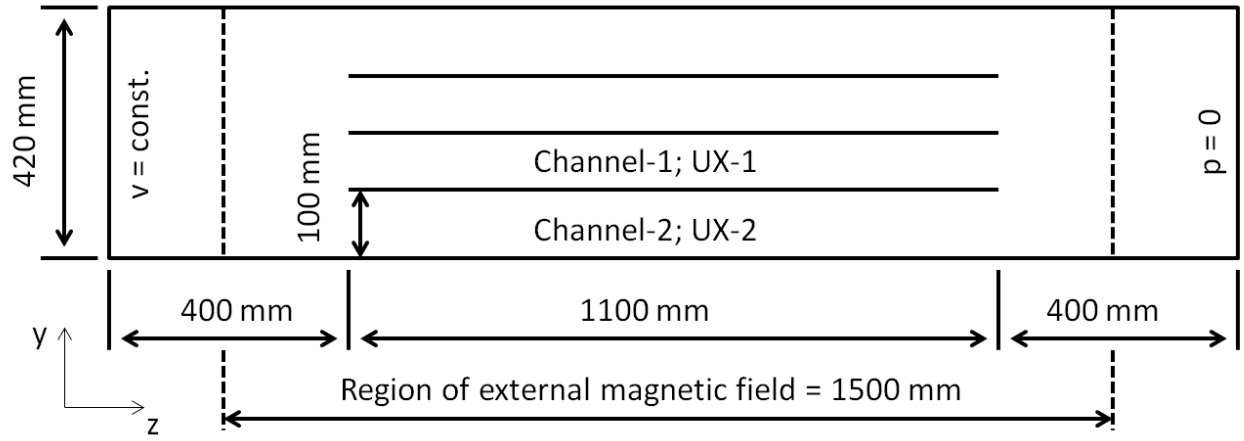

Fig. R 13. Géométrie et la configuration du modèle numérique avec 4 sous-canaux.

Les résultats ont prouvé que dans le modèle numérique avec 4 sous-canaux (Fig. R 13), le champ magnétique et la vitesse axiale sont plus forts dans les canaux latéraux et une zone de recirculation étroite existe près de la paroi externe (Fig. R 14). Avec l'augmentation

du du débit, le champ magnétique et de la vitesse augmentent plus rapidement dans les canaux centraux, les deux étant évidemment corrélés (Fig. R 15, Fig. R 16). L'écoulement a maintenu stable et aucune oscillation n'a été observée. La validité de ces résultats sera comparée aux résultats expérimentaux plus tard.

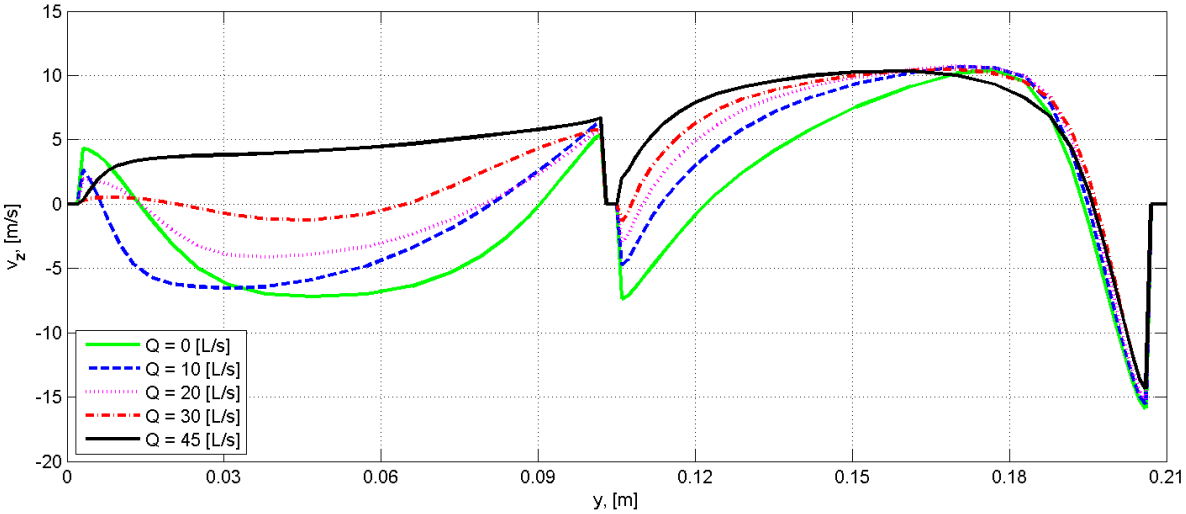

Fig. R 14. Répartition des v_z [m/s] au milieu du canal pour différents débits.

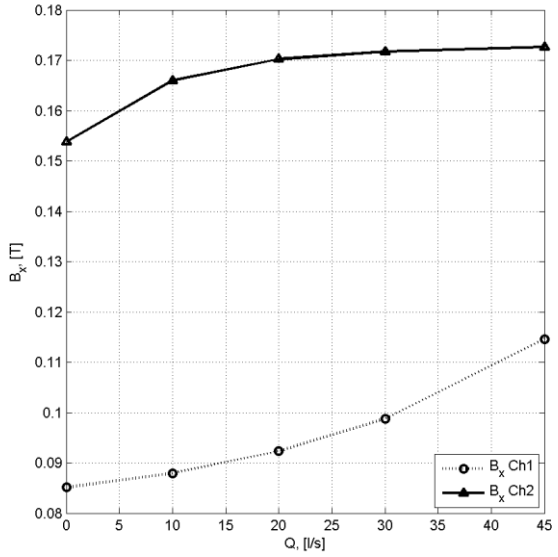

Fig. R 15. Amplitude B_x [T] dans le milieu de la sous-canal en fonction du débit.

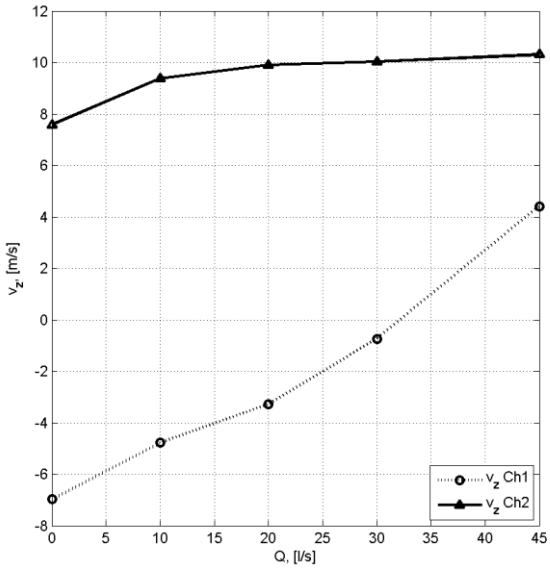

Fig. R 16. v_z [m / s] dans le milieu de la sous-canal en fonction du débit.

Le deuxième modèle numérique sans sous-canaux a été créé prenant en considération la géométrie de la boucle 3D pour calculer l'état réel de l'admission (Fig. R 17). Des méthodes avec traitements plus détaillés ont été aussi développées et employées. Tout d'abord il s'agit du calcul de distribution et de la dynamique utilisant l'enregistrement de données avec la différence de période de ¼ et du calcul du module du champ magnétique dans MatLab. Ceci a permis de démontrer clairement l'influence des perturbations fortes de vitesse du champ mesurable (Fig. R 18 - Fig. R 21).

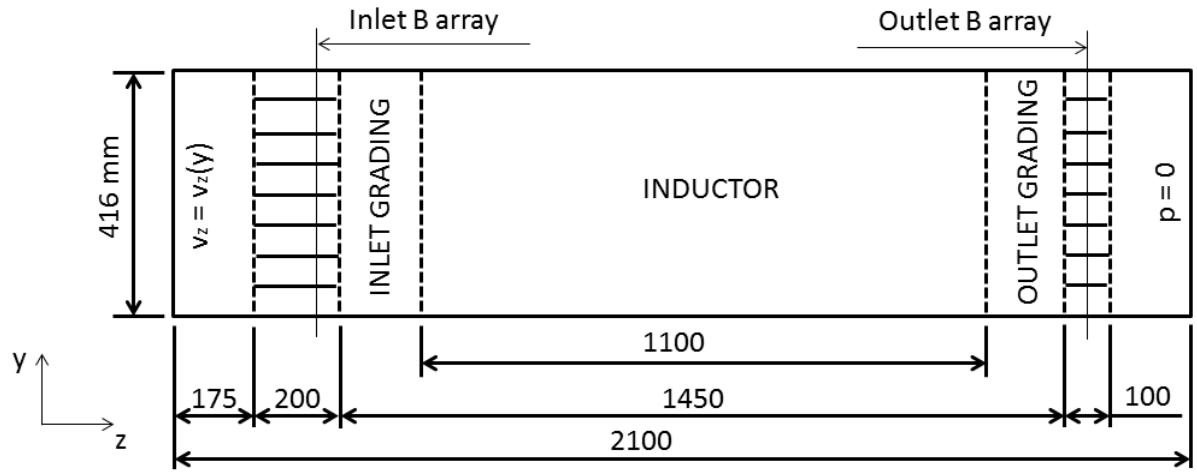

Fig. R 17. Géométrie et la configuration du modèle numérique sans sous-canaux.

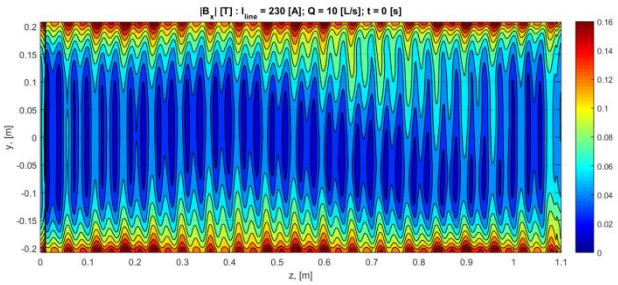

Fig. R 18. $|B_x|$ [T]: $Rm_s = 4.47$, $t = 0$ s.

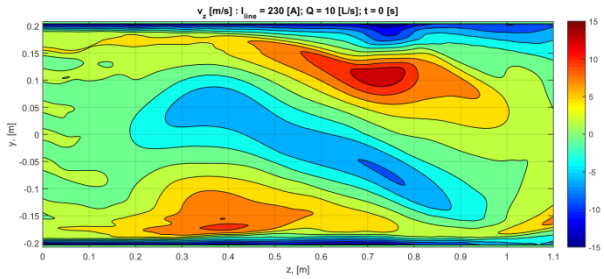

Fig. R 19. v_z [m/s]: $Rm_s = 4.47$, $t = 0$ s.

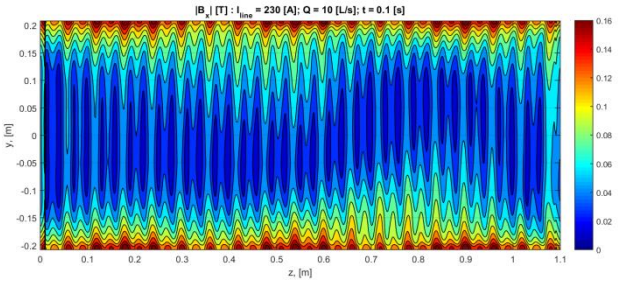

Fig. R 20. $|B_x|$ [T]: $Rm_s = 4.47$, $t = 0.1$ s.

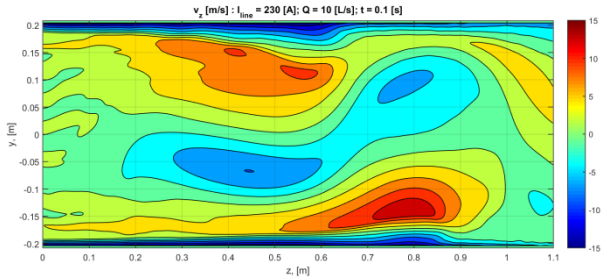

Fig. R 21. vz [m/s]: $Rm_s = 4.47$, $t = 0.1$ s.

Finalement, dans le cas d'un $Rm_s = 3.5$, l'écoulement est jusqu'au milieu de la zone d'inducteur et puis la forme de la distribution de la vitesse non homogène est semblable au cas précédent. Aucun changement évident de la distribution du champ magnétique ne peut être observé.

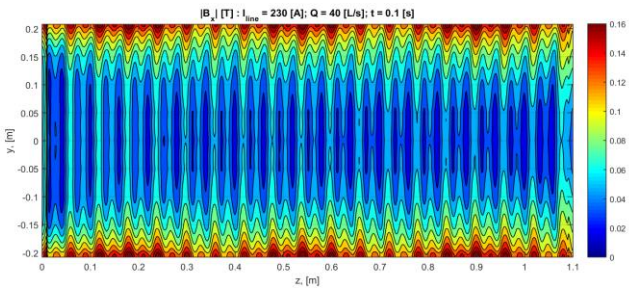

Fig. R 22. $|B_x|$ [T]: $Rm_s = 3.5$, $t = 0.1$s.

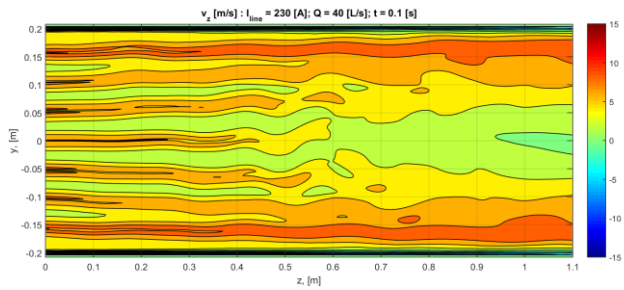

Fig. R 23. v_z [m/s]: $Rm_s = 3.5$, $t = 0.1$s.

Puis le profil de la différence de potentiel entre les parois d'acier inoxydable dans l'entrée et la sortie de la FLIP est calculé en utilisant le champ magnétique DC appliqué. Nous avons prouvé que les perturbations significatives dans le débouché sont prévues dans tous les cas étudiés (Fig. R 24- Fig. R 27).

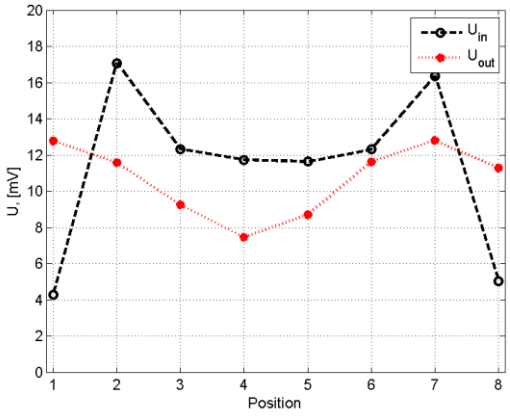

Fig. R 24. Différence de potentiel: $Rm_s = 4.47$.

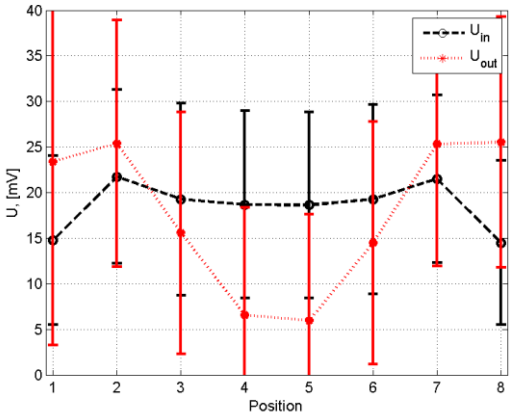

Fig. R 25. Différence de potentiel: $Rm_s = 4.15$.

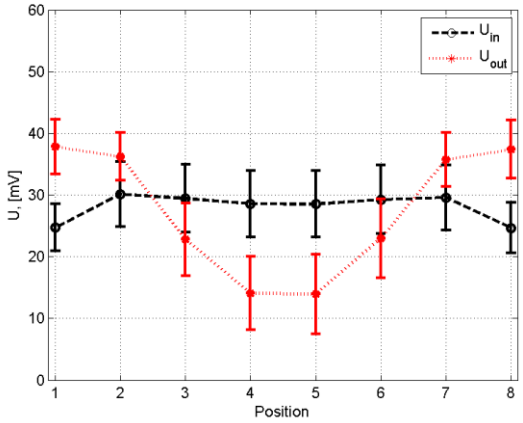

Fig. R 26. Différence de potentiel: $Rm_s = 3.82$.

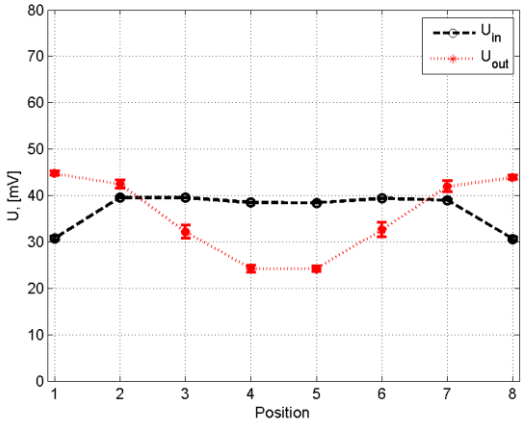

Fig. R 27. Différence de potentiel: $Rm_s = 3.5$.

En conclusion, l'analyse de la pression développée et de ses pulsations a montré un accord qualitatif avec la théorie et la tendance de l'augmentation des pulsations de LF avec la croissance du paramètre Rm_s (Fig. R 28 - Fig. R 31).

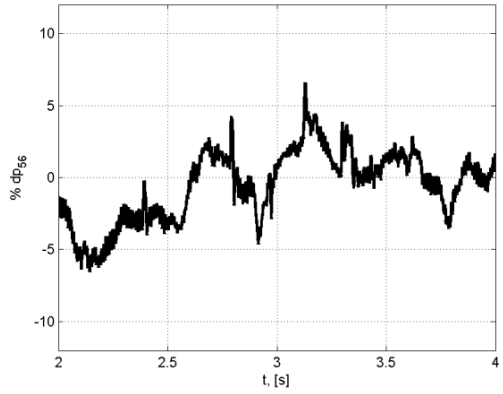

Fig. R 28. Pulsations de pression développée: $Rm_s = 4.47$.

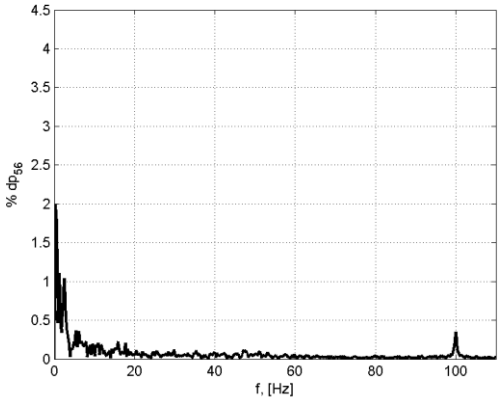

Fig. R 29. Spectre de pulsations de pression: $Rm_s = 4.47$.

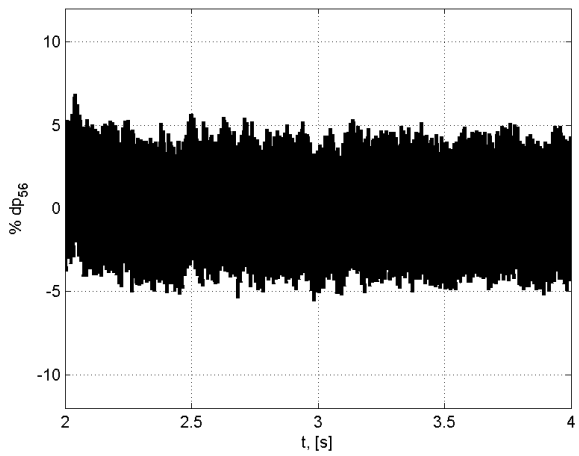

Fig. R 30. Pulsations de pression développée: $Rm_s = 3.5$.

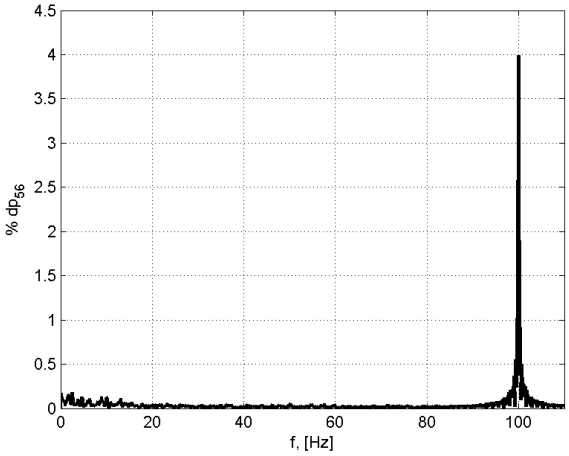

Fig. R 31. Spectre de pulsations de pression: $Rm_s = 3.5$.

CHAPITRE 4 : INVESTIGATIONS EXPÉRIMENTALES

Toutes les activités expérimentales mettant en jeu du sodium ont été effectuées à l'institut de l'université de physique de la Lettonie (IPUL, Salaspils) sur l'installation TESLA-EMP de type FLIP (essai et boucle expérimentale de sodium pour l'analyse des pompes électromagnétiques), voir Fig. R 32 et Fig. R 33.

La boucle peut être divisée en plusieurs parties :

1. Boucle hydraulique de sodium liquide
2. Système de chauffage électrique et de contrôle
3. Système de contrôle d'alimentation
4. Système de gaz et de vide
5. Mesure et système par acquisition de données.

La boucle hydraulique de sodium comprenant un tube de diamètre nominal DN125 a une section carrée avec de chaque côté environ 4m dans la longueur. Elle est conçue avec la possibilité d'actionner deux perturbations en parallèle sur ou l'une ou l'autre série.

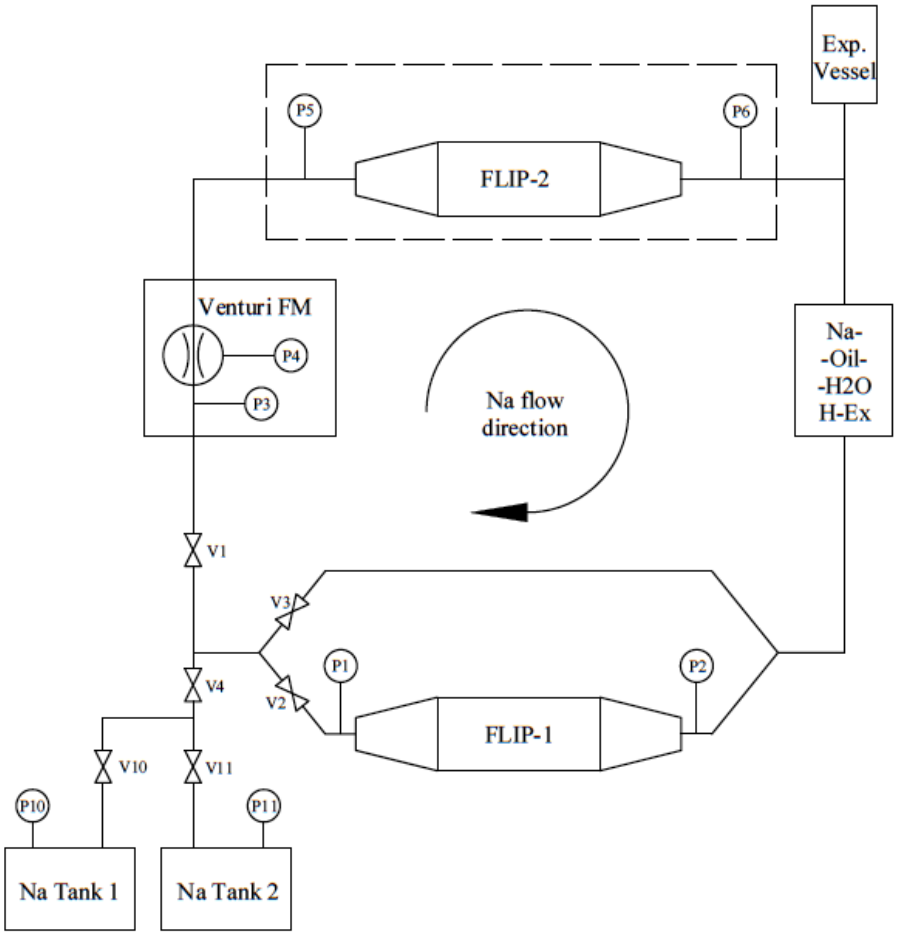

Fig. R 32. Schéma d'installation TESLA-EMP.

Fig. R 33. Photo de l'installation TESLA-EMP.

L'alimentation d'énergie de la pompe FLIP-1 a été réalisée utilisant le générateur mécanique et la tension de 100 kilowatts commandés avec le rhéostat électronique en changeant le courant d'excitation. Quand FLIP-2 a été ajouté, la puissance a été fournie par le transformateur de puissance. Les deux pompes sont actionnées avec la fréquence 50Hz. La tension entre les phases a été mesurée utilisant les transformateurs d'abaissement de type ERA E-I 48/16.8 et le courant de ligne utilisant les transformateurs de courant (E) ASK 51,4 250/5A. Des enroulements de l'inducteur des pompes ont été connectés en triangle (Δ).

La pression de sodium a été mesurée avec les manomètres piézoélectriques de Keller 35XHTC. La pression développée dans FLIP-1 a été mesurée au le débouché et à l'admission de la pompe (P1 et P2), tandis que la pression de FLIP-2 l'a été avec (P5 et P6). Le débit unitaire de la boucle est dans le sens horaire. Il est réglé électriquement ou mécaniquement par la valve (V1) et mesuré par le tube de Venturi interne utilisant des manomètres (P3 et P4). Le côté divisé en deux branches peut être commandé par des valves (2 et 3) électriquement ou mécaniquement. Pendant l'expérience la valve (V3) était toujours en position de fermeture. La boucle a été remplie à partir de deux réservoirs d'approvisionnement et de la pression a été surveillée avec les manomètres électroniques (P10 et P11). Des mesures de champ magnétique ont été effectuées par les échantillonneurs particulièrement développés.

Le système par acquisition de données a consisté principalement en équipement des National Instruments: cDAQ de Ni - 9188, Ni 9213 pour les mesures de la température, Ni 9205 pour toutes autres mesures.

Des mesures lors du fonctionnement ont été enregistrées utilisant le PC avec l'interface du logiciel LabView. Le courant d'entrée de l'EMIP était commandé par l'interface numérique, mais le débit unitaire a été placé sous le contrôle d'utilisation d'opérateur électro/mécanique. La température, la pression, le débit unitaire, le champ magnétique, l'alimentation en courant et la tension ont été mesurés.
Toutes ces mesures peuvent être divisées en deux groupes selon la fréquence de mesure :

- Rapide - 1 ou 2 kilohertz : champ magnétique, courant, tension, pression
- Lente - 75 hertz : la température, débit unitaire, différence potentielle

Puis toutes les échelles de temps nécessaires pour l'analyse sont obtenues en post-traitant des signaux dans LabView directement ou à l'aide des outils externes (MatLab en particulier).

Un des aspects clé dans le travail expérimental est le développement du système de mesure de champ magnétique à l'aide des échantillonneurs munies de petites bobines de noyau de ferrite (EPCOS B82451N). En dépit des avantages comme : le prix bas, la petite taille et le rapport élevé du signal-bruit, la saturation du matériel de noyau et l'influence de la température doivent être considérés. Tous les deux effets étaient étudié séparément. Nous concluons que la mesure du champ magnétique est essentiellement la mesure de la valeur de crête du signal, qui devient plus étroit à mesure que le champ augmente. Par conséquent la bonne discrétisation temporelle est nécessaire. Du point de vue de la température, le matériel du noyau ne doit pas dépasser 130ºC et il doit être commandé par par la mesure de la résistance de fil de bobine. Ceci a été mis en application seulement dans la deuxième installation expérimentale sans sous-canaux.

Dans l'installation expérimentale avec 4 sous-canaux, nous avons utilisés 8 échantillonneurs de champ magnétique ayant chacun 3 points de mesure (canal central, canal latéral et extérieur le canal) avec des mesures différentielles (Fig. R 34). Les signaux obtenus dans les mesures sans sodium ont montré que cela dû aux fréquences fantômes de discrétisation temporelle insuffisante pourrait apparaître dans les cas du champ fort.

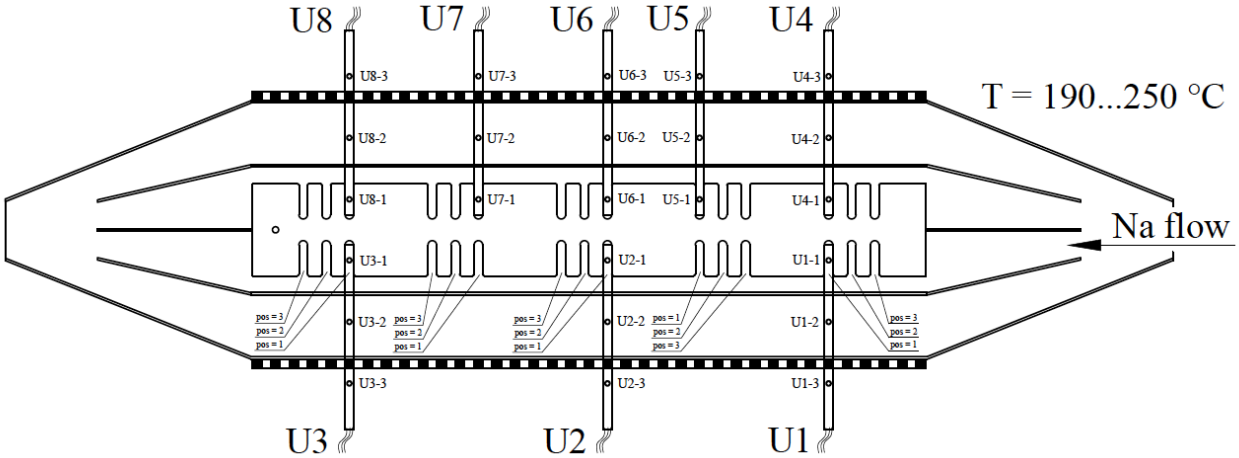

Fig. R 34. Un schéma de mesures dans la configuration expérimentale

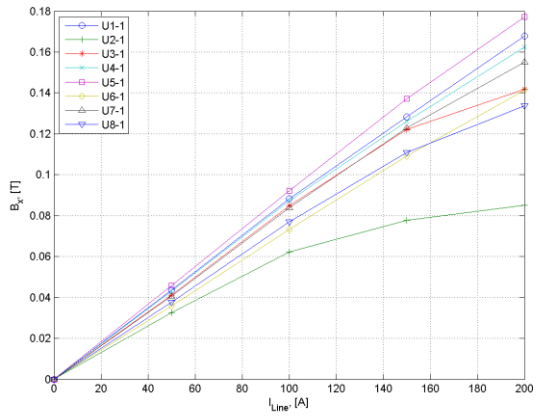

Fig. R 35. $|B_x|$ en tant que fonction of I_{line} pour tous les échantillonneurs 1st bobine.

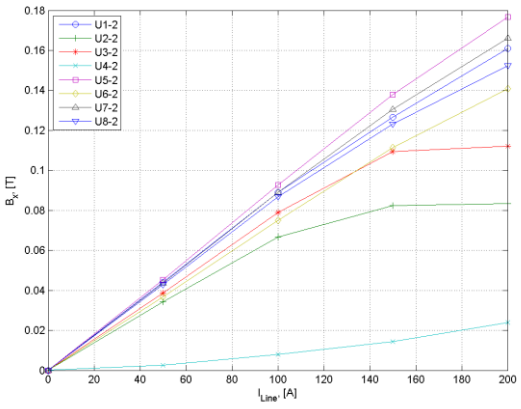

Fig. R 36. $|B_x|$ en tant que fonction of I_{line} pour tous les échantillonneurs 2nd bobine.

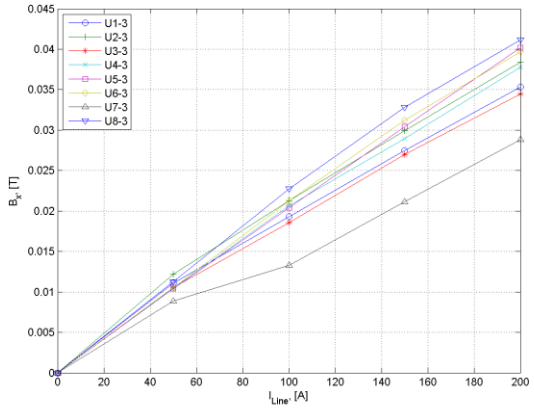

Fig. R 37. $|B_x|$ en tant que fonction of I_{line} pour tous les échantillonneurs 3rd bobine.

Le signal mesuré était fort (le couple de V) et de niveau de bruit n'est pas un problème dans ce cas, suggérant que la mesure simple de bobine pourrait être faite avec la précision suffisante. De façon générale, les mesures du champ magnétique ont montré les linéarités acceptables (Fig. R 35 - Fig. R 37).

Dans l'expérience avec des caractéristiques de sodium liquide et des possibilités globales d'installation de TESLA-EMP ont été examinés. Il était possible d'imposer un débit unitaire jusqu'à 45 [l/s], cependant, un tel régime est toujours avec la valeur haute du nombre de Reynolds magnétique. Il s'est avéré que cette accroissement de la puissance d'alimentation d'énergie était nécessaire pour la FLIP dans le régime de plus haut Net de plus bas Rm_s ce qui permet de caractériser avec plus de précision la transition du régime stable à instable. La solution future serait variation de la fréquence

Les manomètres Keller 35 de XHTC (barre 0-10) disponibles dans le commerce de XHTC se sont avérés être une solution plutôt bonne. En analysant des signaux des pulsations de pression nous avons décelé quelques crêtes de basses fréquences (environ 12 et 25 hertz), bien que leurs amplitudes aient été comparativement petites, environ 0,3% de la pression moyenne (Fig. R 38 - Fig. R 41).

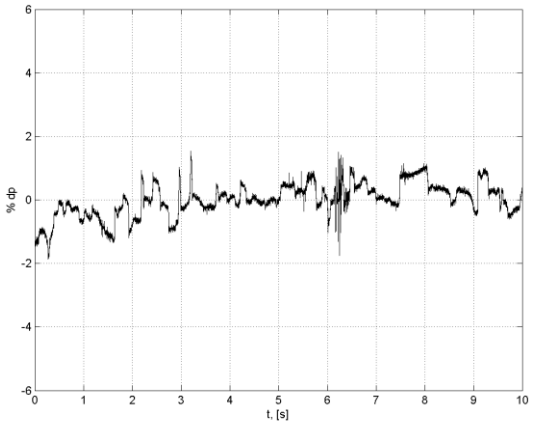

Fig. R 38. Pulsations de différence de pression développée: $N = 0.67$, $Rm_s = 4.8$.

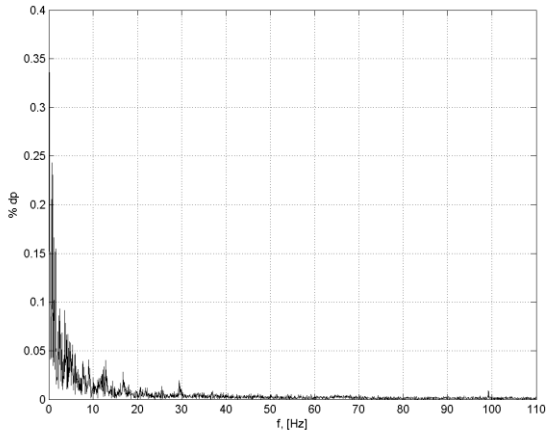

Fig. R 39. Spectre de pulsations de pression: $N = 0.67$, $Rm_s = 4.8$

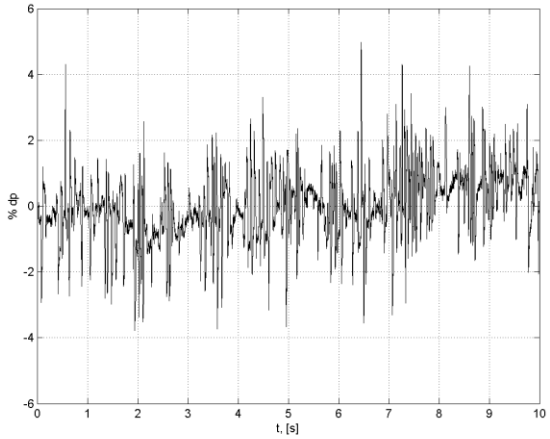

Fig. R 40. Pulsations de différence de pression développée: $N = 0.67$, $Rm_s = 3.33$.

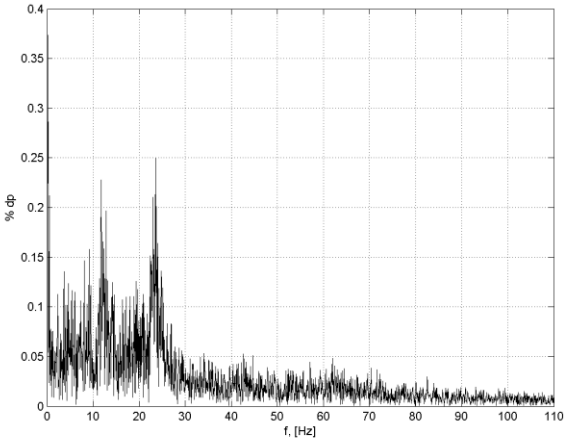

Fig. R 41. Spectre de pulsations de pression: $N = 0.67$, $Rm_s = 3.33$.

Dans la cas avec le métal liquide, nous avons observé qualitativement un comportement du champ magnétique identique à celui du modèle numérique (Fig. R 42 - Fig. R 44):

- Le champ magnétique est plus fort dans le canal latéral
- L'augmentation du champ magnétique de lorsque le débit unitaire croît
- L'augmentation est plus rapide dans le canal latéral.

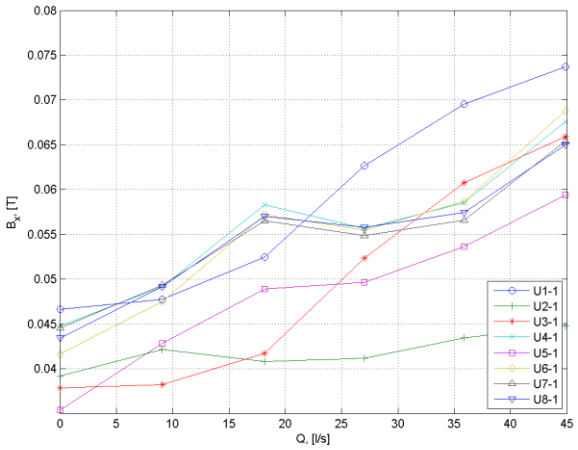

Fig. R 42. $|B_x|$ for UX-1: $N = 0.67$.

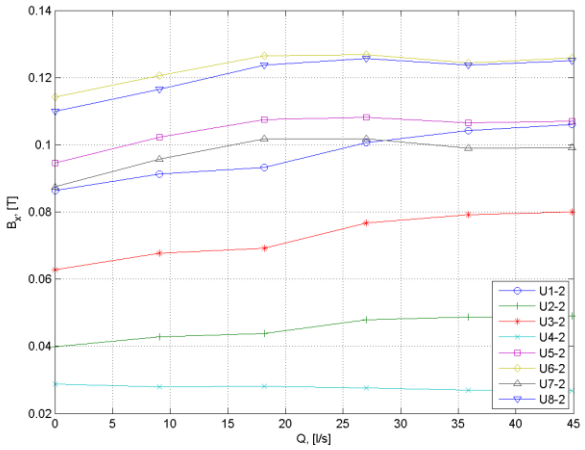

Fig. R 43. $|B_x|$ for UX-2: $N = 0.67$.

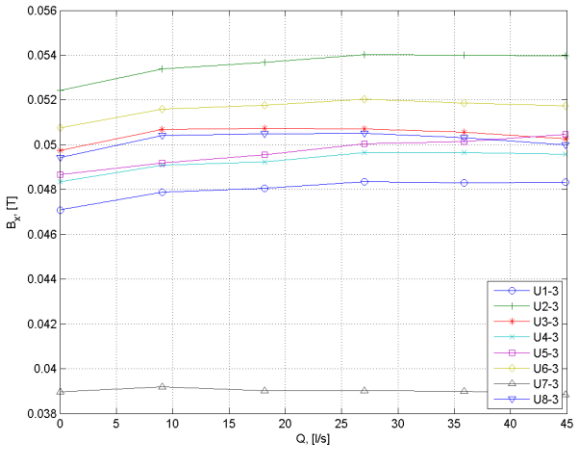

Fig. R 44. $|B_x|$ for UX-3: $N = 0.67$.

Il est intéressant de constater que la distribution et le comportement asymétriques du champ magnétique qui ont été enregistrés, n'ont pas été retrouvés numériquement. Une des raisons d'un tel résultat pourrait être influence de la géométrie et le fait que l'admission que le profil de vitesse dans l'admission n'est pas homogène, qui a été supposée dans le modèle numérique. Cet effet a été en partie pris en considération dans l'étude du dernier développement.

En récapitulation l'expérience préliminaire a montré également un l'accord qualitatif avec l'analyse numérique faite auparavant, même s'il y a un certain manque de cohérence entre eux. Cependant fait le plus marquant, cette expérience a permis d'améliorer les techniques de mesure ainsi que le système d'acquisition de données pour des mesures plus détaillées de champ magnétique dans la prochaine expérience.

Dans l'expérience sans sous-canaux la philosophie des investigations a été modifiée de manière significative. Tout d'abord, une FLIP-2 a été ajoutée dans la boucle avec la géométrie de canal sans parois dans le sens de la longueur. L'écoulement n'a donc pas été limité par certains chemins et de plus grandes structures tourbillonnaires peuvent théoriquement se former. FLIP-1 a été maintenue dans la boucle en tant que pompe technologique. Deuxièmement, dans l'admission et le débouché les 8 zones du canal, sont séparées par des parois en acier inoxydable. Des débitmètres par conduction ont été introduits pour caractériser la distribution de vitesse à l'admission et au débouché. Ceci a été fait utilisant la rangée d'aimants permanents de polarité opposée et de différence de mesure de tension sur la paroi.

En conclusion, des mesures ont été effectuées en 144 points couvrant la surface de l'inducteur du champ magnétique et de la température dans l'entrefer, ce qui a permis d réaliser une 2D image de la distribution.

Le système de mesure détaillé de champ magnétique se compose de 36 échantillonneurs (U1 - 36) avec 4 bobines chacun. Elles sont distribuées dans 18 rangées avec les connexions électriques des deux côtés. Par conséquent les bobines sont également distribuées par un réseau de 18 x 8, bobines distantes de 60 millimètres par 51,5 millimètres, couvrant pratiquement toute la surface d'inducteur. Puisque le signal suffisamment fort a été obtenu dans l'expérience précédente, on a décidé d'employer la bobine simple par point au lieu de la connexion différentielle. Également, la fréquence de mesure de champ magnétique a été augmentée jusqu'à 2 kilohertz. La réalisation du système de mesure est montrée dans la Fig. R 45. La vue globale sur du système de mesure est montrée dans la Fig. R 46.

Fig. R 45. Système magnétique de mesure de champ sur la surface de l'inducteur.

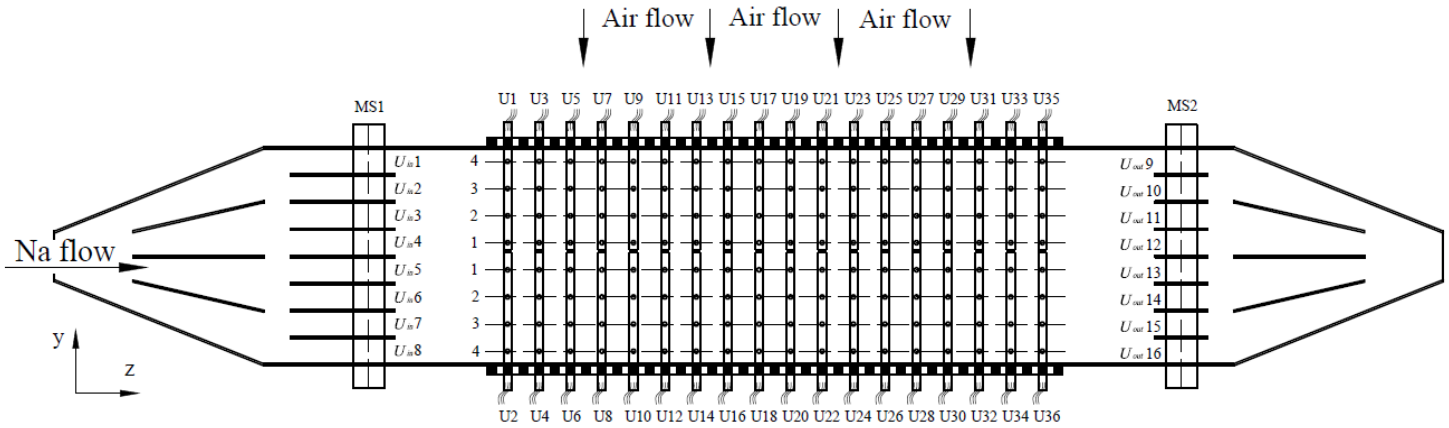

Fig. R 46. Un système de mesure dans l'expérience sans sous-canaux.

L'intervalle de temps de mesure relativement petit permet de capturer la dynamique des structures instables au-dessus du canal. On peut estimer qu'avec une maille de 60 millimètres par 51,5 millimètres et une période de 0,05s, il est possible de capturer avec précision le mouvement des structures avec la vitesse ~1 m/s. Au cas où les structures se déplaceraient avec des vitesses plus élevées, il serait encore possible de les capturer, quoiqu'elles pourraient croiser plusieurs éléments de cellules pendant un intervalle de temps

Toutes les données obtenues ont été traitées à l'aide du logiciel de MatLab en ajoutant également les points extrapolés entre la grille des mesures pour lisser les contours de dessin. Le programme était écrit de manière, pouvoir changer l'intervalle de temps dans lequel le champ magnétique a été calculé.

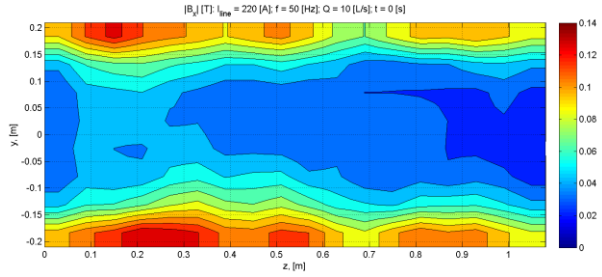

Fig. R 47. $|B_x|$ *[T]:* $Rm_s = 4.47$, *t = 0 s.*

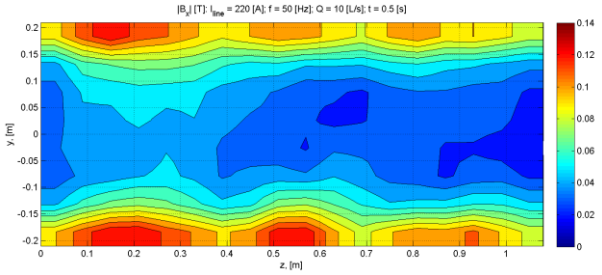

Fig. R 48. $|B_x|$ *[T]:* $Rm_s = 4.47$, *t = 0.5 s.*

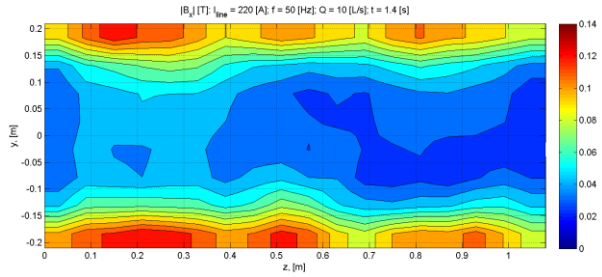

Fig. R 49. $|B_x|$ *[T]:* $Rm_s = 4.47$, *t = 1.4 s.*

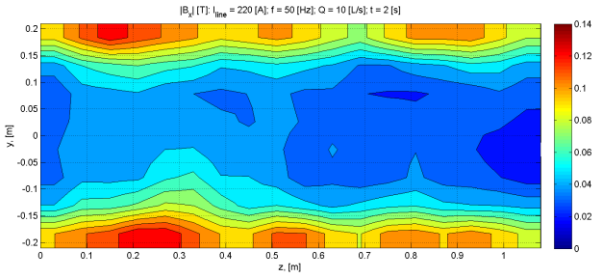

Fig. R 50. $|B_x|$ *[T]:* $Rm_s = 4.47$, *t = 2 s.*

Tout cet effort a eu comme conséquence la possibilité de capturer la dynamique de la distribution de champ magnétique au-dessus de la surface du canal. Les structures périodiques et oscillantes sont obtenues ainsi que l'asymétrie du champ observé en cas de plus haut (Fig. R 47Fig. R 50).

Pour des valeurs plus basses de telles oscillations fortes ne sont pas observés et la distribution du champ est relativement symétrique (Fig. R 51, Fig. R 52). Ceci correspond bien aux prévisions numériques.

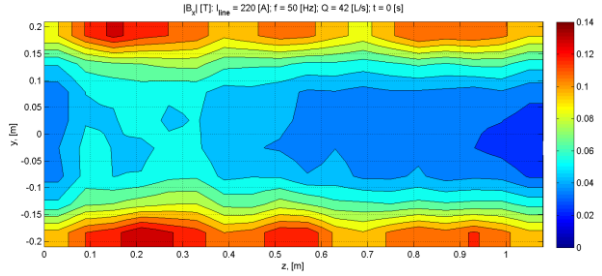

Fig. R 51. $|B_x|$ *[T]:* $Rm_s = 3.43$, *t = 0 s.*

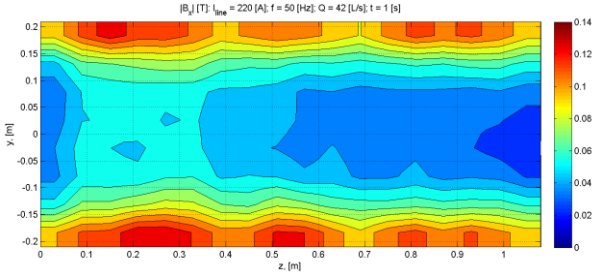

Fig. R 52. $|B_x|$ *[T]:* $Rm_s = 3.43$, *t = 1 s.*

Les différences de potentiel mesurées dans l'admission et le débouché du canal ont de manière étonnante montré une amplitude de perturbation plus élevée des profils et des oscillations plus élevées dans l'admission de la FLIP-2 (Fig. R 53 - Fig. R 56). Ce résultat inattendu doit être vérifié, car les résultats numériques suggèrent l'opposé. Autrement, la forme des profils et leur comportement (les oscillations diminuent avec la diminution de Rm_s) sont conformes aux évaluations numériques.

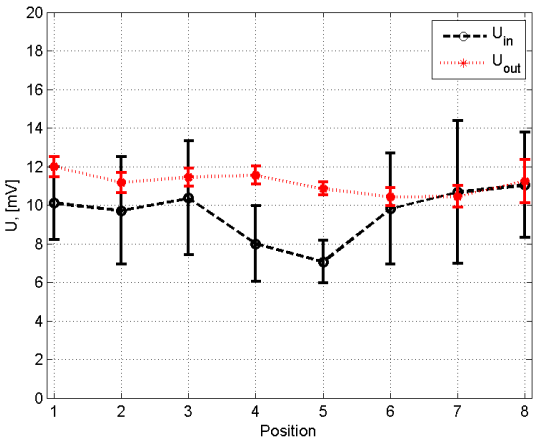

Fig. R 53. Profils de différence de potentiel: $Q = 10\ [L/s];\ Rm_s = 4.47$

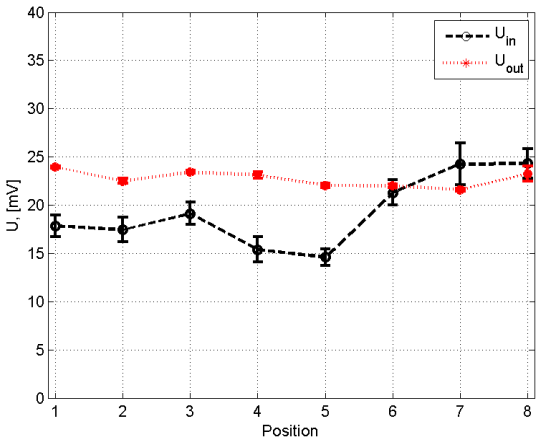

Fig. R 54. Profils de différence de potentiel: $Q = 20\ [L/s];\ Rm_s = 4.15$

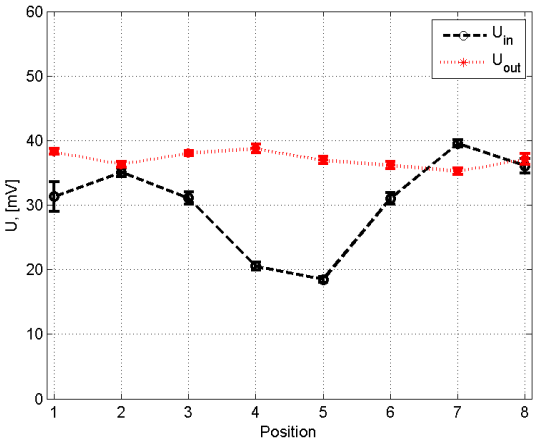

Fig. R 55. Profils de différence de potentiel: $Q = 30\ [L/s];\ Rm_s = 3.82$

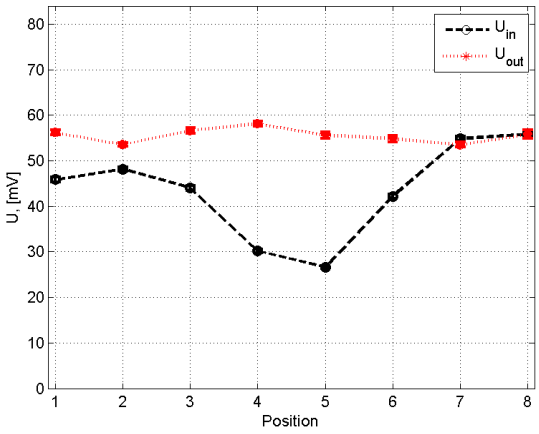

Fig. R 56. Profils de différence de potentiel: $Q = 42\ [L/s];\ Rm_s = 3.43$

La pression et ses pulsations ressemblent qualitativement aux calculs numériques. On observe alors des oscillations de pression de basse fréquences dans tous les cas avec l'ordre de grandeur autour de 1-2% (Fig. R 57, Fig. R 58). En conclusion, des pulsations de DSF ont été également enregistrées en cas où $\mathrm{Rm_s} = 3.43$ (Fig. R 59, Fig. R 60).

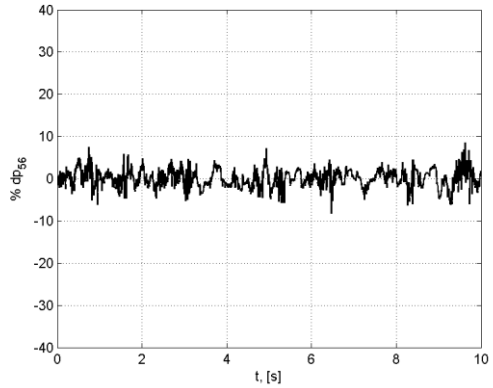

Fig. R 57. Pulsations de différence de pression développée: $Q = 10\ [L/s];\ Rm_s = 4.47$

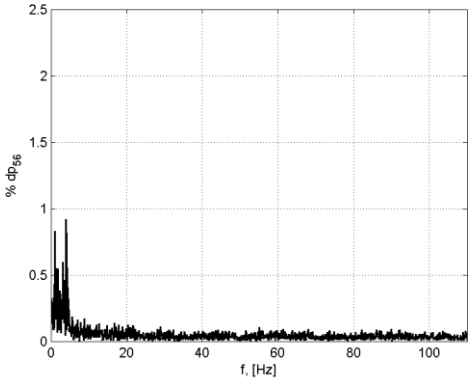

Fig. R 58. Spectre des oscillations: $Q = 10\ [L/s];\ Rm_s = 4.47$

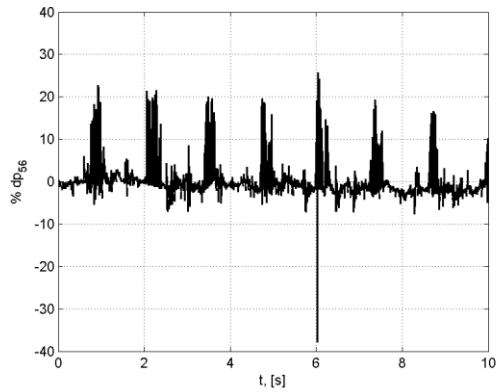

Fig. R 59. Pulsations de différence de pression développée: $Q = 42\ [L/s];\ Rm_s = 3.43$

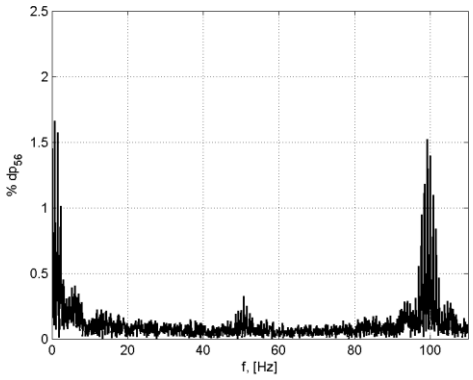

Fig. R 60. Spectre des oscillations: $Q = 42\ [L/s];\ Rm_s = 3.43$

Pour finir, le contrôle présenté de la température montré, cette bobine ne sont pas surchauffés (Fig. R 61, Fig. R 62).

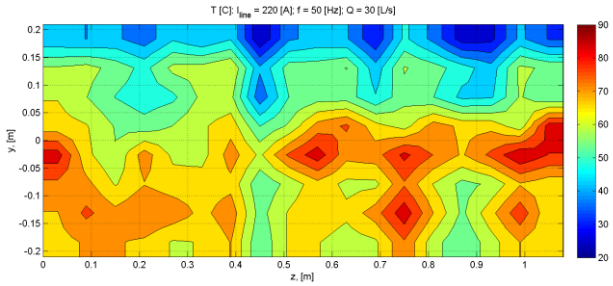

Fig. R 61. La distribution de la température: T [C], $Rm_s = 3.82.$

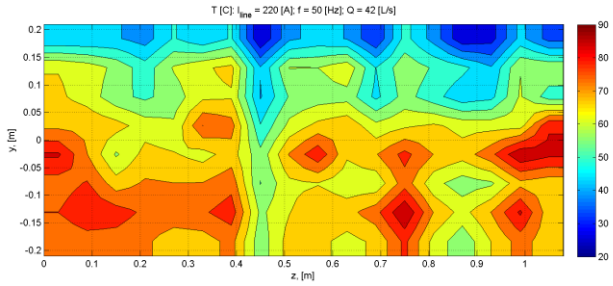

Fig. R 62. La distribution de la température: T [C], $Rm_s = 3.43$

Finalement, on peut conclure que dans ces activités expérimentales un certain nombre de nouvelles approches et de méthodes d'analyse ont été présentées pour capturer le processus d'instabilité. De telles mesures détaillées de dynamique de champ n'ont été jamais faites ou rapportées auparavant. Cette nature originale du travail a également apporté quelques erreurs dans le développement de les investigations expérimentale et numérique, ce qui a introduit ensuite des difficultés de comparaison dans certains cas. Par conséquent le haut niveau d'attention aux détails est indispensable dans ce travail exigeant de précision.

CHAPITRE 5 : CONCLUSIONS ET PERSPECTIVES

Un certain nombre de nouveaux résultats théoriques ont été obtenus et analysés dans ce travail. En outre, le développement des modèles numériques et les nouvelles approches expérimentales donnent une portée plutôt large de l'étude. Prenant en considération la nature de l'étude et la quantité nouvelle de cette investigation, toutes les questions n'ont pas été entièrement résolues. Néanmoins, quelques avancées importantes dans l'étude de l'instabilité de magnétohydrodynamique ont été réalisées et récapitulées complétées par de futures perspectives.

Des résultats mis en évidence **au chapitre 2 sur les investigations théoriques** (estimation du taux de croissance de perturbation (94) et de la vitesse de phase (93)),

l'évaluation du développement spatial de la perturbation (95) peut être trouvée. Cela donne une idée sur l'évolution de la perturbation initiale existante et de son amplification. Cependant, dans la comparaison détaillée avec des résultats expérimentaux trouvés dans la littérature, la théorie ne prévoit pas la perte de la stabilité (Fig. R 3). Apparemment, elle ne capture pas le phénomène complètement et quelques améliorations sont nécessaires. Une des futures tâches sera de construire le seuil d'instabilité absolue en résolvant numériquement la relation de dispersion complète.

Des méthodes opératoire de stabilisation d'une ALIP idéale sont discutées. On montre que si il y a la possibilité de commander la fréquence et le courant dans une plage suffisante, un régime stable d'opération peut être facilement trouvé selon les conditions de fonctionnement désirées (Fig. R 4). Puis la technique de stabilisation comportant l'opération avec une autre fréquence pour rencontrer la vitesse moyenne du métal liquide est étudiée. On lui a montré dans Fig. R 6 utilisant l'analyse de stabilité linéaire que le courant maximal de stabilisation peut être trouvé et il ne dépasse pas 36 % du courant d'entraînement (153). D'une manière primordiale, on a montré que, la stabilisation d'une ALIP est essentiellement liée à la correction du gradient du rapport de force-vitesse au point considéré (Fig. R 5).

Une des futures tâches les plus intrigantes est d'examiner la technique de stabilisation discutée et de vérifier si les évaluations du courant nécessaire présentées dans ce travail sont correctes. On doit également prendre en considération le fait que l'analyse seul les parties quasi-stationnaires de la force ont été considérées. Cependant, la situation est davantage compliquée dans le cas général car la partie pulsante de force régie par la différence de fréquence peut présenter des oscillations non désirées. Une installation expérimentale possible pourrait être construite comprenant la pompe avec deux inducteurs où l'un d'entre eux est fourni par l'entraînement, l'autre stabilisant la source.

Dans le chapitre 3 des investigations numériques relative à une étude d'instabilité magnétohydrodynamique dans une ALIP idéale ont été effectuées. Le modèle périodique comprenant une seule période d'ALIP idéale a été comparé à la théorie et a donné des résultats raisonnables (Fig. R 7 - Fig. R 11), quoique quelques problèmes de la discrétisation spatiale et/ou temporelle n'aient pas été approfondis. La comparaison du taux temporel de croissance prédit numériquement s'agissant du développement de la perturbation avec la théorie a prouvé qu'elle dépend fortement du paramètre d'interaction. La bonne concordance n'est pas obtenue dans tous les cas quoique qualitativement le phénomène soit bien capturé. Dans tous les cas le seuil de stabilité prédit numériquement est plus élevé que celui prédit par l'analyse théorique, particulièrement avec des valeurs de N élevées.

Ces incertitudes définissent la portée des travaux futurs possibles raffinant le modèle numérique. La complexité dans ce cas est également reliée à la nécessité existante d'améliorer la théorie (comme indiqué précédemment). Néanmoins, quelques premières étapes sérieuses ont été faites dans la maîtrise des méthodes théoriques et numériques de cette analyse, qui exige une haute précision.

Par la suite, le premier modèle de la FLIP réaliste avec 4 sous-canaux, n'était qu'un essai, principalement en raison du manque d'expérience avec de tels problèmes. Les résultats obtenus ont indiqué que la vitesse et le champ magnétique est plus fort dans les canaux

latéraux, mais au centre l'écoulement de retour est possible particulièrement dans les cas du bas débit unitaire est faible (Fig. R 15, Fig. R 16). On considère qu'un tel type d'écoulement est principalement dû à la géométrie de la FLIP dans le cas de Rm_s élevé.

Le modèle numérique sans sous-canaux était plus raffiné. La conservations nécessaire des valeurs des nombres sans dimensions a été obtenue par des changements des propriétés matérielles. Un système de distribution de vitesse à l'entrée fournissant un profil réaliste a été ajouté utilisant la géométrie 3D prenant en considération le modèle de la boucle. Les résultats des cas analysés prouvent que les structures tourbillonnaires des oscillations fortes de l'écoulement et du module du champ magnétique sont présentes pour les valeurs les Rm_s plus élevées (Fig. R 18 - Fig. R 21). On observe également des oscillations de basse fréquence dans les profils des spectres de différence potentielle (Fig. R 24 - Fig. R 25) et de pression d'une grandeur de 1-2% (Fig. R 28 - Fig. R 29). D'autre part pour le développement d'une inhomogénéité de vitesse au-dessus de la longueur du canal est observé, mais restant comparativement stable (Fig. R 22 - Fig. R 23). Aucune oscillation importante des profils de différence potentielle n'est observée dans ces cas (Fig. R 26 - Fig. R 27) et DSF dominent avec une amplitude jusqu'à 4% (Fig. R 30 - Fig. R 31).

Avec le futur développement du modèle numérique lui-même, il est nécessaire de développer une méthodologie cohérente d'analyse quantitative, pour que l'on puisse comparer directement les résultats théoriques/numériques ou numériques/expérimentaux. Par exemple pour le champ magnétique ou l'écoulement mesurés, une des manières possibles consiste à décomposer la distribution spatiale du champ en modes longitudinaux et transversaux utilisant la transformée de Fourier.

Le chapitre 4. est basé sur des résultats obtenus dans deux installations expérimentales à IPUL sur la boucle TESLA-EMP. La première installation technologique FLIP-1 comprend 4 sous-canaux tandis que dans la deuxième pompe expérimentale FLIP-2 comprend un système de mesure beaucoup plus détaillé.

Les mesures de champ magnétique, méthode utilisant la bobine de noyau de ferrite, ont joué un rôle fortement important et sont l'une des raisons principales de la réussite des activités expérimentales.

Dans la première expérience le matériel d'essai a été utilisé pour la première fois sur la boucle de TESLA-EMP et a montré de bonnes capacités. Les tendances globales sont conformes qualitativement aux attentes numériques. Cette expérience a été utile pour améliorer l'installation suivante.

Des mesures plus détaillées ont été effectuées dans la section expérimentale finale où FLIP-2 a été présentée. La distribution obtenue du champ magnétique a en effet montré que dans le cas de valeurs plus élevées de $Rm_s = 4.47$, des oscillations champ apparaissaient (Fig. R 47 - Fig. R 50) et diminuaient. Avec la diminution de $Rm_s = 3.43$, conduisant à une situation comparativement stable (Fig. R 51 - Fig. R 52). Ceci est bien en accord avec les résultats numériques.

La situation est légèrement différente avec des profils de différence de potentiel, quoique la même tendance soit observée. Les profils présentent moins d'oscillation et le signal

global se développe avec la diminution de Rm_s, le profil le moins perturbé est obtenu à la sortie et le plus perturbé à l'entrée (Fig. R 53 - Fig. R 56). C'est exactement le contraire dans les simulations numériques. Les raisons d'un tel résultat sont peu claires. Une des possibilités est qu'il y a eu erreur humaine dans le programme du système d'acquisition de données. Une autre raison pourrait être relative à un certain phénomène physique inattendu qui n'est pas pris en considération dans la modélisation numérique.

Les futures améliorations possibles de l'installation expérimentale concernent principalement le système d'alimentation en énergie. Les régimes à bas paramètre d'interaction et à nombre de Reynolds magnétique de glissement élevé sont principalement obtenus pour un courant élevé mais celui-ci est limité par les possibilités de la source de puissance et l'impossibilité du changement de fréquence. En effet si la fréquence pouvait être changée (abaissée en l'occurrence), ceci permettrait d'étudier des régimes dans zone de transition (prédite par la théorie) entre régimes stable et instable. Malheureusement, ce n'était pas possible dans le travail actuel.

Un autre inconvénient dans l'installation actuelle s'est avéré être l'intensité du champ magnétique continu utilisé pour les mesures de potentiels. Le champ magnétique fort garantit un signal suffisamment fort, mais a comme conséquence une baisse de pression inutile. Ce point certainement peut être optimisé.

Des méthodes de traitement des données traitement déjà mentionnées devraient être améliorées. Cependant, une des questions du plus grand intérêt est possibilité de recalculer la distribution de l'écoulement dans le canal à partir des mesures du champ magnétique. La tâche n'est pas simple et exigerait une idée claire sur les potentialités des méthodes requises telles que la corrélation croisée. Néanmoins, avec une quantité appropriée d'effort ceci semble être réalisable et augmenterait l'importance des mesures de champ magnétique présentée.

Enfin, l'auteur voudrait conclure ce mémoire en affirmant que ce problème d'instabilité magnétohydrodynamique dans une pompe ALIP (et aussi dans la pompe FLIP), n'est pas encore résolu et ni complètement n'est étudié. Il est trop important pour être achevé dans un travail simple de doctorat. Néanmoins, l'auteur aimerait penser que le présent travail peut servir au moins de référence à toute autre activité sur ce sujet, car un nombre de questions importantes a été discuté et certains des problèmes ont été résolus. La nature des résultats de ce travail reste encore qualitative et un effort a été réalisé pour se rapprocher des conditions d'une étude quantitative. Dans un avenir proche, un tel but sera sans doute atteint.

ABSTRACT

The research explores the issue of magnetohydrodynamic (MHD) instability in electromagnetic induction pumps with focus on the regimes of high slip Reynolds magnetic number (Rm_s) in Annular Linear Induction Pumps (ALIP) operating with liquid sodium. The context of the thesis is French GEN IV Sodium Fast Reactor research and development program for ASTRID in a framework of which the use of high discharge ALIP in the secondary cooling loops is being studied. CEA has designed, realized and will exploit PEMDYN facility, able to represent MHD instability in high discharge ALIP.

In the thesis stability of an ideal ALIP is elaborated theoretically using linear stability analysis. Analysis revealed that strong amplification of perturbation is expected after convective stability threshold is reached. Theory is supported with numerical results and experiments reported in literature. Stable operation and stabilization technique operating with two frequencies in case of an ideal ALIP is discussed and necessary conditions derived.

Detailed numerical models of flat linear induction pump (FLIP) taking into account effects of a real pump are developed. New technique of magnetic field measurements has been introduced and experimental results demonstrate a qualitative agreement with numerical models capturing all principal phenomena such as oscillation of magnetic field and perturbed velocity profiles. These results give significantly more profound insight in the phenomenon of MHD instability and can be used as a reference in further studies.

Keywords: MHD, instability, pump, electromagnetic, sodium

RESUME

La recherche actuelle dans le domaine des pompes à induction électromagnétique s'oriente sur la question de l'instabilité MagnétoHydroDynamique (MHD) avec un intérêt particulier pour les régimes à haut nombre de Reynolds magnétique de glissement (Rm_s). Notre étude se focalise sur les pompes à induction linéaires annulaires (ALIP) fonctionnant avec du sodium liquide. La thèse s'inscrit dans le contexte du programme français de recherche et développement de réacteur rapide en sodium de la GEN IV. Pour le démonstrateur ASTRID, l'utilisation d'une ALIP à haut débit dans les boucles de refroidissement secondaires est identifiée. Le CEA, a conçu, réalisé et exploitera la boucle PEMDYN, représentative d'instabilités MHD à hauts débits.

Dans cette étude, la stabilité d'une ALIP idéale est abordée du point de vue théorique en se focalisant sur l'analyse de la stabilité linéaire. L'analyse a révélé que la forte amplification de la perturbation est attendue lorsque le seuil de stabilité convective est atteint. La théorie est soutenue par les résultats numériques et des expériences rapportées dans la littérature. Le fonctionnement stable et les moyens de stabilisation jouant avec deux fréquences dans le cas d'une ALIP idéale est discuté et les conditions nécessaires obtenues.

Des modèles numériques détaillés de pompe plate à induction linéaire (FLIP) en tenant compte des phénomènes d'une véritable pompe sont développés. Une nouvelle technique de mesures du champ magnétique est introduite et les résultats expérimentaux démontrent un accord qualitatif avec des modèles numériques permettant de capturer tous les phénomènes principaux tels que l'oscillation du champ magnétique et les profils de vitesse perturbée. Ces résultats précisent les phénomènes d'instabilité MHD qui peuvent être rencontrés et peuvent être utilisés en tant que référence dans des études ultérieures.

Mots-clés: MHD, instabilité, pompe, électromagnétique, sodium